High-Q Low-Impedance MEMS Resonators

Li-Wen Hung
Clark Nguyen

Electrical Engineering and Computer Sciences
University of California at Berkeley

Technical Report No. UCB/EECS-2012-218
http://www.eecs.berkeley.edu/Pubs/TechRpts/2012/EECS-2012-218.html

December 1, 2012

Acknowledgement

I am indebted to Prof. Nguyen for his generous support and guidance. I would like to thank Prof. King Liu and Prof. Lin for serving on my qualifying exam and dissertation committees, as well as Prof. Alon for serving on my qualifying exam committee. Prof. Bhave (Cornell U.), Prof. Gianluca Piazza (U. of Pennsylvania), Prof. Pisano and Prof. Javey, Dr. Justin Black and Dr. Philip Stephanou (Qualcomn). They have provided me timely help when I needed them and valuable feedback to better my research.
I thank my current group members for their friendship and technical supports. I thank all of the BSAC directors and researchers for their endless efforts to make BSAC an even better environment for graduate students to learn and to grow professionally.

The deepest thanks go to my family.

High-*Q* Low-Impedance MEMS Resonators

by

Li-Wen Hung

A dissertation submitted in partial satisfaction of the

requirements for the degree of

Doctor of Philosophy

in

Engineering-Electrical Engineering and Computer Sciences

in the

Graduate Division

of the

University of California, Berkeley

Committee in charge:

Professor Clark T.-C. Nguyen, Chair

Professor Tsu-Jae King Liu

Professor Liwei Lin

Spring 2011

High-*Q* Low-Impedance MEMS Resonators

Abstract

High-*Q* Low-Impedance MEMS Resonators

by

Li-Wen Hung

Doctor of Philosophy in Engineering – Electrical Engineering and Computer Sciences

University of California, Berkeley

Professor Clark T.-C. Nguyen, Chair

The ever increasing need for regional and global roaming together with continuous advances in wireless communication standards continue to push future transceivers towards an ability to support multi-mode operation with minimal increases in cost, hardware complexity, and power consumption. RF channel-select filter banks pose a particularly attractive method for achieving multiband reconfigurability, since they not only provide the needed front-end reconfigurability, but also allow for power efficient and versatile transceiver designs, e.g., software-defined radio. Such channel-select filters, however, impose requirements on their constituent resonators that are not yet achievable on the micro-scale. Specifically, capacitively-transduced micromechanical resonators achieve high *Q*, but suffer from high impedance; while piezoelectric micromechanical resonators offer low impedance, but with insufficient *Q*. This dissertation demonstrates four new techniques to address the issues in both technologies.

Two of the methods recognize that sub-30 nm gap spacing enables electrostatic resonators to achieve acceptably low impedance. Unfortunately, however, such small gaps with the needed high aspect ratios are difficult to achieve via wafer-level batch processing. Two new methods are proposed and experimentally verified for forming sub-30 nm gaps: 1) partial-filling of electrode-to-resonator gaps with atomic layer deposition (ALD) of high-*k* dielectric; and 2) generating gaps via the volume reduction associated with a silicidation reaction. Among the many benefits provided by a silicide-based approach to gap formation is speed of release, where sub-30 nm gaps can be formed and high-aspect-ratio microstructures can be released via anneals lasting from seconds to a few minutes, regardless the lateral dimensions of the devices. Silicide-induced gap formation further does not require any etching and is applicable to a wide range of applications, from electronics to vacuum packaging.

The next two methods seek to circumvent the fact that AlN thin-film resonators have historically been measured with much lower *Q* than capacitive ones at similar frequencies. As a result, it was commonly accepted that the AlN thin films sputtered at low temperatures are to blame for the lower *Q*. This dissertation provides experimental evidence that it is not AlN material loss that restricts the *Q*'s of conventional AlN resonators, but rather the losses associated with their contacting electrodes. Specifically, a new transducer dubbed the “capacitive-piezoelectric” transducer is introduced that lifts the electrodes away from a piezoelectric resonator by tiny nanometer scale gaps that retain strong electric fields for good electromechanical coupling, while eliminating electrode-derived losses. After removing the electrode losses, the *Q*’s of piezoelectric AlN resonators rise by up to 9 times. A new surface-micromachining fabrication process has been developed for the capacitive-piezoelectric resonators, where the metal electrodes are separated from the AlN resonators by small air (or vacuum) gaps. The second approach for tapping the material *Q* of AlN uses *Q*-boosting mechanical circuits, where the electrode-equipped AlN resonators are mechanically coupled to electrode-less ones to form a composite-array. In this structure, the energy shared among all of the resonators in the composite-array effectively ‘boost’ the *Q*’s of the electrode-equipped resonators. The *Q* of electrode-less resonators are extrapolated from the measurement data to be from 14,040 to 15,795. Both methods achieve measured *Q*’s exceeding 10,000, posting the highest reported *Q*’s for resonators constructed of sputtered AlN and confirming that AlN is indeed a high-*Q* material.

Professor Clark T.-C. Nguyen
Committee Chair

To my parents and my brother.

Table of Contents

Chapter 3: Silicide-Induced Gaps

Chapter 4: Capacitive-Piezoelectric Resonators

Acknowledgements

I am indebted to Prof. Clark Nguyen for his generous support and guidance. He transferred me to UC Berkeley after I failed to find a Ph.D. advisor and any funding in the University of Michigan. I have been enjoying doing research with him since then. Later on I started to receive research awards and I thanked him each time. He indeed gave me a chance when I needed it the most, and for that alone, I will forever be grateful. For the past four years, he gave me a lot of freedom to explore what interested me and supported what I eventually decided to do; he did not lose his confidence in me even after my fabrication failed to work for the entire year. His constant trust and patience for me inspired me to achieve more.

I would like to thank Prof. Tsu-Jae King Liu and Prof. Liwei Lin for serving on my qualifying exam and dissertation committees, as well as Prof. Elad Alon for serving on my qualifying exam committee. Prof. Sunil Bhave (Cornell University), Prof. Gianluca Piazza (University of Pennsylvania), Prof. Albert Pisano and Prof. Ali Javey (UC Berkeley), Dr. Justin Black and Dr. Philip Stephanou (Qualcomn). They have provided me timely help when I needed them and valuable feedback to better my research.

I have no idea how the staff of Berkeley Microlab/Nanolab manages to handle a lab filled with tools with chronic disease and naive users who tend to make unintentional mistakes (I was one of them). I can only imagine and appreciate the efforts and patience it takes to maintain such a dynamic, almost chaotic, lab. I am especially thankfully to Dr. XiaoFan Meng, Joe Donnelly, and Jimmy Chang, who shared with me valuable knowledge in microfabrication and mechanics. I had no fabrication experience before I started my Ph.D. studies and no senior student to follow but could still function in the lab, thanks to the generous help from many Microlab members, especially Zach Jacobson, Jason Tien, and Reinaldo Vega. I will miss being surrounded by friends when working in the clean room and the fun we had there.

I thank my current group members for their friendship and technical supports. Their efforts have made our testing lab space organized and convenient. Most of my close friends in Berkeley and the professional connections came through BSAC. I always enjoy the good people and good food during each BSAC IAB meeting, and I am proud to be part of BSAC. I thank all of the BSAC directors, John Huggins, Richard Lossing, and Kim Ly for their endless efforts to make BSAC an even better environment for graduate students to learn and to grow professionally.

The deepest thanks go to my family. My parents showed me how resilience and hard working can make a difference in the end. My father is a wonderful physics teacher and I hope I will turn out to be his best student. During my Ph.D. studies, my brother was also pursuing his Ph.D. degree in mechanical engineering. We explored the unknown together as kids and I am always proud to be the little sister of this smart guy. Science and technology started to endear me at the dinner table twenty years ago and the passion eventually leads me to where I am now.

I am in great debt to my fiancé, Reinaldo Vega, yet another engineer. We spent more time together in Cory 373 and Berkeley Microlab than anywhere else for the past four years. We challenged each other's research yet encouraged and supported each other's ambition and passion like no one else. He has made my thousands of 12-hour long working days delightful and continues to inspire me with his generosity for the unprivileged. To me, he is the major award.

I am privileged to receive enormous support and encouragements from many capable and wonderful people, who want me to succeed. That realization, along with my own passion, will continue to drive myself to accomplish and to contribute.

Chapter 1: Introduction

1.1 Channelization of Multi-Standard Receivers

With increasing need for the regional and global roaming of transceivers and continuous advances on wireless communication protocols, future transceivers need flexibility across various mobile communication standards and environments. To understand the design challenge, it is instructive to first review a conventional receiver of heterodyne architecture shown in Fig. 1-1. This receiver relies on multiple frequency-dependent passive components, such as dielectric or bulk-acoustic wave (BAW) filters for RF band selection and surface acoustic wave (SAW) filters in the IF stage. For the past decade, RF MEMS has emerged as a potential solution for miniaturization of transceivers by replacing the bulky off-chip components with on-chip and small-sized MEMS components [1][2].

The center frequencies and the passband width of these frequency-dependent filters can be fine-tuned via applications of mechanical strain [3], electric DC voltages to ferroelectric material [4], piezoelectric material [5], electrostatic transducers [6], and thermal stress [7]. However, it proves very difficult, if possible, to extend the tunable range of filter passband to cover all the commercially available communication standards, roughly from 900 MHz to 5 GHz. The most intuitive way to achieve a transceiver that can support multiple communication standards is to switch among multiple transceivers corresponding to each standard. Even with the help of small-sized MEMS components, such a brute force approach is not cost-effective with the overwhelming hardware count and complexity of the system.

With the rapid advances in computing power enabled by aggressive scaling of CMOS technology, there is a steady trend towards using digital circuits to assist the analog circuits or to replace them. Following this trend, software defined radio (SDR) has been proposed to expand the digital processing from baseband towards the antenna, replacing analog front-ends with digital ones [8]. As hardware for digital signal processing is inherently reconfigurable and

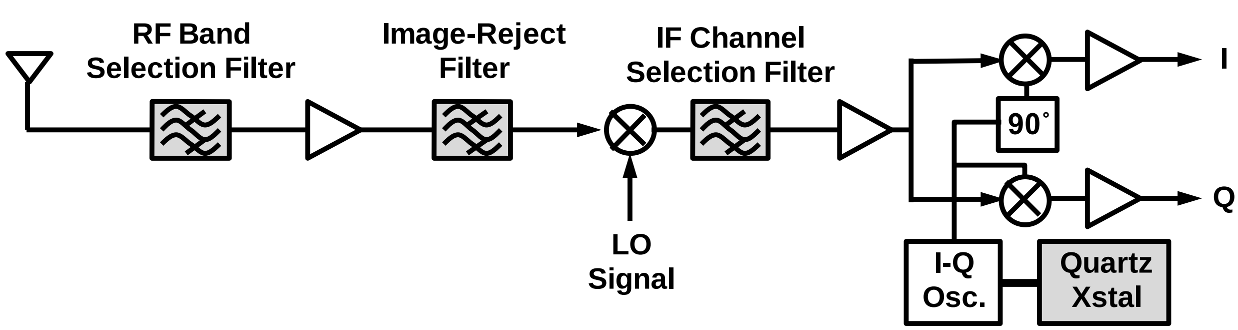

Fig. 1-1 Super-heterodyne receiver with off-chip band selection radio-frequency (RF) filter, image-reject filters, and intermediate-frequency (IF) channel selection filter, quartz crystal as the source of frequency reference.

versatile, SDR is promising for a flexible transceiver that can operate under any available standard within commercial communication RF bands (from 0.9 GHz to 5 GHz).

An ultimate SDR (i.e., use as minimum analog components as possible) shown in Fig. 1-2(a) digitizes the entire receiving RF band right after the antenna or after a wideband low-noise amplifier (LNA) via an analog-to-digital converter (ADC). Such an ADC needs to operate at multiple GHz to fulfill the Nyquist criterion across the entire receiving band (e.g., sample rate of 12 Gigabytes per second to accurately digitalize RF signals up to 6 GHz). On the other hand, without any RF filtering, the ADC has to cope with high dynamic range of the received signals. For example, the Global System for Mobile Communications (GSM) requires an RF front-end dynamic range as high as ~100 dB with signal in the vicinity. In principle, the dynamic range of memory-less ADCs can rise by 3 dB per doubling the oversampling ratio and by 6 dB per additional bit of quantization resolution. Given this trend, 100 dB dynamic range is not achievable with practical power consumption. For example, the work in [9] achieves 2 bits resolution at 4 GS/s (giga-samples per second) operation and 34 mW power using 180 nm CMOS and 1.8 V power supply; the work in [10] achieves 5 bits resolution at effectively 1.75 GS/s operation and 7.6 mW power using 90 nm CMOS and 1 V power supply; the work in [11] achieves 6 bits resolution at 5 GS/s operation and 320 mW power using 65 nm CMOS and 1.3 V power supply. The low-power realization of ADC's with operation speed exceeding 1 GS/s and quantization resolution larger than 10 bits remain elusive.

To avoid the above problem, alternatively, received signals are first down-converted to zero IF or low IF with harmonic-suppression mixing via multi-phased local oscillators (LO) [12][13] before digitization, shown in Fig. 1-2(b). This architecture facilitates the ADC design but puts challenges on the mixer design. In particular, the need for large tuning range of LO signals to

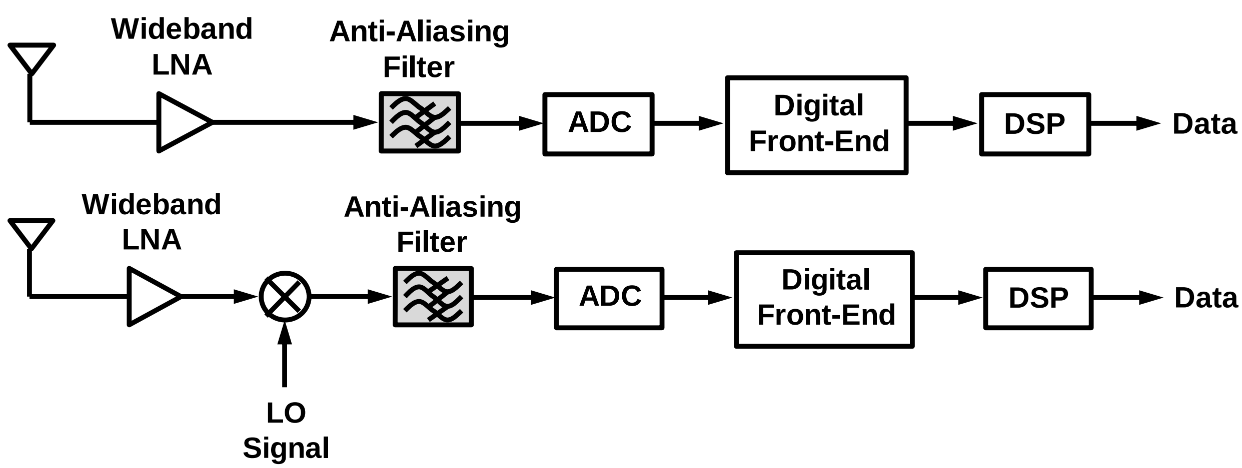

Fig. 1-2: (a) Block diagram of ultimate software-defined radio (SDR), where a wideband antenna and wideband low-noise amplifier (LNA) receive all the signals reside in the RF commercial band, followed by ADC and digital circuits. Here, ADC needs to operate at multiple GHz frequency with high dynamic range. (b) Feasible SDR with frequency down-conversion before ADC. Without pre-filtering, phased local-oscillation signal is required for an interference robust design.

cover the entire receiving RF band and highly linear mixers operating at RF frequency range impedes further reduction of power consumption down to < 1 mW range.

Note that the high dynamic range and interference-resistant requirements are a direct result of wide-band reception for narrow-band signals such as GSM, in which each channel is only 200 kHz wide. Selection of the entire receiving band, *e.g.*, 25 MHz for GSM at 900 MHz, usually will include not only the single in the target channel but also all the signals in the other channels within the receiving band, *i.e.*, interferences. Given the same target single power level, the wider the receiving band, the more inferences likely to exist. This is especially a problem for receivers designed to operate by multiple standards by using a wideband LNA shown in Fig. 1-2(b).

On the other hand, when signals of various communication standards can be selected directly from the targeted channel by filters of appreciate passband widths, as shown in Fig. 1-3 [1], the dynamic range requirement of the following circuits remains similar to a single standard receiver, regardless the total operational receiving band width covered by the receiver. Such approach requires a bank of narrow-band filters, each designed for a receiving channel. Indeed, the current trend of SDR architecture design remains to avoid analog RF filtering altogether stems from the fact that today's off-chip filters are bulky and expensive compared to digital circuits. For the same reason, conventional analog filters are not suitable for a cost and area effective implementation of the filter bank in a channel-selection receiver in Fig. 1-3. MEMS filters are one of the most promising solutions for such filter bank.

Before the design principals of MEMS narrow-band filters are presented, it is illustrative to first look at the parameters commonly used to evaluate filter performance shown in Fig. 1-4. Of special interest is the filter insertion loss and 20 dB filter shape factor. Insertion loss is measured as the difference in loss between a through measurement (*i.e.*, by replacing the filter with a highly conductive metal strip on the chip or PCB board in the measurement setup) and a measurement after the filter has been inserted. 20 dB filter shape factor is the ratio between the 3 dB-bandwidth to the 20dB-bandwidth. 20 dB filter shape factor describes how sharp the filter

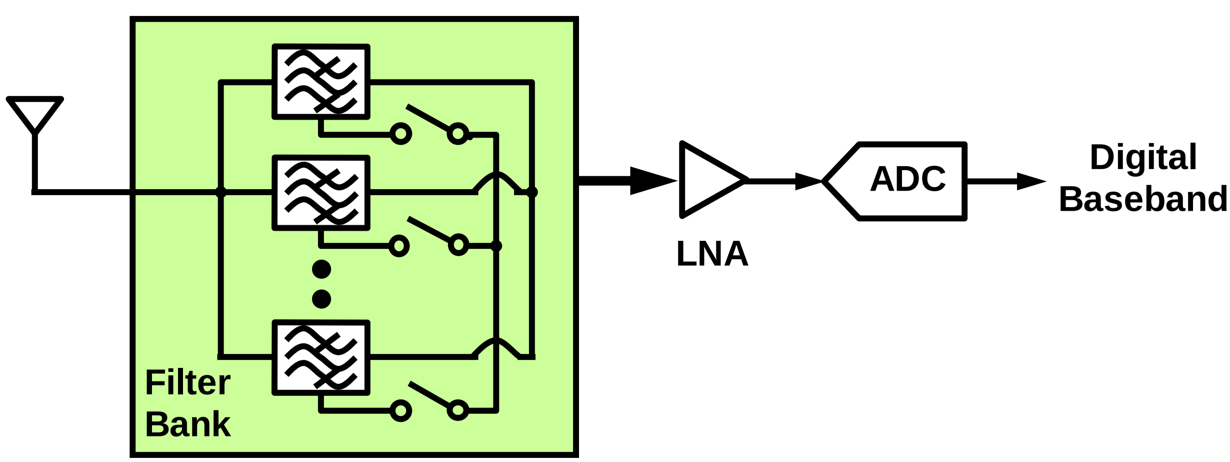

Fig. 1-3: channel-selection RF filters reject all the interference signals and allow the receiver to operate with relaxed dynamic range requirements, simplified circuits, and lower power consumption.

passband is.

The rest of this chapter briefly reviews the design of narrow-band filters to illustrate the performance requirements posted on the constituent MEMS resonators, followed by reviews on previous work using both electrostatic and piezoelectric resonators. This thesis sets out to address the current challenges of implementing MEMS resonators suitable for synthesizing such narrow-band MEMS filters.

1.2 Narrow-Band MEMS Filters

The basic circuit modeling of resonators and mechanical coupling beams is presented here as background knowledge for narrow-band filter design.

1.2.1 Fundamentals of Micromechanical Resonators

A MEMS resonator consists of a resonant mechanical structure and transducers for energy conversion between electrical and mechanical domains, shown in Fig. 1-5. The resonant mechanical structures, regardless of whether their shapes are that of beams, disks, rings, or plates, can all be modeled as spring-mass-damper systems. The equivalent mass at any given point of the resonator is determined from the total kinetic energy of the resonator KE_{tot} and the velocity at that point $v(x,y)$, as given by [15]

$$\begin{aligned} m_{re} &= \frac{2KE_{tot}}{v(x,y)^2} = \frac{2H}{v(x,y)^2}\int_A \rho(x,y)\cdot v(x,y)^2 dxdy \\ &= \frac{2H}{\Phi(x,y)^2}\int_A \rho(x,y)\cdot \Phi(x,y)^2 dxdy \end{aligned} \tag{1-1}$$

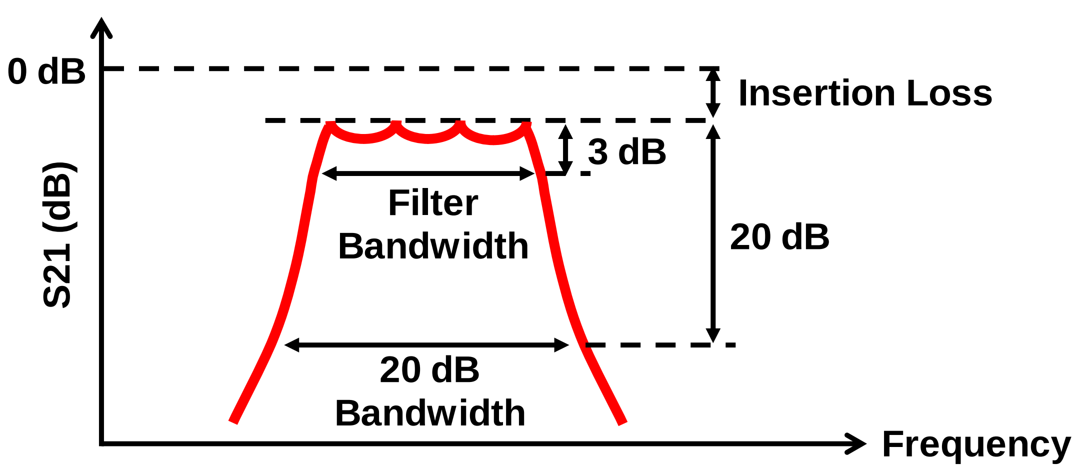

Fig. 1-4: Parameters commonly used to evaluate filter performance.

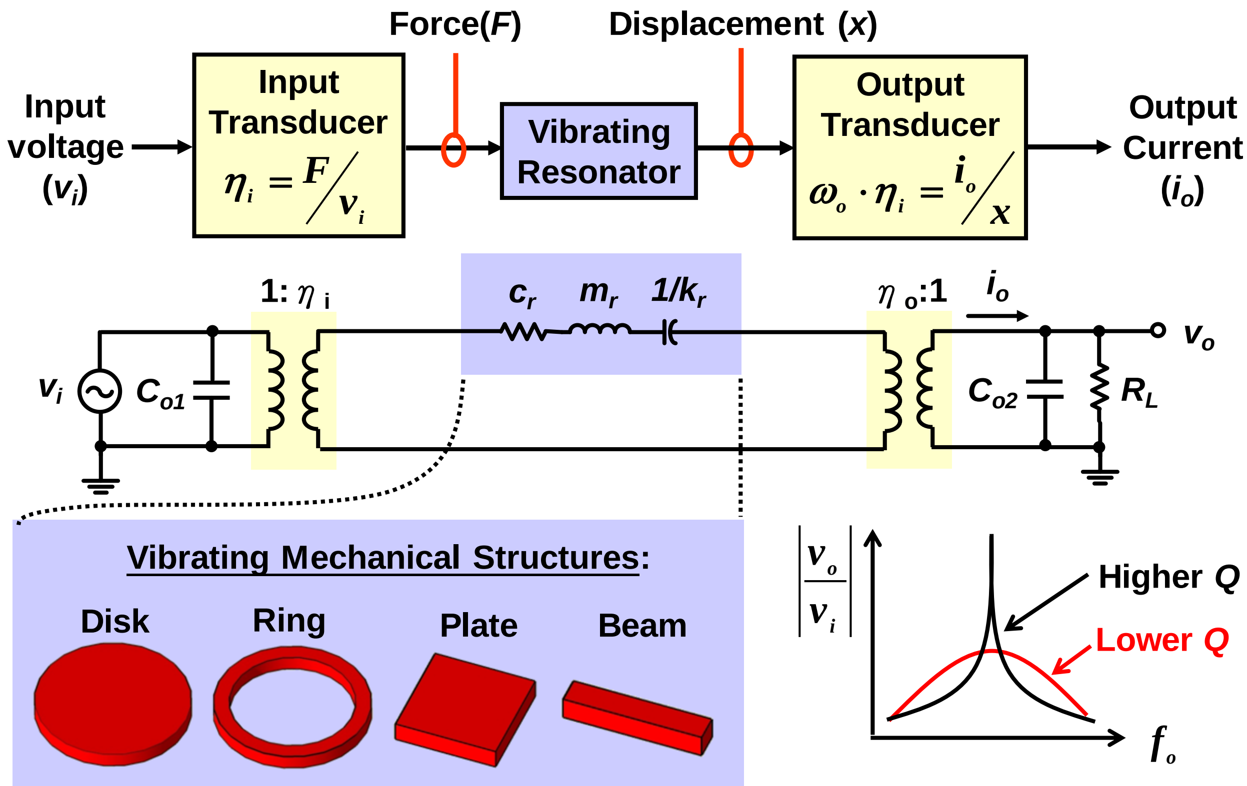

Fig. 1-5: (a) block diagram of a MEMS resonator consisting of electro-mechanical transducers and vibrating mechanical structures, and (b) a general electric model for a MEMS resonator.

where H, $\rho(x,y)$ and $\Phi(x,y)$ are the thickness, density, and vibration mode shape of the resonator. The effective stiffness of the resonator k_{re} can be related to m_{re} via the radian resonance frequency ω_o

$$k_{re} = \omega_o^2 m_{re} \tag{1-2}$$

Finally, the value of the damping element is related to mass, stiffness, and the Q of the resonator, by

$$c_{re} = \frac{\sqrt{k_{re} m_{re}}}{Q} = \frac{\omega_o m_{re}}{Q} \tag{1-3}$$

To the first order, a micromechanical resonator can be modeled by the electrical circuit in Fig. 1-5 regardless of the geometry, mode shape, and transduction methods. The values of inductance, capacitance, and resistance correspond to values of equivalent mass m_{re}, reciprocal of stiffness, $1/k_{re}$, and damping factor c_{re}. The two physical capacitors, C_{o1} and C_{o2}, represent the total capacitance contributed by the transducers and parasitic capacitance at the input or output ports. The transduction coefficients, η_i and η_o, model energy transduction efficiency between electrical and mechanical domains by considering the amount of mechanical force F generated from voltage input v_i and the output current i_o generated from mechanical displacement x, respectively:

$$\eta_i = \frac{F}{v_i} \qquad\qquad \eta_o = \omega_o \frac{i_o}{x} \tag{1-4}$$

The simplified model presented here intends to prepare readers for the following filter design. More details on design of capacitive and piezoelectric resonator designs will be presented in Chapter 3 and Chapter 5, respectively.

The electro-mechanical transducer in the input port converts input electrical energy (i.e., voltage) to mechanical energy (i.e., strain or stress). On the output port, the transducer converts the mechanical energy (i.e., displacement) back to electric energy (i.e., output currents). The efficiency of such energy transduction is quantified by electromechanical coupling coefficient, η, and is modeled by the turn ratios of the transformers on the input and output ports, respectively.

A filter can be implemented by a system of the degree of freedom larger than one. For example, two resonators mechanically coupled to each other together form a two-pole filter. To understand the mechanical circuit design from the perspective of equivalent electrical circuit design, it is instructive to first be familiar with the electrical circuit model for a coupling beam with a resonator attached to each end.

1.2.2 Modeling of Micromechanical Couplers

The micromechanical coupling beams connected between resonators function as acoustic transmission lines. The coupling beam in consideration has cross-sectional dimensions of width W_c and height H_c, shown in Fig. 1-6(a) and vibrates in the extensional mode shape, i.e., the beam expands and contracts along the length of the beam L_c. It can be modeled by the T-shaped capacitor combination [14][15] shown in Fig. 1-6(b) with the impedance value of each capacitor written as:

$$Z_a = Z_b = \frac{\cos(2\pi \cdot L_c / \lambda_c) - 1}{jZ_o \sin(2\pi \cdot L_c / \lambda_c)} \tag{1-5}$$

$$Z_c = \frac{1}{jZ_o \sin(2\pi \cdot \lambda_n)} \tag{1-6}$$

with Z_o and λ_n being the normalized impedance and normalized wavelength, respectively

$$Z_o = \frac{1}{H_c W_c \sqrt{E\rho}} \tag{1-7}$$

$$\lambda_c = \frac{v_e}{f_o} = \frac{\sqrt{E/\rho}}{f_o} \tag{1-8}$$

where E and ρ are the Young's modulus and density of the resonator structural material, respectively, and f_o is the resonant frequency.

1.2.3 Transfer Functions of Mechanical Circuits

Fig. 1-7 shows a mechanical circuit composed of two contour-mode disk resonators mechanically coupled to each other with resistors R_Q connected to both the input and the output ports. Fig. 1-7(b)-(c) show its equivalent mechanical and electrical circuits, respectively.

The transformer turns ratios associated with the couplers in Fig. 1-7(c), η_{c1} and η_{c2}, model the mechanical impedance transformation realized by mechanically coupling one resonator to the other at a location different from the reference point based on which the electrical models of each resonator is calculated. Usually the reference point is chosen as the location with the maximum mechanical displacement. Expressed in terms of a stiffness ratio, the equation for the mechanical transformer turns ratio when coupling at a distance from an anchor takes the form [16]

$$\eta_c = \sqrt{\frac{k_{rc}}{k_{re}}} \tag{1-9}$$

where k_{rc} is the resonator stiffness at the coupling position and k_{re} is the equivalent stiffness as derived in (1-2). Note that when η_{c1} and η_{c2} have equal values, they only modify the values of Z_a, Z_b, and Z_c, and have no effect on the other circuit elements. Such coupling has been utilized in filters to obtain smaller bandwidth [17]. As will be seen, such coupling will be required when implementing filters with two or more resonators.

To simplify the analysis, the circuit in Fig. 1-7(c) is reduced to (d) by absorbing all of the transformer ratios, η_i, η_o , η_{c1} , and η_{c2}, into the values of the circuit elements, yielding

$$L_x = m_r / \eta_i \eta_o \tag{1-10}$$

$$C_x = \eta_i \eta_o / k_r \tag{1-11}$$

$$R_x = c_r / \eta_i \eta_o \tag{1-12}$$

$$C_{ca} = C_{cb} = \eta_i \eta_o \eta_{c1} \eta_{c2} / k_{ca} \tag{1-13}$$

$$C_{cc} = \eta_i \eta_o \eta_{c1} \eta_{c2} / k_{cc} \tag{1-14}$$

As the mechanical circuit in Fig. 1-7(a) is a system of two degrees of freedom, a 2-rank matrix equation can fully describe its equivalent circuit in Fig. 1-7(d):

$$\begin{bmatrix} \left(\delta + \frac{1}{sC_{sa}} + \frac{1}{sC_{sc}}\right) & -\frac{1}{sC_{ss}} \\ -\frac{1}{sC_{ss}} & \left(\delta + \frac{1}{sC_{sa}} + \frac{1}{sC_{sc}}\right) \end{bmatrix} \begin{bmatrix} i_1 \\ i_2 \end{bmatrix} = \begin{bmatrix} v_{in} \\ v_1 \end{bmatrix} \tag{1-15}$$

where δ is the impedance of each resonator in the array and is a function of frequency

$$\delta = sL_x + \frac{1}{sC_x} + R_x \tag{1-16}$$

It is worth noting that solving this matrix to obtain output current given applied voltage is equivalent to solving the vibration velocity, i.e., time derivation of vibration amplitude x, given applied force of a two-degree freedom coupled mechanical system, as shown in Fig. 1-7(b):

$$\begin{bmatrix} s^2m_r + sc_r + k_r + k_{sa} + k_{sc} & -k_{sc} \\ -k_{sc} & s^2m_r + sc_r + k_r + k_{sa} + k_{sc} \end{bmatrix} \begin{bmatrix} x_1 \\ x_2 \end{bmatrix} = \begin{bmatrix} F_1 \\ F_2 \end{bmatrix} \tag{1-17}$$

where (1-17) is related to (1-15) with the relation

$$\frac{i}{v} = \frac{\dot{x}}{F} = s\frac{x}{F} \tag{1-18}$$

The current-to-voltage relationship of the circuit in Fig. 1-7(d) can be obtained by solving (1-15) as

$$\frac{i_1}{v_1} = \frac{1 + sC_{sc}\left(\delta + \frac{1}{sC_{sa}}\right)}{\left(\delta + \frac{1}{sC_{sa}}\right)\left[SC_{sc}\left(\delta + \frac{1}{sC_{sa}}\right) + 2\right]} = \frac{\delta + \frac{1}{sC_{sa}} + \frac{1}{sC_{sc}}}{\left(\delta + \frac{1}{sC_{sa}}\right)\left(\delta + \frac{1}{sC_{sa}} + \frac{2}{sC_{sc}}\right)} \tag{1-19}$$

$$\frac{i_2}{v_1} = \frac{1}{\left(\delta + \frac{1}{sC_{sa}}\right)\left[SC_{sc}\left(\delta + \frac{1}{sC_{sa}}\right) + 2\right]} = \frac{\frac{1}{sC_{sc}}}{\left(\delta + \frac{1}{sC_{sa}}\right)\left(\delta + \frac{1}{sC_{sa}} + \frac{2}{sC_{sc}}\right)} \tag{1-20}$$

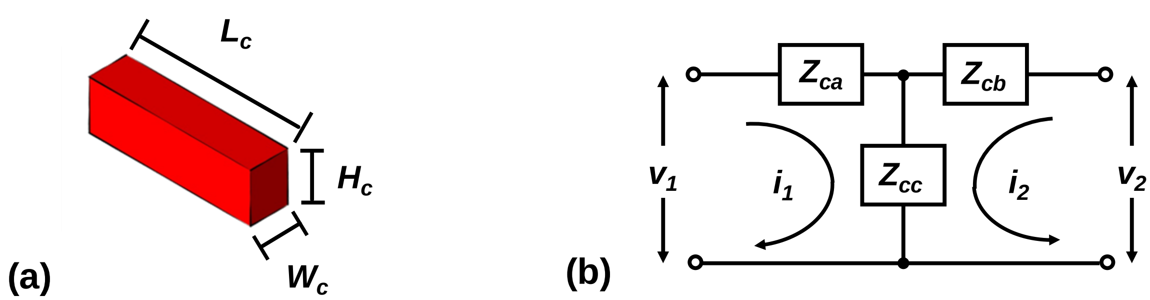

Fig. 1-6: (a) dimension of a coupling beam to vibrate in the extensional mode shape along its length L_c. (b) Equivalent T-shaped capacitor combination model for the coupling beam, where Z_{ca} and Z_{cb} share the same value. The equivalent wavelength of the coupler governs the ratio of Z_{ca} to Z_{cc}.

where i_1 and i_2 represent the output currents generated by the first and the second resonators, respectively. The values of C_{sa} and C_{sc} are not independent and the ratio is a function of the length of the extensional-mode coupling beams. Of particular interest are cases when the length is equivalent to quarter and half wavelength, as discussed the following two sections.

1.2.4 Quarter-Wavelength Couplers for MEMS Filters

For extensional mode coupling beams of length designed to be integer number of quarter-wavelength coupler, i.e., $L_c/\lambda_n = N \pm 0.25$, N=1, 2,…, equations (1-5) and (1-6) yields to the relation

$$Z_a = Z_b = -Z_c \tag{1-21}$$

or

$$C_{ca} = C_{cb} = -C_{cc} \tag{1-22}$$

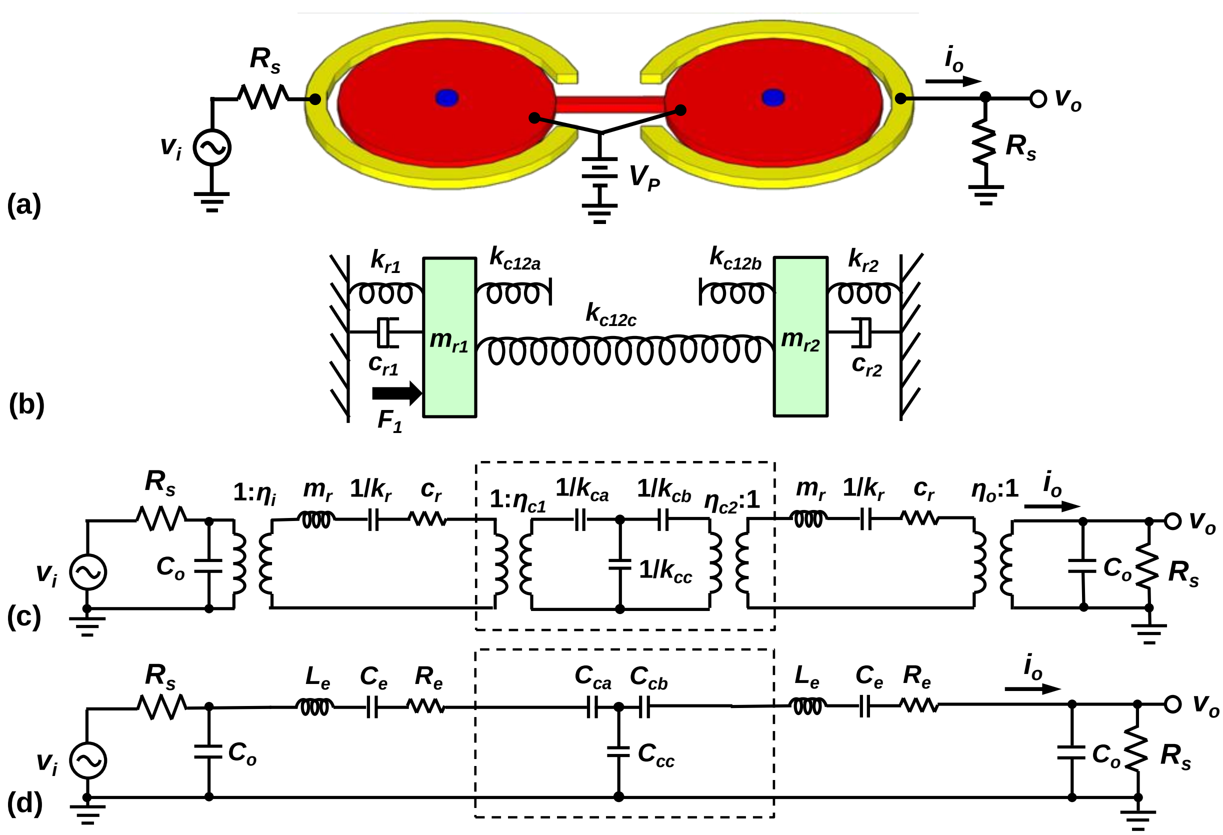

Fig. 1-7: (a) An un-terminated MEMS filter composed of two identical disk resonators, one of which is the input resonator and the other is the output resonator; (b) mass-stiffness-damper model of the filter in (a); (c) equivalent electrical circuit of the filter in (a); (d) a simplified version of the circuit in (c).

Plugging (1-21) and (1-22) to (1-19) and (1-20) yields

$$\frac{i_1}{v_1}=\frac{\delta}{\left(\delta+\frac{1}{sC_{sa}}\right)\left(\delta-\frac{1}{sC_{sa}}\right)}=\frac{0.5}{\delta+\frac{1}{sC_{sa}}}+\frac{0.5}{\delta-\frac{1}{sC_{sa}}} \tag{1-23}$$

$$\frac{i_2}{v_1}=\frac{\frac{1}{sC_{sc}}}{\left(\delta+\frac{1}{sC_{sa}}\right)\left(\delta-\frac{1}{sC_{sa}}\right)}=\frac{-0.5}{\delta+\frac{1}{sC_{sa}}}+\frac{0.5}{\delta-\frac{1}{sC_{sa}}} \tag{1-24}$$

Each term in (1-23) and (1-30) takes the mathematical form of resonator response, where the resonant frequency is different from f_o through addition or subtraction of C_{sa} to or from the motional capacitor of the constitute resonator, C_r. The magnitudes of the output currents therefore show peak values at two frequencies, $f_o+\Delta f$ and $f_o-\Delta f$, respectively. The magnitude of $\Delta f/f_o$ (i.e. percentage of frequency change relative to the center frequency f_o) is

$$\frac{\Delta f}{f_o}=\sqrt{1+\frac{C_r}{C_{ca}}}-1 \tag{1-25}$$

As will be shown in Section 1.3.4, a filter response with center frequency f_o and bandwidth $2\Delta f$ can be realized from the un-terminated filter response in Fig. 1-10 by flattening the passband with proper termination. (1-25) shows that Δf, therefore the filter passband bandwidth after termination, is controllable by stiffness of the coupling beam to that of the resonator at the coupling location. In particular, for narrow-band filters, $\Delta f/f_o$ is small, and (1-25) can be simplified to

$$\frac{\Delta f}{f_o}\cong\left(1+\frac{1}{2}\cdot\right)-1=\frac{C_r}{2C_{ca}}=\frac{k_{ca}}{2\eta_{c1}\eta_{c2}k_r} \tag{1-26}$$

The last equation is established by substituting C_r and C_{ca} with the expressions in (1-11) and (1-13), respectively.

1.2.5 Half-Wavelength Couplers for Composite-Array Resonators

For extensional mode coupling beams of length designed to be integer number of half-wavelength coupler, i.e., $L_c/\lambda_n=N\pm0.5$, N=1, 2,…, equations (1-5) and (1-6) yields to the relation

$$Z_a=Z_b=-2Z_c \tag{1-27}$$

or

$$2C_{ca} = 2C_{cb} = -C_{cc} \tag{1-28}$$

Plugging (1-27) and (1-28) to (1-19) and (1-20) yields

$$\frac{i_1}{v_1} = \frac{\delta + \frac{1}{2sC_{sa}}}{\delta\left(\delta + \frac{1}{sC_{sa}}\right)} = \frac{0.5}{\delta} + \frac{0.5}{\delta + \frac{1}{sC_{sa}}} \approx \frac{0.5}{\delta} \tag{1-29}$$

$$\frac{i_2}{v_1} = \frac{\frac{1}{2sC_{sa}}}{\delta\left(\delta + \frac{1}{sC_{sa}}\right)} = \frac{0.5}{\delta} + \frac{-0.5}{\delta + \frac{1}{sC_{sa}}} \approx \frac{0.5}{\delta} \tag{1-30}$$

The approximation holds true as the value of C_{sa} approaches infinite as the length of the coupling beam approaches half-wavelength. The resonant frequency of this resonator array-composite is the same as that of its constituent resonator, f_o. Ideally, array-composite resonator behaves as a single resonator, with impedance related to the drive and sense schemes.

If one resonator is excited and the in-phase output current is collected from the other resonator, shown in Fig. 1-8(b), and assuming each electrode has identical dimension, the magnitude of the output current is

$$\left|\frac{i_2}{v_1}\right|_{C_{sa}\propto 0} = \frac{0.5}{\delta} \tag{1-31}$$

Compared to a single resonator in Fig. 1-8(a), this array-composite generates half of the output currents and has twice the impedance.

Another case is when one resonator is excited and the in-phase output currents are collected from both resonators. Again, assuming each electrode is identical in dimension, the magnitude of the total output currents is

$$\left|\frac{i_1}{v_1}\right|_{C_{sa}\propto 0} + \left|\frac{i_2}{v_1}\right|_{C_{sa}\propto 0} = \frac{1}{\delta} \tag{1-32}$$

If both resonators are excited and both resonators are sensed, superposition of voltage sources can be used to obtain

$$\left|\frac{i_1}{v_1}\right|_{C_{sa}\propto 0,\, v_2=0} + \left|\frac{i_2}{v_1}\right|_{C_{sa}\propto 0,,\, v_2=0} + \left|\frac{i_1}{v_2}\right|_{C_{sa}\propto 0,\, v_1=0} + \left|\frac{i_2}{v_2}\right|_{C_{sa}\propto 0,,\, v_1=0} = \frac{2}{\delta} \tag{1-33}$$

The output current is twice than that of a single resonator. Chapter 5 will explore the effect on electrode placement and mechanical coupling on the impedance of similar resonator array in greater details.

The above circuit analysis can be applied to analyze systems with even higher degrees of freedom by using matrixes of higher ranks.

1.2.6 Filter Termination

As discussed in Section 1.2.4, two identical resonators coupled by quarter-wavelength coupling beams show two peaks on the frequency spectrum, corresponding to two mode shapes of the two-degree freedom system. Fig. 1-9 shows the simulation results of such coupled resonators, where the in-phase and out-of-phase mode shapes render resonant peaks at lower and

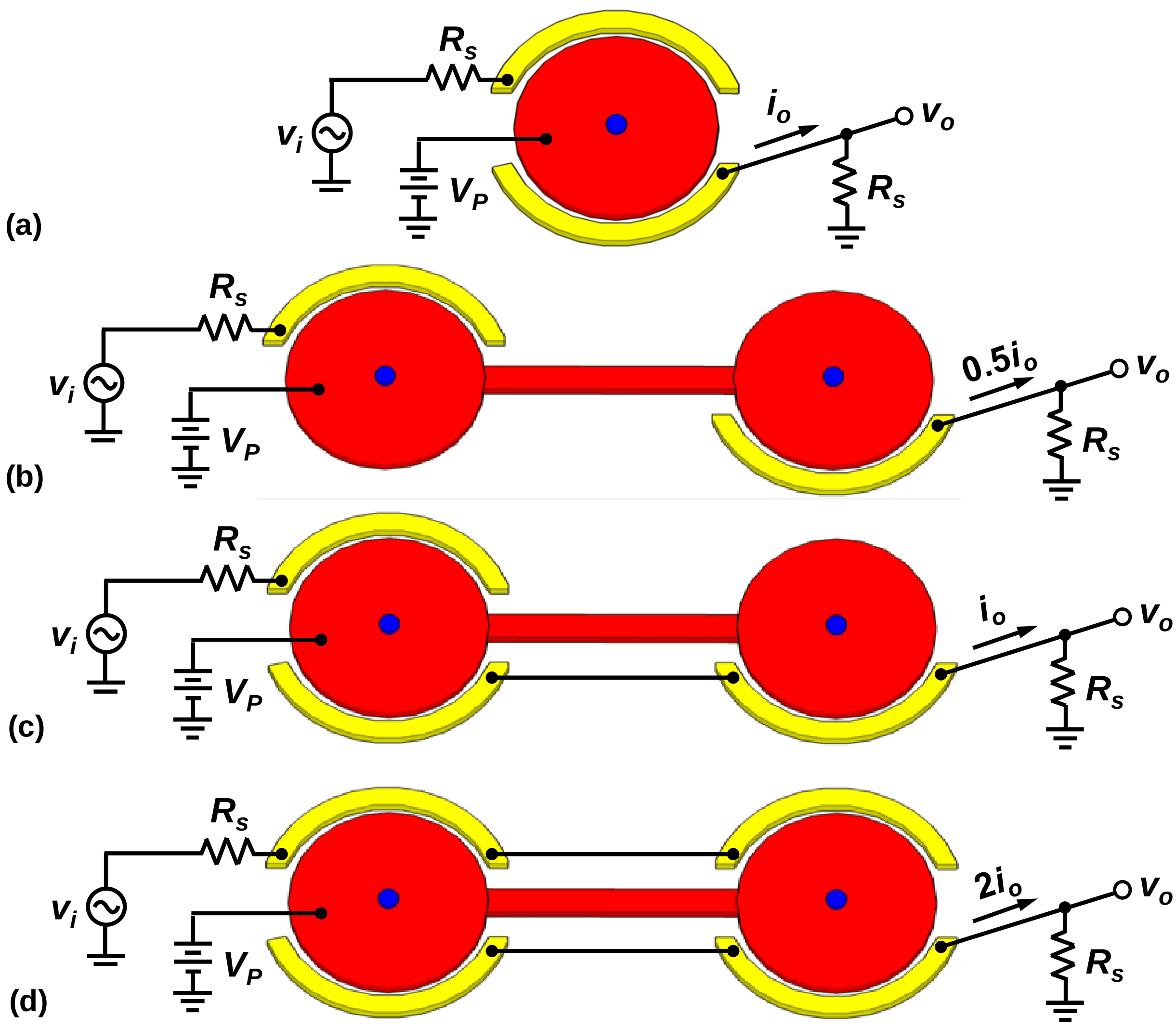

Fig. 1-8: (a) a single disk resonator with the input signal v_i and output current i_o; (b)-(d) disk array-composite resonator with different measurement setup: (b) drive one resonator and sense the other; (c) drive one resonator and sense both resonators; (d) drive and sense both resonators renders twice the output currents, thus half the impedance, compared to a single resonator in (a).

higher frequencies, respectively.

To flatten the filter passband in Fig. 1-10, the Q's of the end resonators must be loaded via resistive termination with value of R_Q given by [16]

$$R_Q = \left(\frac{Q_r}{qQ_f} - 1\right) \cdot R_x \approx \frac{Q}{qQ_f} \cdot \frac{m_r \omega_o}{Q \eta_e^2} \approx \frac{m_r B}{q \eta_e^2} \tag{1-34}$$

where R_x is the motional resistance of a constituent end resonator; Q is the unloaded quality factor of the resonator; $Q_{fltr} = f_o/B$, B being the filter passband width; q is a normalized parameter obtained from a filter cookbook [18]; m_r is the dynamic mass of the resonator at its point of maximum displacement; and η_e is the electromechanical coupling factor.

Fig. 1-10(a) shows a typical terminated micromechanical filter consisting of two identical contour-mode disk resonators. The termination resistance R_Q affects the input and output impedances of the filter, which must be considered in the design of the neighboring circuits, such as low-noise amplifier, to optimize the power transfer and noise figure. From the expression of R_Q in (1-34), manipulation of η_e is the most convenient way for achieving a specific value of R_Q. While it is an option to increase η_e by increasing the transducer and resonator sizes, the interaction of R_Q and the physical capacitance at the input and output ports dictates another requirement on the resonator performance, as will be discussed in the next section.

1.2.7 Filter FOM

As shown in Fig. 1-10(a), the R_Q and C_o essentially combine to generate a pole at $\omega_b = 1/(R_Q C_o)$ that sets the 3 dB bandwidth of a low-pass filter, ω_b. C_o models the physical capacitance

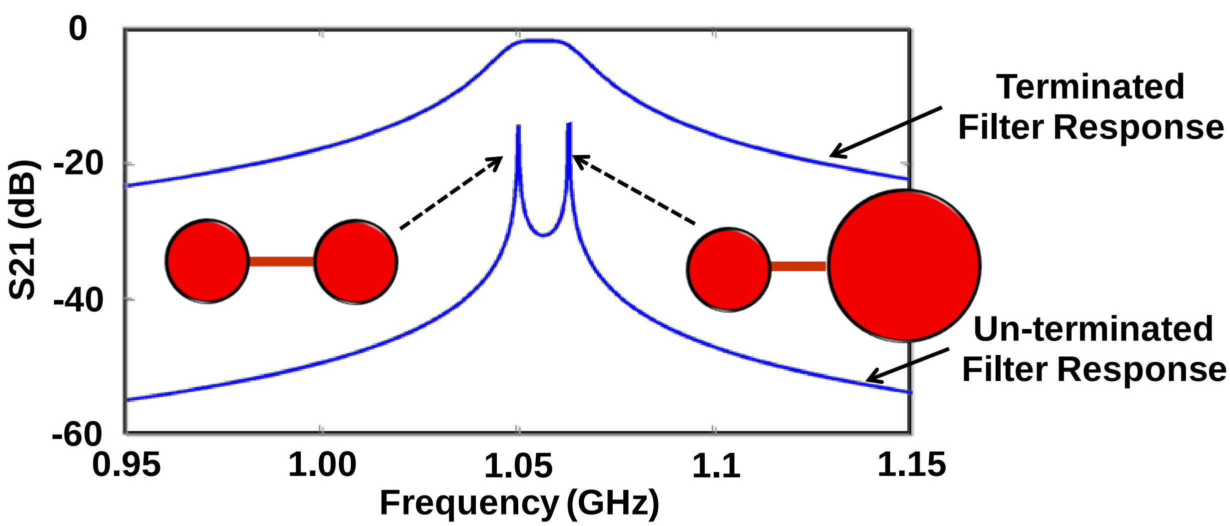

Fig. 1-9: Simulation results of terminated and un-terminated filter responses. The termination resistors R_Q's 'flatten' the peaks corresponding to two mode shapes of the mechanically coupled two-resonator composite.

associated with the input and output ports, including those of the transducers, interconnects, and the neighboring circuits. Therefore, a terminated MEMS filter can be modeled by a bandpass filter in series with two low pass filters, shown in Fig. 1-10(b). If ω_b is lower than the center frequency ω_o of the filter, it will add undesired passband loss. When ω_b is larger than ω_o but somewhat close to ω_o, it may cause the phase lag significant enough to distort the passband [14]. $1/(R_Q C_o)$ can also be considered as the transducer bandwidth and it is not a function of resonator Q. (1-34) suggests that m_r and η_e are the only tunable parameters to optimize R_Q given filter bandwidth B and normalized parameter q for a specific application. Therefore, the filter figure of merit aimed to evaluate a resonator (more precisely, a transducer) can be defined as,

$$\boldsymbol{FOM} = \frac{\boldsymbol{\eta_e^2}}{\boldsymbol{m_r C_o}} \tag{1-35}$$

(1-35) reveals that η_e^{2}/C_o needs to be maximized for sufficient transducer bandwidth as well as optimized η_e for impedance matching. The problem associated with the low-pass filters shown in Fig. 1-10(b) is actually fixable by using an (on-chip) inductor to resonate out the C_o, but it would be preferable if an inductor were not needed. As will be derived in Chapter 4-1, the value of $1/(R_Q C_o)$

The filter FOM in (1-35) is defined from the perspective of filter design. Another parameter, k_t^2, called the coupling efficiency, is more commonly used to evaluate the performance of piezoelectric transducers and resonators. For resonators at the same frequency, the value of the filter FOM is proportional to k_t^2 and both can be used to evaluate resonator performance interchangeably. To see this, consider the electric model of a one port resonator, shown in Fig. **, where the feedthrough capacitance C_o is parallel to the series resonator tank. The impedance of this circuit reaches the minimum and maximum at its series and parallel resonance frequencies, respectively. The series resonance frequency is written as

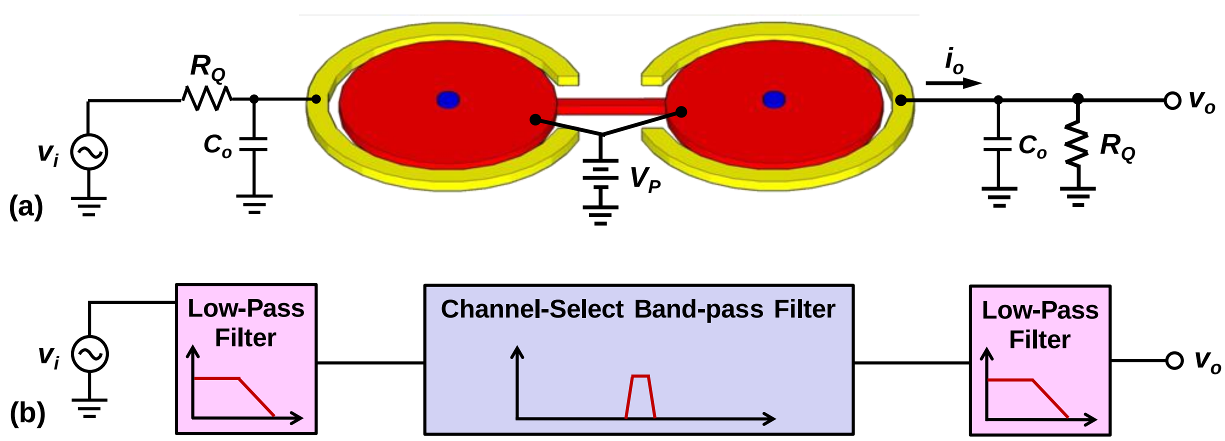

Fig. 1-10: (a) A MEMS filter properly terminated with resistors R_Q connected to both input and output ports. The physical capacitance associated with the transducers and parasitic capacitance, is modeled with C_o. (b) R_Q and C_o form undesired low-pass filters which could affect the signal integrity if their cut-off frequencies are lower than the passband of the band-pass filter.

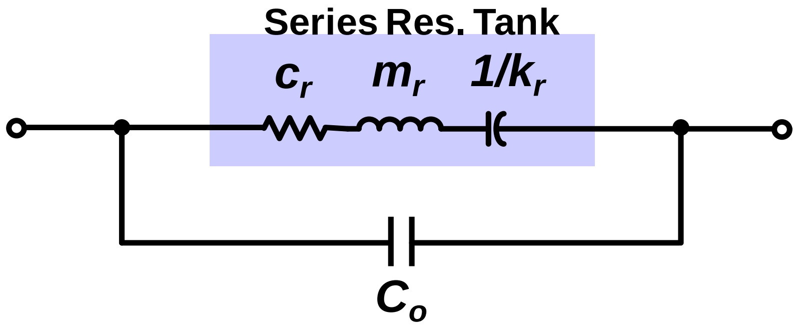

Fig. 1-11: Equivalent electrical model of a one-port resonator.

$$f_s = \frac{1}{2\pi}\sqrt{\frac{1}{L_x C_x}} \tag{1-36}$$

The parallel resonance frequency is written as

$$f_p = \frac{1}{2\pi}\sqrt{\frac{1+\frac{C_x}{C_o}}{L_x C_x}} \approx \frac{1}{2\pi}\sqrt{\frac{1}{L_x C_x}}\left(1+\frac{C_x}{2C_o}\right) \tag{1-37}$$

The approximate was valid as long as C_o is much larger than C_x, which is true for properly designed MEMS resonators at the frequencies of interest.

k_t^2 is defined as

$$k_t^2 = \frac{\pi^2}{4}\cdot\frac{f_p - f_s}{f_p} \tag{1-38}$$

Replacing f_s and f_p with the expressions in (1-36) and (1-37) gives

$$k_t^2 \approx \frac{\pi^2}{8}\cdot\frac{C_x}{C_o} \tag{1-39}$$

Replacing C_x in (1-38) with the expression in (1-11) results

$$k_t^2 = \frac{\pi^2}{8}\cdot\frac{\eta_e^2}{k_r C_o} = \frac{\pi^2}{8}\cdot\frac{\eta_e^2}{\omega_o^2 m_r C_o} \propto \frac{\eta_e^2}{m_r C_o} \tag{1-40}$$

(1-40) states that given the same resonator design, the value of k_t^2 is proportional to that of the FOM defined in (1-35) and both parameters can be interchangeable to evaluate the resonators.

1.2.8 Filter Insertion Loss

The insertion loss of the filter, as shown in Fig. 1-4, can be written as:

$$IL = 20\log\left(\frac{R_x + R_Q}{R_Q}\right) = 20\log\left(\frac{Q_r}{Q_r - q\,Q_f}\right) \tag{1-41}$$

where Q_r is the Q's of constituent resonators and Q_f is the ratio of the filter center frequency to the filter bandwidth. Q_f is the reciprocal of the filter percent bandwidth. (1-41) shows dependence of insertion loss on Q's of constituent resonators and the filter, where q is the same normalized parameter used in (1-34), which value depends on the filter type, ripple requirement, and filter order. As the insertion loss of an RF filter directly adds to the noise figure of the preceding low-noise amplifier (LNA), it is important to minimize the filter insertion loss.

Fig. 1-12 illustrates the dependence of insertion loss on resonator Q via plots of frequency response for 2-resonator filters with 1% (*i.e.*, Q_f = 1,00) and 0.1% (*i.e.*, Q_f = 1,000) bandwidths, over various constituent resonator Q's. Here, to assure less than 3 dB insertion loss, the minimum required resonator Q is only 1,000 for a 1%-bandwidth filter, but as high as 10,000 for 0.1%-bandwidth, clearly emphasizing the importance of Q when small percent bandwidths are needed.

Fig. 1-13 shows simulation of the dependence of filter insertion loss on resonator Q using q=1.6 for a two-pole Gaussian filter with different filter passband percent bandwidth. Most band-select filters have small Q_f, *e.g.*, Q_f = 36 for GSM (with receiving bandwidth of 25 MHz and center frequency of 900 MHz) and Q_f = 95.5 for UMPS (with receiving bandwidth of 20 MHz

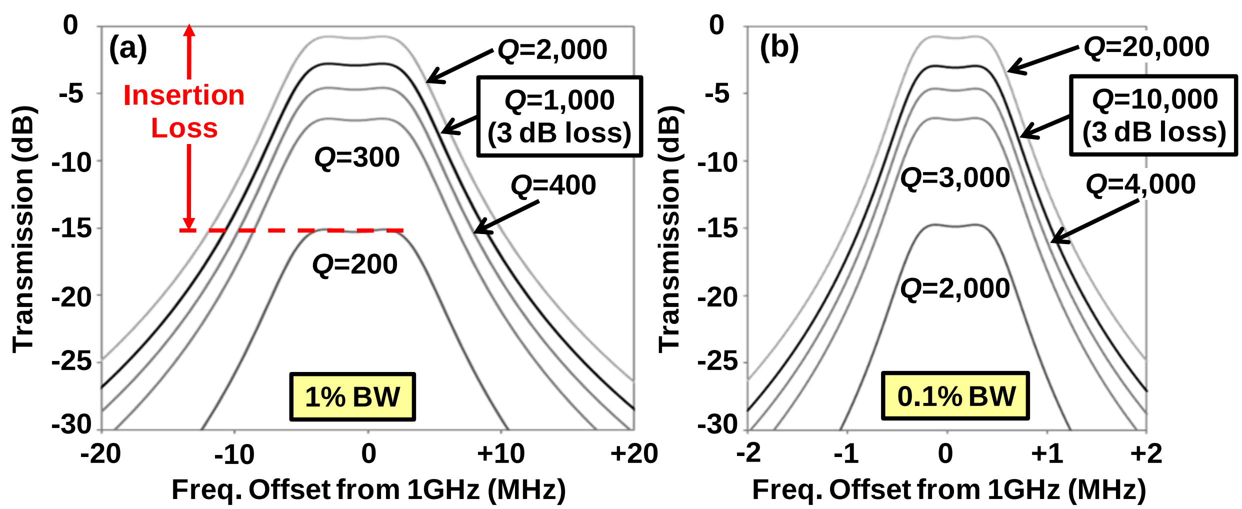

Fig. 1-12: Simulated frequency characteristics for 1-GHz filters with varying constituent resonator Q's, illustrating how resonator Q governs the insertion loss of a filter. (a) For an insertion loss less than 3 dB, resonator Q's must be larger than 1,000 for a 1 % bandwidth filter. (b) When the filter bandwidth shrinks to 0.1 %, even higher resonator Q > 10,000 is needed.

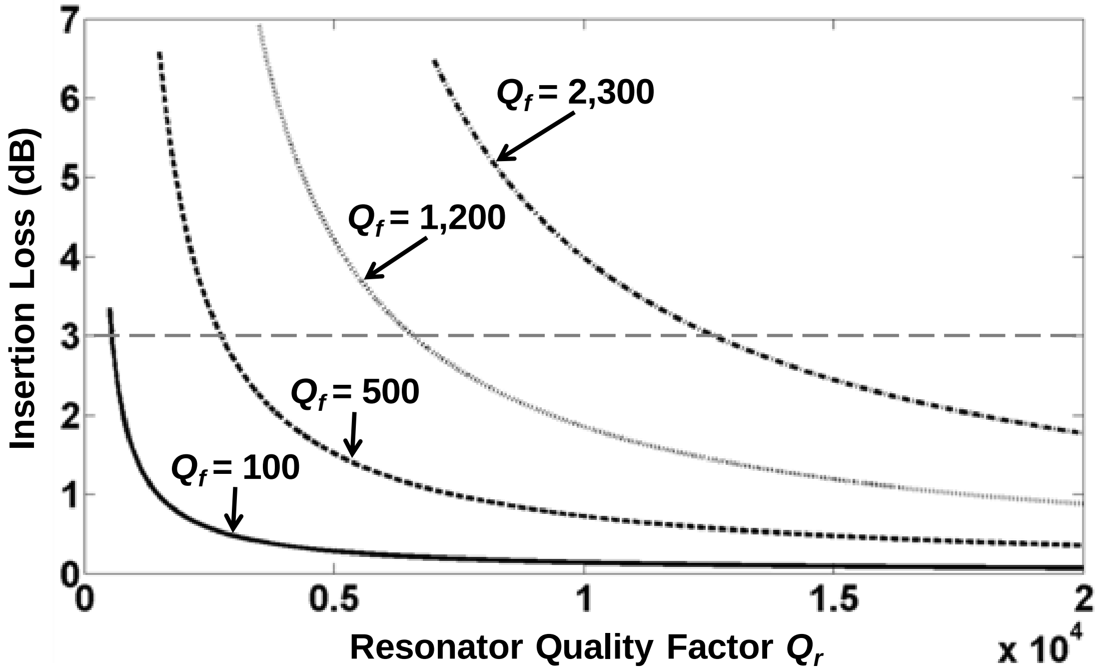

Fig. 1-13: Simulated dependence of filter insertion loss on Q_r for different Q_f. To ensure less than 3 dB insertion loss, the required Q_r increases as Q_f increases (*i.e.*, narrower bandwidth for the same filter center frequency.)

and center frequency of 1910 MHz), and require only $Q_r > 523$ to maintain the insertion loss to be less than 3 dB. Channel-select filters, on the other hand, needed at the front-end of a cognitive radio require small percent bandwidth filters that in turn demand very high Q resonators to avoid excessive insertion loss. In particular, channel-select filters designed for 900MHz GSM will have Q_f = 2,250 (with filter bandwidth of 0.4 MHz) and demands Q_r > 12,300 for insertion loss less than 3 dB.

The requirement on resonator Q for low filter insertion loss further sets the requirement on the resonator impedance R_x For the same filter percent bandwidth (*i.e.*, same Q_f) and resonator Q (*i.e.*, same Q_r), achieving lower filter insertion loss requires larger R_Q/R_x, and thus larger R_Q and transducer bandwidth. In particular, to ensure less than 3 dB filter insertion loss, the R_Q/R_x ratio needs to be larger than 2.4. Therefore, if the optimal design requires R_Q = 1 kΩ, the resonator needs to be designed with R_x = 417 Ω.

It should be noted that according to (1-41), filter insertion loss is only a function of filter percent bandwidth and is independent of filter center frequency. However, it is generally more difficult to achieve higher Q at higher frequencies as the resonators suffer from more phonon-phonon interaction loss and prone to anchor loss at higher frequencies.

In summary, narrow-band MEMS filters operating at GHz require high coupling to ensure sufficient transducer bandwidth and high resonator Q to ensure low insertion loss. Unfortunately, current MEMS resonators can meet only one requirement, but not both. The following two sections review the previous work of the two most promising transduction methods for MEMS resonators: capacitive and piezoelectric transduction.

1.3 Previous Work on Capacitive MEMS Resonators

Capacitive, or electrostatic, resonators enjoy a wide range of resonant structure materials, as any conductive material, or insulators coated by conductive thin films, can form parallel plate capacitors for electrostatic transduction. This section outlines the common materials used for capacitive resonators in the literature.

1.3.1 Single-Crystal Silicon Capacitive Resonators

The two main advantages of using single-crystal silicon as the resonator structure are larger vertical dimension for larger transducer forces and consistent material properties. Resonators as thick as 20 µm [19] have been successfully fabricated on SOI wafer using DRIE to pattern the resonator structure and HF etch of box oxide to release the structure. The single-crystal property allows resonator dimension to scale down to 10 nm [20] with predictable material properties. On the other hand, single-crystal silicon is anisotropic such that its Young's modulus is different along different crystalline planes, which could possibly cause problems to movable mechanical structures with certain geometries.

1.3.2 Poly-Si and Poly-SiGe Capacitive Resonators

Unlike single crystal silicon wafer substrate, poly-Si and poly-SiGe thin-films deposited via low-temperature chemical vapor deposition (LPCVD) do not have homogeneous material properties on the nano-meter scale due to various grain sizes and grain boundaries. However, they are sometimes the preferred materials to use for better defined support beam lengths and anchoring positions, exemplified by a disk resonator with self-aligned anchor in Fig. 1-14 [21]. In particular, low-temperature deposition of SiGe with SiH_4 and GeH_4 allow the MEMS resonators to be built directly on CMOS for the MEMS-last integration scheme [22].

1.3.3 Metal Capacitive Resonators

Even lower process temperature for CMOS integration, cheaper process, smaller parasitic resistance drive the efforts for developing metal capacitive resonators, either using the back-end metal stacks of CMOS or metal thin-films deposited on CMOS back-end. Implementing MEMS resonators using the CMOS back-end metal and inter-layer dielectric (ILD) stacks [6][23] provided by foundry services has the advantage of well-controlled material property but with limitations on film thickness and difficulty of realizing small lateral transducer gap spacing. An example of CMOS-MEMS resonator is shown in Fig. 1-15(a). Among metal capacitive resonators in the published literature, both the highest frequency and quality factor Q have been achieved with electroplated nickel, shown in Fig. 1-15(b), demonstrating Q=54,507 at 59.96 MHz for a stemless disk resonator [24] and Q=2,467 at 425.7 MHz for a ring resonator [25]. There is strong evidence that anchor loss dominates the Q for resonators measured in vacuum. Reduction of anchor loss via optimized design of support beams and anchoring points has been shown to successfully enhance the Q by as much as 28 times for beam resonators [26] and 2.5 times for ring resonators [27], respectively. Such optimal anchors are difficult to achieve from back-end metal stacks with stringent design and layout rules.

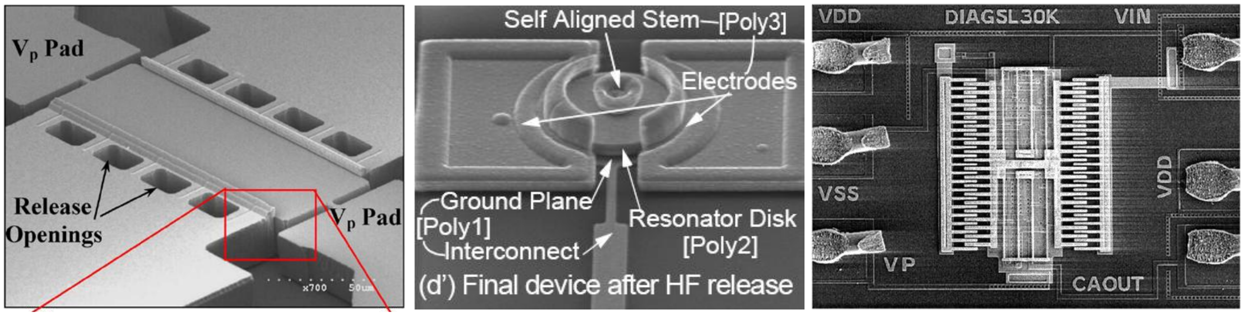

(a) (b) (c)

Fig. 1-14: (a) a bar resonator made of 20 µm thick single-crystal silicon [19]; (b) a poly-silicon disk resonator with self-aligned stem [21]; (c) a P$^+$ poly-$Si_{0.35}Ge_{0.65}$ resonator fabricated on top of a CMOS amplifier [22].

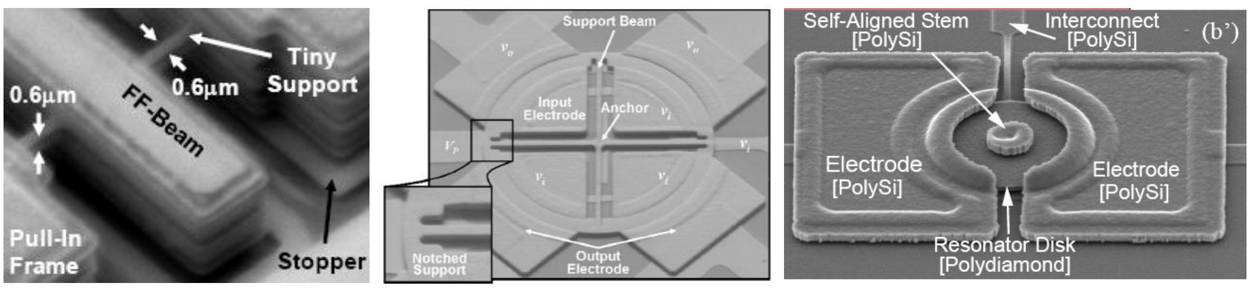

(a) (b) (c)

Fig. 1-15: (a) a CMOS-MEMS beam resonator made of backend ILD and metal of a CMOS chip [6]; (b) a ring resonator made of electroplated nickel [25]; (c) a poly-diamond disk resonator [28].

1.3.4 Other Materials

Some exotic materials (exotic compared to silicon and metal) arise as the promising materials for extremely high performance MEMS resonators due to their theoretically higher $f{\cdot}Q$ products than silicon and metal. In particular, diamond disk resonators (Q = 55,300 at f_o= 497.6 MHz), shown in Fig. 1-15(c) achieved 13.86x higher $f{\cdot}Q$ product than poly-silicon ones (Q = 8,100 at f_o= 245.1 MHz) with the same geometry (contour-mode disk with diameter of 22 µm) and anchoring method (center stem with diameter of 1.6 µm) [28].

1.4 Previous Work on Piezoelectric MEMS Resonators

As will be discussed in more detail in Chapter 4.1, piezoelectric transduction offers order of magnitudes higher coupling coefficient than capacitive ones for similar resonator geometry. Although the *Q*'s of thin-film piezoelectric resonators have been measured to be historically lower than those of capacitive counterparts, the low impedance enabled by the much higher coupling of piezoelectric transduction makes piezoelectric resonators the preferred technology in some applications. Unlike capacitive transduction in which any conductive material can be used, piezoelectric transduction relies on the piezoelectricity that only exists in some materials, i.e., piezoelectric materials. Common materials for MEMS piezoelectric resonators are thin quartz plates, sputtered ZnO, and sputtered AlN.

1.4.1 SAW Resonators

Surface Acoustic Wave (SAW) resonators normally use inter-digital transducer (IDT) electrodes to convert electric energy to mechanical energy in the form of Rayleigh waves, which have a longitudinal and a vertical shear component and propagate along the surface of bulk piezoelectric substrates [29], a schematic of which is shown in Fig. 1-16(a) [29]. While the IDT electrodes can be patterned using standard lithography, the need for bulk piezoelectric substrates impedes the single chip integration with today's silicon-based CMOS chips.

1.4.2 FBAR and BAW Resonators

A film piezoelectric thickness-extensional bulk mode resonator consists of a piezoelectric material film, normally on the order of several micrometers to tenth of micrometers, sandwiched between electrodes [31]. Such devices are called film bulk acoustic resonators (FBAR) or bulk acoustic wave (BAW) resonators depending on the thickness of the piezoelectric film. To achieve higher *Q*, the resonant structure is acoustically isolated from the surrounding medium via air gaps [32] or Bragg acoustic deflectors [33] composed of stacked layers of materials with mismatched acoustic impedances (Fig. 1-16(c); the latter has better power handling capability. Common piezoelectric thin-film materials include AlN, ZnO, and PZT, among which PZT gives the highest piezoelectric coupling coefficients (~60x higher than AlN), which is good, but also undesirably high permittivity (~100x higher than AlN), which is usually not suitable for high frequency applications. Sputtered AlN offers decent coupling and permittivity and is easier to process at room temperature, therefore has proven commercially viable for RF applications [34].

1.4.3 Lateral-Mode Thin-Film AlN Resonators

Despite the current market dominance of FBAR in the RF filter market for wireless handsets, the dependence of resonant frequency on the AlN film thickness preclude realization of multiple-frequency resonators with one AlN deposition step. Piazza *et. al.* pioneered the research in lateral-mode thin-film AlN resonators [35], shown in Fig. 1-16(c), as a technically feasible way to expand the major advantage of FBAR devices have over capacitive ones, namely, low motional impedance, to single chip implementation of multiple frequencies. This is possible as

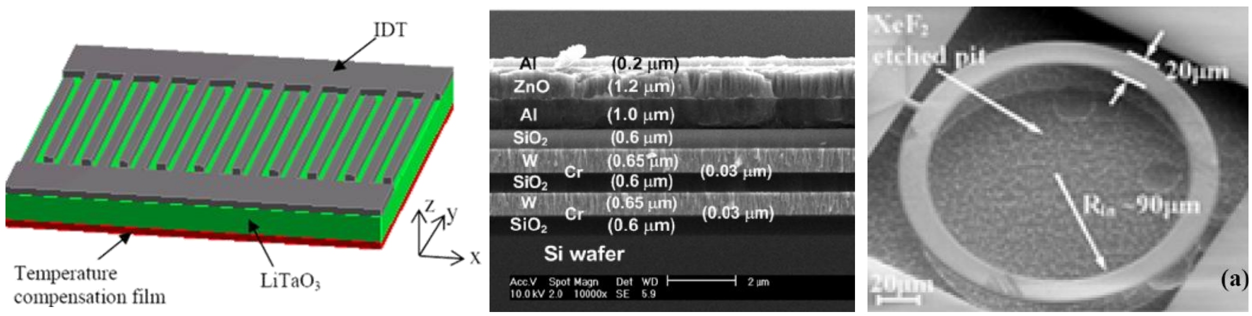

(a) (b) (c)

Fig. 1-16: (a) schematic of a typical SAW resonator [29] where metal layers are patterned to be inter-digital transducers on bulk piezoelectric materials, such as quartz crystal and $LiTaO_3$. (b) SEM cross-sectional image of[33] (c) SEM image of a contour-mode AlN ring resonator which achieve motional impedance of 56 Ω [35]a contour-mode AlN ring resonator which achieve motional impedance of 56 Ω [35].

for lateral mode devices, resonant frequency is determined by the lateral dimensions defined by lithography, rather than AlN film thickness. However, for the current lateral mode resonators made of sputtered AlN thin films, quality factors remain less than 3,500. *Q*'s less than 10,000 render insertion loss of channel-select filters larger than 3 dB, as shown in Fig. 1-16. This prevents the current AlN resonators to be applied to channel-select filters, despite its advantage on easier filter termination.

1.5 Thesis Outline

This thesis is organized as follows:

In Chapter 2, simulation shows insufficient coupling efficiency of current electrostatic transducers to be used in GHz channel-select filters. Close examination on the equation governing the force transduction and transducer efficiency reveals that reduction of transduction gap spacing is the most effective way among others to enhance coupling efficiency. To address the difficulty in release sub-50nm gap spacing, a new technique in which partial filling of the gap with high-*k* dielectric deposited via atomic layer deposition (ALD) reduces the gap spacing from 97nm down to effectively 32nm.

Chapter 3 first reviews the inherent limitations on release high-aspect ratio MEMS structures using either dry or wet etch. Realizing that the limitation exists regardless the chemicals involved in the etching, as long as one or more sacrificial materials need to be removed, a etch-free release method is purposed and demonstrated, in which the volume reduction property of silicidation is, for the first time, being used to generate gaps and to release MEMS structures using only seconds of silicidation annealing.

Another direction to achieve simultaneously low-impedance and high *Q* resonators is to raise the *Q* of piezoelectric resonators without raising their impedance. Chapter 4 proposes and demonstrates a method for raising *Q* by eliminating losses associated with contacting electrodes.

Chapter 5 further provides an alternative solution for raising the *Q* of piezoelectric resonators by energy sharing among resonators with and without electrodes. This method can further be used to combine the advantages of high coupling from piezoelectric transducers and low loss property from extremely high *Q* materials.

Chapter 6 concludes the above research and provides a view on the future research.

1.6 References

[1] C. T.-C. Nguyen, "Integrated micromechanical RF circuits for software-defined cognitive radio," *26th Sym. on Sensors, Micromachines, and App. Sys*., 2009, pp. 1-5.

[2] G. Piazza, P. J. Stephanou, and A. P. Pisano, "Piezoelectric Aluminum Nitride Vibrating Contour-Mode MEMS Resonators," *J. Microelectromech. Syst.*, vol. 15, no. 6, pp. 1406-1418, 2006.

[3] E. A. Gerber and M. H. Miles, "Reduction of the frequency-temperature shift of piezoelectric resonators by mechanical stress," Proceedings of the IRE, vol. 49, pp. 1650-1654, 1961.

[4] J. Berge, M. Norling, A. Vorobiev, and S. Gevorgian, "Field and temperature dependent parameters of the dc field induced resonances in $Ba_xSr_{1-x}TiO_3$- based tunable thin film bulk acoustic resonators," Journal of Applied Physics, vol. 103, pp. 064508-064508-8, 2008.

[5] C. Qingming, Z. Tao, and W. Qing-Ming, "Frequency-temperature compensation of piezoelectric resonators by electric DC bias field," Ultrasonics, Ferroelectrics and Frequency Control, IEEE Transactions on, vol. 52, pp. 1627-1631, 2005.

[6] W.-C. Chen, W. Fang, and S.-S. Li, "Quasi-linear frequency tuning for CMOS-MEMS resonators," *Proceedings*, 24th Int. IEEE Micro Electro Mechanical Systems Conf., pp. 784-787, 2011.

[7] L. Hurley, "A temperature-controlled crystal oscillator," in Frequency Control, 1989., Proceedings of the 43rd Annual Symposium on, 1989, pp. 55-57.

[8] A. S. Margulies and J. Mitola, III, "Software defined radios: a technical challenge and a migration strategy," *Proceedings*, Spread Spectrum Techniques and Applications, IEEE 5th International Symposium on, 1998, pp. 551-556 vol.2.

[9] L. Canxing, H. Lu, and L. Wenjia, "A 2-Bit 4GS/s flash A/D converter in 0.18 µm CMOS for an IR-UWB communication system," in Solid-State and Integrated-Circuit Technology, 2008. ICSICT 2008. 9th International Conference on, 2008, pp. 1965-1968.

[10] B. Verbruggen, P. Wambacq, M. Kuijk, and G. Van der Plas, "A 7.6 mW 1.75 GS/s 5 bit flash A/D converter in 90 nm digital CMOS," in VLSI Circuits, 2008 IEEE Symposium on, 2008, pp. 14-15.

[11] M. Choi, L. Jungeun, L. Jungho, and S. Hongrak, "A 6-bit 5-GSample/s Nyquist A/D converter in 65nm CMOS," in VLSI Circuits, 2008 IEEE Symposium on, 2008, pp. 16-17.

[12] R. Bagheri, A. Mirzaei, S. Chehrazi, M. Heidari, M. Lee, M. Mikhemar, W. Tang, A. Abidi, "An 800MHz to 5GHz software-defined radio receiver in 90nm CMOS," *Dig. of Tech. Papers*, Int. Conf. on Solid-State Circuits (ISSCC), 2006, pp. 1932-1941.

[13] Z. Ru, E. A. M. Klumperink, G. J. M. Wienk, B. Nauta, "A software-defined radio receiver architecture robust to out-of-band interference," *Dig. of Tech. Papers*, Int. Conf. on Solid-State Circuits (ISSCC), 2009, pp. 230-231.

[14] K. Wang, A.-C. Wong, and C. T.-C. Nguyen, "VHF free–free beam high-*Q* micromechanical resonators," *J. Microelectromech. Syst.*, vol. 9, no. 3, pp. 347–360, 2000.

[15] R. A. Johnson, Mechanical Filters in Electronics. New York: Wiley, 1983.

[16] F. D. Bannon, J. R. Clark, and C. T.-C. Nguyen, "High-*Q* HF microelectromechanical filters," *J. Solid-State Circuits*, vol. 35, no. 4, pp. 512–526, 2000.

[17] S.-S. Li, Y.-W. Lin, Y. Xie, Z. Ren, and C. T.-C. Nguyen, "Small percent bandwidth design of a 431-MHz notch-coupled micromechanical hollow-disk ring mixer-filter," *Proceedings*, IEEE Int. Ultrasonics Symposium, Sept. 18-21, 2005, 1295-1298.

[18] A. I. Zverev, Handbook of Filter Synthesis. NY: Wiley, 1967.

[19] S. Pourkamali, G. K. Ho, and F. Ayazi, "Low-Impedance VHF and UHF Capacitive Silicon Bulk Acoustic Wave Resonators Part I: Concept and Fabrication," in Transactions, IEEE Electron Devices, vol. 54, pp. 2017-2023, 2007.

[20] D. Weinstein1 and S. A. Bhave, "Acoustic resonance in an independent-gate FinFET," *Tech. Digest*, Solid-State Sensor, Actuator, and Microsystems Workshop, Hilton Head, South Carolina, 2010, pp. 459-462.

[21] J. Wang, Z. Ren, and C. T.-C. Nguyen, "Self-aligned 1.14-GHz vibrating radial-mode disk resonators," *Dig. of Tech. Papers*, Int. Conf. on Solid-State Sensors & Actuators (Transducers'03), Boston, Massachussets, June 8-12, 2003, pp. 947-950.

[22] A. E. Franke, J. M. Heck, T.-J. King, and R. T. Howe, "Polycrystalline silicon—Germanium films for integrated microsystems," *J. Microelectromech. Syst.*, vol. 12, no. 2, pp. 160–171, 2003.

[23] C-C Lo, F. Chen, and G. K. Fedder, "lntegrated HF CMOS-MEMS square-frame resonators with on-chip electronics and electrothermal narrow gap mechanism," in *Tech. Dig., Transducers'05*, 2005, pp. 2074–2077.

[24] W.-L. Huang, Z. Ren, and C. T.-C. Nguyen, "Nickel vibrating micromechanical disk resonator with solid dielectric capacitive-transducer gap," in Proc. IEEE Int. Freq. Control Symp. pp. 839-842, 2006.

[25] W.-L. Huang, S.-S. Li, Z. Ren, and C. T.-C. Nguyen, "UHF nickel micromechanical spoke-supported ring resonators," *Dig. of Tech. Papers*, Int. Conf. on Solid-State Sensors & Actuators (Transducers'07), 2007, pp. 323–326.

[26] K. Wang, A.-C. Wong, C. T.-C. Nguyen, "VHF Free–Free Beam High-Q Micromechanical Resonators," *J. Microelectromech. Syst.*, vol. 9, no. 3, pp. 346–360, 2000.

[27] S.-S. Li, Y.-W. Lin, Y. Xie, Z. Ren, and C. T.-C. Nguyen, "Micromechanical "hollow-disk" ring resonators," in Tech. Digest., 17th IEEE Int. MEMS Conf., pp. 821-824, 2004.

[28] J. Wang, J. E. Butler, T. Feygelson, and C. T.-C. Nguyen, "1.51-GHz nanocrystalline diamond micromechanical disk resonator with material-mismatched isolating support," *Proceedings*, 17th Int. IEEE Micro Electro Mechanical Systems Conf., Maastricht, The Netherlands, Jan. 25-29, 2004, pp. 641-644.

[29] P. S. Cross, "Reflective arrays for SAW resonators," in Ultrasonics Symposium, 1975, pp. 241-244.

[30] H. Kando, M. Watanabe, S. Kido, T. Iwamoto, K. Ito, N. Hayakawa, K. Araki, I. Hatsuda, T. Takano, Y. Nagao, T. Nakao, T. Toi, and Y. Yoshii, "Improvement in temperature characteristics of plate wave resonator using rotated Y-cut $LiTaO_3$ structure," 24th Int. IEEE Micro Electro Mechanical Systems Conf., 2011, pp. 768-771.

[31] M. Berte, "Acoustic bulk wave resonators and filters operating in the fundamental mode at frequencies greater than 100 MHz," in 31st Annual Symposium on Frequency Control. 1977, 1977, pp. 122-125.

[32] M. Hara, J. Kuypers, T. Abe, and M. Esashi, "Aluminum nitride based thin film bulk acoustic resonator using germanium sacrificial layer etching," *Dig. of Tech. Papers*, Int. Conf. on Solid-State Sensors & Actuators (Transducers'03), 2003, pp. 1780-1783.

[33] L. Mai, V.-S. Pham, and G. Yoon, "ZnO-based film bulk acoustic resonator devices on a specially designed Bragg reflector," *J. Applied Physics*, vol. 95, pp. 667-671, 2009.

[34] R. Ruby and P. Merchant, "Micromachined thin film bulk acoustic resonators", Freq. Control Symp., pp.135-138, 1994.

[35] G. Piazza, P. J. Stephanou, J. M. Porter, M. B. J. Wijesundara, and A. P. Pisano, "Low motional resistance ring-shaped contour-mode aluminum nitride piezoelectric micromechanical resonators for UHF applications," 18th Int. IEEE Micro Electro Mechanical Systems Conf., 2005, pp. 20-23.

Chapter 2: ALD Partially-Filled Gaps

2.1 Introduction

To date, capacitively transduced micromechanical resonators have posted the highest Q's of room temperature on-chip resonator technologies, with Q values exceeding 150,000 in the VHF range [1], 14,600 in the GHz range [2], and 560 up to 37 GHz [3]. This makes them strong candidates for use as RF channel-selectors in next generation software-defined cognitive radios [4], or as ultra-low noise oscillators in high performance radar applications and space exploration.

Unfortunately, the exceptional Q's of these resonators are not easy to access, because the impedances they present are often much larger than that of the system that uses them. For example, many of today's board-level systems are designed around 50Ω impedance, which is much smaller than the 2.8 kΩ termination resistors required by the 163 MHz differential disk array filter of [5]. Thus, even though the filter of [5] attains an impressively low insertion loss of 2.43 dB for a 0.06% bandwidth, it requires an L-network to match to 50Ω. While it is true that as micromechanical filters are integrated together with transistors on single silicon-chips impedance requirements will grow to the kΩ range for best performance [6], off-chip board-level applications will still need lower impedance.

Pursuant to attaining lower capacitive micromechanical resonator impedances, this work, first published in [7], employs atomic layer deposition (ALD) [8] to partially fill the electrode-to-resonator gaps of released disk resonators with high-k dielectric material and thereby achieve substantially smaller gap spacing, as small as 32 nm. This reduction in gap spacing increases the electromechanical coupling factors (η_e's) of capacitive-transducers by a factor of 8.1×; this not only lowers termination impedances for *capacitively transduced* micromechanical filters from the kΩ range to the sub-100Ω-range, thereby making them compatible with board-level RF circuits, but does so in a way that reduces micromechanical filter termination resistance R_Q much faster than the electrode-to-resonator overlap capacitance C_o. Thus, gap reduction substantially increases the $1/(R_Q C_o)$ figure of merit (*FOM*). The increase in the FOM is also n^2× faster (hence, better) than that of fully-filled solid-dielectric gap methods for R_x reduction [9]. This partial dielectric-filling based approach further prevents shorting of the resonator to its electrode, which greatly improves the resilience of micromechanical resonators against ESD or other events that might pull a resonator into its electrode.

2.2 Coupling Efficiency of Capacitive Transducers

2.2.1 Capacitive Transducers

Fig. 2-1(a) shows a parallel plate capacitor system in which one plate is fixed and the other plate is attached to a spring, forming a spring-mass-damper system, which is essentially a resonator. With the input signal v_i and DC bias V_P applied to the system, the electrostatic force

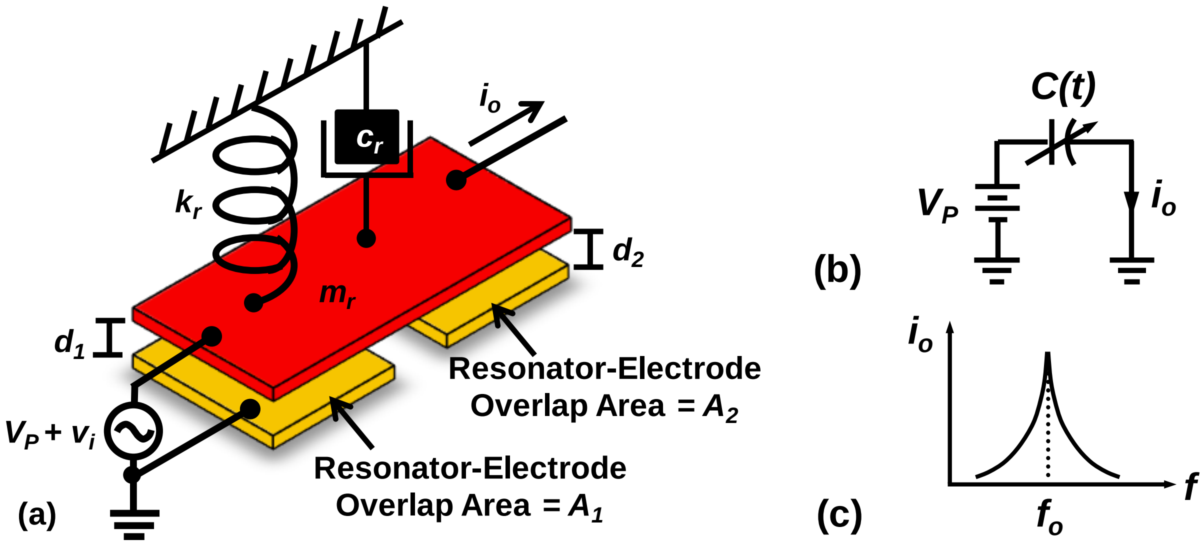

Fig. 2-1: (a) Schematic of a capacitive transducer. (b) A simplified circuit model of (a) upon resonance, where the V_P biased time varying capacitor generate output current. (c) The output current has energy concentrated at the resonant frequency of the resonator, showing a resonant peak on the frequency domain.

generated between the resonator and the electrode plates can be written as

$$F = (V_P + v_i)^2 \frac{\partial C}{\partial x} \tag{2-1}$$

where V_P is a DC bias applied to the conductive resonator structure; $\partial C/\partial x$ is the change in electrode-to-resonator overlap capacitance per displacement. Assuming the time-varying displacement x is much larger than gap spacing d, such that the nonlinearity can be ignored for now, the force component in (2-1) that has a frequency component the same as v_i is

$$F_{\omega_o} = V_P v_i \cdot \frac{A\varepsilon_r\varepsilon_o}{d^2} \tag{2-2}$$

where A is the electrode-to-resonator overlap area; ε_r is the relative permittivity of the electrode-to-resonator gap material (=1, if not present); ε_o is the permittivity in vacuum; and d is the electrode-to-resonator gap spacing. The electromechanical coupling coefficient on the input side models how efficiently the input electrical signal can be transduced to mechanical energy in the form of mechanical force. It can therefore be written as the magnitude of mechanical force generated per unit magnitude of input voltage:

$$\eta_{e,i} = \frac{F_{\omega_o}}{v_i} = V_P \cdot \frac{A_1\varepsilon_r\varepsilon_o}{d_1^2} \tag{2-3}$$

Upon resonance, the vibration amplitude, x, modulates the gap spacing and therefore the capacitance. With constant DC bias applied across the parallel plate, the stored charge changes accordingly, resulting in output current when the output electrode is connected to a resistor. The difference in stored charge, ΔQ, when the gap spacing changes from d to (d-x) is:

$$\Delta Q = V_P \cdot A_2 \varepsilon_r \varepsilon_o \cdot \left(\frac{1}{d_2 - x} - \frac{1}{d_2} \right) \approx V_P \cdot \frac{A_2 \varepsilon_r \varepsilon_o}{d_2^2} \cdot x \tag{2-4}$$

The electromechanical coupling coefficient on the output side, η_o, models how efficiently the mechanical energy stored in the resonator can be transduced to electrical energy as output currents. It can be written as the amount of charge generated per mechanical displacement:

$$\eta_{e,o} = \frac{\Delta Q}{x} = V_P \cdot \frac{A_2 \varepsilon_r \varepsilon_o}{d_2^2} \tag{2-5}$$

To simplify the following analysis, the parameters of both transducers on input and output ports will be assumed to be the same, which results in equal electromechanical coupling coefficients, denoted as η_e:

$$\eta_e = \eta_{e,i} = \eta_{e,o} = V_P \cdot \frac{A_o \varepsilon_r \varepsilon_o}{d_o^2} \tag{2-6}$$

2.2.2 Filter FOM of Capacitive Resonators

Consider a capacitive disk resonator with radius of R and thickness of H. The filter figure of merit (FOM) defined in Chapter 1 for capacitive resonators can be related to parameters of constituent resonators by plugging the coupling coefficients η_e in (2-6) into (1-33):

$$FOM = \frac{1}{R_Q C_o} = \frac{q \eta_e^2}{B m_r} \cdot \frac{d_o}{A_o \varepsilon_o \varepsilon_r} \propto \frac{q}{B} \frac{1}{\pi} \frac{\varepsilon_o}{\kappa \rho R} \cdot \frac{V_P^2 \varepsilon_r}{d^3} \tag{2-7}$$

Where B is the filter passband width; q is a normalized parameter obtained from a filter cookbook [10]; m_r is the dynamic mass of the resonator at its point of maximum displacement; κ is a modifier that accounts for the integration needed to obtain dynamic stiffness [11]; ρ is the density of the disk structural material; and (2-7) was reduced to its final form by recognizing that the dynamic mass of the disk at a maximum velocity point on the disk is $m_r = \kappa\rho\pi R^2 H$.

Of the variables in (2-7), only ε_r, V_P, and d are truly adjustable, although the motional impedance R_x can often be minimized by operating at a fundamental mode, rather than higher modes. This implies that arraying approaches [12] or parallel combinations of multiple resonators, shown in Fig. 2-2, reduces R_x and essentially increase the electrode-to-resonator overlap area do not in fact raise the *FOM*. As the impedance reduces linearly to the number of resonators involved, the capacitance also increases by the same rate. An approach similar to parallel combinations for reducing the impedance is to increase the electrode-to-resonator overlap area by increasing the lateral dimension of the resonator. This approach is applicable to certain mode-shapes, such as the contour-mode ring in [2], where the resonant frequency is determined by the width of the ring and independent of the average radius, as long as the latter is

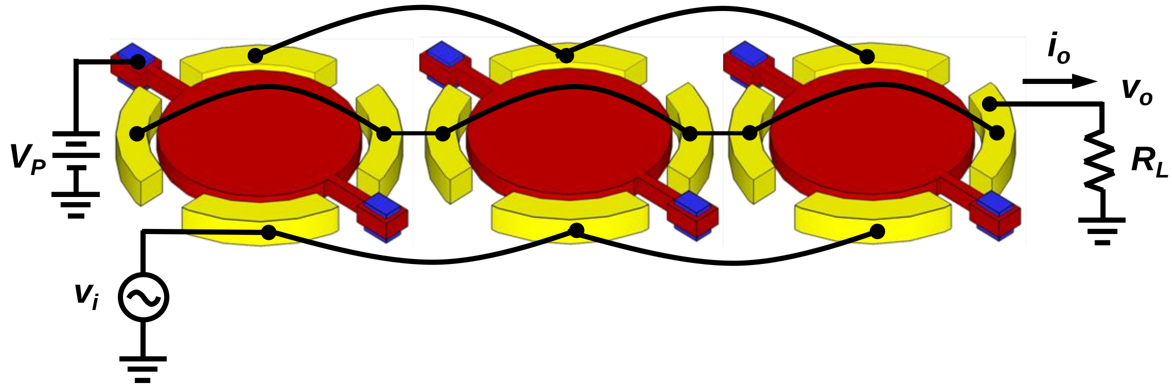

Fig. 2-2: Connecting resonators in parallel reduces R_x linearly, but filter *FOM* remains the same.

Table 2-1: Comparison of approaches for R_Q reduction and filter *FOM* improvement

Approach	η_e	R_Q	C_o	*FOM*
Arraying with *n* resonators	n x	n^{-1} x	n x	1 x
Solid-gap filling with ε_r=*n*	n x	n^{-2} x	n x	n x
Increasing DC bias V_P by *n* x	n x	n^{-2} x	1 x	n^2 x
Air gap reduction from d_o to $d=d_o/n$	n^2 x	n^{-4} x	n x	n^3 x

much larger than the former. This approach, however, also gives only smaller impedance but the same filter *FOM*. On the other hand, solid-gap filling methods, such as in [9] and Fig. 2-3(a), that raise ε_r and reduce gap spacing at the same time, do improve the *FOM*, although the improvement ends up being much less than the factor by which ε_r increases, since the need to compress the gap material often greatly reduces the benefits. In particular, the resonators measured in [9] with 80 nm air gaps and 20 nm nitride solid gaps, with other parameters being the same, show Q=52,400, R_x=12.36 kΩ and Q=25,300, R_x=1.51 kΩ, respectively, based on which the improvement in the coupling coefficient is calculated to be 4x. This value is far from the expected improvement factor of 112x gained from 4x reduction in gap spacing and 7x increase from ε_r of silicon nitride compared to air (or vacuum) as the gap material. Finally, although *FOM* increases with the square of V_p, its value is often limited by the level of the DC power supply, especially for the cases for on-chip integration, unless charge pumps can be used to increase the available V_P. Thus, it seems to still be gap spacing reduction that provides the largest gain in *FOM*, with very strong third power dependence. In particular, a reduction in gap spacing by 5× yields a 125× increase in *FOM*. Table 2-1 summarizes the efficacy of different approaches to reducing R_Q and increasing *FOM*.

Linearity issues will need to be curtailed, as the *IIP3* of the disk will reduce as the gaps shrink [14], but the effects are less consequential as frequencies rise (*e.g.*, at GHz) and can be alleviated in certain mechanical circuit networks.

2.3 Gap Reduction via Partial Gap Filling

2.3.1 Methods for Achieving Small Gaps

Evidently, from an *FOM* perspective, reducing the electrode-to-resonator gap spacing is the best way to reduce R_Q. Achieving smaller gaps, however, might not be so straightforward. This is especially true for small lateral gaps, which is essential for lateral mode capacitive resonators. The work in [15], with SEM shown in Fig. 2-3(b), demonstrated ~100 nm gap spacing by direct dry etching a blanket Ge film to form a Ge blade, which is removed via wet etch to form an air gap. In this case, the resolution in lithography and dry etch determines the minimum achievable gap spacing. While photoresist lines as small as ~100 nm and ~10 nm can be patterned by deep UV source and electron beam source, respectively, the real challenge lies in transferring such small patterns to 1 µm or thicker films, resulting in high aspect ratio structures, via anisotropic etching.

A more scalable method is to use sacrificial material deposition. For example, the process of [16] achieves its sub-100nm lateral gaps using a sacrificial oxide sidewall film that is sandwiched between the resonator and electrode during intermediate process steps, but then removed via a liquid hydrofluoric acid release etchant at the end of the process to achieve the small gap. Fig. 2-4 shows the last step of the fabrication process. Here, sacrificial sidewall layers are removed via wet etching to release structures that will eventually move. This approach to achieving lateral gaps, while effective for gap spacings above 50 nm, proves difficult for smaller gap spacings with acceptable yield. In particular, smaller gap spacings make it more difficult for etchants to diffuse into the gap toward the etch front and for etch by-products to diffuse away from the etch front. While there is some evidence that a gaseous etchant capable of more easily accessing and escaping the gap, such as vapor phase HF, might prove effective for releasing structures with 10 nm gaps or less [17][18], with SEM of [18] shown in Fig. 2-3(c), gaps so small (once released) might be overly susceptible to inadvertent shorting, due to ESD or other catastrophic events.

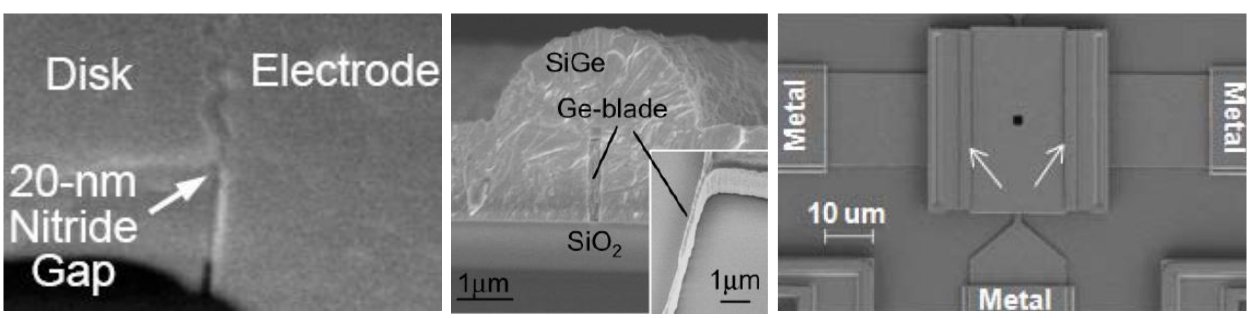

(a) (b) (c)

Fig. 2-3: Methods for resolving small lateral transduction gaps for capacitive resonators. (a) Solid gap formed by 20 nm thick nitride does not require release step for small gaps [9]. (b) A ~100 nm gap for SiGe resonators is formed by dry etching a Ge blade followed by SiGe deposition and finally H_2O_2 etching to remove the sacrificial Ge [15]. (c) 10 nm air gaps, where the arrows point to, are released by the vapor HF [18].

2.3.2 ALD Partial-Filling for Sub-50nm Gap Spacing

Rather than removing material from small gaps by etching as drawn in Fig. 2-4, one alternative approach to attaining both sub-50nm high-aspect-ratio gaps and protection against ESD events is to partially fill an already released gap with a non-conductive dielectric material, as shown in Fig. 2-5(a). Here, filling via a dielectric is just as effective as if filling were performed with a metal if the permittivity of the dielectric is high enough to allow the air (or vacuum) gap of Fig. 2-5(b) to set the overall capacitance value. Specifically, the capacitance between the electrode and resonator of Fig. 2-5(a) can be modeled by the series connection of three capacitors shown in Fig. 2-5(b). Here, the total electrode-to-resonator capacitance is given by

$$C(x) = C_{coat} \parallel C_{air}(x) \parallel C_{coat} = \frac{C_{coat}}{2} \parallel C_{air}(x) \tag{2-8}$$

where both C_{coat} have identical values as the same thickness of dielectric is deposited on all of the surfaces. From (2-8), $(\partial C/\partial x)$ can be written (for small x) as

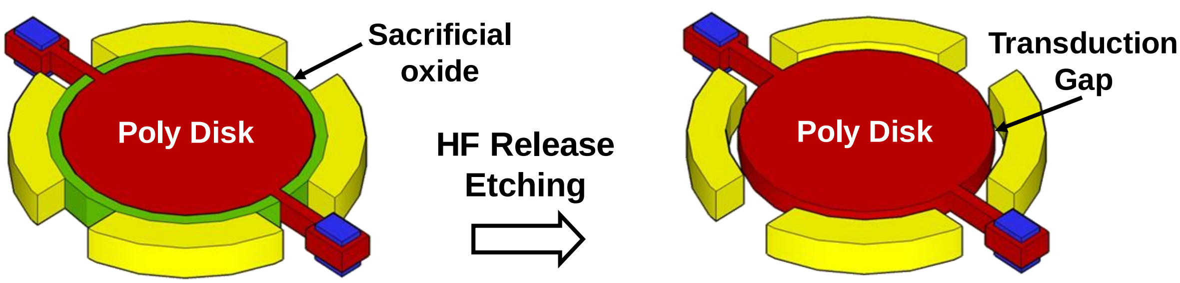

Fig. 2-4: Cross-sections depicting the final release step in the fabrication sequence for a laterally driven wine-glass disk resonator.

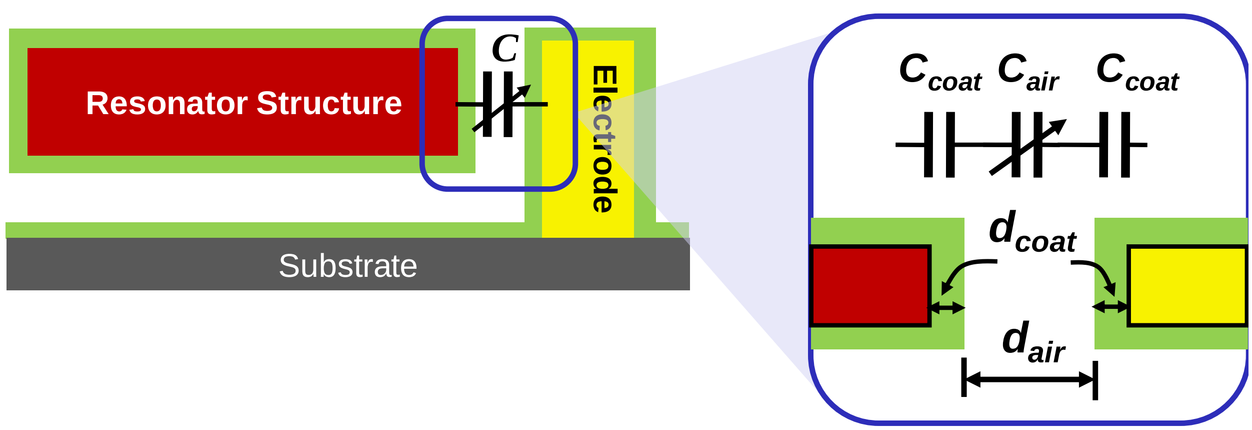

Fig. 2-5: (a) Schematic of a partial-dielectric-filled gap. (b) Enlarged view of the gap and its equivalent series capacitances.

$$\frac{\partial C}{\partial x} = \frac{1}{\varepsilon_o A_o}\left[\frac{C_{coat}}{2} \parallel C_{air}\right]^2 = \frac{1}{d_{air} C_{air}}\left[\frac{C_{coat}}{2} \parallel C_{air}\right]^2 \tag{2-9}$$

where C_{air} is the capacitance across the air gap for $x = 0$ (*i.e.*, no displacement); $C_{air}(x)$ is this capacitance as a function of displacement x; C_{coat} is the capacitance across each dielectric-coated region; A_o is the resonator-electrode overlapping area. Naturally, if $C_{coat} >> C_{air}$, then the capacitance and ($\partial C/\partial x$) reduce to

$$C(x) = C_{air}(x) \tag{2-10}$$

Therefore,

$$\frac{\partial C}{\partial x} = \frac{C_{air}}{d_{air}} \tag{2-11}$$

which are the values that would ensue if there were no dielectric and if the electrode-to-resonator gap were equal to d_{air}. In practice, $C_{coat}/2$ should be at least 10 times larger than C_{air} in order for (2-11) to be valid, which means that the dielectric constant of the filling material should be at least

$$\varepsilon_{coat} \geq 20\varepsilon_o \frac{d_{coat}}{d_{air}} \tag{2-12}$$

where the gap dimensions d_{coat} and d_{air} are indicated in Fig. 2-5. For the case where the gap spacing of a disk resonator is reduced from 94 nm to 32 nm with high-*k* dielectric coating, achieving a (d_{coat}/d_{air}) ratio of (31/32) and providing a 74x reduction in R_Q, (2-12) suggests that the relative permittivity of the dielectric filling material should be >19.4 to allow the use of (2-11) to determine ($\partial C/\partial x$); otherwise (2-9) should be used. Hafnium oxide (HfO_2) comes close and so is a reasonable choice of dielectric.

As the impedance is sensitive to the final gap spacing, the deposition of high-*k* dielectric films must provide precise thickness control. Furthermore, to attain high-aspect-ratio sub-50nm gaps, the starting gap size should already be small (*e.g.*, on the order of 100 nm), so the method used to fill the gaps should be very conformal. Recognizing this, atomic layer deposition (ALD) is uniquely suited for this gap-coating process, since its two-step precursor, monolayer-by-monolayer deposition methodology effects very precise film thicknesses with conformality sufficient to uniformly cover the surfaces of the 30:1 aspect ratio (100 nm initial gaps of the 3 μm thick resonators).

2.3.3 Atomic Layer Deposition (ALD)

Indeed, thin high-*k* dielectric films, such as hafnium and zirconium oxide films, have been prepared by a variety of physical vapor deposition (PVD) methods, such as laser pulse ablation [19] and sputtering [20], and chemical vapor deposition (CVD) with various precursors [21]. PVD methods provide excellent film composition and thickness control, but they do not deposit conformally over high-aspect-ratio structures and so are not suitable to partially refill lateral

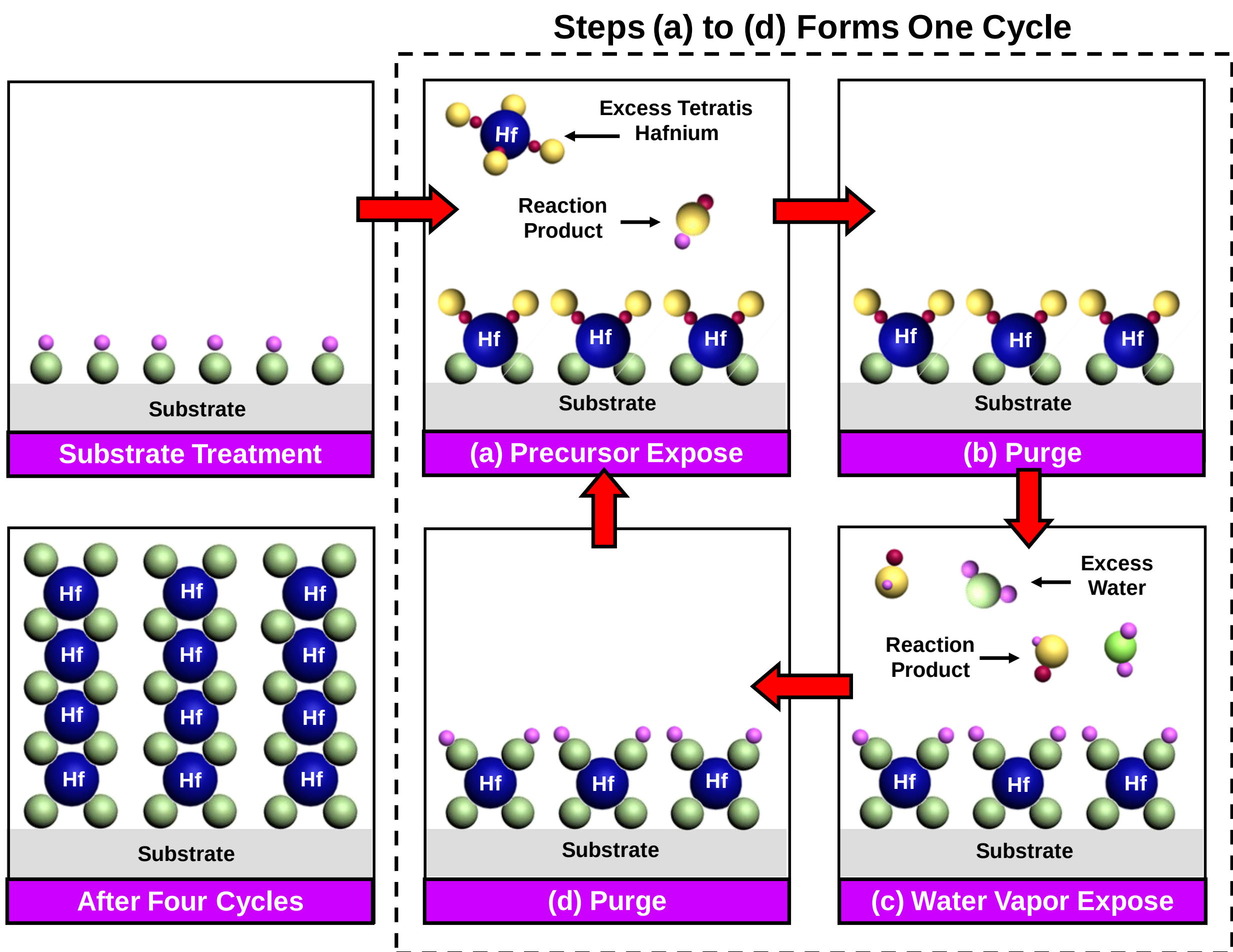

Fig. 2-6: HfO_2 as an example to illustrate the steps of ALD of high-*k* dielectrics, where repeated exposure and purge cycles of metal and oxygen precursors are performed.

gaps; CVD method typically requires deposition temperature higher than 300°C, which causes formation of crystalline films with detectable surface roughness.

Atomic layer deposition (ALD) offers conformal high-*k* dielectric thin films by alternately exposing the surface to reactive metal and oxygen precursors. Water vapors or ozone are common choices of oxygen precursors. A purge step follows each precursor exposure step. Such exposure-purge combination results in successive surface reaction between the precursor introduced and the other precursor already adsorbed to the surface in the previous exposure step. Each cycle deposits only an atomic layer of the target metal dielectric. The ALD process of HfO_2 is summarized in Fig. 2-6. Among a variety of possible precursors, this work uses tetrakis (ethylmethylamido) hafnium and water vapor [23].

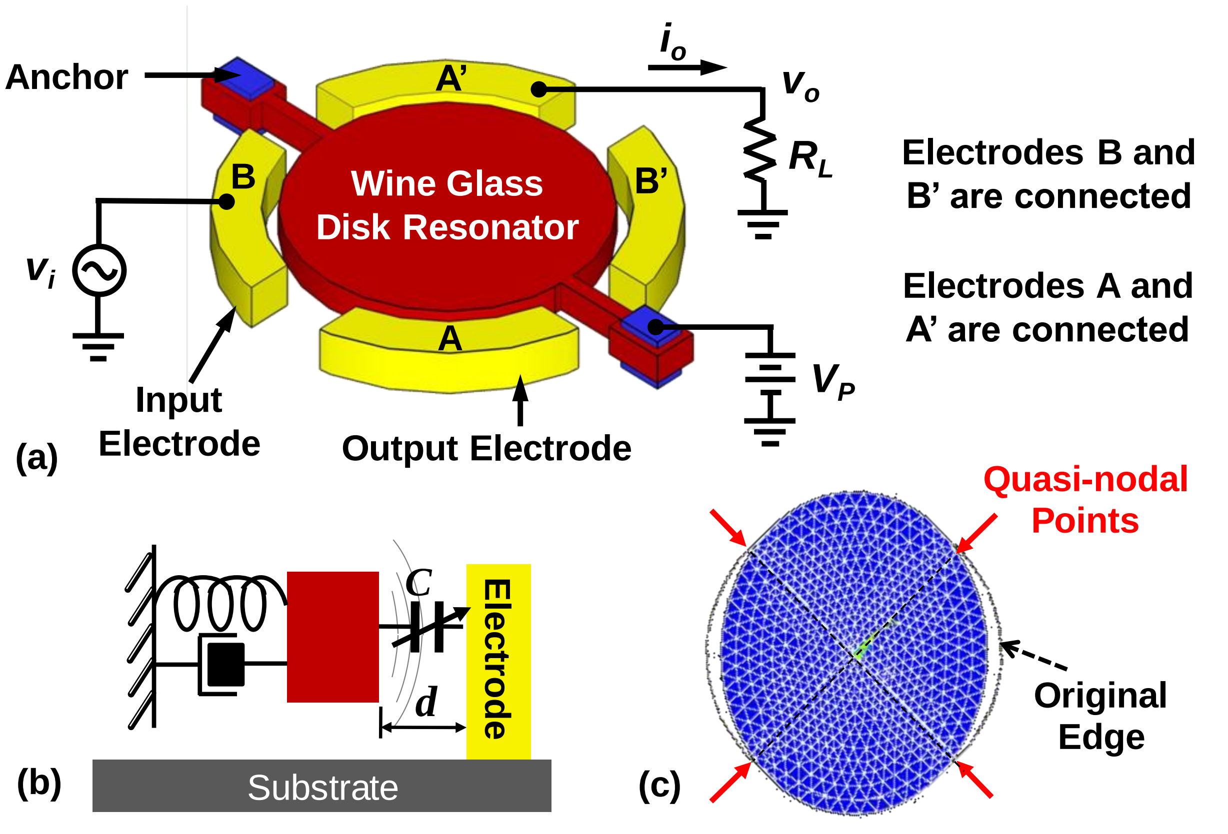

Fig. 2-7: (a) Schematic of measurement setup for a wine-glass disk resonator. (b) Equivalent mechanical mass-spring-damper system of (a). (c) The mode shape of wine-glass mode vibration, where the disk expands and contracts along orthogonal axes.

2.4 Experimental Results

2.4.1 Wine-Glass Disk Resonator

Fig. 2-7(a) shows a wine-glass disk resonator with the measurement setup where AC signal is applied to one set of the electrodes (B-B') and the output current is sensed from the other set (A-A'); DC bias is applied to the conductive resonator structure. The disk is suspended above the substrate and supported by beams attached to the disk at two of the four quasi-nodal points of the wine-glass mode shape, shown in

Fig. 2-7(c), where the disk expands and contracts along orthogonal axis. When the frequency of input AC signal matches the wine-glass mode resonance frequency, the disk starts to vibrate. The resonant frequency f_o is given by [24]

$$\left[\Psi_n\left(\frac{\zeta}{\xi}\right)-2-q\right]\cdot\left[\Psi_n(\zeta)-2-q\right]=4(q-1)^2 \qquad (2\text{-}13)$$

where

$$\Psi_n(x)=\frac{xJ_{n-1}(x)}{J_n(x)}, \qquad q=\frac{\zeta^2}{6}, \qquad \zeta=2\pi f_o R\sqrt{\frac{\rho(2+2\sigma)}{E}}, \qquad \xi=\sqrt{\frac{2}{1-\sigma}} \qquad (2\text{-}14)$$

where $J_n(x)$ is Bessel function of first kind of order n; R is the disk radius; ρ, σ, and E, are the density, Poisson ratio, and Young's modulus, respectively, of the disk structural material, in this case, poly-silicon. The resonance frequency of the wine-glass mode is, to the first order, inversely proportional to disk radius R. The complete equations for calculating the equivalent mass, stiffness, and coupling coefficients can be found in [25], which will not be repeated here.

These wine-glass disk resonators were fabricated with a three-polysilicon process described in [26] and released in hydrofluoric acid (HF). Fig. 2-8 shows SEM's of an as-released device and zoomed-in view on the transduction gap. The post-release process used to reduce gap spacings in this work then consisted of an ALD step using a custom-built system (Fig. 2-9) to deposit HfO_2 into the gaps of already-released disk resonator devices as illustrated in Fig. 2-5. Then, a simple lithography and HF dip step were performed to remove HfO_2 over the bond pads, followed by photoresist etching in oxygen plasma. The ALD of HfO_2 was performed at 140 ^oC using tetrakis (ethylmethylamido) hafnium and water vapor prepared at 120 ^oC.

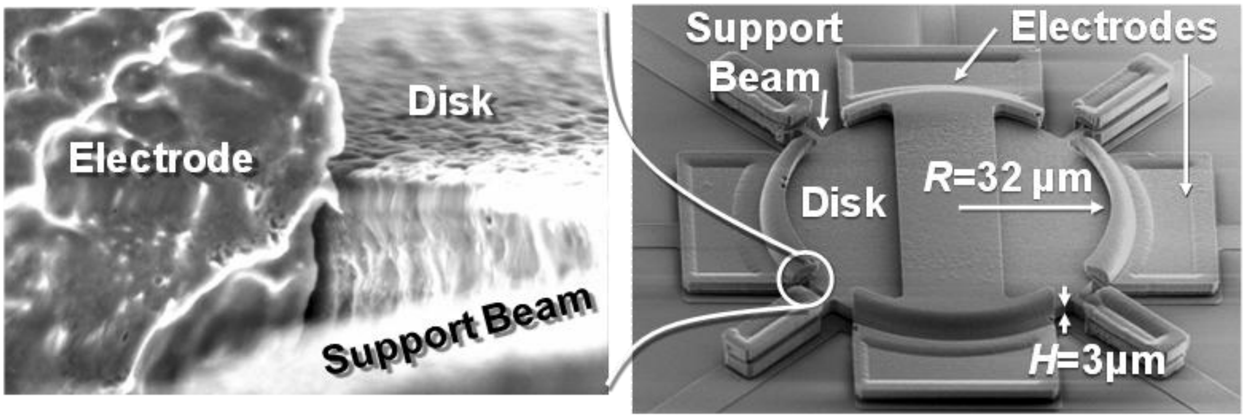

Fig. 2-8: SEM of a fabricated 60 MHz polysilicon wine-glass disk resonator with zoomed-in view on the ~97 nm transduction gap and the support beam.

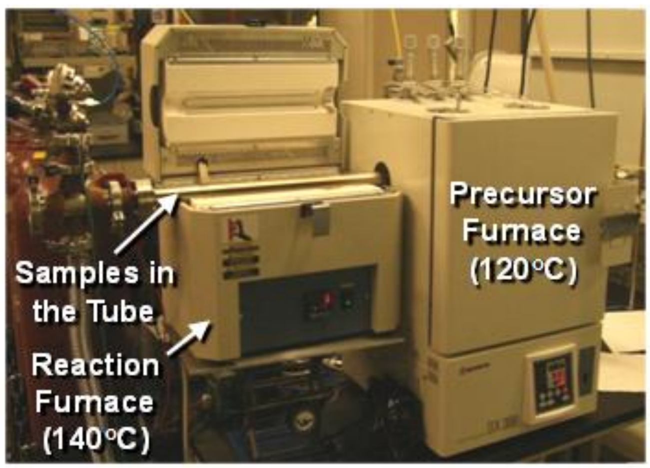

Fig. 2-9: A custom-built atomic layer deposition tool for HfO_2 deposition, assembled by Professor Ali Javey's research group at UC Berkeley.

2.4.2 Extrapolation of Gap Spacing Before and After ALD

Perhaps the most accurate way to determine the electrode-to-resonator gap spacing for capacitively transduced resonators is to use advantageously the frequency dependence on V_P. The frequency dependence on V_P is a result of nonlinearity inherent to capacitive resonators of which the vibration amplitude modulates the transduction gap spacing. As the displacement x is small compared to gap spacing d, performing a Taylor series expansion on the dynamic capacitance yields

$$\frac{\partial C}{\partial x} = -\frac{C_o}{d}\left(1 - \frac{2}{d}x + \frac{3}{d^2}x^2 - \frac{4}{d^3}x^3 + \cdots\right) \tag{2-15}$$

Plugging (2-15) into the force equation previously presented in (2-1) and collecting the terms at ω_o results in

$$F(\omega_o) = V_P \frac{C_o}{d} v_{in}(\omega_o) + V_P^2 \frac{C_o}{d^2} x(\omega_o) \tag{2-16}$$

The first term on the right-hand side equals $F_{\omega o}$ in (2-2). The second term has the form of spring restoring force with the equivalent stiffness of

$$k_e = V_P^2 \frac{C_o}{d^2} \tag{2-17}$$

where k_e is usually called the electrical stiffness. Note that (2-17) is for the case of a two rectangle parallel plate system with displacement orthogonal to the plates. For resonators vibrating in a wine-glass mode shape, (2-17) no longer holds and needs to be modified to

$$\left\langle \frac{k_e}{k_r} \right\rangle = \int_{\theta_1}^{\theta_2} \frac{1}{k_r(\theta)} \cdot \left(V_P{}^2 \frac{\varepsilon_o RHd\theta}{d^3} \right) \tag{2-18}$$

where k_r is the stiffness of the resonator; θ_1 and θ_2 are the angles of the surrounding electrodes, as shown in Fig. 2-10(a); other parameters are defined in Fig. 2-8. The electrical stiffness is subtracted from k_r and therefore influences the measured resonant frequency:

$$f_o = \frac{1}{2\pi}\sqrt{\frac{k_m - k_e}{m_r}} = \frac{1}{2\pi}\sqrt{\frac{k_m}{m_r}\left(1 - \left\langle \frac{k_e}{k_m} \right\rangle\right)} \tag{2-19}$$

From (2-19) and (2-19), the dependence of measured resonant frequency f_o on DC bias voltage V_P is strongly influenced by the gap spacing d_o, suggesting that plots of f_o versus V_P can be used to very accurately extract d_o.

Fig. 2-11 plots frequency f_o versus dc-bias V_P for two devices before and after HfO_2 coating, for which curve-fitting with the theoretical prediction of (2-19) yields gaps of 97 nm for the uncoated disk and 37 nm for the HfO_2-coated one — both very close to expectations given that ~30 nm of HfO_2 was deposited, all attesting to the precision with which ALD can achieve a specific film thickness. Note that these theoretical curves are calibrated according to one data point, as it is difficult to predict the exact resonant frequency given fabrication variability. However, the resonator frequency has no effect on the curvature, which is used to extract the gap spacing.

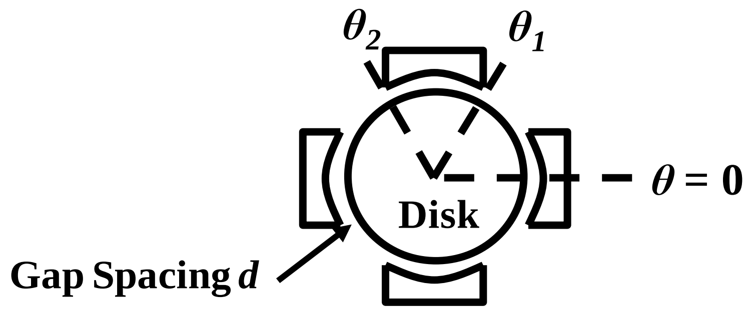

Fig. 2-10: Arrangement of the electrode surrounding a disk resonator designed for wine-glass mode vibration.

Using V_P dependence on frequency to determine gap spacing is convenient and powerful, as the gap spacing is obtained from fitting measurement data to the entire theoretical curve for different V_P's rather than the absolute values of simulation results. Fig. 2-12 plots similar measured and theoretical curves for another device after HfO_2 ALD, but this time also plotting the theoretical prediction for a 33 nm gap (dashed line). The offset in the curves at higher applied V_P's shows just how sensitive the f_o versus V_P curve can be in determining gap spacing.

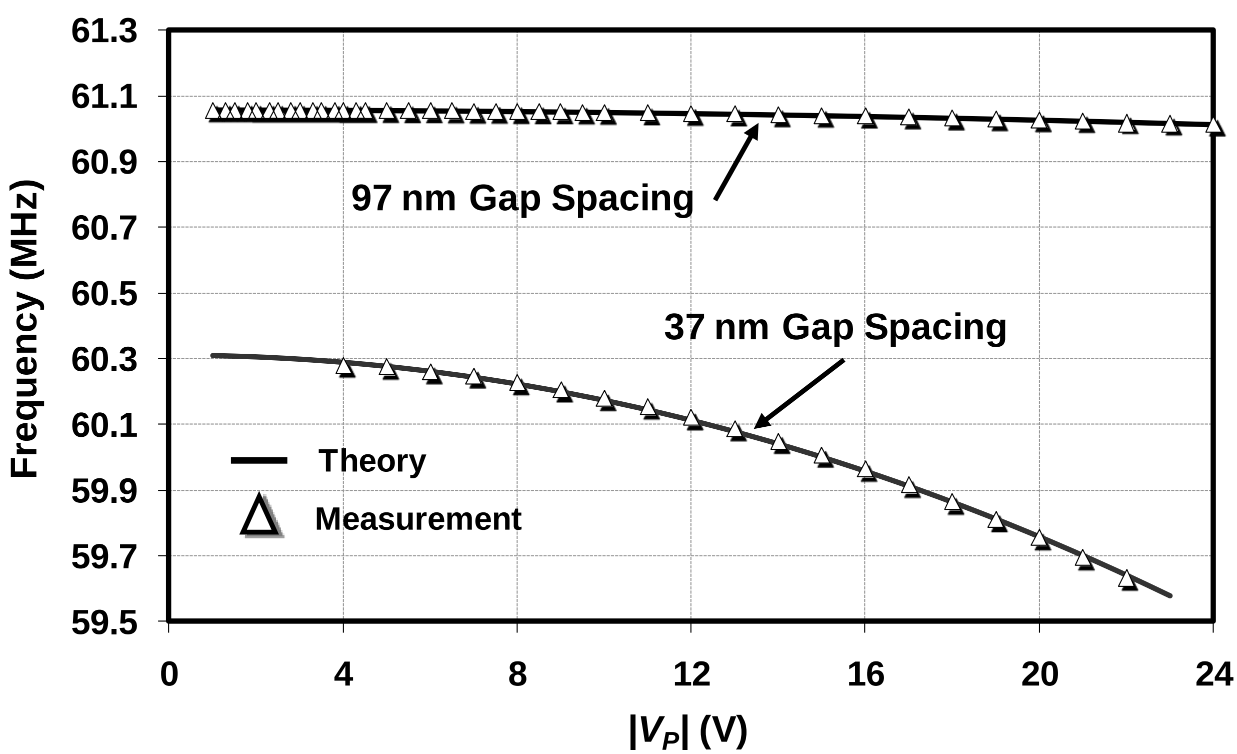

Fig. 2-11: Resonance frequency f_o vs. DC bias V_P plots of measurement data and theory for a 97 nm gap resonator before and after 30 nm HfO_2 coating.

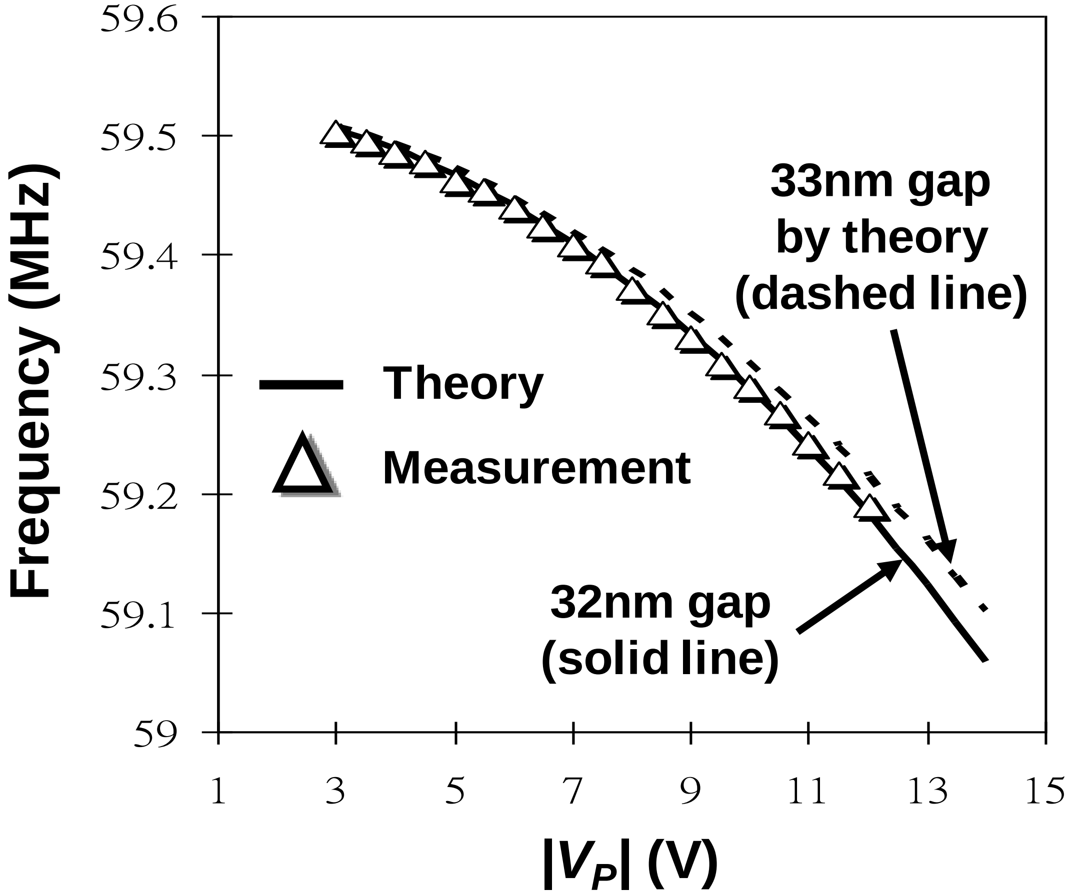

Fig. 2-12: Resonance frequency f_o vs. DC bias V_P plots of measurement data and theory for a 32 nm gap partial-filled HfO_2 device and the simulated curve for a 33 nm gap device.

2.4.3 Extrapolation of Interconnect Resistance

The resonator model presented in Chapter 1 includes only the motional resistance of the resonator and leaves out resistance also existing on the signal path during measurement, such as the contacting resistance of the probe and the bond pad or resistance of the bond wire, and the interconnect resistance. The interconnect resistance is usually much larger than the rest, especially for interconnects made of doped semiconductor material, in this case, n+ polysilicon. Upon resonance, the interconnect resistance is in series with the resonator tank and loads the resonator Q according to the expression

$$Q_{Measure} = Q \cdot \frac{R_x}{R_x + R_s} \tag{2-20}$$

where $Q_{Measure}$ is the quality factor measured from the 3 dB width of the resonant peak, Q is the unloaded quality factor of the resonator, and R_s and R_x are the interconnect resistance and motional resistance, respectively. Interconnect resistance was not a significant issue for the capacitive resonators demonstrated before as R_s is much less than the resonator motional impedance R_x. This is no longer the case for resonators equipped with sub-50nm air gaps. Therefore, precise measurement of interconnect resistance is important to determine the real Q of the resonator. While it is possible to estimate the interconnect resistance from sheet resistance or to directly measure it by positioning the probes as close to the electrode as possible, a more convenient and accurate approach is to use the motional impedance dependence on V_P.

The total impedance on the signal path can be calculated from the measured peak height relative to the 0 dB line, S21, from the expression

$$\boldsymbol{R_x + R_s = (R_i + R_o)(10^{\frac{-S21}{20}} - 1)} \tag{2-21}$$

where R_i and R_o are the input and output impedance of the network analyzer, respectively. Typically, both R_{in} and R_{out} equal 50 Ω. As R_x is inversely proportional to V_P^2 and R_s is a constant value for the same measurement setup, the value of R_s can be extrapolated from the measured (R_x+R_s) value with V_P (and V_P^2) approaching infinity.

Fig. 2-13 plots the measured (R_x+R_s) value against $1/V_P^2$. The y-axis intercept is 600 Ω, which is the extrapolated value of R_s. Fig. 2-14 plots the simulation curve of R_x versus V_P and the

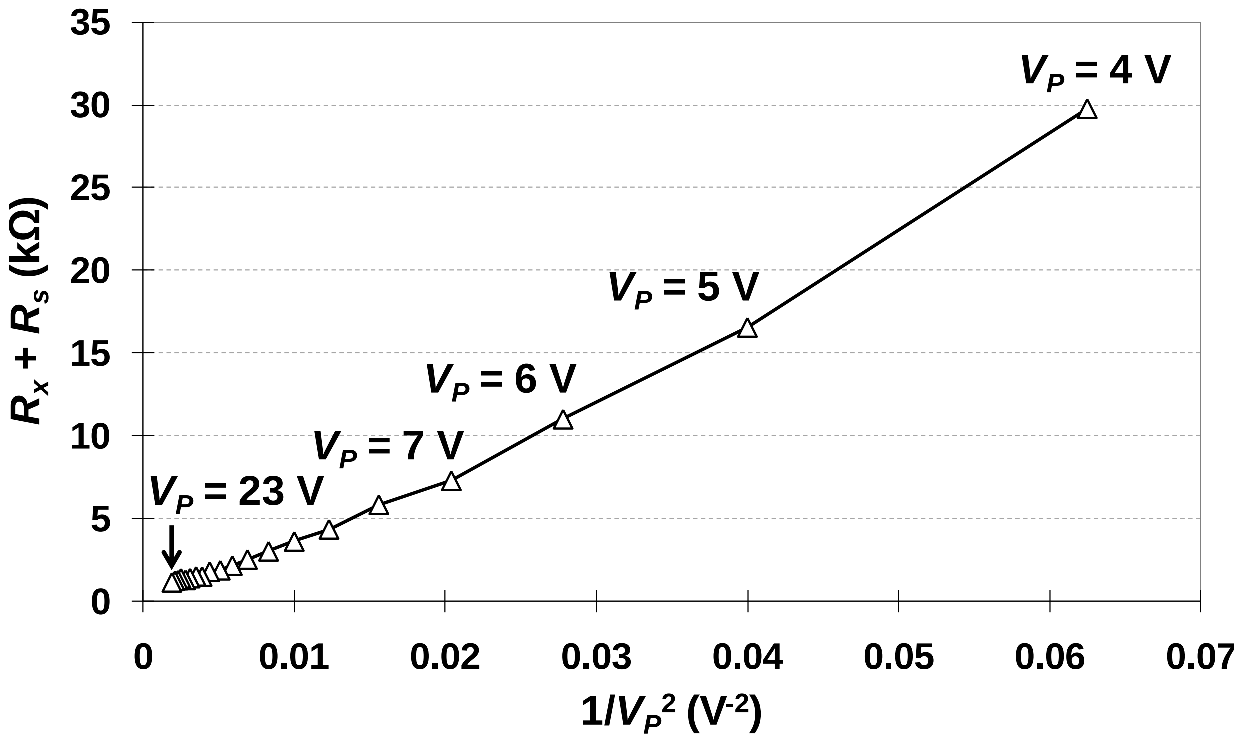

Fig. 2-13: Measured (R_x+R_s) values plotted against inverse of square of V_P from which R_s can be extrapolated from the value of (R_x+R_s) when $1/V_P^2$ approaches to zero.

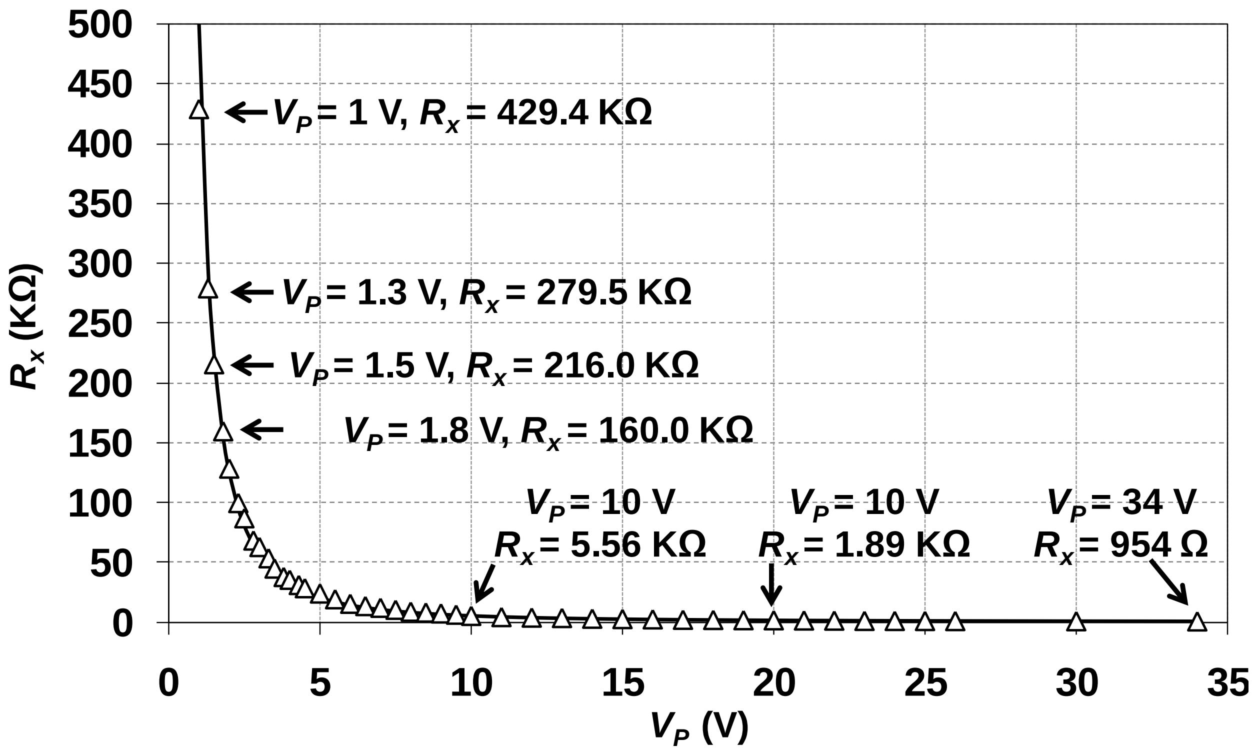

Fig. 2-14: Simulated curve and measured data of R_x versus V_P using R_s = 600 Ω obtained from Fig. 2-13.

values of R_x obtained by subtracting 600 Ω from the measured data of (R_x+R_s). The consistency of the theoretical and the measured values confirms that 600 Ω is a good estimation of the series resistance associated with interconnect and measurement setup.

2.4.4 Measurement Results – Improved FOM

Fig. 2-15 presents the measured frequency response characteristics for a 94 nm-gap wine-glass mode disk resonator, with design summarized in Fig. 2-8, and one coated with 30.7 nm of ALD HfO_2 using the process described above in Section 2.3.1, then sintered in forming gas (97% N_2 and 3% H_2) at 400˚C for 3 minutes (for reasons to be described later). Here, the measured Q of the coated resonator is considerably lower than that of the uncoated one—an observation to be discussed in more detail later. For now, though, accounting for the reduced Q, the extracted η_e's are 19.84 μC/m and 2.44 μC/m at V_P = 16V for the coated and uncoated devices, respectively, yielding an η_e improvement of 8.1×, which is very close to the expected 8.6× difference from (2-6). With an 8.1× increase in η_e, the filter FOM increases by $(8.1)^2$×=65.6×. The motional resistance R_x at this point is 966 Ω. Note that the motional impedance R_x is not reduced by the same ratio as the η_e increase, as Q is degraded and R_x is inversely proportional to Q according to (1-3) and (1-11). After another 3 minutes of sintering at 400˚C, the same device achieves R_x=685 Ω and Q = 7,368 at V_P = 19 V, as shown in Fig. 2-16.

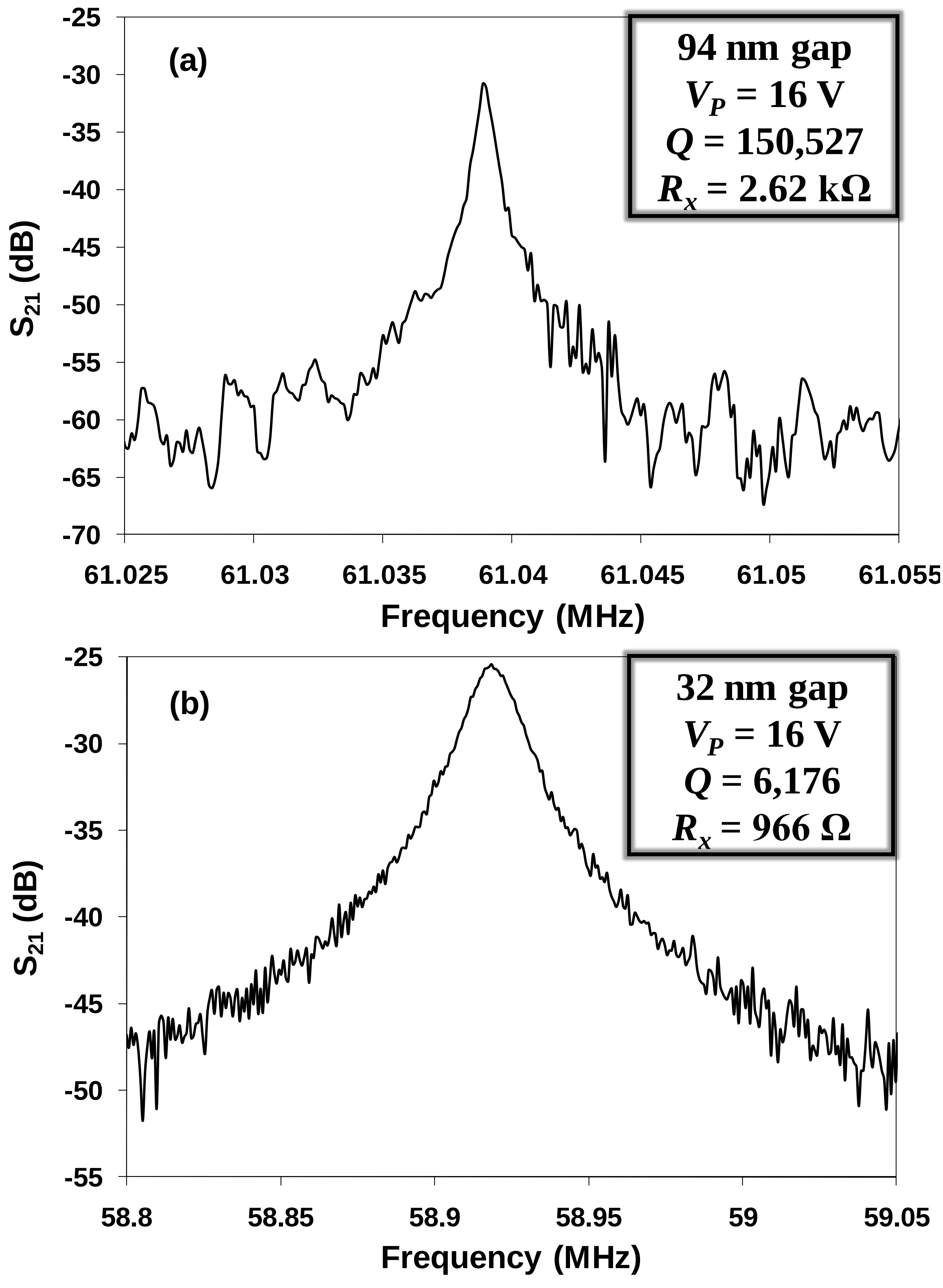

Fig. 2-15: Frequency characteristics of an initially 94 nm gap resonator before and after ALD coating. (a) right after HF release; (b) after partially filling the gap with 30.7 nm HfO_2 and sintering at 400˚C for 3 minutes, showing $R_x < 1$ kΩ.

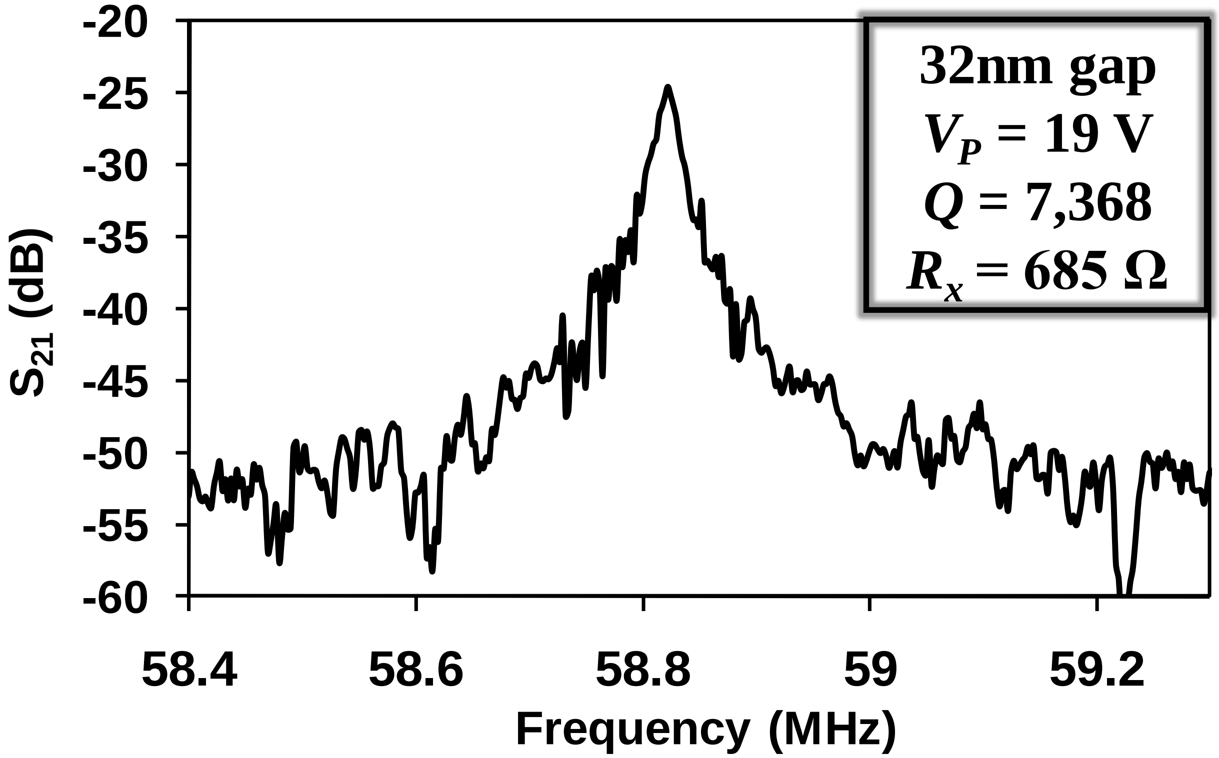

Fig. 2-16: Frequency characteristics of an initially 94nm gap resonator after HF release and partially filling the gap with 30.7 nm HfO_2 and sintering at 400˚C for 6 minutes, showing Q > 10,000. Here, V_p is lower than in Fig. 2-15(b), but all the other parameters are the same.

2.4.5 Methods for Restoring *Q*

Part of the reason for the reduction in Q seen in Fig. 2-*15*(b) and Fig. 2-16 derives from the fact that the Q of a resonator with a smaller R_x is loaded more heavily by parasitic interconnect resistance than one with a large R_x. But comparisons of Q versus V_P plots suggest that more of the Q reduction derives from interface losses introduced by the HfO_2 film. In particular, the same resonator that achieves Q=6,176 at V_p=16 V, shown in Fig. 2-15(b), is measured with much higher Q, Q=10,510 at V_p = 5 V, shown in Fig. 2-17. In this respect, the quality of the HfO_2 deposited film very likely governs the final Q of an ALD-filled device.

a. Annealing

To gauge the degree with which Q depends upon film quality, ALD-filled devices were sintered at 400 ˚C in forming gas for varying time periods in order to improve the HfO_2 film quality, as is done for VLSI transistors [22]. Fig. 2-18 presents measured frequency characteristics for a 61-MHz wine-glass disk resonator with ALD-coated gaps, showing a marked improvement in Q after 6 minutes of sintering at 350 ^{o}C. More work is needed to find the best recipe, but it appears that a method to restore Q is at least feasible.

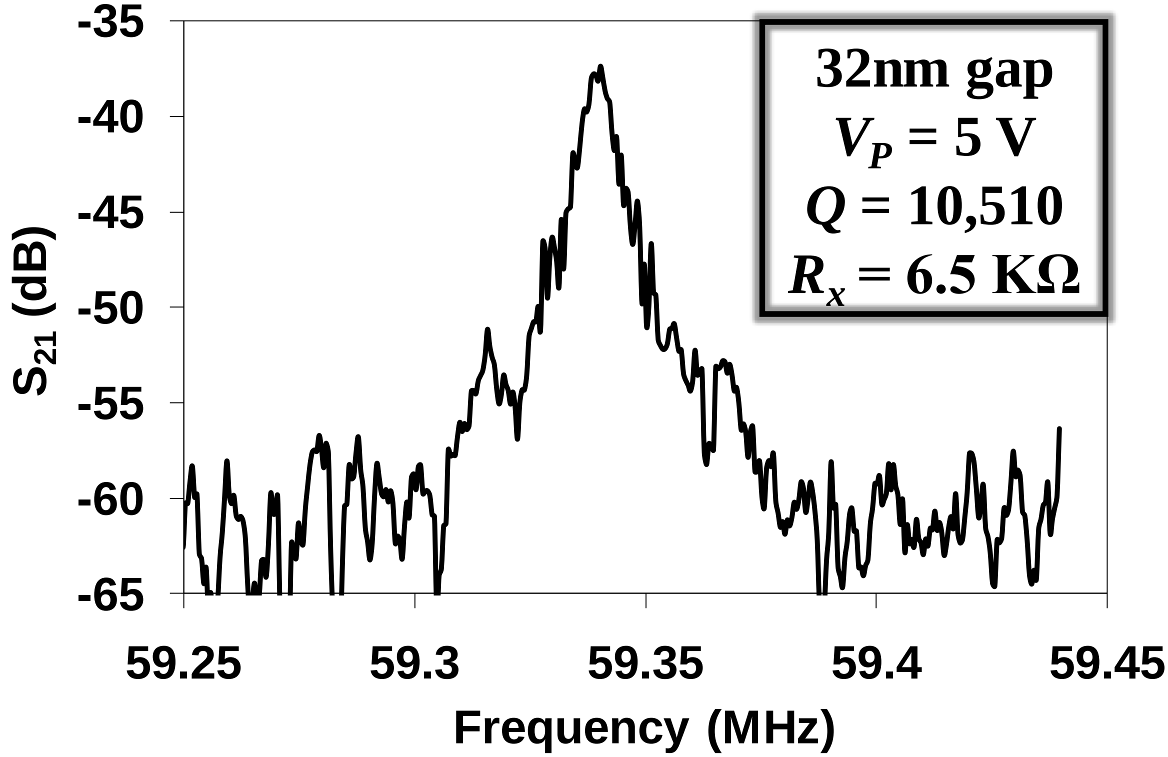

Fig. 2-17: Frequency characteristics of the resonator in Fig. 2-15(b) but with lower V_p, showing Q > 10,000.

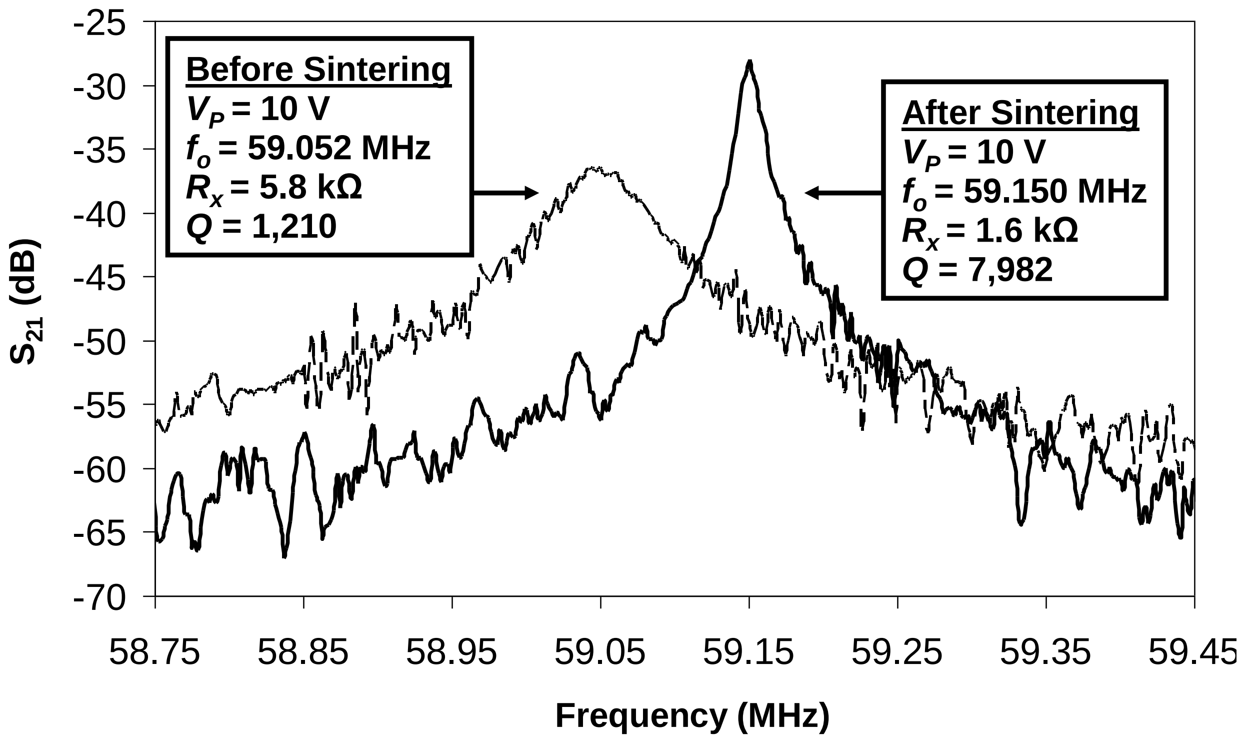

Fig. 2-18: Frequency characteristic of a 37 nm gap resonator before and after sintering, showing marked improvement in Q, from 1,210 to 7,982, a 6.6 x increase.

It should also be noted that the thicker the ALD coating, the lower the Q of a HfO_2 ALD-coated disk resonator. Thus, another approach to retaining Q's >100,000 for disk resonators is to merely start with a smaller initial gap and deposit a much thinner ALD coating. For example, if the initial gaps were 50 nm, then only 9 nm of ALD would be needed to match the 32 nm gaps of this work, and the Q should be higher.

Although annealing enhances Q, the effective gap spacing appears to increase after annealing. In particular, the gap spacing of the resonator in Fig. 2-18 is measured using the method described in section 2.3.2 before and after annealing and show 32 nm and 38 nm, respectively, as plotted in Fig. 2-19. This explains why the R_x reduction is only 3.6x, instead of 6.6x, with 6.6x improvement in measured 'unloaded' Q before and after annealing, shown in Fig. 2-18. Three possible scenarios, or any combination of them, as drawn in Fig. 2-19, can cause the effective gap spacing to increase after annealing: first, the physical thickness of HfO_2 decreases, i.e., the film becomes denser; second, the dielectric constant of HfO_2 decreases, contributing to larger effective air gap spacing; third, an interfacial layer forms from the HfO_2-silicon interface into the polysilicon such that the total dielectric thickness increases.

The first scenario, a change in physical HfO_2 film thickness, is tested out by measuring the step height change of patterned HfO_2 on polySi films before and after the same annealing conditions. To ensure that the step height change, if any, is well above the resolution of the profilometer used for step height measurement, patterned 120 nm thick HfO_2 is subjected to the same annealing conditions. If a change in physical HfO_2 film thickness is solely responsible for the effective air gap increase, based on Fig. 2-19, 30.7nm thick HfO_2 decreases to 27.7 nm after annealing. If the densification ratio is the same for thin and thicker films, 120 nm thick HfO_2 should exhibit a step height change of 11.7 nm after annealing. However, no change in step

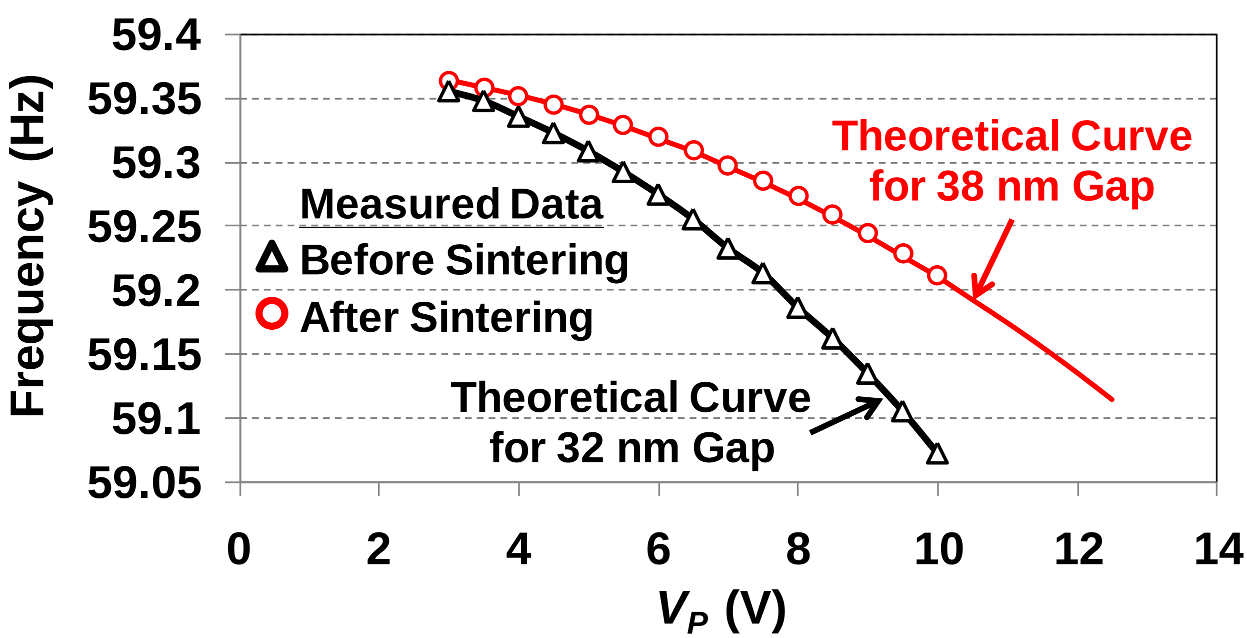

Fig. 2-19: The effective gap spacing changes from 32 nm to 38 nm after 6 minutes of sintering at 350°C. This explains why the impedance reduction is not as much as the Q improvement in Fig. 2-18.

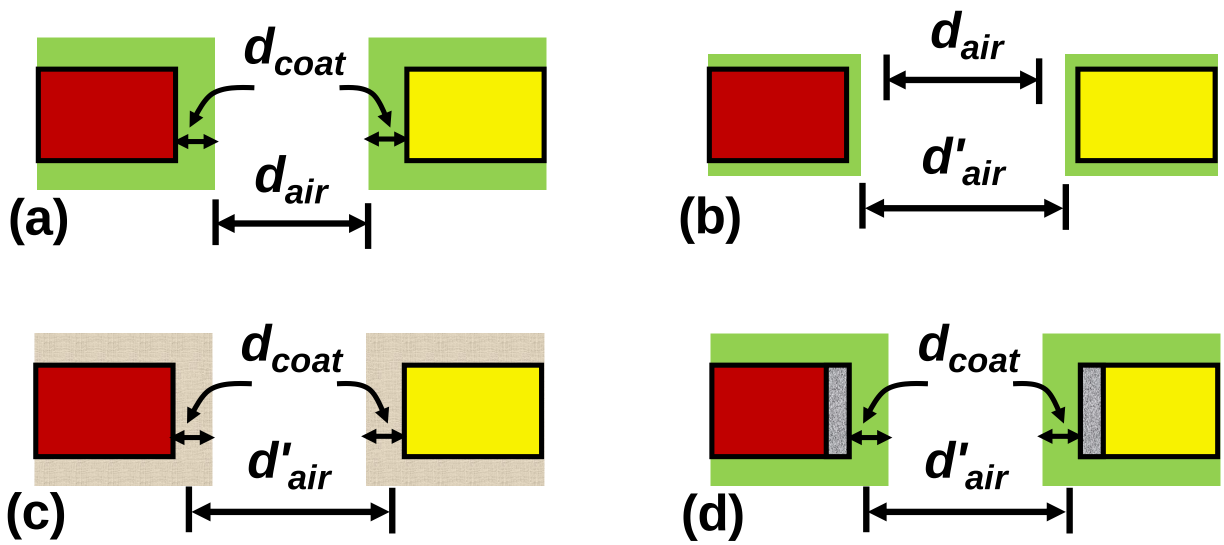

Fig. 2-20: (a) the partial-filled gap before sintering with effective gap spacing of 32 nm; (b)-(c) three scenarios that can cause the effective gap spacing to increase to 38 nm after annealing: (b) physical thickness of ALD film decreases by ~3 nm on each side; (c) dielectric constant of the ALD film drops such that the ALD film contributes to extra effective air gap spacing; (d) interfacial layer with lower dielectric constant than HfO_2 forms at the HfO_2-poly-Si interface.

height is observed.

Next, the second scenario is considered, where the increase of the effective gap spacing is caused by a decrease in the dielectric constant of HfO_2. A 6 nm difference in gap spacing, or 3 nm difference from 30.7nm HfO_2 film on each side, corresponds to a dielectric constant change from the original value of 18 to ~6.5. No literature has been found which reports such a dramatic reduction in dielectric constant. Instead, some literature reports that the dielectric constant increases as the annealing temperature increases as the annealing temperature increases [28]. It is therefore unlikely that the effective gap spacing increase after annealing is entirely due to a drop in the dielectric constant of HfO_2.

On the other hand, the work in [29] investigated the thermal stability of thin ALD HfO_2 films and suggested the formation of an interfacial layer at HfO_2-Si interface as the main cause of increased capacitance equivalent oxide thickness (CET) after anneal at 700 °C in nitrogen. In particular, for HfO_2 with physical thickness of ~4.5 nm, the CET is ~0.7 nm (using dielectric constant of 25 and 4 for HfO_2 and SiO_2, respectively) before annealing and increases to 0.9 nm and 1.3 nm after 10 seconds and 15 seconds of annealing, respectively, at 700 °C. Such a large increase in CET is similar to what has been observed in the effective gap spacing increase shown in Fig. 2-19. X-ray photoelectron spectroscopy (XPS) further reveals the formation of an interfacial layer at the interface, which is likely to contribute to the CET increase [29].

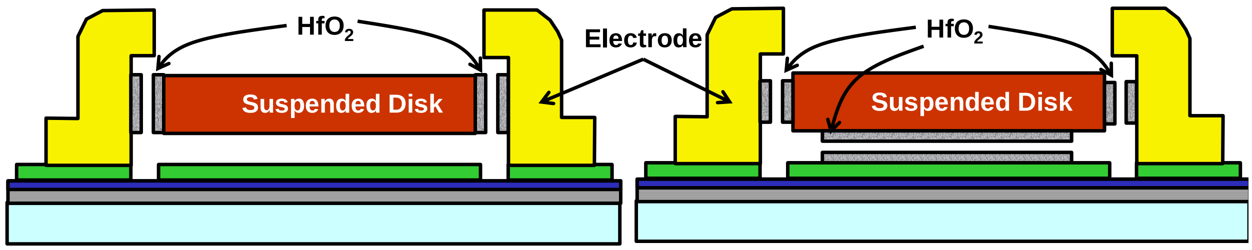

(a) (b)

Fig. 2-21: (a) a short HF etching is expected to remove HfO_2 above and below the disk resonator without removing HfO2 in the high-aspect-ratio lateral transduction gaps due to limited mass transportation rate; (b) what is possibly the actual case, where HfO_2 remains underneath the disk.

b. Remove Undesired HfO_2 Film

The ALD process coats every exposed surface with HfO_2, but only the HfO_2 film in the transduction gap contributes to coupling enhancement. HfO_2 on top of and beneath the disk resonator does not help reduce the gap spacing; even worse, it dissipates energy, thus causes lower Q. Another approach for improving Q is to retain the HfO_2 film only in the transduction gap and to remove HfO_2 from the other areas. This could be achieved by taking advantage of the much slower etching rate for materials in a high aspect ratio trench (*i.e.*, the transduction gap) due to limited mass transportation rate. A HF etch with optimal etching time may render a cross section like Fig. 2-21(a). Unfortunately, no resonant peak was measured after short HF etching. A possible failure mechanism is the unbalanced stress imposed on the disk resonator by the remaining HfO_2 underneath the disk if only HfO_2 above the disk is removed, resulting in the cross section in Fig. 2-21(b).

c. Reduce surface loss via barrier layer

There are two approaches for minimizing the energy dissipation at the interface of poly-silicon and ALD films, which can be the main cause of lower Q. One approach is to minimize the energy dissipation per unit area of the interface; another approach is to minimize the total interface area. This and the next subsection discuss the first and the second approaches, respectively.

The purpose of the barrier layer is to better prepare the rather rough poly-silicon surface, especially on the dry etched sidewalls, for ALD. It can also ensure good thermal stability of the device with ALD coating by serving as a blocking layer for inter-diffusion of silicon and atoms which are mobile at elevated temperatures. In practice, this barrier layer can be only a few monolayers thick and can comprise either dielectric or metal. This concept has been demonstrated in [30] by using 3 nm Al_2O_3 as the barrier layer for 25 nm thick TiO_2. Al_2O_3 can be deposited on silicon without special surface treatment [31] – an advantage over TiO_2. Q improvement of 1.35 x is achieved compared to identical devices with ALD Al_2O_3 coating alone.

d. Reduce surface loss via smoother surface

The zoomed-in SEM in Fig. 2-8 shows the surface roughness along the sidewalls of the poly-Si disk. A rough surface increases the total poly-Si and high-*k* dielectric interface areas, as ALD is extremely conformal. While it is possible to reduce the sidewall roughness by optimizing the dry etch recipe, a more efficient way is perhaps to reflow silicon to smooth the surface. Annealing in a hydrogen-rich environment to enable silicon reflow has been applied to numerous applications, including packaging [32], eliminating the scalloping of silicon trenches created by deep reactive ion etch (DRIE) and 3D features for MEMS [33], smooth surfaces of optical waveguides [34], and smoother sidewall of the FinFET [35]. Note that all of the above examples mobilize silicon atoms in a single crystal silicon substrate; little has been reported on applying the same annealing step to polycrystalline silicon. This approach for improving Q of ALD high-*k*-dielectric-coated resonators has not yet been experimentally confirmed.

2.4.6 Dielectric Charging

In addition to Q-reduction, another concern regarding dielectric-partial-filled devices is charging. In particular, any 'net' charge in the ALD oxide, or at the oxide-silicon interface, will impose a change in electrical stiffness that will pull the frequency of the resonator up or down, according to the sign of the net charge and the polarity of V_P. The existence of such charge is discernable by comparing plots of f_o versus V_P, one with positive V_P, another with the polarity of the V_P reversed (i.e., with $V_P = -V_P$). Here, a shift in the curve identifies the presence of charge. Based on the electric stiffness equation of (2-18) and (2-19), the amount of the 'net' change can be calculated from the frequency shift when the polarity of V_P is reversed. Related equations have been derived in [36] and will not be repeated here.

Fig. 2-22 presents plots of f_o versus V_P and reverse polarity V_P for a partial-ALD-filled gap device before and after sintering at 400^{o}C in forming gas (97% N_2 and 3% H_2) for 3 minutes. Before sintering, the curve of positive V_P is horizontally right-shifted from that of negative V_P, while no difference is seen after sintering. It seems that sintering is a very effective means by which to virtually eliminate the oxide charging issue, at least for HfO_2 ALD gap coatings.

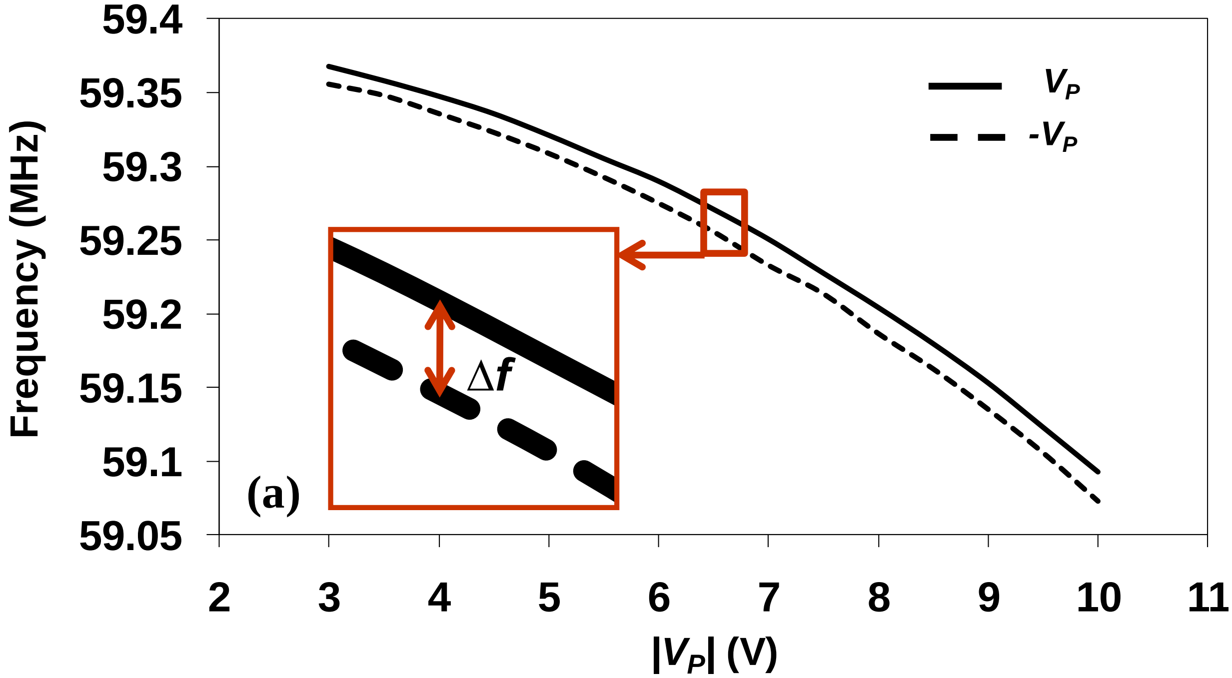

(a)

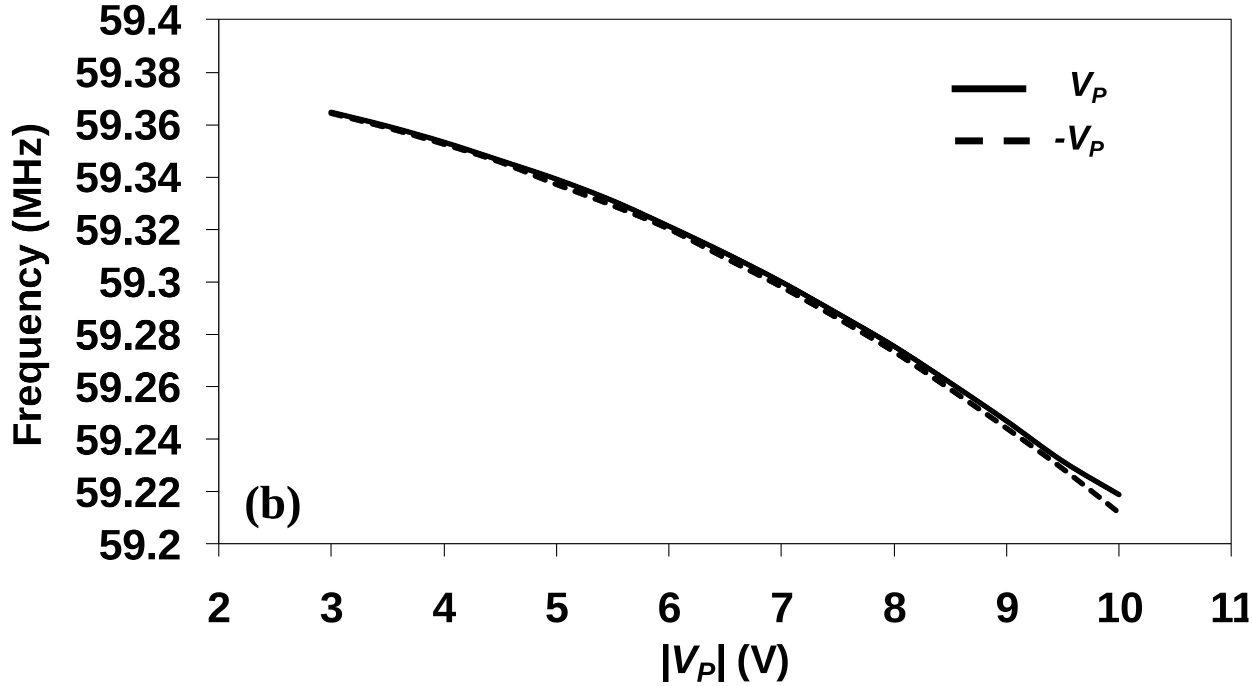

(b)

Fig. 2-22: Resonance frequency f_o vs. dc-bias V_P plots of a 32 nm gap resonator (a) before sintering; and (b) after sintering.

2.5 References

[1] Y.-W. Lin, L.-W. Hung, S.-S. Li, Z. Ren, and C. T.-C. Nguyen, “Quality factor boosting via mechanically-coupled arraying,” *Dig. of Tech. Papers*, the 14th Int. Conf. on Solid-State Sensors & Actuators (Transducers’07), Lyon, France, June 11-14, 2007, pp. 2453-2456.

[2] S.-S. Li, Y.-W. Lin, Y. Xie, Z. Ren, and C. T.-C. Nguyen, “Micromechanical “hollow-disk” ring resonators,” *Proceedings*, 17th Int. IEEE Micro Electro Mechanical Systems Conf., Maastricht, The Netherlands, Jan. 25-29, 2004, pp. 821-824.

[3] D. Weinstein1 and S. A. Bhave, “Acoustic resonance in an independent-gate FinFET,” *Tech. Digest*, Solid-State Sensor, Actuator, and Microsystems Workshop, Hilton Head, South Carolina, 2010, pp. 459-462.

[4] C. T.-C. Nguyen, "Integrated micromechanical RF circuits for software-defined cognitive radio," 26th Sym. on Sensors, Micromachines, and App. Sys., 2009, pp. 1-5.

[5] S.-S. Li, Y.-W. Lin, Z. Ren, and C. T.-C. Nguyen, “An MSI micromechanical differential disk-array filter,” *Dig. of Tech. Papers*, the 14th Int. Conf. on Solid-State Sensors & Actuators (Transducers’07), Lyon, France, June 11-14, 2007, pp. 307-311.

[6] Y. Xie, S.-S. Li, Y.-W. Lin, Z. Ren, and C. T.-C. Nguyen, "1.52-GHz micromechanical extensional wine-glass mode ring resonators," *IEEE Trans. Ultrason., Ferroelect., Freq. Contr.*, vol. 55, no. 4, pp. 890-907, April 2008.

[7] L.-W. Hung, Z. A. Jacobson, Z. Ren, A. Javey, and C.T.-C. Nguyen, “Capacitive transducer strengthening via ALD-enabled partial-gap filling,” *Tech. Digest*, Solid-State Sensor, Actuator, and Microsystems Workshop, Hilton Head, South Carolina, 2008, pp. 208-211.

[8] D. M. Hausmann, E. Kim, J. Becker, and R. G. Gordon, “Atomic layer deposition of hafnium and zirconium oxide using metal amide precursors,” *Chem. Mater.*, vol. 14, 2002, pp. 4350-4358.

[9] Y.-W. Lin, S.-S. Li, Z. Ren, and C. T.-C. Nguyen, “Vibrating micromechanical resonators with solid dielectric capacitive transducer gaps,” *Proceedings*, Joint IEEE Int. Frequency Control/Precision Time & Time Interval Symposium, Vancouver, Canada, Aug. 29-31, 2005, pp. 128-134.

[10] A. I. Zverev, Handbook of Filter Synthesis. NY: Wiley, 1967.

[11] F. D. Bannon III, J. R. Clark, and C. T.-C. Nguyen, “High-*Q* HF microelectromechanical filters,” *IEEE J. Solid-State Circuits*, vol. 35, no. 4, pp. 512-526, April, 2000.

[12] M. Demirci and C. T.-C. Nguyen, “Mechanically corner-coupled square microresonator array for reduced series motional resistance,” *IEEE/ASME J. Microelectromech. Syst.*, vol. 15, no. 6, pp. 1419-1436, Dec. 2006.

[13] H. Chandrahalim, D. Weinstein, L. F. Cheow, and S. A. Bhave, “Channel-select micromechanical filters using high-k dielectrically transduced resonators,” *Technical Digest*, Int. IEEE Micro Electro Mechanical Systems Conference, 2006, pp. 894-897.

[14] R. Navid, J. R. Clark, M. Demirci, and C. T.-C. Nguyen, “Third-order intermodulation distortion in capacitively-driven CC-beam micromechanical resonators,” *Technical Digest*,

Int. IEEE Micro Electro Mechanical Systems Conference, Interlaken, Switzerland, Jan. 21-25, 2001, pp. 228-231.

[15] H. Takeuchi, E. Quévy, S. A. Bhave, T.-J. King, and R. T. Howe “Ge-blade damascene process for post-CMOS integration of nano-mechanical resonators,” *IEEE ELECTRON DEVICE LETTERS*, vol. 25, no. 8, August 2004, pp. 529-531.

[16] Y.-W. Lin, S.-S. Li, Z. Ren, and C. T.-C. Nguyen, “Low phase noise array-composite micromechanical wine-glass disk oscillator,” *Technical Digest*, IEEE Int. Electron Devices Mtg. (IEDM), Washington, DC, Dec. 5-7, 2005, pp. 287-290.

[17] K. Hamaguchi, T. Tsuchiya, K. Shimaoka, and H. Funabashi, "3-nm gap fabrication using gas phase sacrificial etching for quantum devices," *Technical Digest*, Int. IEEE Micro Electro Mechanical Systems Conference, 2004, pp. 418-421.

[18] T. J. Cheng and S. Bhave, “High-Q, low impedance polysilicon resonators with 10nm air gaps,” *Technical Digest*, Int. IEEE Micro Electro Mechanical Systems Conference, 2010, pp. 695-698.

[19] M. A. Sahiner, J. C. Woicik, P. Gao, P. McKeown, M. C. Croft, M. Gartman, and B. Benapfla, "Pulsed laser deposition and characterization of Hf-based high-*k* dielectric thin films," *J. of Thin Solid Films*, vol. 515, pp. 6548-6551, 2007.

[20] B.-Y. Tsui and H.-W. Chang, “Formation of interfacial layer during reactive sputtering of hafnium oxide,” *J. Appl. Phys*. vol. 93, vol. 12, pp. 10119-10124, 2003.

[21] S. Sayan, S. Aravamudhan, B. W. Busch, W. H. Schulte, F. Cosandey, G. D. Wilk, T. Gustafsson, E. Garfunkela, “Chemical vapor deposition of HfO_2 films on Si (100),” *J. Vac. Sci. Technol.* , Mar/Apr, 2002, pp.-507-512. …

[22] D. M. Hausmann, E. Kim, J. Becker, and R. G. Gordon, “Atomic layer deposition of hafnium and zirconium oxides using metal amide precursors,” *Chem. Mater*. 2002, 14, 4350-4358.

[23] K. Kukli, M. Ritala, T. Sajavaara, J. Keinonen, M. Leskela, “Atomic layer deposition of hafnium dioxide films from hafnium tetrakis (ethylmethylamide) and water,” *Chem. Vap. Deposition*, vo. 5, pp. 199-204, 2002.

[24] M. Onoe, “Contour vibrations of isotropic circular plates,” *J. of the Acoustical Society of America*, vol. 28, no. 6, pp. 1158-1162, Nov. 1956.

[25] Y.-W. Lin, S. Lee, S.-S. Li, Y. Xie, Z. Ren, C. T.-C. Nguyen, “Series-resonant VHF micromechanical resonator reference oscillators,” *IEEE J. of solid-state circuits*, vol. 39, no. 12, 2004, pp. 2477-2491.

[26] J. Wang, Z. Ren, and C. T.-C. Nguyen, “Self-aligned 1.14-GHz vibrating radial-mode disk resonators,” *Dig. of Tech. Papers*, the 12th Int. Conf. on Solid-State Sensors & Actuators (Transducers’03), Boston, Massachussets, June 8-12, 2003, pp. 947-950.

[27] S. W. Jeong, H. J. Lee, K. S. Kim, M. T. You, Y. Roh, T. Noguchi, W. Xianyu, and J. Jung, "HfO2 gate insulator formed by atomic layer deposition for thin-film-transistors," *Thin Solid Films*, vol. 515, pp. 5109-5112, 2007.

[28] S. W. Jeong, H. J. Lee, K. S. Kim, M. T. You, Y. Roh, T. Noguchi, W. Xianyu, and J. Jung, "Effects of annealing temperature on the characteristics of ALD-deposited HfO_2 in MIM capacitors," *Thin Solid Films*, vol. 515, pp. 526-530, 2006.

[29] B. H. Lee, L. Kang, R. Nieh, W.-J. Qi, and J. C. Lee. “Thermal stability and electrical characteristics of ultrathin hafnium oxide gate dielectric reoxidized with rapid thermal annealing,” *Appl. Phys. Lett*. vol. 76, pp. 1926-1928, 2000.

[30] M. Akgul, B. Kim, Z. Ren, and C. T.-C. Nguyen, “Capacitively transduced micromechanical resonators with simultaneously low motional resistance and Q>70,000,” *Tech. Digest*, Solid-State Sensor, Actuator, and Microsystems Workshop, Hilton Head, South Carolina, 2010, pp. 467-470.

[31] A. C. Dillon, A. W. Ott, J. D. Way, and S. M. George, "Surface chemistry of Al_2O_3 deposition using $Al(CH_3)_3$ and H_2O in a binary reaction sequence," Surface Science, vol. 322, pp. 230-242, 1995.

[32] S. Sedky, H. Tawfik, A. Abdel Aziz, S. ElSaegh, A. B. Graham, J. Provine, and R. T. Howe, ‘Low thermal-budget silicon sealed-cavity microencapsulation process,’ *Technical Digest*, Int. IEEE Micro Electro Mechanical Systems Conference, 2011, pp. 276-279.

[33] M. C. M. Lee and M. C. Wu, "Thermal annealing in hydrogen for 3-D profile transformation on silicon-on-insulator and sidewall roughness reduction," Microelectromechanical Systems, Journal of, vol. 15, pp. 338-343, 2006.

[34] F. Gao, Y. Wang, G. Cao, X. Jia, and F. Zhang, ‘reduction of sidewall roughness in silicon-on-insulator rib waveguides,’ *J. of Applied Surface Science* 252, 2006, 5071–5075.

[35] R. J. Zaman, W. Xiong, R. Quintanilla, T. Schulz, C. R. Cleavelin, R. Wise, M. Pas, P. Patruno, K. Schruefer and S. K. Banerjee, ‘Effects of hydrogen annealing process conditions on nano scale silicon (011) fins,’ in Proc., *Mater. Res. Soc. Symp.*, vol. 872, pp. J3.1.1-J3.1.5, 2005.

[36] G. Bahl, R. Melamud, B. Kim, S. A. Chandorkar, J. C. Salvia, M. A. Hopcroft, D. Elata, R. G. Hennessy, R. N. Candler, R. T. Howe, T. W. Kenny, ‘Model and observations of dielectric charge in thermally oxidized silicon resonators,’ *IEEE/ASME J. Microelectromech. Syst.*, vol. 19, no. 1, 2004, pp. 162-174.

Chapter 3: Silicide-Induced Gaps

3.1 Fabrication of High Aspect Ratio Microstructures

3.1.1 Need for High Aspect Ratio Microstructures

From the view point of fabrication, the aspect ratio of a released or suspended microstructure can be defined as the ratio of the largest to the smallest dimensions of the released gap spacing. As an example, for a square diaphragm which has lateral dimension W on each side and is suspended H distance above the substrate, the aspect ratio is W/H. High aspect ratio structures are useful in many ways, including but not limited to:

1. The coupling coefficient of a capacitive transducer force is inversely proportional to the square of the transduction gap spacing. Large coupling coefficients are desirable for applications where low impedance of resonators, high sensitivity of sensors, or large actuation forces of actuators are essential. For example, the aspect ratio reaches 1,000 for a diaphragm that is 10 μm wide and suspended 10 nm above the substrate.
2. Some applications require either more compliant microstructures or larger mass, which usually require larger lateral dimensions. Applications like these can be found in accelerometer proof masses and pressure sensor diaphragms. Although small gap spacing may not be necessary, the resulting aspect ratio remains high due to large lateral dimensions. For example, the aspect ratio is 1,000 for a diaphragm that is 1,000 μm wide and suspended 1 μm above the substrate.
3. Many MEMS sensors offer better sensitivity than their macro-scale counterparts due to the much larger surface to volume ratio achievable when the devices are scaled down to micrometer scale. The surface to volume ratio of a channel or a tube increases as the radius decreases, therefore the aspect ratio increases.

Very often, the bottleneck of fabricating high aspect ratio microstructures lies in the difficulty in forming high aspect ratio gaps or releasing the microstructures. The following sections discuss the three most common approaches forming high aspect ratio gaps and the related issues. The discussions in this chapter focus on high aspect ratio microstructures made of non-polymer material. As a side note, many methods have been developed to form high aspect ratio polymer structures, such as hot embossing and LIGA process.

3.1.2 Wafer Bonding

Intuitively, a suspended microstructure can be fabricated by bonding two pieces together [1]. This is accomplished by either bonding a recessed microstructure to a flat substrate as illustrated in Fig. 3-1(a) and demonstrated in [2], or bonding a microstructure to a recessed substrate, as illustrated in Fig. 3-1(b) and demonstrated in [3]. The patterning of the microstructures can be performed either before or after the bonding process. Although the concept is straightforward, this method has inherent limitations:

First, most bonding processes require elevated temperatures or pressures. The induced thermal and mechanical stresses during and after the bonding process can fail the suspended microstructures, especially the compliant ones. Techniques for bonding wafers with limited thermal budget have been improved dramatically, thanks to the efforts pursuing hetero-integration for MEMS and readout circuitry and, recently, 3D integration to continually increase transistor density. Bonding processes for silicon wafers at temperatures less than 400 °C and with low to moderate bonding pressure typically utilizes an intermediate layer, ranging from polymer adhesives [4] such as parylene [5], melting glass [6], and metals at eutectic temperatures [3].

The control and the minimum requirement on thickness of the intermediate layer affects the minimum achievable gap spacing beneath the suspended structure resulted from wafer bonding. It is therefore difficult to scale the uniform gap spacing down to less than 50 nm, as needed by the electrostatic transducers.

Moreover, the bonding rim surrounding the suspended structures is usually > 50 µm wide to ensure sufficient bonding strength and to accommodate misalignment during the bonding process. While a > 50 µm wide bonding rim is not a significant problem for devices with dimensions as large as 500 µm, such as the silicon diaphragm in [7], it consumes a relatively large silicon footprint for devices of only 50 µm wide or smaller. The excess demand for space is even worse if the MEMS suspended structures are fabricated directly on a CMOS chip via low temperature bonding. Wafer bonding is good for MEMS structures with lager dimensions and when only a few of them are required on a functional chip. It is not a useful solution for many small devices needed to work together as a functional unit. In other words, wafer bonding is not an easily scalable process. Finally, the bonding process shown in Fig. 3-1 cannot be applied to form lateral gaps.

3.1.3 Direct Dry Etching

Another approach is to directly define the gap spacing by anisotropic etching. A comb-drive resonator [8] (Fig. 3-2(a)) is an example of using anisotropic etching to define the gap spacing between each comb-drive finger functioning as capacitive transducers. The achievable minimum gap spacing is limited by how anisotropic the etching is. Among all of the known methods for etching silicon, deep reactive ion etch (DRIE) offers the most anisotropic etching.

DRIE was developed in 1994 by Bosch, where alternation of polymer passivation cycles and etching cycles results in silicon trenches with high aspect ratios unachievable using previous

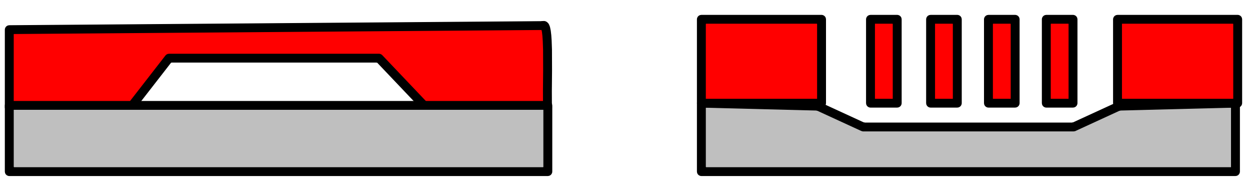

(a) (b)

Fig. 3-1: A suspended microstructure can be formed by either (a) bonding a recessed and patterned wafer to a flat substrate, or (b) bonding a patterned water to a recessed substrate.

reactive ion etch (RIE) techniques. This process has since become one of the most important processes of enabling MEMS technologies based on silicon. DRIE is also useful for fabricating through silicon wafer vias (TSV) and high density capacitors for dynamitic random access memory (DRAM). Some variations of the original Bosch DRIE process have resulted in aspect ratios of 107:1 and 40:1 for 374 nm wide and 130 nm wide trenches, respectively [9][10] (Fig. 3-2(b)). The achievable aspect ratio is expected to be lower with even smaller trench openings. The gap spacing of the wine-glass disk resonators presented in Chapter 2 have an effective gap spacing of 32 nm and a disk height of 3 μm, resulting in an aspect ratio of 94:1, which is much higher than the achievable aspect ratio of current silicon etching technologies.

3.1.4 Release by Etching Sacrificial Materials

Release processes, whereby sacrificial material between two structural materials is removed to free them from one another, often comprise the most limiting and costly steps in MEMS fabrication. Such processes generally employ liquids or gases to etch and are fraught with numerous perils, including

1. Stiction [11]: The stiction failures of MEMS devices are related to the capillary force when the release occurs in a wet environment. Logically, absence of the liquid-gas interface eliminates the capillary pull force. Methods for anti-stiction release based on this idea include critical point drying and dry etching. In the former approach, liquid CO_2 gradually replaces the rinse solution, e.g., methanol or IPA, at elevated pressures and eventually is taken to the critical point of CO_2 where the liquid-gas interface does not exist. Dry etch, on the other hand, avoids liquid all together. Examples of isotropic dry etch include using vapor HF to etch oxide, using XeF_2 to etch silicon, germanium, molybdenum, using oxygen plasma to etch sacrificial polymers, and using SF_6 to etch silicon.
2. Diffusion-limited etch rate: To react with the sacrificial material within a trench, etchants need to diffuse to the etch front. For long trenches, the diffusion process governs the etch rate with a time dependence of $t^{-0.5}$ [12], similar to the diffusion-limited thermal oxidation rate

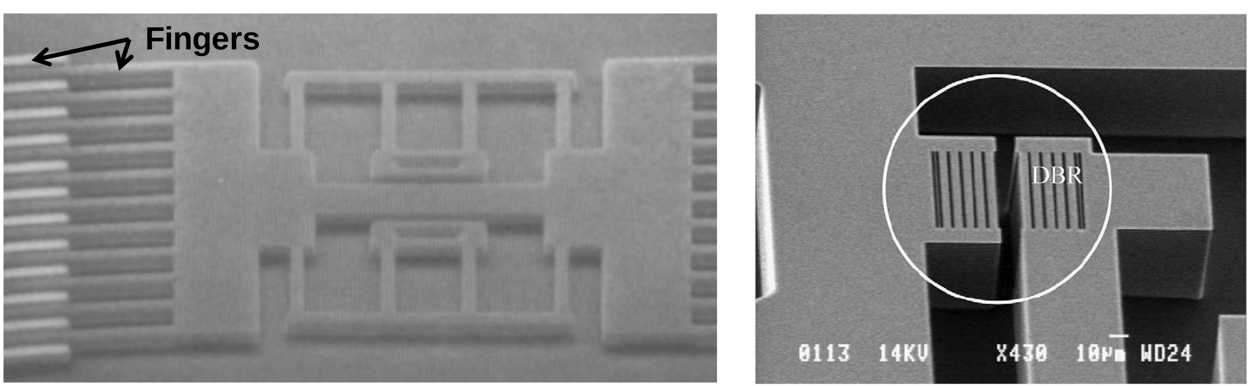

(a) (b)

Fig. 3-2: (a) SEM of a comb-drive resonator in [8]; (b) Tunable optical filter consisting of two free standing vertical distributed Bragg reflector (DBR) mirrors demonstrated in [9]. The high aspect ratio DBR is fabricated by DRIE with air gap spacing defined by the direct etching.

modeled by the Deal-Grove model. As the gap aspect ratio increases, the required etch time increases. The need for longer etch time, combined with limited etch selectivity among materials for any etching process, limits the geometry of releasable microstructures.

3. The attack of unintended layers due to finite etchant selectivity and the formation of etch by-products (*e.g.*, bubbles, residuals) that remain in the gaps.

These yield-limiting phenomena often force alterations in MEMS designs (e.g., release holes) that compromise the performance of applications employing high-aspect ratio gaps. Indeed, the set of affected applications is quite large, from inertial sensors that must incorporate mass-reducing etch holes into their proof masses to speed up the release process [13]; to sealed encapsulation chambers, many of which are achieved via cap-to-wafer bonding methods rather than more area-efficient film deposition strategies [14], since the latter often ending up requiring lengthy etches to release structures within the encapsulation; to GHz high-*Q* mechanical resonators [15], for which the size of the electrode-to-structure gap spacing needed to achieve low impedance and good power handling is limited nearly entirely by the release etch process.

This work erases such limits by introducing a new method for forming high aspect ratio gaps between movable (or immovable) structures that avoids etching and its associated drawbacks, entirely. Instead, the method here employs a self-sufficient silicide chemical reaction to provide volume shrinkage which then induces a gap between surfaces involved in the reaction. Using this silicide-based approach, $100\times100\ \mu m^2$ membranes with membrane-to-substrate gaps of only 385 nm—a 260:1 lateral dimension-to-vertical gap aspect ratio—have been released in only 2 minutes, which is much shorter than the 40 minutes or more that would be required to wet-etch a 385 nm sacrificial oxide under a membrane of similar size. In addition, 32.5 nm gaps have been formed between a SiGe film and a silicon substrate, verifying the efficacy of this method for attaining sub-50nm gaps, as needed for capacitive RF micromechanical resonators.

3.2 Silicide-Induced Gaps

3.2.1 Better Ways for Forming Internal Gaps

The etch-based release is plagued by limited diffusion paths and limited etch selectivity of sacrificial materials over other materials also exposed to the etchant. To address these issues, researchers have tried to enhance the etch selectivity by using different sacrificial materials, such as using cross-linked PMMA [16] and polymer [17] for which isotropic oxygen plasma etching can release the device; by changing the etching conditions, such as the chemical compositions of the etchant and etching temperatures. Researchers also tried to increase the etchant diffusion rate by replacing liquid etchants with gaseous etchant, and to facilitate easier access to the etch front-end by employing release holes to the microstructures. However, the need for mass transportation and finite etch selectivity is inherent to any etching process; the achievable aspect ratio of the microstructures is therefore always limited, as long as etching is required to release the microstructures.

The key recognition behind the present work is that etching is not needed to form a gap. Rather, a gap can also form if a method is available for shrinking the volume of a submerged layer. It is desirable if the reaction used in this method also exhibits the following features:

1. The reaction is self-sufficient such that all of the reactants present on the wafer and the products of the reaction remain on the wafer. This self-sufficient property eliminates the need for diffusion paths, therefore eliminating the root of the problem that plagues etch-based release processes.
2. All of the reaction and the products are solid-phase. This solid-phase property enables the ability of forming a vacuum within the sealed cavity after the reaction as no gaseous products are generated.
3. This reaction is activated only at specific conditions. This property ensures that the wafers can be processed as usual and the gaps are formed only at the last step of fabrication upon subjection to a specific process condition. Examples of possible controllable process conditions are temperature, pressure, or PH value.
4. The reaction only happens with specific material pairing. This material pairing property ensures that when the wafer is subjected to proper process conditions to start this reaction, gaps only form at places with suitable material pairing by design. This is analogous to the 'selectivity' associated with this reaction.
5. As the self-sufficient property dictates that all the reactants present and products remain on the wafer, both the reactants and products need to be common materials for MEMS and solid-state transistors.
6. This reaction must be compatible to transistor fabrication, cost-effective, suitable for mass production, and can be performed in a standard microfabrication tool.

One reaction that satisfies the above criteria is silicidation, whereby silicon, the most commonly used material in CMOS and MEMS, reacts under elevated temperatures with a variety of metals to form silicides.

3.2.2 A Brief Introduction to Silicidation

Silicides are widely used in electronic devices to reduce contact resistance. Silicides can be formed by either a solid-state reactive diffusion between the metal and Si or by co-sputtering the metal and Si. Of particular interest here are the refractory metal silicides formed in the self-aligned silicidation, or salicide, process by rapid thermal annealing (RTA). Salicide process has been commonly used to form low-resistance contacts to the terminals of field effect transistors (FETs), *i.e.*, gates, sources, and drains. Fig. 3-3 illustrates different steps of a typical salicide process. After the polysilicon gate and source/drain junctions are fabricated, shown in Fig. 3-3(a), a conformal blanket of metal is deposited onto the structure (Fig. 3-3(b)), followed by rapid thermal annealing to form silicide. At the silicidation temperature, the metal reacts with only the underlying polysilicon but not the dielectric, resulting in the cross-section in Fig. 3-3(c). Finally, a selective wet etch removes the un reacted metal on the dielectric and does not etch much or any of the silicide formed over the contact areas, shown in Fig. 3-3(d).

Table 1 [18] lists properties of some common silicides where the metal reacts with single crystal silicon. Depending on the type of metal used and the particular phase of silicide formed, the silicidation temperature ranges from 350 °C for nickel silicide up to 800 °C for titanium silicide.

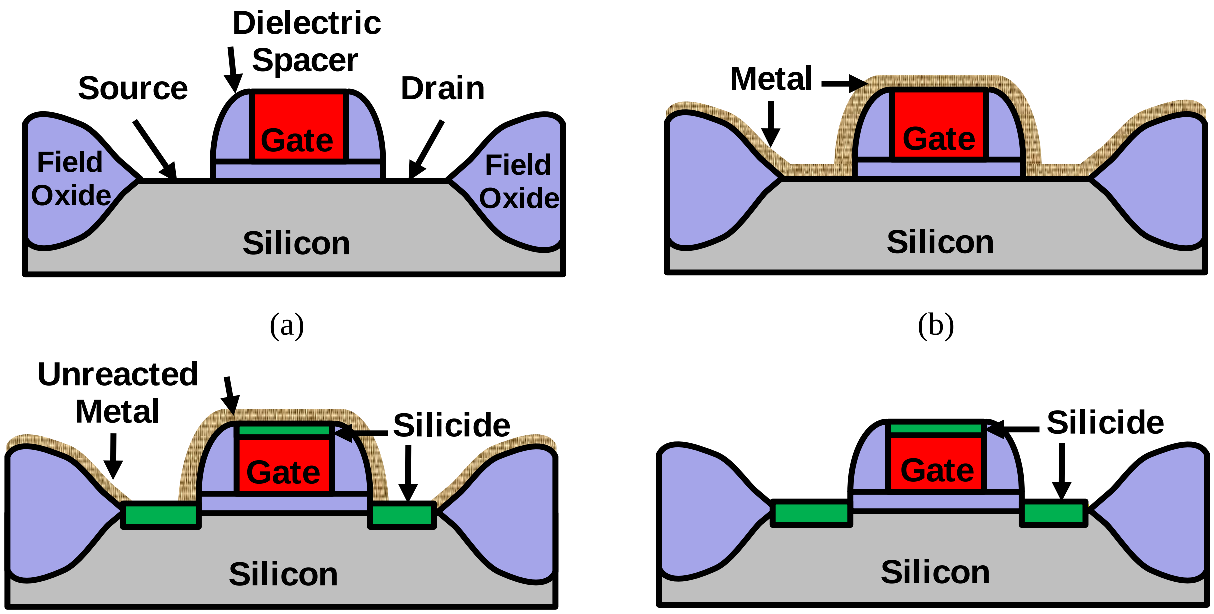

Fig. 3-3: (a) Fabricated polysilicon gate, dielectric sidewall spacers, source and drain; (b) deposition of conformal blanket metal; (c) thermal treatment, typically rapid thermal annealing at silicidation temperature, to form silicide selectively; (d) wet etch to selectively remove un-reacted metal over dielectric and other materials.

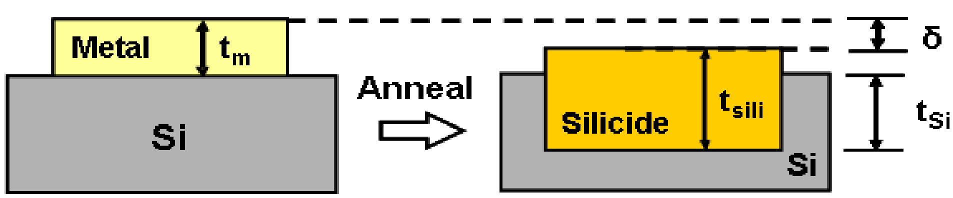

Table 3-1: Properties of common silicides

Silicide	Silicidation Temp.	t_{Si}	t_{sili}	Volume Shrinkage	δ
Ni_2Si	~250C	0.91	1.47	23.0%	0.44
NiSi	~400˚C	1.84	2.22	21.8%	0.62
$TiSi_2$	~850˚C	2.30	2.50	24.1%	0.8
PtSi	~500˚C	1.30	1.95	15.1%	0.35
$CoSi_2$	~750˚C	3.60	3.53	23.2%	1.07
$MoSi_2$	~750˚C	2.56	2.59	27.25%	0.97

t_{si} = nm of Si consumed per nm of metal (t_m=1)
t_{sili} = nm of silicide formed per nm of metal (t_m=1)
δ = nm of step height change per nm of metal (t_m=1)

3.2.3 Silicide-Induced Gaps

Table 3-1 also shows the theoretical volume ratio of consumed metal to silicon for different silicides. The data also includes information gauging the amount of “volume shrinkage” afforded by a given silicidation reaction, assuming a starting metal sitting flush atop a silicon substrate, as illustrated in the schematic above Table 3-1. Specifically, the combined thickness of the metal and the silicon consumed is less than the thickness of the silicide formed. As a result, the step height decreases after the silicide forms.

Fig. 3-4 illustrates one method by which silicidation can be used to form a submerged gap. Here, 10nm of molybdenum (Mo) is sandwiched between silicon (Si) below and a capping layer of oxide above. Upon heating via rapid thermal annealing in a low oxygen environment, the Mo and Si react to form $MoSi_2$, whereby 10x2.56 = 25.6 nm of silicon is consumed to form 10x2.59 = 25.9 nm of $MoSi_2$. This means the step height changes from the 10nm original metal thickness to now only 25.9-25.6 = 0.3 nm, leaving a 10-0.3 = 9.7 nm gap between the top of the silicide and the bottom of the oxide cap.

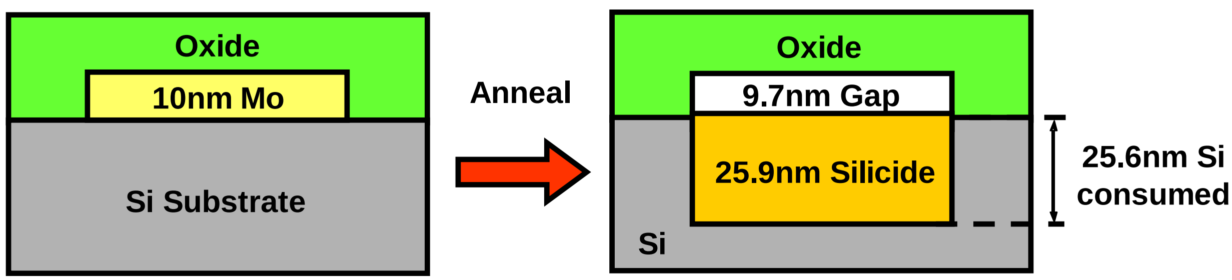

Fig. 3-4: Schematic of how to form a submerged gap using the volume reduction property of Mo silicide.

The advantages of this silicide-based approach over etch-based release processes are numerous and include:

1) Greatly reduces the time needed for release, since the time required is governed by a single interface reaction time rather than by lateral transport rates.

2) Avoids damage to structures not involved in the release, which is an important limiting side-effect of sacrificial layer-based approaches, where the etchant used often has a finite selectivity to other surrounding layers.

3) Avoids surface tension-based sticking or problems with bubble formation during release that commonly plague wet release approaches.

4) Allows the formation of gaps in sealed chambers (*i.e.*, no need for access routes).

3.3 Experimental Results

3.3.1 Demonstration of Silicide-Induced Gaps

Fig. 3-5 and Fig. 3-6 summarize processes used for basic demonstration of silicide-induced gaps. In Fig. 3-5, 200 nm of sputtered molybdenum is patterned by wet etching into strips, followed by 600 nm of PECVD capping oxide deposited at 300 ˚C. After just 1 minute of annealing at 750 ˚C, a gap forms when volume shrinkage during silicidation pulls the silicided surface away from the capping oxide. The rounding at the gap edges results from rounding of the original metal corners during isotropic wet etching. The gaps essentially take on the shape of the metal layer, and the shape of silicide is a mirror image of the metal relative to the silicon surface.

The process of Fig. 3-6 differs from that of Fig. 3-5 only in the use of a semiconductor top layer, where PECVD amorphous silicon is used instead of oxide. Otherwise, the silicidation procedure is essentially the same, except that now silicides form on both the top and bottom surfaces of the gap. This process has the advantage of allowing a conductive semiconductor structural material, which is needed for electrostatic transduction. For applications where silicidation at the bottom of the conductive microstructure is not desired, (*e.g.*, due to stress imbalance issues), it can be prevented by depositing a thin layer of dielectric between the microstructure and the metal, similar to the thin sidewall spacers used in CMOS to prevent silicidation on the polysilicon gate [19]. For applications where sub-10 nm dielectric layers can compromise device performance, such as capacitively transduced high-*Q* resonators and switches, conductive materials that do not react with metal at the silicidation temperatures can be used as structural layers. Some good candidates include doped silicon carbide, doped polycrystalline diamond, or metals with higher silicidation temperatures.

It should be noted that this method is not suitable for forming >1 µm gap spacing for two reasons. First, it is challenging to deposit blanket metal films thicker than 1 µm without excess residual stress and vertical stress distribution, which can cause non-uniform silicide and therefore non-uniform gap spacing. Second, silicidation introduces stress to the reactant silicon, either the silicon substrate or the silicon microstructures or both, due to volume change, lattice mismatch, and thermal stress. The latest is the dominating factor for silicide formed at higher temperatures. In this case, a metal film is deposited and reacts with silicon in a stress-free state at higher temperatures and subsequently cooled to device operational temperature, typically room temperature. As the thermal expansion coefficients of most silicides (*e.g.*, thermal expansion coefficients of solid-state reaction polycrystalline $TiSi_2$, $CoSi_2$, and NiSi are 12.5×10^{-6}, 10.4×10^{-6}, and $16 \times 10^{-6}\ K^{-1}$, respectively) are about five times larger than that of silicon ($2.6 \times 10^{-6}\ K^{-1}$), a tensile stress is induced in the silicide when cooled down.

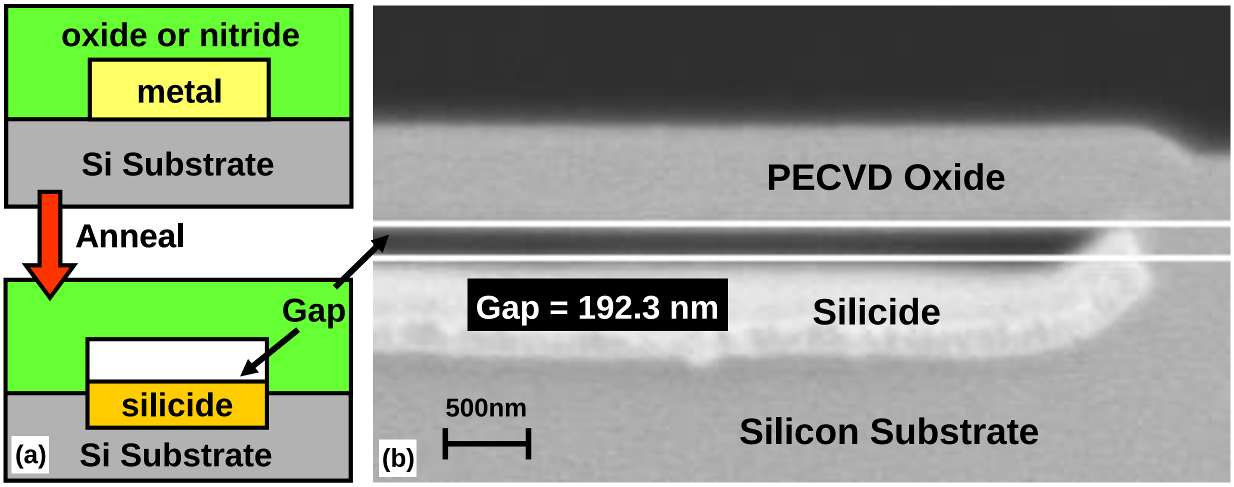

Fig. 3-5: (a) Process flow and (b) SEM cross-section of a 192nm air gap formed between oxide and silicide. Here, 200nm-Mo reacts with silicon but not oxide at the anneal temperature.

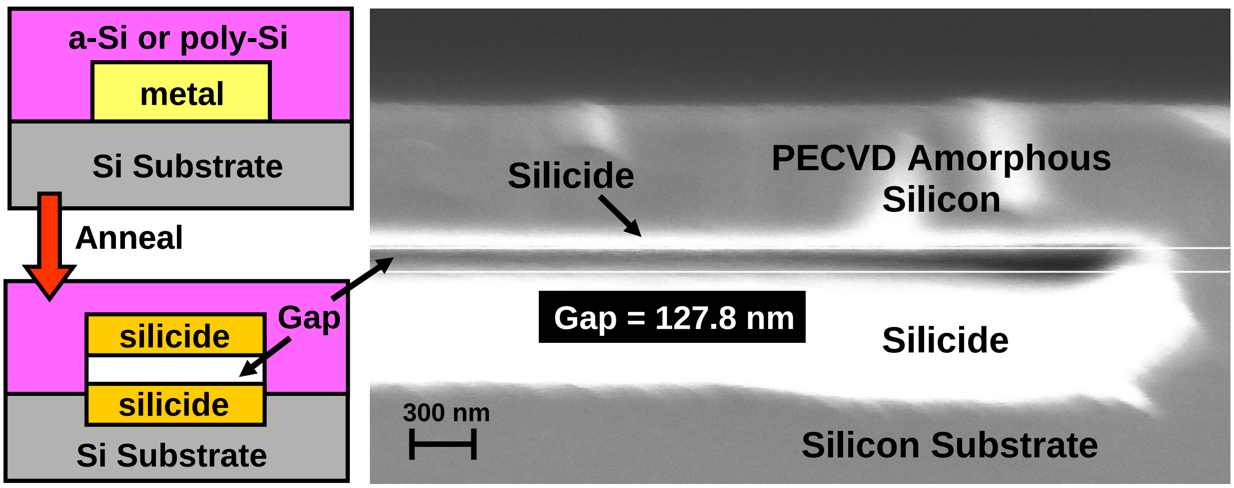

Fig. 3-6: Process flow and SEM cross-section of a 128 nm air gap formed between amorphous silicon and silicide. Here, 150 nm Mo forms silicides unevenly on both sides due to differences in single-crystal and amorphous Si silicidation behavior and also likely due to presence of hydrogen and oxygen in the amorphous Si.

3.3.2 Repeatability

The solid-state silicide reaction is sensitive to impurities at the metal-Si interface and in the metal itself. Three precautions have been experimentally found useful for repeatable and high quality silicide formation:

1. The interface between the metal and semiconductor must be clean and free from native oxide. To ensure this, samples are dipped into 5:1 buffered hydrofluoric acid (BHF) prior to metal sputtering.
2. Native oxide can further be removed by a slight *in-situ* sputter etch preceding the actual

metal sputtering step. Caution should be taken here, as an aggressive sputter etch may make the silicon surface and the resulting silicide surface rougher.

3. To reduce the background concentration of water vapor in the process chamber, wafers are baked at 200 °C for 20 minutes in vacuum to degas before metal sputtering. In this work, Mo is sputtered at 200 °C, so no cool down is required after dehydration baking. Caution should be taken when sputtering nickel. As dinickel silicide, Ni_2Si, starts to form at ~300 °C, elevated temperature in the substrate and high sputtering power can allow the nickel to react with silicon immediately, which affects the resulting gap spacing after silicidation annealing.
4. To minimize the impurities within the metal film, it is helpful to keep the base pressure of the metal sputter tool below $1x10^{-7}$ Torr and run several dummy wafers to clean up the metal target prior to processing device wafers.
5. Annealing must be performed with a low concentration of oxygen to ensure that the metal does not oxidize during silicide formation. This is especially important for samples with very thin metal (<10 nm) and anneal at high temperatures, as oxygen can quickly diffuse through the thin metal and passivate the metal-silicon interface by forming silicon dioxide, which prevents metal and silicon from reacting. The RTA tool in the Berkeley Microlab is not equipped with a pump to remove the contamination from atmosphere before flowing inert gases. A long purge of N_2 in the RTA chamber is found to help silicide formation.

The importance of obtaining a clean metal-silicon interface is immediately apparent when oxide is present at the interface. In particular, when samples before metal deposition are shortly dipped in piranha (H_2SO_4+H_2O_2) instead of BHF with no sputter etch, and the same thermal annealing conditions applied, silicidation either does not happen or the silicide surface becomes very rough, as shown in Fig. 3-7. The wavy surface can be explained by silicide protrusions through areas with thinner oxide or without native oxide, causing nonuniform reaction between the metal and the silicon.

Repeatable and uniform silicide-induced gaps can be formed with all of the above procedures taken. Fig. 3-8 shows the fabrication process flow where an array of microchannels with various dimensions is formed with one mask and only 1 minute of annealing to release. A blanket Mo is sputtered followed by lithography and wet etching to pattern Mo (Fig. 3-8(a)). Then, PECVD oxide is deposited on the entire wafer (Fig. 3-8(b)). RTA at 750 °C for 1 minute forms the channel (Fig. 3-8(c)). As full 6” wafer RTA for this process is not possible in the Berkeley Microlab, nine samples from the same 6” wafer (one from center, four from 4” area and four from edges), were annealed and examined for uniformity and repeatability. Microchannels form uniformly on die located at the same distance away from the center. The gap spacing is larger on the center die as the Mo sputtering is not uniform, with thickest metal at the center. Fig. 3-9 shows five of the 15 um wide and 0.8 um high microchannels on one die with a zoomed-in view on the insert that confirms the repeatability of this method.

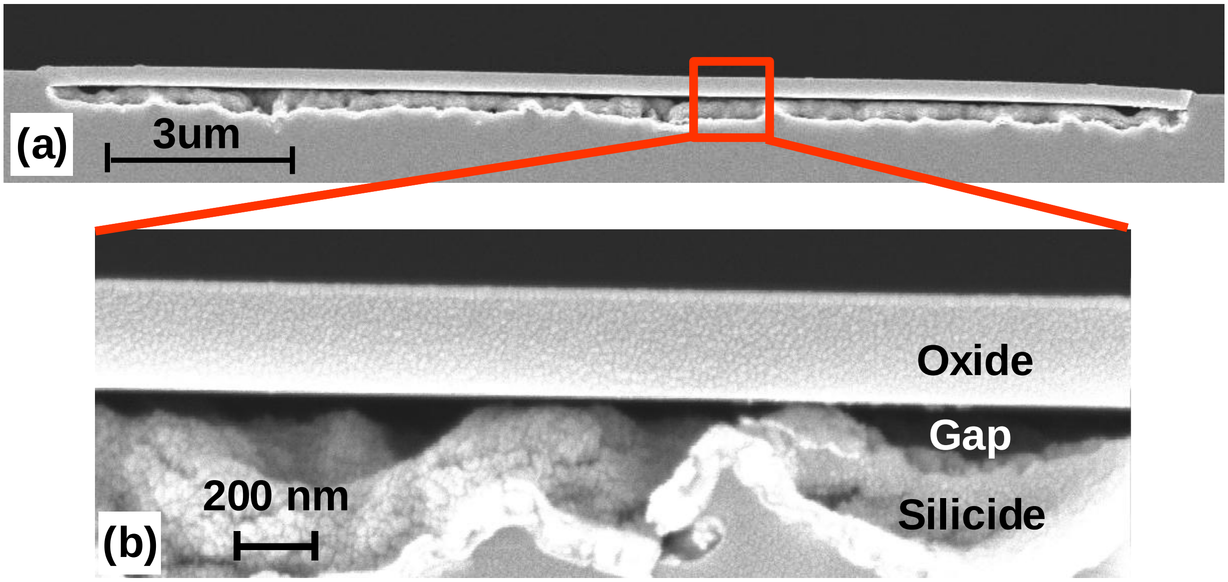

Fig. 3-7: SEM cross-section showing a roughened silicide surface caused by thin oxide at the silicon-metal interface.

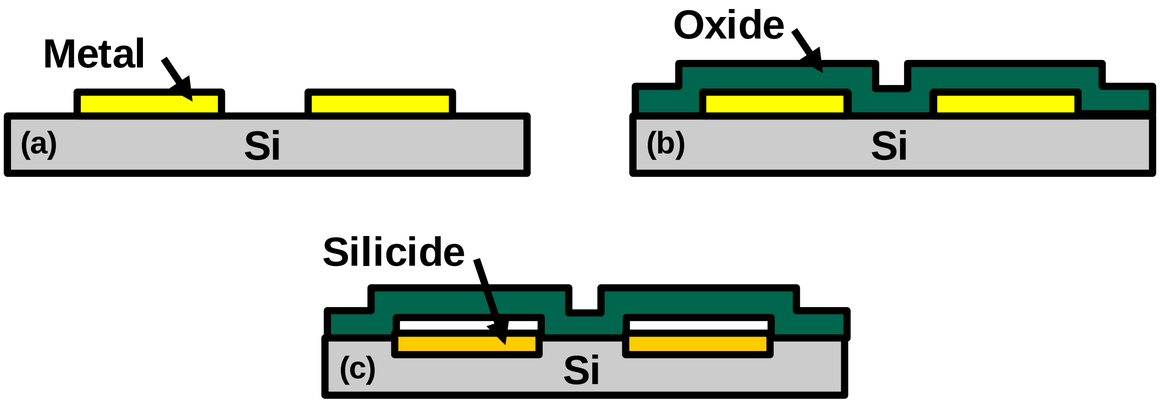

Fig. 3-8: Fabrication process flow of the microchannels in Fig. 3-9; (a) sputter blanket Mo films on a single-crystal wafer and pattern via wet etch; (b) PECVD oxide; no pattern and etch is required; (c) anneal to release the microchannels.

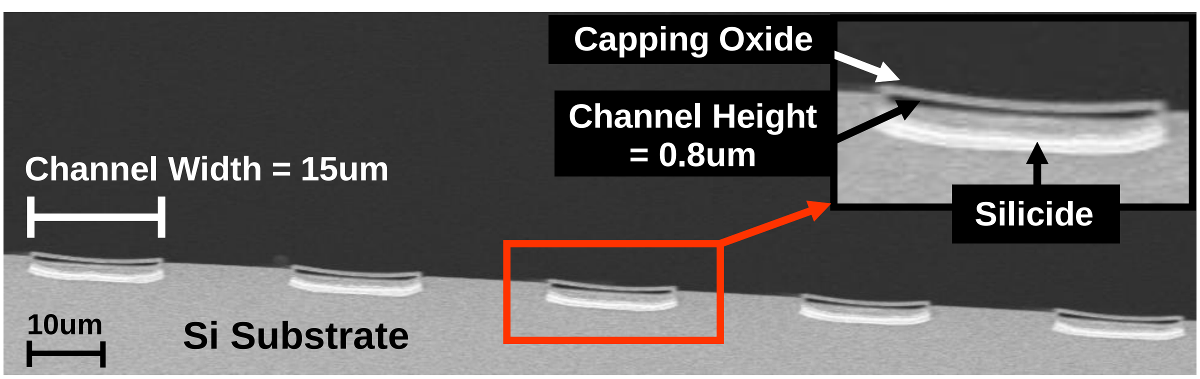

Fig. 3-9: Cross-sectional SEM of an array of oxide-capped micro-channels on a silicon substrate fabricated via silicide-induced release.

3.3.3 Operational Temperature Range

To gauge the permissible temperature ceiling during process steps before and after the silicidation anneal, samples of patterned Mo over Si were heated in a conventional oven at 350 ˚C for 6 hours before and after the 1 minute 750˚C silicidation anneal, with no change in silicide step height, versus a sample without extra thermal treatments. This confirms that microstructures can be released at the very end of a process as long as processing temperatures after metal deposition do not exceed the silicidation temperature. Moreover, once the silicide is formed, thermal processes with temperature much lower than the original silicidation temperature generally do not change the size of the gap.

However, thermal treatments at temperatures higher than the initial silicide formation temperature will affect the silicide morphology, of which the important consequence for silicide-induced gaps here is the surface roughness and the silicide step height change. The effects of thermal treatment on silicide-induced gaps can be considered in two ways:

First, different silicide phases can form at higher temperatures and different phases have different metal to silicon consumption ratio. For example, for Ni deposited on single crystal Si, Ni reacts with Si at about 250 °C to form nickel-rich silicide, Ni_2Si, with volume ratio of consumed Ni:Si=1:0.91. When the temperature increases to around 350 °C, monosilicide, NiSi, starts to form by consuming more Si and the volume ratio of consumed Ni:Si=1:1.84. The gap spacing is expected to increase with more Ni_2Si turning into NiSi. NiSi is stable on single crystal Si until about 750 °C, at which point the high resistivity and silicon-rich phase, $NiSi_2$, forms. As temperature increases, the metal to silicon consumption ratio increases, as does the gap spacing.

Second, thermal treatments can change the silicide morphology via silicide agglomeration, where the silicide agglomerates into discrete islands, as a result of a reduction of surface energy. In the case of silicide formed with polysilicon, silicide-enhanced grain growth in the polysilicon also increases the surface roughness. With even longer annealing time, silicide/poly-Si layer inversion has been reported for both Ni and Co deposited on polycrystalline silicon [20][21]. The onset of layer inversion can be detected by a sharp increase in resistance of the top thin film. Both processes increase the surface roughness and resistance of the final silicide. The work in [22] investigates how metal thickness (in particular, Co) relative to the polysilicon grain size affects the degree of polysilicon grain growth, silicide agglomeration, and layer inversion.

In general, it is desirable to use silicide of a silicon-rich phase for better thermal stability. Different approaches for improving the thermal stability of silicides have been reported, including nitrogen implantation into the metal film before silicidation [23].

3.3.4 Small Gaps and Lateral Gaps

Among the most powerful capabilities provided by silicidation is its ability to achieve tiny sub-50 nm gaps, which are essential to vibrating RF micromechanical resonators using capacitive transduction. Fig. 3-10 shows a 32.5 nm gap underneath a SiGe capping layer, achieved via a silicidation reaction between Mo metal and the underlying silicon substrate, with comparatively little reaction with the capping SiGe layer. The thirty seconds required for silicidation contrasts sharply with the 40+ minutes of wet-etching often required for small-gapped RF micromechanical resonators [15]. Indeed, release times required by etch-based

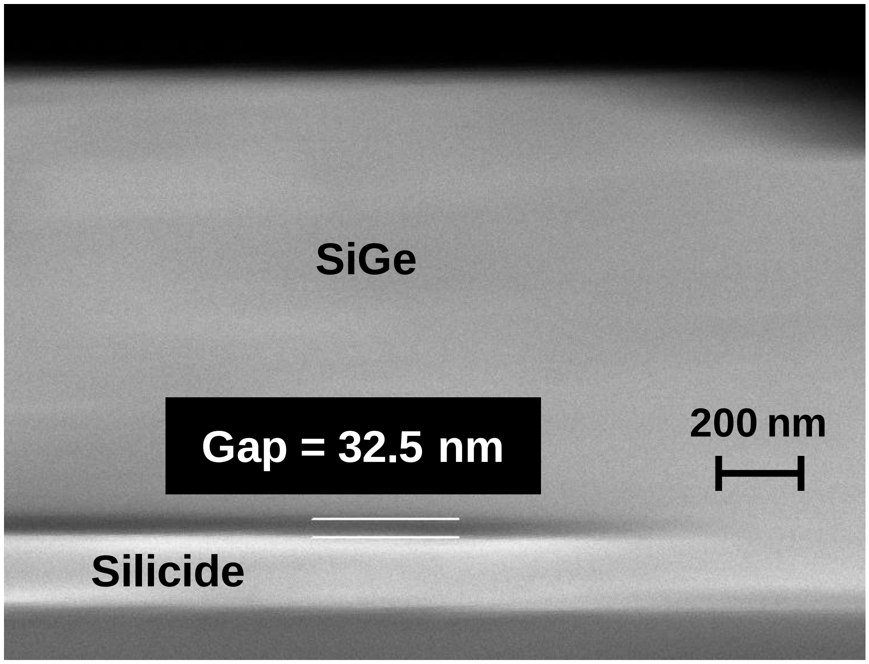

Fig. 3-10: SEM cross-section of a 32.5nm gap formed between a bottom MoSi2 and a top SiGe capping layer. Even smaller gaps should be achievable via a thinner metal layer.

release processes increase with gap aspect-ratio, while those needed for silicide-based release remain virtually the same. Clearly, the described silicide-based release process scales much better than etch-based counterparts. The smallest achievable gap is ultimately limited by the surface roughness of the silicide which is generally on the order of 10 nm or less for nickel [24], titanium [25], and cobalt [26] with proper thermal treatments. Gap spacings this small should be very helpful towards capacitively transduced resonators with the sub-50 Ω impedances desired by conventional wireless circuits.

The silicide-induced release can also be applied to form lateral gaps, perhaps using PECVD and/or atomic layer deposition (ALD) methods to deposit conformal lateral semiconductor and metal films with well-controlled thicknesses at temperatures lower than the silicidation temperature.

3.3.5 CMOS Compatibility

It should be noted that silicide-induced release is not limited to silicidation with single crystal silicon, but also works with amorphous and polycrystalline systems, and with semiconductor materials other than silicon, e.g., SiGe. For example, Fig. 3-11 presents a gap formed between a top oxide capping layer and a 1.2 µm PECVD amorphous-silicon layer deposited at 300˚C. This confirms that the described silicide-based release process can be applied to MEMS/NEMS built atop CMOS or on substrates other than silicon, such as glass, as long as a thin layer of semiconductor is available.

Another requirement for CMOS compatibility is that the process temperature and time cannot exceed the thermal budget of the underlying transistors. In that case, Ni silicide can be used instead of Mo and Ti silicides, as Ni starts to react with silicon at temperatures as low as ~250 °C. The work in [27] has successfully shown that 5.8 GHz microwave annealing can facilitate low resistance NiPtSi silicide formation at reduced process temperature at 250 °C compared to the 600 °C required if conventional RTA were used. Laser annealing, with only mili-second anneal, has been demonstrated to form shallow silicide without degradation on the performance of transistors [28]. Another possible approach is to use embedded micro-heaters, such as polysilicon strips, to perform local anneal and release by applying electrical currents.

3.3.6 Released Microstructure

Mere patterning of the capping layer before the silicidation anneal yields suspended movable structures with more general geometries. Fig. 3-13 presents SEM cross-sectional images of multiple oxide diaphragms released via the described silicide approach, including a 100×100 μm^2 membrane with a 260:1 lateral dimension-to-vertical gap aspect ratio and membranes with smaller sizes formed by the same one minute thermal anneal step (Fig. 3-13 (c)-(d)).

The required anneal time is independent of the lateral dimension. Therefore, diaphragms of even larger lateral dimensions can be released with the same anneal time. On the other hand, the smaller the gap spacing, the less annealing time is required to fully silicide the metal film. As the lateral dimension of the structure and the gap spacing continue to increase and decrease,

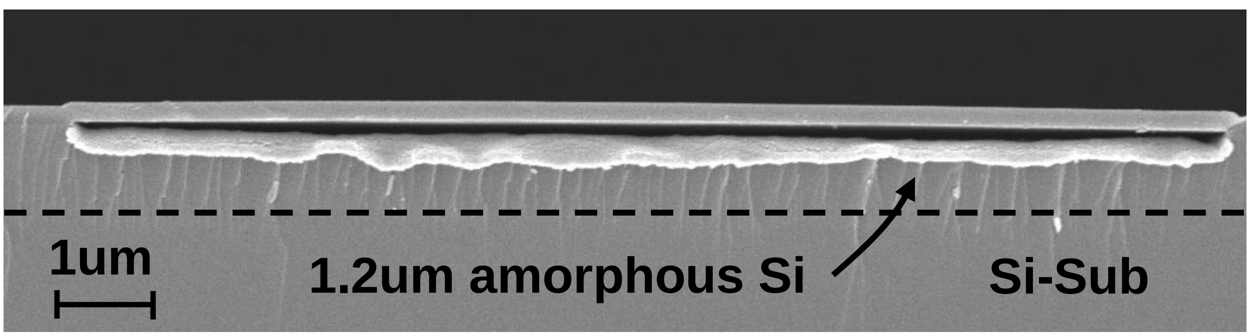

Fig. 3-11: A silicide-induced gap formed over a 1.2 µm PECVD amorphous silicon film deposited at 300 °C.

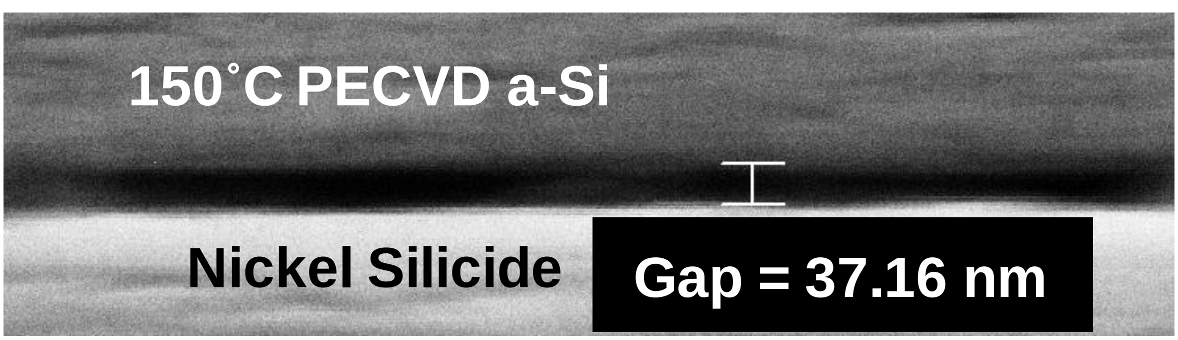

Fig. 3-12: A 37 nm silicide-induced gap formed using low temperature nickel silicide. The deposition temperature of the capping layer is 150 °C.

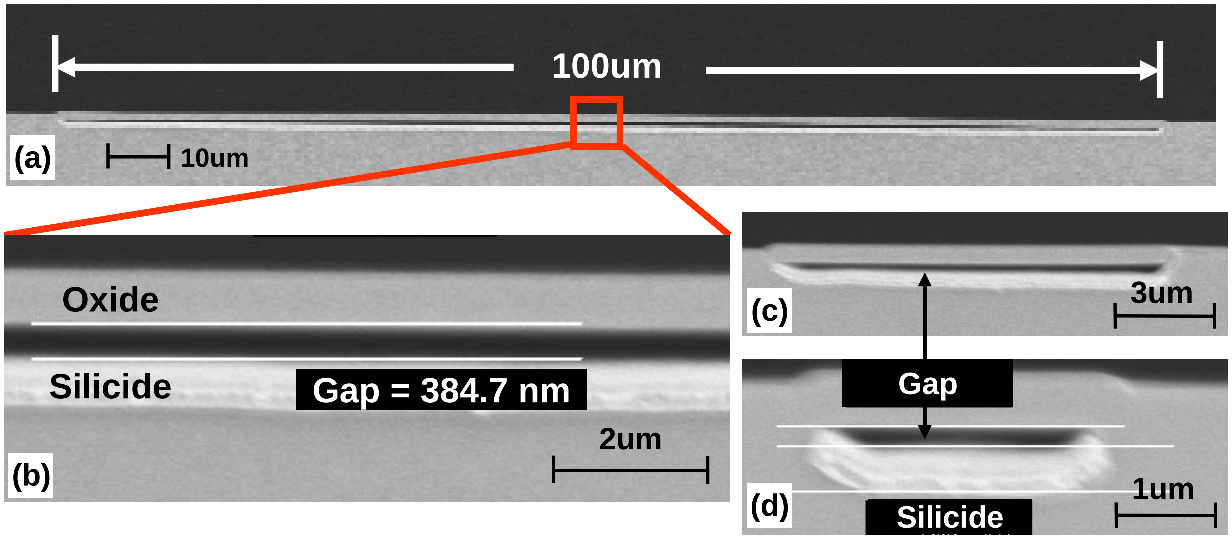

Fig. 3-13: SEM cross-sections of (a) a 100μm-wide 410nm-thick oxide diaphragm suspended 385nm above the substrate and (b) a zoom-in. The original Mo thickness was 400nm. (c) and (d): Smaller diaphragms released in the same annealing step.

respectively, the aspect ratio increases from both factors with decreasing required annealing time. From this perspective, the method of silicide-induced gaps for releasing microstructures offers infinite achievable aspect ratio with minimum release time, on the order of one minute of less, compared to hours or days required by sacrificial material etch for such high aspect ratio microstructures.

Theoretically, as silicidation is a solid-state reaction without gaseous reaction byproducts, the silicide-induced gaps are expected to have vacuum. If the cavity underneath the released diaphragm is at vacuum state, the calculation shows that the force generated from pressure difference above and below the diaphragms would push these ~400 nm diaphragms down to the substrate. This behavior is, however, not observed in the inspections using both optical and mechanical probing methods. As the oxide is deposited via low temperature plasma enhanced CVD, the oxide film showed obvious pin holes. It is very possible that gas diffuses through the thin diaphragms or the PECVD oxide outgases during annealing such that vacuum state is not achieved. More careful selection of materials and dimensions of the capping/sealing layers is expected to address this issue.

Fig. 3-14 and Fig. 3-15 present 20 μm long, 2 μm wide oxide cantilever and a folded-beam comb-driven resonator with springs bent by a probe, confirming that they are released. Successful release of such compliant microstructures is possible because silicidation is a dry process, so does not suffer from stiction. In all cases, the release anneal takes no more than two minutes, and no etchant is consumed, making this approach much faster and cheaper than etch-based release methods.

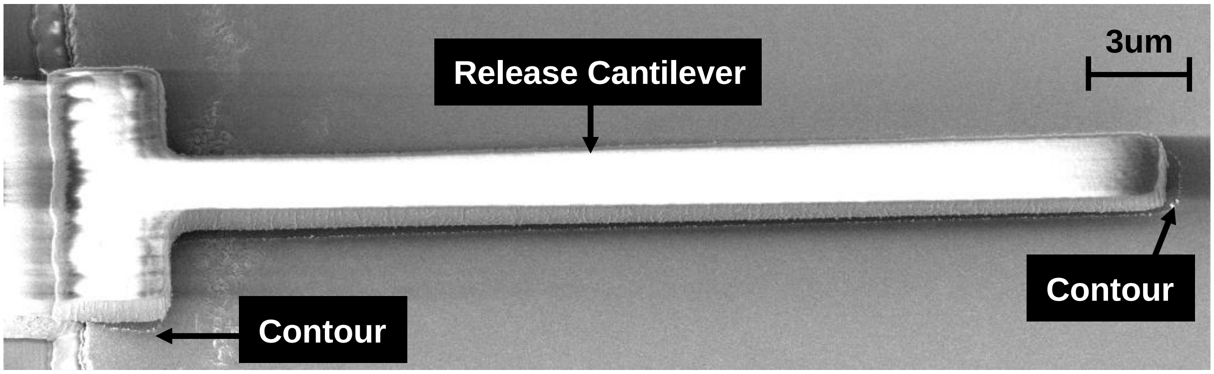

Fig. 3-14: SEM of a 1.2μm-thick oxide cantilever separated from the substrate by a silicide-induced gap.

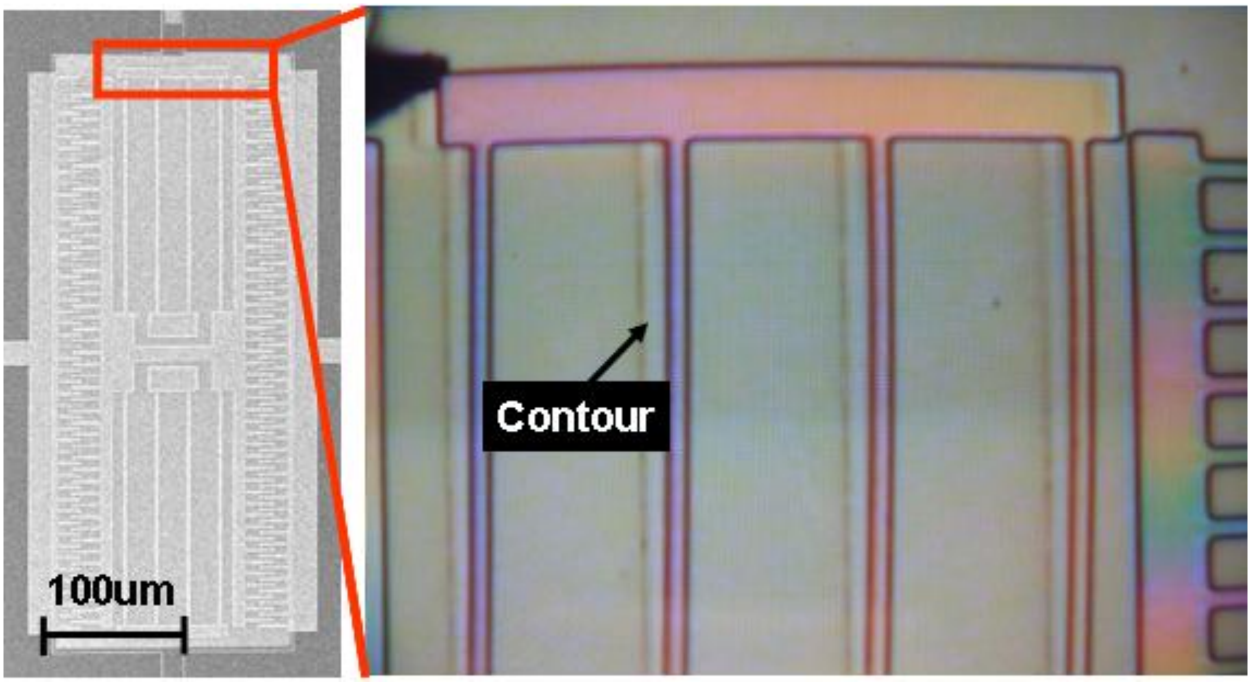

Fig. 3-15: SEM of a released folded-beam comb-driven structure with springs bent by a probe tip.

3.3.7 Released Titanium Beam Resonators

To demonstrate the use of silicide-induced gaps in a practical application, the three-mask process shown in Fig. 3-16 uses titanium (Ti) as a structural material and Mo as the siliciding metal to fabricate beam resonators. Here, Mo is sputter deposited after a short in-situ sputter etch to remove native oxide, then patterned using a commercial aluminum wet etchant (pre-mixed phosphoric and acetic acid mixture) at 50 ˚C. Next, 300nm of 300˚C PECVD oxide isolation liner is deposited and patterned via a BHF dip, followed by sputter deposition of 700 nm of Ti structural material at 300 ˚C. The Ti is then dry etched via a Cl_2/BCl_3 plasma, with the etch stopping on the underlying Mo or oxide layer. The structure is finally released via a one minute rapid thermal anneal step. As shown in Fig. 3-16, MoSi2 forms the ground plane/drive electrode for this clamped-clamped beam, and the oxide layer prevents the beam from shorting with the silicide.

Fig. 3-17 presents the SEM of a released 320 μm long, 3 μm wide Ti clamped-clamped beam displaced laterally by a probe tip. Fig. 3-18 further presents the mixing-measured [15] frequency characteristic (in vacuum) for a 20 μm long, 2 μm wide beam with 150 nm electrode-to-resonator vertical gap spacing, confirming functionality of the beam and applicability of the silicide-based release process in an actual application.

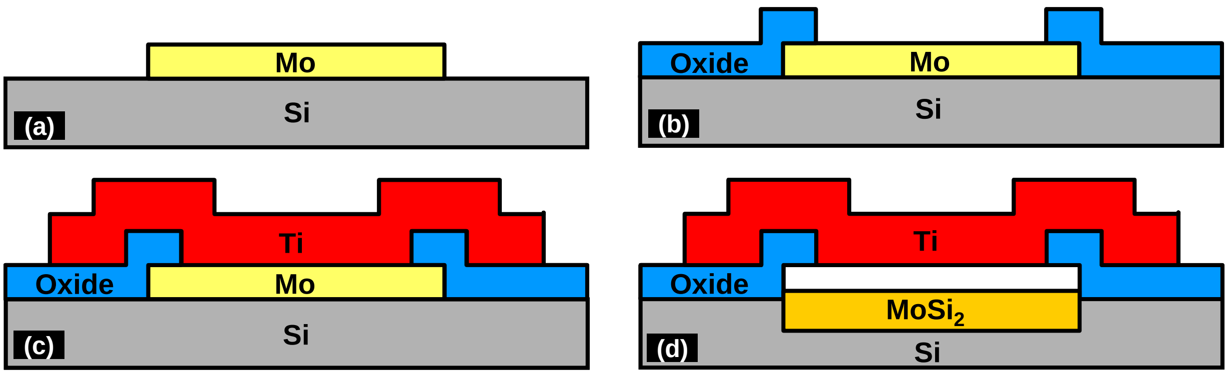

Fig. 3-16: Process flow yielding a titanium clamped-clamped beam released via silicidation: (a) Sputter and pattern molybdenum over silicon substrate; (b) deposit 300 nm thick 300 ˚C PECVD oxide and remove over device areas and bond pads; (c) sputter and pattern 700 nm thick titanium structural material; and (d) release via rapid thermal annealing at 750 ˚C.

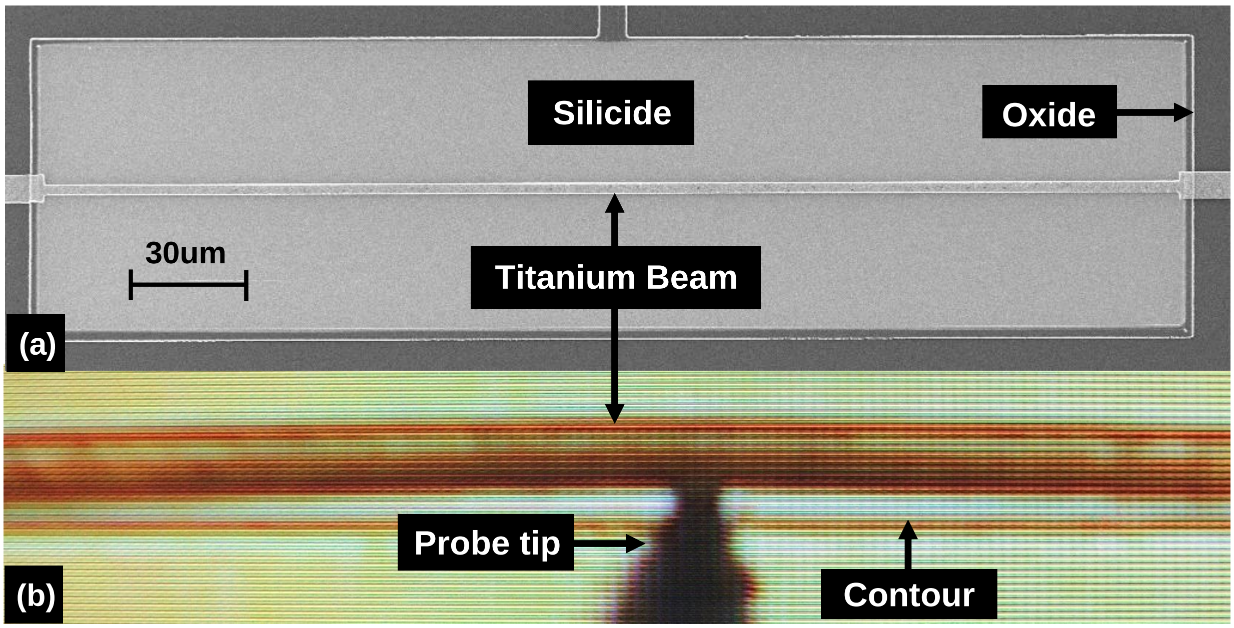

Fig. 3-17: (a) SEM of a 320 μm long, 3 μm wide, 700 nm thick titanium clamped-clamped beam using the process of Fig. 3-16. (b) Bending via a probe tip confirming release.

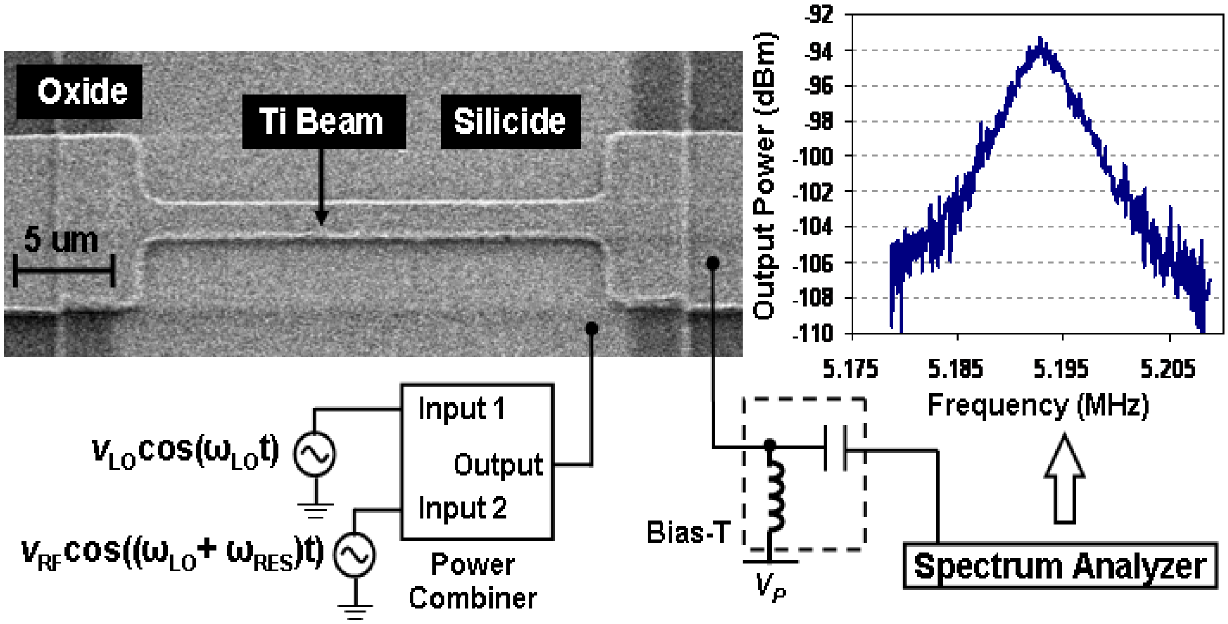

Fig. 3-18: Mixing measurement setup and measured resonant peak under vacuum for a Ti clamped-clamped beam released via silicidation, with Q = 1,082. Here, P_{RF} = 10 dBm (network analyzer output), V_{LO} = 10 $V_{P\text{-}P}$, and V_P = 20 V.

3.4. Conclusions and Future Work

By utilizing a volume shrinkage-based method for forming gaps between structural layers and thereby avoiding the need for etching, the silicide-based release process demonstrated in this work is cheaper, cleaner, and faster than conventional etch-based methods, as it requires no etching, consumes no chemicals, and has little dependence on mass transport processes. Using this method, structures with aspect-ratios exceeding 260:1 have been released in less than two minutes—substantially less than the 40 minutes otherwise required by an etch-based release process. Although this work features silicides based on Mo, it should be understood that any of the metals in Table 3-1 could also be used.

But the benefits of silicidation methods go far beyond mere release of high-aspect ratio gaps. In particular, the fact that silicidation is a heat-induced and self-sufficient reaction that does not require a diffusion path suggests the possibility for localized and post-package release without any need for release holes in the package structure. To expand upon this, Fig. 3-19(a) [29] presents one conventional approach to wafer-level encapsulation where release holes in the encapsulating cap are needed to allow release etchants to access a sacrificial layer that completely encases the structure under the cap. Since the diffusion paths are quite tortuous, the time required for release is generally quite long and etch by-products have difficulty diffusing out. On top of this, the need to seal the etch holes can compromise both the package and device within (if the sealant also deposits on the device).

In contrast, silicidation (requiring no diffusion path) can form gaps submerged beneath the cap layer with no need for etch holes, as shown in Fig. 3-19(b). The packaging process would require just minutes of anneal time and would be local to areas with the right metal-semiconductor pairings. Efforts towards post-package and release of capacitive resonators are ongoing.

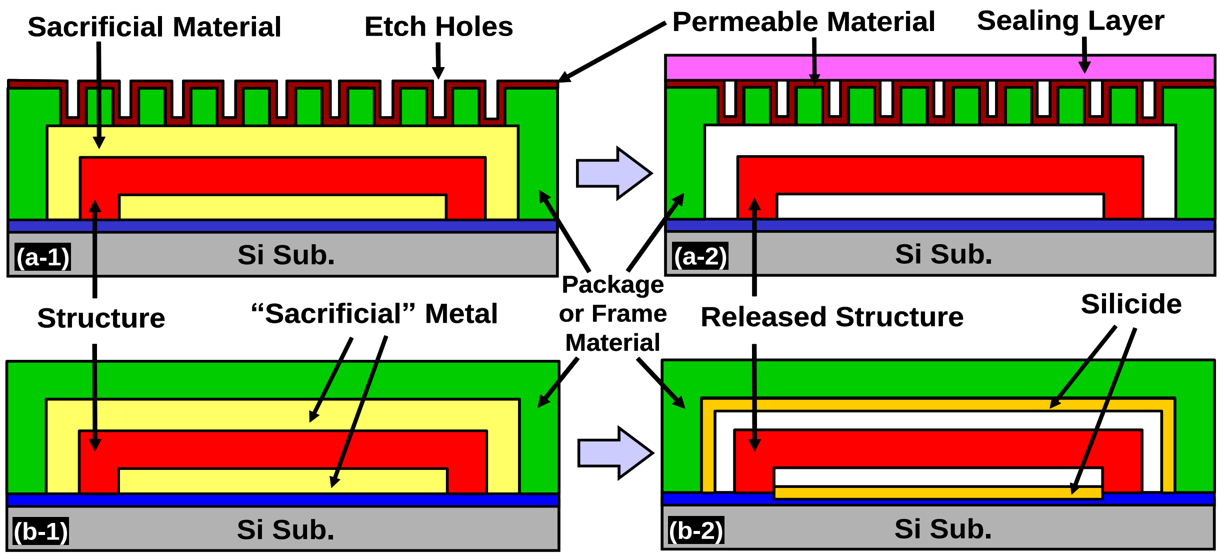

Fig. 3-19: Cross-sectional summaries of (a) a conventional thin-film package where (a-1) etch holes provide access for sacrificial material removal and (a-2) a deposition step is required to seal; and (b) a silicide-based release packaging method that obviates the need for etch holes and sealing that comprises (b-1) deposition and patterning of a proper succession of semiconductors and metals and (b-2) a short silicidation anneal.

3.5. References

[1] M. A. Schmidt, "Wafer-to-wafer bonding for microstructure formation," Proceedings of the IEEE, vol. 86, pp. 1575-1585, 1998.

[2] D. Xu, L. Wang, G. Ding, Y. Zhou, A. Yu, B. Cai, "Characteristics and fabrication of NiTi/Si diaphragm micropump," Sensors and Actuators, A93 (2001) 87-92.

[3] J. Chae, H. Kulah and K. Najafi "A CMOS-compatible high aspect ratio silicon-on-glass in-plane micro-accelerometer," *J. Micromech. Microeng*. vol. 15. 2005, pp. 336-345.

[4] F. Niklaus, G. Stemme, J.-Q. Lu, and R. J. Gutmann, "Adhesive wafer bonding," *J. OF APPLIED PHYSICS*, vol. 99, 031101, 2006.

[5] H.-S. Noh, K.-S. Moon, A. Cannon, P. J Hesketh and C P Wong, “Wafer bonding using microwave heating of parylene intermediate layers,” *J. Micromech. Microeng.* 14 (2004) 625–631.

[6] R. F. Wolffenbuttel and K. D. Wise, "Low-temperature silicon wafer-to-wafer bonding using gold at eutectic temperature," Sensors and Actuators A: Physical, vol. 43, pp. 223-229, 1994.

[7] T. Suni, K. Henttinen, J. Dekker, H. Luoto, M. Kulawski, J. Makinen, R. Mutikainen, “Bonded thick film SOI with pre-etched cavities,” Microsyst Technol (2006) 12: 406–412.

[8] W. C. Tang, T.-C. H. Nguyen, M. W. Judy, and R. T. Howe, "Electrostatic-comb drive of lateral polysilicon resonators," Sensors and Actuators A: Physical, vol. 21, pp. 328-331, 1990.

[9] F. Marty, L. Rousseau, B. Saadany, B. Mercier, O. Français, Y. Mita, and T. Bourouina, "Advanced etching of silicon based on deep reactive ion etching for silicon high aspect ratio microstructures and three-dimensional micro- and nanostructures," J. of Microelectronics, vol. 36, pp. 673-677, 2005.

[10] R. Abdolvand and F. Ayazi, "An advanced reactive ion etching process for very high aspect-ratio sub-micron wide trenches in silicon," Sensors and Actuators A: Physical, vol. 144, pp. 109-116, 2008.

[11] R. Maboudian and R. T. Howe, “Critical review: Adhesion in surface micromechanical structures,” J. Vacuum Sci. Technol., vol. B15, no. 1, pp. 1–20, Jan./Feb. 1997.

[12] C. Torres-Raya, D. Hernandez-Maldonado, J. Ramirez-Rico, C. Garcia-Gañan, A. R. de Arellano-Lopez, and J. Martinez-Fernandez, “Fabrication, chemical etching, and compressive strength of porous biomimetic SiC for medical implants” J. Ma-ter. Res., vol. 23, no. 12, Dec 2008.

[13] I. Lee, G. H. Yoon, J. Park, S. Seok, K. Chun, and K.-I. Lee, "Development and analysis of the vertical capacitive accelerometer," Sensors and Actuators A: Physical, vol. 119, pp. 8-18, 2005.

[14] K. R. Lee, K. Kim, H.-D. Park, Y. K. Kim, S.-W. Choi, and W.-B. Choi, “Fabrication of capacitive absolute pressure sensor using Si-Au eutectic bonding in SOI wafer,” J. Phys.: Conf., ser. 34 393-398, 2006.

[15] J. Wang, Z. Ren, and C. T.-C. Nguyen, “1.156-GHz self-aligned vibrating micromechanical disk resonator,” IEEE Trans. Ultrason., Ferroe-lect., Freq. Contr., vol. 51, pp. 1607-1628, Dec. 2004.

[16] W. H. Teh, C.-T. L., M. Graham, and C. G. Smith, "Cross-linked PMMA as a low-dimensional dielectric sacrificial layer," Microelectromechanical Systems, Journal of, vol. 12, pp. 641-648, 2003.

[17] A Bagolini, L Pakula, T LMScholtes, H TMPham, P J French and P M Sarro, “Polyimide sacrificial layer and novel materials for post-processing surface micromachining,” *J. Micromech. Microeng.* 12 (2002) 385–389.

[18] K. Maex and M. Rossum, Properties of Metal Silicides, IN-SPEC Publication, 1995.

[19] L. J. Sung and C. Y. Lu, "Limitation of spacer thickness in titanium salicide ULSI CMOS technology," Electron Device Letters, IEEE, vol. 10, pp. 481-483, 1989.

[20] E. G. Colgan, J. P. Gambino, and B. Cunningham, "Nickel silicide thermal stability on polycrystalline and single crystalline silicon," Materials Chemistry and Physics, vol. 46, pp. 209-214, 1996.

[21] E. G. Colgan, J. P. Gambino, and Q. Z. Hong, "Formation and stability of silicides on polycrystalline silicon," Materials Science and Engineering: R: Reports, vol. 16, pp. 43-96, 1996.

[22] J. P. Gambino, E. G. Colgan, A. G. Domenicucci, and B. Cunningham "The Thermal Stability of CoSi2 on Polycrystalline Silicon: The Effect of Silicon Grain Size and Metal Thickness," J. Electrochem. Soc., Vol. 145, No. 4, April 1998, pp. 1384-1389.

[23] S. Wein-Town, L. Ming-Chi, and C. C. H. Hsu, "Suppression of cobalt silicide agglomeration using nitrogen (N_2+) implantation," Electron Device Letters, IEEE, vol. 19, pp. 163-166, 1998.

[24] M. Bhaskaran, S. Sriram, A. S. Holland, and P. J. Evans, "Characterisation of nickel silicide thin films by spectroscopy and microscopy techniques," Micron, vol. 40, pp. 99-103, 2009.

[25] C. Lavoie, R. Martel, C. Cabral, Jr., L.A. Clevenger and J.M.E. Harper, "Surface roughening during titanium silicide formation: a comparison between Si(100) and poly-Si substrates," Proceedings of MRS, vol. 440, pp. 389-394, 1997.

[26] G.-P. Ru, B.-Z. Li, G.-B. Jiang, X.-P. Qu, J. Liu, R. L. Van Meirhaeghe, and F. Cardon, "Surface and interface morphology of $CoSi_2$ films formed by multilayer solid-state reaction," Materials Characterization, vol. 48, pp. 229-235, 2002.

[27] T. Yamaguchi, Y. Kawasaki, T. Yamashita, Y. Yamamoto, Y. Goto, J. Tsuchimoto, S. Kudo, K. Maekawa, M. Fujisawa, and K. Asai, "Low-resistive and homogenous NiPt-silicide formation using ultra-low temperature annealing with microwave system for 22nm-node CMOS and beyond," in Electron Devices Meeting (IEDM), 2010 IEEE International, pp. 26.1.1-26.1.4.

[28] C. Ortolland, E. Rosseel, N. Horiguchi, C. Kerner, S. Mertens, J. Kittl, E. Verleysen, H. Bender, W. Vandervost, A. Lauwers, P. P. Absil, S. Biesemans, S. Muthukrishnan, S. Srinivasan, A. J. Mayur, R. Schreutelkamp, and T. Hoffmann, "Silicide yield improvement with NiPtSi formation by laser anneal for advanced low power platform CMOS technology," in Electron Devices Meeting (IEDM), 2009 IEEE International, 2009, pp. 1-4.

[29] K. S. Lebouitz, A. Mazaheri, R. T. Howe, and A. P. Pisano, "Vacuum encapsulation of resonant devices using permeable polysilicon," *Technical Digest*, 12^{th} Int. IEEE Micro Electro Mechanical Systems Conference (MEMS). 1999, pp. 470-475.

4. Capacitive-Piezoelectric Resonators

4.1 Raising Q of Piezoelectric Resonators

In pursuit of a solution for applications mandating low process temperature and high linearity, this section focuses on enhancing Q of piezoelectric resonators to achieve simultaneous high-Q and low impedance resonators. Plenty of researchers have recognized the adverse effects of metal electrodes on Q and sought to raise the Q's of thin-film piezoelectric resonators, with approaches that span from reducing electrode roughness [2], to optimizing the electrode material [3], to carefully balancing the AlN-to-electrode thickness ratio [4], to use of a Bragg reflector to prevent energy loss [5], none of the above methods raises the Q's of on-chip piezoelectric resonators anywhere near the >10,000 values needed for RF channel-selection and frequency gating spectrum analyzers.

Yet, polysilicon resonators easily achieve such Q values (but with higher than-desired impedances). To date, the measured Q's of polysilicon resonators are on the order of 20 times larger than that of sputtered AlN resonators at similar frequencies. Interestingly, material loss theory [6][7][8] predicts that the (f•Q) product limit due to (dominant) phonon-phonon interactions in the AlN material itself is less than two times lower than that of silicon, shown in Table 1. While the measured Q of silicon (either poly-silicon (e.g., Q=161,000 at 61.9 MHz [9]) or single-crystal silicon (e.g., Q=77,000 at 85.9MHz [10])) resonators have approached the theoretical value, Q's of AlN resonators demonstrated so far fall far behind the theoretical value.

Table 4-1: Material properties of doped silicon and aluminum nitride used for simulation of the theoretical phonon-phonon-limited damping coefficient and the corresponding material Q at 1GHz.

Parameter	Doped Si	AlN	Unit
Density, ρ	2330	3230	Kgm^{-3}
Specific Heat, C_V	$1.658x10^{6}$	$1.374x10^{6}$	$Jm^{-3}K^{-1}$
Thermal Conductivity, K	130	285	$Wm^{-1}K^{-1}$
Velocity of Longitudinal Wave, V_L	8387	10908	ms^{-1}
Velocity of Shear Wave, V_S	5830	5567	ms^{-1}
Debye Velocity, V_D	6337	6237	ms^{-1}
Thermal Relaxation Time, τ	$5.85x10^{-12}$	$1.64x10^{-11}$	s
Gruson number	1.054	1.236	—
Damping Coefficient, α_{p-p}	$4.64 x10^{-17}$	$4.86 x10^{-17}$	$m^{-1}s^{-2}$
Phonon-phonon limited material Q at 1 GHz	50,745	37,609	—

This large deviation is unlikely due to the difference between material properties of single-crystal AlN used for simulation and sputtered AlN used in the experiments, given the fact that the measured Q of a thickness-mode FBAR made of epitaxial single-crystal AlN deposited via MOCVD (Metalorganic Chemical Vapor Deposition) on SiC wafer at extremely high temperature (1200~1300°C) [11] is essentially the same Q, Q~1,000, as FBARs made of sputtered AlN. The only data point of high-Q MOCVD epitaxial AlN resonator is 21,000 measured at cryogenic temperature of 4K for a 82.585-MHz clamp-clamp beam resonator via magneto transduction [12], while Q at room temperature is unknown.

This suggests that the sputtered AlN material itself might not be the principal culprit among Q-limiting losses, but rather the metal electrodes or the electrode-to-resonator interface strain might be more responsible. In fact, experimental data shows that as the thickness of a piezoelectric resonator's electrode increases, both the resonance frequency and Q of the resonator drop due to mass loading and electrode loss, respectively [13]. Electrode-derived energy loss perhaps also contributes to the lower Q's measured in d_{31}-transduced AlN resonators, where the electrodes often cover locations with the maximum strain, versus the Q's of d_{33}-transduced thickness-mode resonators, where electrodes are placed very close to the nodes of the acoustic standing waves. Despite their lower Q's, d_{31}-transduced resonators are arguably more attractive than d_{33}, since their frequencies are set by CAD-definable lateral dimensions, so are more suitable for on-chip integration of multiple frequencies.

Whether a resonator uses d_{31} or d_{33}, both share the common problem that Q degrades as dimensions scale to achieve larger coupling and/or higher frequencies. In particular, while a piezoelectric structure can be scaled, its electrode thickness often cannot scale as aggressively, since doing so incurs excessive electrical loss derived from increased electrode and interconnect electrical resistance. If a designer attempts to compensate for this by using thinner, but wider, metal traces, then the beams supporting the resonator would need to be wider to accommodate the wider metal traces, and wider beams incur more energy loss through supports and anchors, hence lower Q. If the width of the support beams are decreased in order to reduce anchor losses and raise Q, the width of the metal traces must also be decreased, which then increases their resistance, again, lowering Q and negating the gains.

Admittedly, there are materials with higher predicted intrinsic material Q values, such as diamond [14] and SiC, which may be better candidates to serve extremely-high-Q demands (Q>100,000). However, those materials demand high temperature deposition steps and so are not CMOS compatible. On the other hand, AlN can be deposited at room temperature via reactive sputtering of a pure aluminum target in nitrogen. The measured Q's of low-temperature resonators capable of being built directly on CMOS with process temperature less than 400°C (i.e. without using silicon substrate as the resonator structure layer), either use purely back-end metal ([16], IBM process), ([17], AMS process), back-end metal and dielectric composite ([18], TSMC process) [19], sputtered titanium [20], AlSi 1% [21], or electroplated nickel resonators [22], are lower than 2,000, except for the work of disk and ring resonators made of electroplated Ni by Huang, *et. al*. [23][24]. Inspired by the theoretical prediction of Q values in Table 4-1, if there is a way to eliminate the adverse effects of metal electrodes, AlN is likely to provide a high Q and simultaneously low-impedance solution for low-temperature, CMOS-integration applications. The significance of eliminating electrode-associated losses to restore Q of thin-film piezoelectric resonators made of sputtered AlN thus transcends scientific interest and may offer practical value.

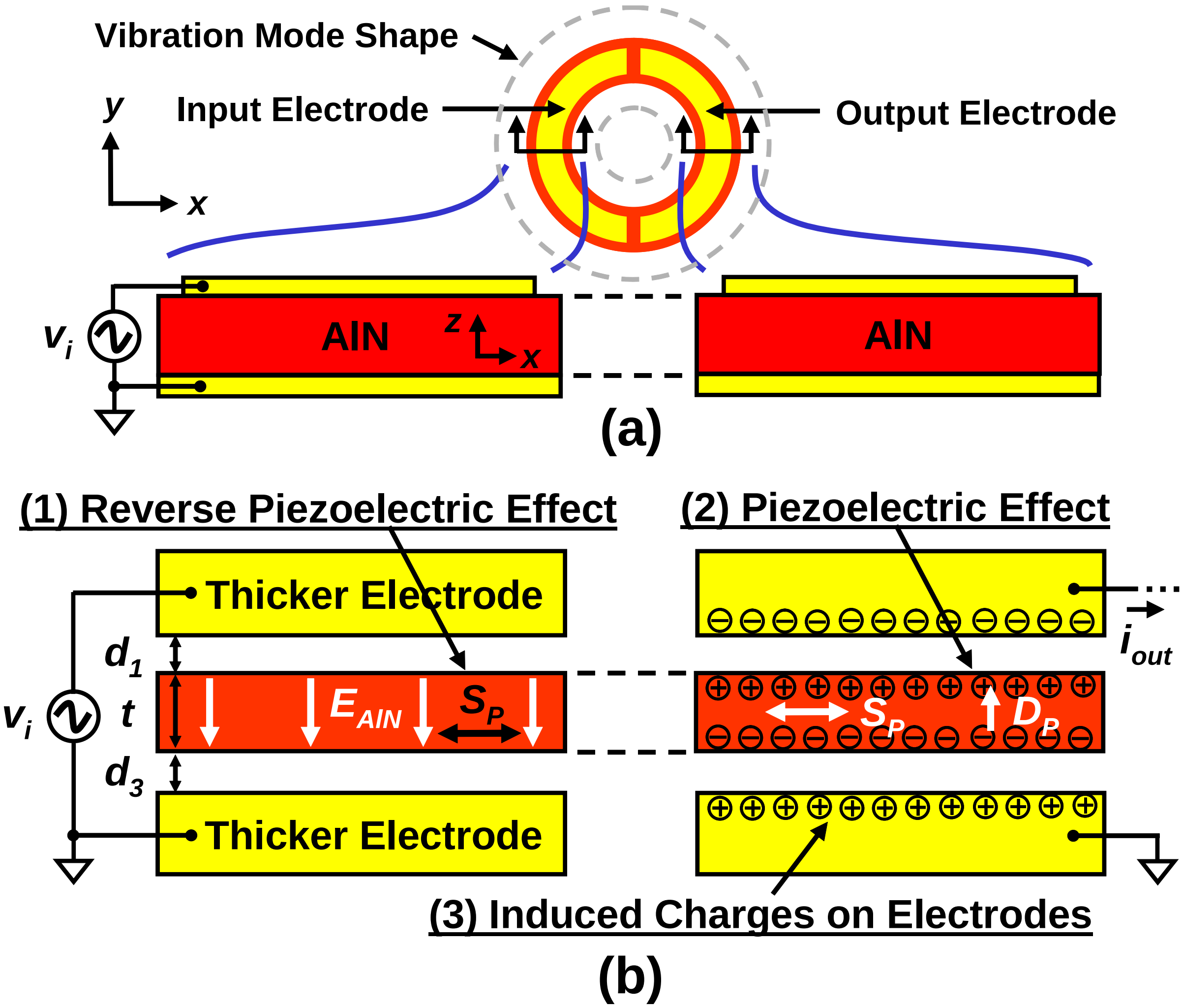

Fig. 4-1: (a) Conventional piezoelectric transducers employing electrodes that directly contact the piezoelectric structure (i.e. AlN film); and (b) working principal of a capacitive-piezo resonator for which electrodes are separated from the piezoelectric structure via small air gaps.

4.2 Capacitive-Piezoelectric Transducers

From the above discussion, it seems that *Q* degradation cannot be avoided as long as the electrode is in physical contact with the piezoelectric structure (which generates loss through strain coupling) and as long as the piezoelectric structure governs the size and thickness of the electrode (which governs electrical loss). To minimize the energy loss associated with electrodes and the resonator-electrode interfacial defects, researchers have used undoped AlGaAs for a piezoelectric resonator and doped AlGaAs with Si (AlGaAs:Si) for its electrodes to replace metals conventionally used in piezoelectric resonators, all of which are single-crystal deposited via MOCVD at 580°C, and have demonstrated *Q* of 25,390 at 21.77 MHz [25]. However, the process temperature is too high for on-chip integration. Interestingly, instead of using high-*Q* materials for the electrodes, all of these issues can be circumvented by mechanically decoupling

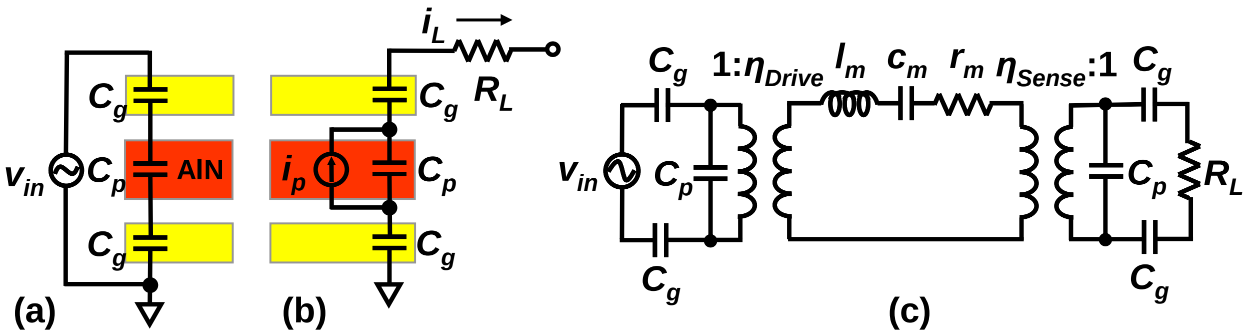

Fig. 4-2: Equivalent electrical circuit at (a) input and (b) output, modeling the effect of gap spacing on the electromechanical coupling coefficient; (c) equivalent circuit of a capacitive-piezo resonator.

the electrodes from the resonating body via separation of the electrodes from the vibrating structure so that they are no longer in contact, as shown in Fig. 4-1(b).

The working principal of the resulting transducer, dubbed the "capacitive-piezo" transducer, is similar to a conventional piezoelectric resonator: (1) on the input, voltage applied across two electrodes generates an electric field across the piezoelectric resonator, which induces mechanical strain via the reverse-piezoelectric effect; (2) on the output, the mechanical strain induces electrical displacement current D_z via the piezoelectric effect; (3) the equivalent bonded surface charge further induces charges of opposite sign on the electrodes separated by a gap.

The capacitive-piezo transducer should not only raise the Q of the piezoelectric film, but should also allow much thicker (and thus much less resistive) electrodes without the electrode loss and mass loading penalties that would otherwise result if the electrode is contacted as in Fig. 4-1(a). Thicker electrodes should also further increase the Q, since the electrode parasitic series resistance would be smaller.

Although not a well known technique, the use of contactless electrodes on piezoelectric resonators is actually not new. This strategy had in fact been demonstrated on 5- and 10-MHz quartz crystal resonators, called BVA resonators, as far back as 1977 [26]. Since the piezoelectric-to-electrode thickness ratio of these devices was on the order of 100μm-to-100nm, or 1000, separating the electrode from the piezoelectric did little to increase the Q of the device. It did, however, allow for a more stable device against drift, since it eliminates electrode-to-resonator stress variations over time [27]. This was the main reason for investigating such devices in the past.

For micromechanical resonators, on the other hand, the piezo-electric-to-electrode thickness ratio is much smaller, on the order of 10. Thus, the case for using a "capacitive-piezo" transducer is much stronger on the micro-scale. In addition, the ease with which small electrode-to-resonator gaps can be achieved via MEMS technologies further encourages the use of contactless electrodes. In effect, capacitive-piezo transducers stand to improve the Q and drift stability of micro-scale thin-film piezoelectric resonators with very little increase in fabrication cost.

4.3 Analytical Modeling

4.3.1 Electromechanical Coupling Coefficients

Electrical models for AlN contour-mode resonators with contacting electrodes are discussed in Chapter 1 and will not be repeated here. The present approach to modeling the capacitive-piezo resonator focuses on how electrode-to-resonator air gaps influence the electrical model parameters, specifically, the electromechanical coupling coefficients, η_{Drive} and η_{Sense} in Fig. 2(c), defined as

$$\eta_{Drive} = \frac{F(j\omega)}{V_{in}(j\omega)} \tag{4-1}$$

at the input (or 'driving' port), where $F(j\omega)$ is the generated modal force and $V_{in}(j\omega)$ is the input voltage across the top and bottom electrodes. Sinusoidal input is assumed through the entire analysis. η_{Drive} models how efficiently the energy in the electrical domain as a voltage input can be transduced into mechanical domain as a force driving the resonator to vibration, and

$$\eta_{Sense} = \frac{Q_P(j\omega)}{U(j\omega)} = \frac{\int_A D_z dA}{U(j\omega)} \tag{4-2}$$

at the output (or 'sensing' port), where Q_P is the total charge induced via the piezoelectric effect and equals the displacement current (charge/area), D_z, integrated over the electrode area; $U(j\omega)$ is the value of the maximum displacement. η_{Sense} models how efficiently the energy in the mechanical domain as displacement can be transduced into electrical domain as a current output.

When the input signal is applied across the top and bottom electrodes, mechanical strain, S_r, is induced on the AlN film via the reverse piezoelectric effect. The induced strain equals the product of the piezoelectric stress constant, e_{31} (e_{31}~0.7 C/m^2 for sputtered AlN), and the electric field established within the AlN film, E_{AlN}. The gap-AlN-gap stack can be modeled by three capacitors in series, as shown in Fig. 2(a), from which E_{AlN} can be written as

$$E_{AlN} = \frac{v_{in}}{H + \varepsilon_z d_{Total}} = \frac{v_{in}}{H} \cdot \alpha = E_{AlN, d_{Total}=0} \cdot \alpha \tag{4-3}$$

where ε_z (~9) and H are the relative permittivity in the c-axis direction and thickness of AlN, respectively; d_{Total} is the total gap spacing ($d_{Total}=d_1+d_3$); α is a function gauging how much the coupling coefficient degrades with increasing air gap spacing:

$$\alpha = \frac{H}{H + \varepsilon_z d_{Total}} \tag{4-4}$$

(4-4) shows that α is no larger than unity and α = 1with no air gaps, *i.e.*, $d_{Total} = 0$.

Fig. 4-4(a) plots α against gap spacing d on both sides for different piezoelectric materials with 1.5 µm thick piezoelectric resonator structure. To maximize E_{AlN} given a fixed input voltage, α must be maximized by utilizing small gaps and piezoelectric materials with low permittivity.

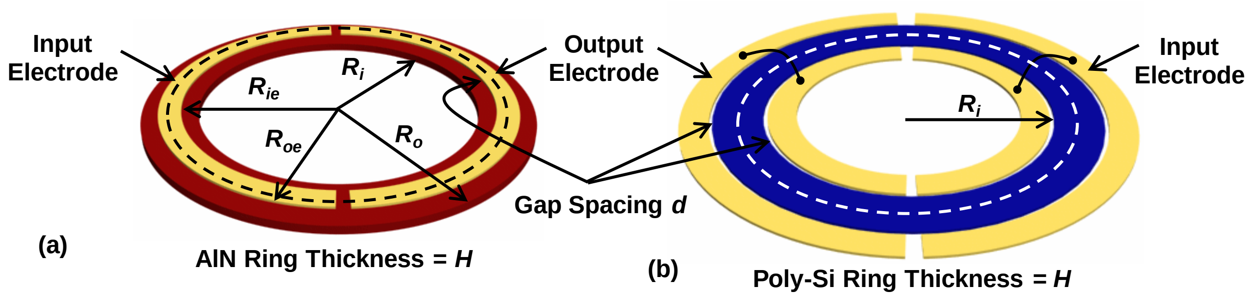

Fig. 4-3 : Electrode arrangement of (a) capacitive-piezo AlN ring resonator and (b) capacitive poly-Si ring resonator for the same mode shape with resonance frequency at 1.2 GHz.

When the input frequency matches the resonance frequency, the lateral force associated with the induced strain S_r excites the resonator into lateral-mode vibration, with the interested mode shape shown in Fig. 4-1. Note that for this particular mode shape, there is ideally no strain, stress, or displacement associated with the angular component. The generated modal force can be written as the product of the induced stress, T_r, the cross-sectional area normal to the stress, ($r\mathrm{d}r\mathrm{d}\theta$), and the normalized mode shape, $\Phi(r,\theta)$, together integrated over the electrode coverage area:

$$F = \int_0^{2\pi}\int_{R_{ie}}^{R_{oe}} T_r(Hrdrd\theta)\Phi(r,\theta) = (T_rH)\cdot\int_0^{2\pi}\int_{R_{ie}}^{R_{oe}} r\Phi(r,\theta)drd\theta \tag{4-5}$$

where R_{ie}, and R_{oe} are the inner and outer radius of the electrode, respectively, as indicated in Fig. 4-3(a). The distributed stress T_r is

$$T_r = E_P S_r = e_{31}E_z = e_{31}\left(\frac{V_{in}}{H}\cdot\alpha\right) \tag{4-6}$$

where E_P is the Young's modulus. The normalized mode shape is

$$\Phi(r,\theta) = \frac{\varphi(r,\theta)}{\int_{R_i}^{R_o}\varphi(r,\theta)dr} \tag{4-7}$$

where $\varphi(r)$ is the mode shape normalized to the maximum value (i.e. $\varphi(r)$<=1 for any r in the domain and $\varphi(r)$=1 at the largest displacement point). For a ring vibrating in the lateral direction, $\varphi(r)$ can be expressed as

$$\varphi(r,\theta) = \varphi_r(r)e_r + \varphi_\theta(r)e_\theta \tag{4-8}$$

where

$$\varphi_r(r,\theta) = \left\{A\frac{dJ_n(hr)}{dr} + B\frac{dY_n(hr)}{dr} + C\frac{n}{r}J_n(kr) + D\frac{n}{r}Y_n(kr)\right\}\cos(n\theta) \tag{4-9}$$

$$\varphi_\theta(r,\theta) = -\left\{A\frac{n}{r}J_n(kr) + B\frac{n}{r}Y_n(kr) + C\frac{dJ_n(hr)}{dr} + D\frac{dY_n(hr)}{dr} + \right\}\sin(n\theta) \tag{4-10}$$

where $J_n(x)$ and $Y_n(x)$ are the Bessel functions of the first kind and the second kind, respectively, and h and k are functions of resonant frequency defined as:

$$h = \omega_o \sqrt{\frac{\rho}{E_P(1-\sigma^2)}} \tag{4-11}$$

$$k = \omega_o \sqrt{\frac{\rho}{2E_P(1+\sigma)}} \tag{4-12}$$

where ω_o is the resonant angular frequency and ρ, σ, E_P are the AlN density, Poisson ratio, and Young's modulus, respectively.

The four unknown constants, A, B, C, D, can be obtained by applying the traction-free boundary conditions at the inner and outer radius of the ring

$$T_{rr}|_{r=r_i} = 0, \quad T_{rr}|_{r=r_o} = 0, \quad T_{r\theta}|_{r=r_i} = 0, \quad T_{r\theta}|_{r=r_o} = 0 \tag{4-13}$$

Eq. (4-13) represents four equations which can be written in a 4x4 matrix form

$$\begin{bmatrix} M_{11} & M_{12} & M_{13} & M_{14} \\ M_{21} & M_{22} & M_{23} & M_{24} \\ M_{31} & M_{32} & M_{33} & M_{34} \\ M_{41} & M_{42} & M_{43} & M_{44} \end{bmatrix} \begin{bmatrix} A \\ B \\ C \\ D \end{bmatrix} = \begin{bmatrix} 0 \\ 0 \\ 0 \\ 0 \end{bmatrix} \tag{4-14}$$

where

$$M_{11} = n(n-1)J(n,hr_i) - 0.5k^2r_i^2J(n,hr_i) + hr_iJ(n+1,hr_i) \tag{4-15-1}$$

$$M_{12} = n(n-1)Y(n,hr_i) - 0.5k^2r_i^2Y(n,hr_i) + hr_iY(n+1,hr_i) \tag{4-15-2}$$

$$M_{13} = n(n-1)J(n,kr_i) - nkr_iJ(n+1,kr_i) \tag{4-15-3}$$

$$M_{14} = n(n-1)Y(n,kr_i) - nkr_iY(n+1,kr_i) \tag{4-15-4}$$

$$M_{21} = n(n-1)J(n,hr_o) - 0.5k^2r_o^2J(n,hr_o) + hr_oJ(n+1,hr_o) \tag{4-15-5}$$

$$M_{22} = n(n-1)Y(n,hr_o) - 0.5k^2r_o^2Y(n,hr_o) + hr_oY(n+1,hr_o) \tag{4-15-6}$$

$$M_{23} = n(n-1)J(n,kr_o) - nkr_oJ(n+1,kr_o) \tag{4-15-7}$$

$$M_{24} = n(n-1)Y(n,kr_o) - nkr_oY(n+1,kr_o) \tag{4-15-8}$$

$$M_{31} = n(n-1)J(n,hr_i) - nhr_iJ(n+1,hr_i) \tag{4-15-9}$$

$$M_{32} = n(n-1)Y(n,hr_i) - nhr_iY(n+1,hr_i) \tag{4-15-10}$$

$$M_{33} = n(n-1)J(n,kr_i) - 0.5h^2r_i^2J(n,kr_i) + kr_iJ(n+1,kr_i) \tag{4-15-11}$$

$$M_{34} = n(n-1)Y(n,kr_i) - 0.5h^2r_i^2Y(n,kr_i) + kr_iY(n+1,kr_i) \tag{4-15-12}$$

$$M_{41} = n(n-1)J(n, hr_o) - nhr_o J(n+1, hr_o) \tag{4-15-13}$$

$$M_{42} = n(n-1)Y(n, hr_o) - nhr_o Y(n+1, hr_o) \tag{4-15-14}$$

$$M_{43} = n(n-1)J(n, kr_o) - 0.5h^2 r_o^2 J(n, kr_o) + kr_o J(n+1, kr_o) \tag{4-15-15}$$

$$M_{44} = n(n-1)Y(n, kr_o) - 0.5h^2 r_o^2 Y(n, kr_o) + kr_o Y(n+1, kr_o) \tag{4-15-16}$$

For a ring vibrating at the 2nd contour mode (anti-symmetric mode), n=0 in (4-9) and (4-10), such that all terms related to the tangential direction, θ, become zero (i.e. the displacement is independent of θ). The following analysis focuses on this particular mode shape.

The modal force F and η_{Drive} can therefore be found by plugging (4-7) and (4-6) into (4-5) and further into (4-1):

$$F = \alpha \cdot e_{31} \cdot v_{in} \cdot 2\pi \int_{R_{ie}}^{R_{oe}} r\Phi(r)dr \tag{4-16}$$

$$\eta_{Drive} = \alpha \cdot e_{31} \cdot 2\pi \int_{R_{ie}}^{R_{oe}} r\Phi(r)dr \tag{4-17}$$

(4-17) indicates two interesting facts. First, η_{Drive} is proportional to both e_{31} and α, which is a function of the permittivity ε_z. The optimized piezoelectric materials require high e_{31} and low permittivity at the same time to achieve high electromechanical coupling coefficient. This is a distinct feature of capacitive-piezoelectric versus piezoelectric transducers. Fig. 4-4(a) plots the (e_{31} • α) product against total gap spacing, d_{Total}, for different piezoelectric materials. In general, small gap spacing is preferred to maintain a high coupling coefficient. It should be noted that a large e_{31} does not guarantee a large coupling coefficient. As shown in Fig. 4-4(b), even though PZT has a larger e_{31} than AlN and ZnO, its capacitive-piezo coupling is weaker at most gap spacings due to its much higher relative permittivity.

The electrode configuration affects η_{Drive} via the last term in (4-17). Given the same electrode area and the static capacitance, coupling coefficient η_{Drive} is maximized by placing electrodes on large displacement areas. This however degrades Q with larger energy dissipation due to larger strain at the electrode/resonator interface and larger strain coupled to the electrodes.

On the sense side, vibration-induced strain polarizes the AlN film via the piezoelectric effect, and the resulting electric displacement (charge per area) can be expressed as (with displacement only in the radius direction)

$$D_z = e_{31} S_{r,Sense} = e_{31}\left[\frac{\partial u_r}{\partial r} + \frac{u_r}{r}\right] \tag{4-18}$$

where $u_r(r,j\omega)$ is the time-varying mechanical displacements in the radius direction as a function of position r and can be decomposed into the product of a time-varying function $U(j\omega)$ and the stationary mode shape

$$u_r(r, j\omega) = U(j\omega)\varphi(r) \tag{4-19}$$

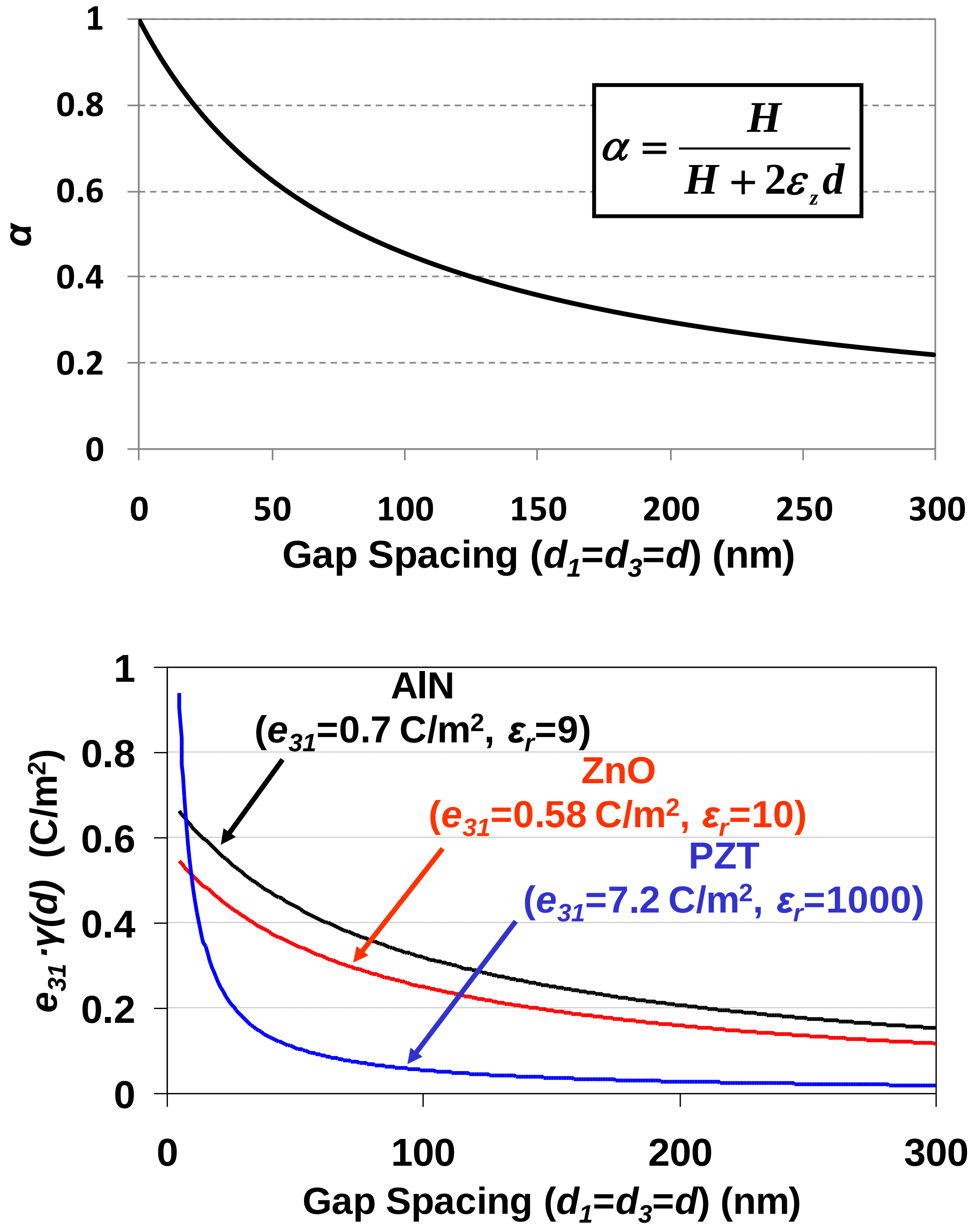

Fig. 4-4: (a) Plot of α versus gap spacing (on each side) according to (4-4). The induced electrical field within AlN film decreases by a factor of α with air gaps between the electrodes and the resonator structure. The equivalent electromechanical coupling coefficients and static capacitance on both input and output ports are all linear functions of α, therefore functions of gap spacing. (b) The effective e_{31} on the drive side decreases as the gap spacing increases. The gap spacing affects the coupling of PZT the most due to its much larger relative permittivity ε_r.

Integration of D_z over the electrode area gives the total induced charge, Q_P

$$\begin{aligned} Q_P &= \int_0^{2\pi} \int_{Rie}^{Roe} D_z r dr d\theta \\ &= 2\pi e_{31} U(j\omega) \int_{Rie}^{Roe} \left(r \frac{\partial \varphi(r)}{\partial r} + \varphi(r) \right) dr \end{aligned} \tag{4-20}$$

η_{Sense} can therefore be found by plugging (4-20 into (4-2):

$$\eta_{Sense} = 2\pi e_{31} \int_{Rie}^{Roe} \left(r \frac{\partial \varphi(r)}{\partial r} + \varphi(r) \right) dr \tag{4-21}$$

The time derivative of Q_P becomes the output current i_p. The piezoelectric effect on the sense side can thus be modeled by a current source with magnitude $i_p = \omega \bullet Q_P$ as shown in Fig. 4-2(b), and the output current, i.e., the current flowing though R_L (R_L =50 Ω for measurement with a network analyzer), becomes

$$i_O = i_P \cdot \frac{Z_P}{Z_P + Z_g + Z_g + R_L} \approx i_P \cdot \frac{t}{t + \varepsilon_r (d_1 + d_2)} = i_P \cdot \alpha \tag{4-22}$$

The parameter α can be absorbed into η_{Drive} to give a symmetric circuit shown in Fig. 4-2(c):

$$\eta_{Sens,eq} = \alpha \cdot e_{31} \cdot 2\pi \int_{Rie}^{Roe} \left(r \frac{\partial \varphi(r)}{\partial r} + \varphi(r) \right) dr \tag{4-23}$$

$\eta_{Sense,eq}$, the same as η_{Drive}, is proportional to e_{31} and α. The impedance of the resonator can therefore be calculated according to

$$R_x = \frac{r_m}{\eta_{Sense} \eta_{Drive}} \tag{4-24}$$

where r_m is the mechanical damping and is defined as

$$r_m = \frac{\omega_o m_r}{Q} = \frac{\omega_o l_m}{Q} \tag{4-25}$$

where ω_o is the resonant angular frequency, m_r the effective mass, with value equivalent to l_m in Fig. 4-2(c).

Even though the coupling coefficients are each reduced by a factor of α compared to those of contacting electrodes from (4-17) and (4-23), the impedance is not necessary lager. In fact, according to (4-24) and (4-25), it is possible to obtain lower impedance with capacitive-piezo transducers via lower mechanical damping r_m with enhanced Q, if the increase in Q is larger than α^2.

From (4-17) and (4-23), neither of the electromechanical coupling coefficients is a function of resonator thickness. In fact, thinner AlN structures offer the benefit of lower impedance due to a reduction of effective mass m_r and therefore the damping r_m according to (4-24) and (4-25). This is a distinct feature of capacitive-piezo lateral-mode resonators compared to capacitive

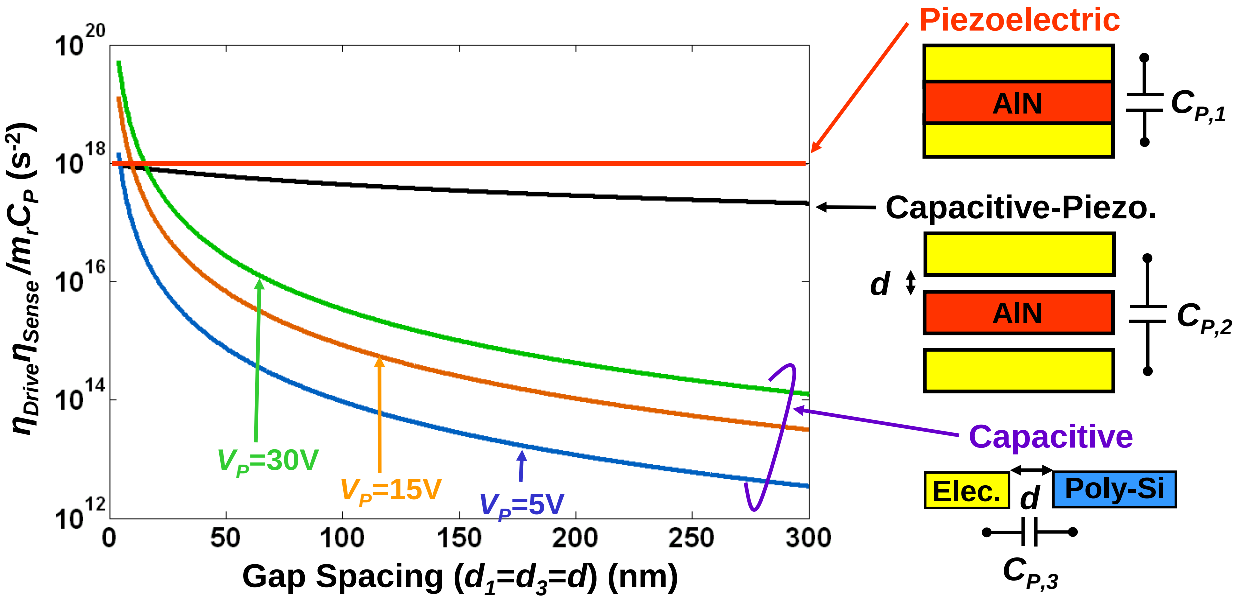

Fig. 4-5: Comparison of filter FOM of capacitive with V_P of 5 V to 30 V, piezoelectric, and capacitive-piezo transducers as a function of gap spacing, given the same filter bandwidth and type. Capacitive-piezo transducers equipped with small gaps maintain high filter FOM as piezoelectric ones, both filter FOMs are orders of magnitude higher than the case of capacitive transducers. At V_P=30 V, capacitive transducer has larger filter FOM when the gap is scaled below 20 nm.

ones, where in the latter the coupling coefficients are proportional to the resonator thickness such that a thinner resonator structure increases the impedance linearly. The benefit of scaling piezoelectric resonator thickness emphasizes the need for separating electrodes as the electrode-to-resonator volume increases with a thinner resonator.

Moreover, both η_{Sense} and η_{Drive} are functions of the gap spacing through α. Although air gaps degrade effective coupling efficiency k^2_{eff} by a factor of α^2, the higher Q provided by non-contacting electrodes together with sufficiently small gap spacings actually make it possible to achieve higher Q• k^2_{eff} than piezoelectric resonators with contacting electrodes.

Perhaps the best way to compare different transducers is via the filter FOM previously defined in Chapter 2 (2-7), repeated here

$$FOM = \frac{1}{R_Q C_o} \propto \frac{\eta_{Drive}\eta_{Sense}}{m_r C_o} \tag{4-26}$$

where R_Q is the filter termination resistor, C_o the static input capacitance, and m_r the motional mass of a constituent resonator in the filter. The right most form delineates parameters in the expanded equation most relevant to resonator design.

Fig. 5 compares simulated plots of ($\eta_{Drive}\eta_{Sense,eq}/m_rC_o$) in the filter FOM for three different transducers (i.e. piezoelectric, capacitive-piezo, and capacitive alone) versus gap spacing d at the same frequency. The simulation uses a ring inner radius and thickness of 25.6 μm and 1.5 μm, respectively; and ring widths of 5 μm for AlN and 4.3 μm for polysilicon, both chosen to achieve a 1.2-GHz resonance frequency for both materials under the same mode shape, neglecting DC bias-induced electrical spring softening inherent to capacitive resonators. In addition, the electrodes for the polysilicon resonator are assumed to be placed both inside and outside the ring, similar to [1] and plotted in Fig. 3(b). As expected, the FOM of the capacitive-piezo transducer depends on gap spacing, but not as strongly as one might think, mainly because C_o drops by the same ratio α as the electromechanical coupling coefficient when the gap spacing increases. Even so, a capacitive-piezo transducer with a 200 nm gap spacing achieves a filter FOM of $2.7\text{x}10^{17}$ s^{-2}, for which a capacitive (alone) transducer with dc bias of 15V (V_P=15V) would require a much smaller gap spacing of 23 nm. This relaxed gap spacing is a distinct advantage of capacitive-piezo transducers over capacitive ones. At V_P=30V, the capacitive transducer has a larger filter FOM when the gap is scaled below 20 nm.

4.3.2 Frequency Shift and k^2_{eff}

This section focuses on a pure circuit method to investigate how gap spacing affects the resonant frequency and the electromechanical coupling coefficients, reaching the same result as the mechanical analysis in the previous section. Fig. 4-6(a) shows a typical BVD model for a resonator with two capacitors, C_{g1} and C_{g2}, representing capacitance contributed by air-gaps in series to input/output ports and a parasitic capacitance C_p shunting to the ground. C_{g1} and C_{g2} can be absorbed into the resonator branches to form an equivalent BVD model, shown in Fig. 4-6(b), with modified component values

$$\boldsymbol{L_x^{'} = L_x \cdot \left(\frac{C_g + C_o}{C_g} \right)^2} \tag{4-27}$$

$$C_x^{'} = C_x \cdot \left(\frac{C_g^2}{(C_g + C_o)(C_g + C_o + C_x)} \right) \tag{4-28}$$

$$R_x^{'} = R_x \cdot \left(\frac{C_g + C_o}{C_g} \right)^2 \tag{4-29}$$

where C_g is the total capacitance contributed by the air gaps on both sides:

$$C_g = \frac{C_{g1} \cdot C_{g2}}{C_{g1} + C_{g2}} \tag{4-30}$$

The last term in (4-*29*) is essentially α^{-2}, which says that the addition of air gaps increases the impedance by α^{-2}. This is the same result as (4-17) and (4-23), where the equivalent electromechanical coupling coefficients on both the input and output each contributes a degradation ratio of α.

The series resonant frequency of Fig. 4-6(b) is

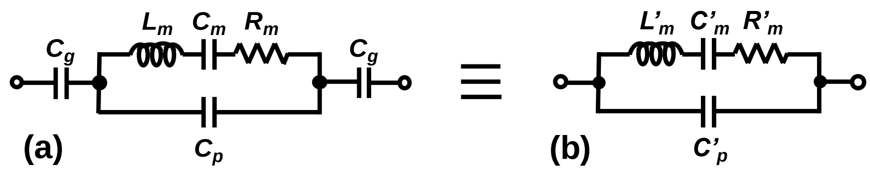

Fig. 4-6: Plot of a circuit method to show how air gaps affect both series and parallel resonance frequencies and equivalent coupling coefficient. (a) a BVD model with two series capacitors, C_{g1} and C_{g2}, representing air gaps on both input and output of the resonator; (b) equivalent BVD model by absorbing C_{g1} and C_{g2} into the resonator branches.

$$f_s^{'} = \frac{1}{2\pi}\sqrt{\frac{1}{L_x^{'}C_x^{'}}} = \frac{1}{2\pi}\sqrt{\frac{1+\dfrac{C_x}{C_o+C_g}}{L_xC_x}} = f_s \cdot \sqrt{1+\frac{C_x}{C_o+C_g}} \tag{4-31}$$

The series resonant frequency increases with the addition of air gaps. This upward frequency shift comes from frequency-dependent impedance change on the signal path in the electrical domain and should be considered separately from the frequency shift due to elimination of electrode mass loading, which modifies the equivalent mass and stiffness of the resonator in the mechanical domain. In fact, connecting a variable capacitor with a mechanical resonator is a well-known technique to tune the mechanical resonator frequency [28].

When considering parallel resonance frequency, air-gap capacitor C_g is essentially in series with the parasitic capacitance C_p, which originates mostly from interconnects and bonding pads.

$$f_p^{'} = \frac{1}{2\pi}\sqrt{\frac{1+\dfrac{C_x}{C_o+\dfrac{C_gC_p}{C_g+C_p}}}{L_xC_x}} \tag{4-32}$$

The parallel resonant frequency decreases with air gaps compared to that of a resonator with contacting electrodes (i.e. C_p becomes infinity in (4-32)),

The effective electromechanical coupling coefficient, k'^2_{eff}, can be calculated by plugging (4-31) and (4-32) into

$$k_{eff}^{'2} = \frac{\pi^2}{4}\cdot\frac{f_p^{'}-f_s^{'}}{f_p^{'}} \tag{4-33}$$

and rearranging into

$$k_{eff}^{'2} = k_{eff}^{2}\cdot\frac{C_g}{C_g+C_o}\cdot\frac{C_g}{C_g+C_p}\cdot\frac{C_o+C_p}{C_o+C_gC_p/(C_g+C_p)} \tag{4-34}$$

where k^2_{eff} is the effective electromechanical coupling coefficient without gap spacing (i.e. with C_g approaching infinity). When the parasitic capacitance C_P is minimized such that $C_P << C_g$, the

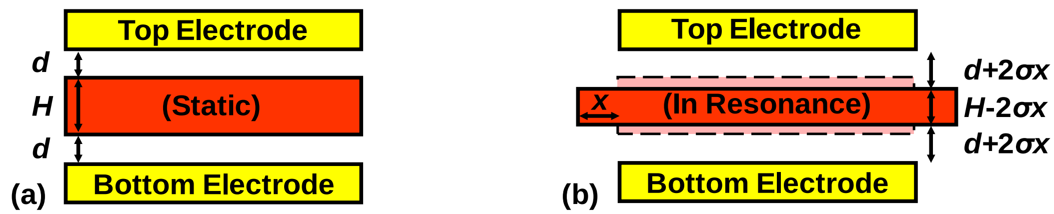

Fig. 4-7: Cross-section of a capacitive-piezo resonator (a) before deformation and (b) after deformation, showing how gap spacing is modulated by lateral vibration amplitude x during the Poisson ratio σ.

last two terms in (4-34) become unity. Therefore,

$$k_{eff}^{'2} = k_{eff}^{2} \cdot \frac{C_g}{C_g + C_o} = k_{eff,o}^{2} \cdot \alpha \tag{4-35}$$

The result in (4-35) is not surprising because both the FOM described in (4-26) and k^2_{eff} defined in (4-33) gauge the 'bandwidth' of a micromechanical resonator, though their absolute values are not the same.

Admittedly, capacitive-piezo transducers trade effective electromechanical coefficient for higher Q. The good news is that the trade is not a one-to-one ratio. Specifically, the theoretical prediction posts the Q ceiling of a AlN resonator to be ten to twenty times higher than the current measurement data, while α is 0.45 for gap size of 100 nm and can be increased to 0.625 for 50 nm, as shown in Fig. 4(a). Note that losses associated with electrodes can be eliminated as long as the strain is not coupled to the electrodes, regardless the gap size. Therefore, capacitive-piezo transducers are likely to give the higher ($k^2_{eff} \cdot Q$) product.

(4-34) also indicates that for capacitive-piezo transducers, it is important to minimize parasitic capacitance to ensure the condition C_P<<C_g holds such that k'^2_{eff} differs from k^2_{eff} only by a factor α.

4.3.3 Linearity (P_{IIP3})

The addition of air gaps introduces a more dominating nonlinearity factor into the transduction process than the nonlinearity of AlN material identified as the main contribution of nonlinearity in other piezoelectric resonators without air gaps. The following analysis estimates the degree of nonlinearity introduced by the air gaps. As the resonator is vibrating in the lateral mode, the gap spacing is modulated by the lateral mechanical displacement, x, via the Poisson ratio σ, as shown in Fig. 4-7. The total induced force with gap spacing modulation is obtained by modifying α in (4-16):

$$F_{Total} = v_{in} \cdot \beta \cdot \frac{(H - 2\sigma x)}{(H - 2\sigma x) + 2\varepsilon_r (d + \sigma x)} \tag{4-36}$$

where σ is the Poisson ratio; to simplify the expression, parameters independent of x have been lumped into one parameter β defined as

$$\beta = 2\pi e_{31} \int_{R_{ie}}^{R_{oe}} r\Phi(r)dr \tag{4-37}$$

Here, a time-varying, position-independent lateral mechanical displacement amplitude, $x(j\omega)$ is used instead of $u_r(r,j\omega)$ defined in (4-19) to simplify the equation. Using Taylor expansion, (4-36) becomes

$$F_{Total} = v_{in}(j\omega)\cdot\beta\cdot\alpha\cdot\left\{1-\left(\frac{2\sigma\varepsilon_r x(j\omega)}{H+2\varepsilon_r d}\right)+\frac{1}{2}\left(\frac{2\sigma\varepsilon_r x(j\omega)}{H+2\varepsilon_r d}\right)^2-\cdots\right\} \tag{4-38}$$

The first term is the fundamental response; the second and the third terms are the sources of intermodulation forces, F_{IM2} and F_{IM3}, respectively, when the input signal contains interferences at frequencies spaced equally from each other and from the center frequency of the resonator. Specifically, when the input signal is

$$v_{in} = v_o\cdot\cos(\omega_1 t+\phi_1)+v_o\cdot\cos(\omega_2 t+\phi_2) \tag{4-39}$$

where

$$\omega_1 = 2\pi(f_o-\Delta f)\ ;\ \omega_2 = 2\pi(f_o-2\Delta f) \tag{4-40}$$

where f_o is the resonance frequency and Δf is the frequency difference. The mechanical displacement x also contains terms at both frequencies ω_1 and ω_2

$$x = X_1\cdot\cos(\omega_1 t+\phi_1)+X_2\cdot\cos(\omega_2 t+\phi_2) \tag{4-41}$$

The amplitude X_1 and X_2 are related to the input signal via

$$X_{1,2}(j\omega)=\frac{F}{k_{re}}\cdot\Theta(\omega)=v_{in}\cdot\beta\cdot\frac{1}{k_{re}}\cdot\frac{H}{H+2\varepsilon_r d}\cdot\Theta_{1,2} \tag{4-42}$$

where Θ_1 and Θ_2 are the biquad systems transfer functions of two interferer signals, defined as

$$\Theta_{1,2}(j\omega)=\left[1-\left(\frac{\omega_{1,2}}{\omega_o}\right)^2+\left(\frac{j\omega_{1,2}}{Q\cdot\omega_o}\right)\right]^{-1} \tag{4-43}$$

The 3rd-order intermodulation force F_{IM3} can be found by plugging (4-41) and (4-39) into the third term of (4-38) and selecting the terms with frequency component equaling to f_o

$$F_{IM3}=(v_o\alpha\beta)^3\cdot\left(\frac{2\varepsilon_r\sigma}{k_{re}(H+2\varepsilon_r d)}\right)^2\cdot\gamma \tag{4-44}$$

where

$$\gamma=\left(\frac{1}{2}\Theta_1\Theta_2+\frac{1}{4}\Theta_1^2\right)\cdot\cos(2\omega_1 t-\omega_2 t+2\phi_1-\phi_2) \tag{4-45}$$

To compare the linearity performance of capacitive-piezo versus capacitive transducers, it is useful to compare P_{IIP3} value. At this extrapolated input power, the 3rd intermodulation component of the total generated force in a two-tone test has the same value as the linear force component. The required input voltage amplitude, V_{IIP3}, can be found by equating F_{IM3} in (4-44) to F in (4-16) and solve for v_o:

$$V_{IIP3}=\frac{k_{re}(H+2\varepsilon_r d)}{2\eta_{Drive}\varepsilon_r\sigma}\cdot\left(\frac{1}{2}\Theta_1\Theta_2+\frac{1}{4}\Theta_1^2\right)^{-1/2} \tag{4-46}$$

As expected, the expression of V_{IIP3} only contains the electromechanical coupling coefficient on the drive side, regardless of how the output signals are sensed on the sense side. P_{IIP3} can then be written as

$$P_{IIP3}(dBm)=10\cdot\log_{10}\left(\frac{V_{IIP3}^2}{1000\cdot R_x}\right) \tag{4-47}$$

Fig. 4-8 compares P_{IIP3} of AlN and poly-Si ring resonators with the same dimensions as those considered earlier for FOM comparison. Here, Q=3,073 are assumed for both resonators and V_P=25V for the capacitive resonator. P_{IIP3} (in dBm) of capacitive-piezo resonators degrades with decreasing gap spacing by $(H+2\varepsilon_z d)^2$, while P_{IIP3} of capacitive resonator, according to the equations derived in [29], is affected by the gap spacing up to 7th power, which is responsible for the lower P_{IIP3} value and a sudden drop once the gap spacing is scaled down to 50nm or less. At V_P=25 V and d=18 nm, both resonators give R_x~80 Ω but the capacitive-piezo resonator offers 39dB higher P_{IIP3} than the capacitive resonator. It should be noted that capacitive-piezo resonators utilize the high coupling nature of piezoelectric resonators to eliminate the need for deep-submicron gap spacing as required by capacitive resonators to obtain low impedance. The relaxed gap spacing facilitates fabrication and linearity requirement.

Moreover, the fact that AlN is a dielectric material with large dielectric strength (100 MV/µm) and that no DC voltage is required for normal operation spares capacitive-piezo resonators the catastrophic failure mechanism inherent to capacitive resonators, whereby DC bias across the electrode and conductive resonator structure generates large current when they touch each other upon application of large driving force and permanently fuses the resonator and the

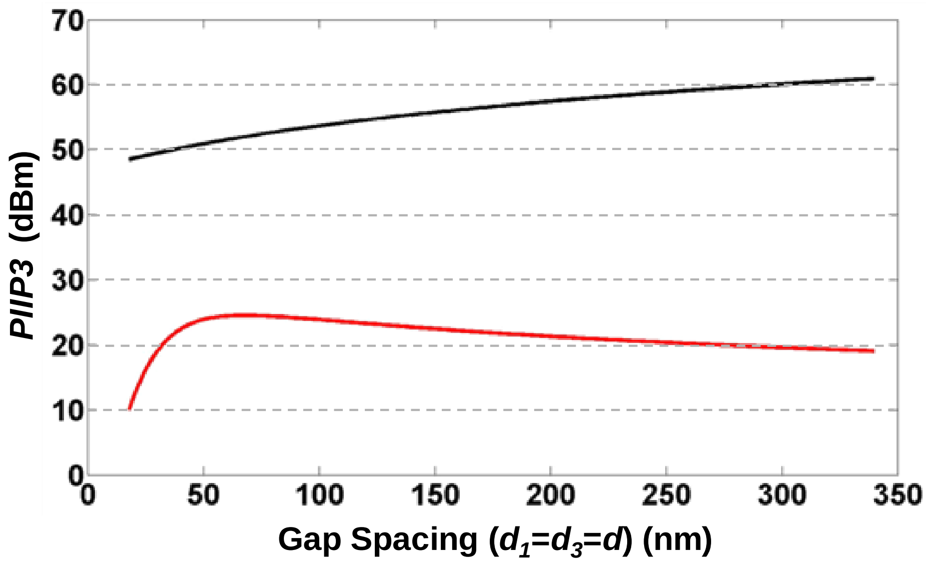

Fig. 4-8: Simulated PIIP3 (in dBm) of capacitive and capacitive-piezo transducers versus gap spacing d on each side. The latter has much larger PIIP3 given the same gap spacing.

electrodes. Overall, addition of small air gaps to the traditional piezoelectric resonators offers benefits of higher *Q* and possibly better long-term stability without suffering from linearity or catastrophic failure as encountered by capacitive resonators.

4.4. Fabrication Process

4.4.1 Overall Fabrication Flow

AlN resonators employing capacitive-piezo transducers were fabricated using a newly-developed 6-mask low-temperature CMOS-compatible process summarized in Fig. 4-9. This section walks through the fabrication flow step-by-step and the following sections provide more details on some critical steps. Here, 250 nm oxide and 200 nm nitride as isolation layers are first deposited on 6" high-resistance wafers, followed by lift-off of 30 nm aluminum and 60 nm nickel, both deposited by evaporation, as interconnections and bottom electrodes (step #1). This Ni layer will later serve first as an etch stop for patterning the structural layer and second as a seed layer for electroplating the Ni anchor. The lift-off process uses two photoresist layers (I-line resist on LOR3A) to realize fine Ni/Al features with smooth edges critical to AlN quality, as shown in Fig. 4-12(b). The relatively thin bottom electrodes and interconnects here is a compromised design to ensure good sputtered AlN quality and thin sacrificial molybdenum step coverage in the following steps. A planarization step incorporated into the fabrication will allow for thicker bottom electrodes and interconnects and further reduce the parasitic resistance.

To fully take advantage of capacitive-piezo transducers, 250nm molybdenum is then sputtered at 200 °C to serve as the sacrificial layer. Sputtered molybdenum is used instead of more common sacrificial materials such as oxide, silicon, or germanium to attain better c-axis orientation of the sputtered AlN film. Next, molybdenum is patterned into patches covering each individual device to further improve AlN quality (step #2 in Fig. 4-9). Reactive puttering of AlN directly on molybdenum renders films of very high tensile stress (>500MPa). After patterning molybdenum into patches with only ~5um distance between each molybdenum patch (*i.e.*, molybdenum still covers ~99% of the entire wafer area), AlN can be sputtered on molybdenum with low stress (< ±50MPa) and high FWHM (~1.7°). After sputtering 1.5 μm AlN, several layers are sputtered in sequence: 250 nm molybdenum as a second sacrificial layer between the resonator and the top electrode, 400 nm aluminum as the top electrode, 20 nm molybdenum as a barrier layer between aluminum and oxide, and lastly, 1.2 μm PECVD oxide deposited at 300 ˚C to serve as a hard mask, yielding the cross-section of (step #3). The 20nm molybdenum between aluminum and oxide first prevents aluminum from reacting with PECVD oxide during deposition, and second, prevents the remaining oxide mask from contacting the top electrode after release, which may degrade *Q*. Figs. 4-10(a) and (b) show photos after blanket PECVD oxide deposition on blanket 120nm-thick aluminum with patterned titanium electrodes and blanket AlN underneath, with and without 20 nm thick Mo as a barrier layer between aluminum and oxide layers, respectively. It clearly shows that aluminum surface becomes rough after oxide deposition. Note that, unlike piezoelectric resonators with contacting electrodes, the roughness on the aluminum electrodes' top surfaces will not affect *Q* of the capacitive-piezo resonators, as the electrodes are separated from the resonant body. However, the smooth surface is critical to facilitate lithography resolution and etching for 1μm-thin beams.

The oxide mask is then patterned using a CF_4/CHF_3 RIE that stops on the 20 nm molybdenum barrier layer (step #4), followed by dry etch of the film stack of Mo/Al/Mo/AlN without breaking vacuum (step #5). By tuning the process gas ratios (Cl_2, BCl_3, O_2), high etch selectivity is achieved among different thin films, which is critical to the following steps of this process.

Anchors are formed by refilling trenches with conductive materials. Instead of depositing a conformal layer followed by etching (the 'top-down' approach), which usually requires evaluated temperatures, electroplating (the 'bottom-up' approach) is a low-temperature solution for refilling high-aspect-ratio trenches. To prepare the wafer for electroplating, 20 nm molybdenum is sputtered to electrically connect the whole wafer by connecting the individual molybdenum patches (step #6). This sputtering is performed at a lower chamber pressure (3 mTorr) to prevent sidewall coverage. After patterning thick photoresist, molybdenum within the trenches is dry etched to expose Ni on interconnects (step #7) and the nickel anchor is electroplated from the underlying nickel seed layer at 60 °C (step #8). For resonator arrays, filters, and wine-glass disk resonators, another lithography and etch step is used to remove oxide/molybdenum/aluminum from coupling beams and disk areas without electrodes (step #8, step #9, and step #10). After a simple lithography step to cover the exposed isolation oxide/nitride layers with photoresist, the thin molybdenum layer and the remaining oxide mask are removed by dry etching (step #10), and the device is released in XeF_2/N_2 mixed gases. After sacrificial molybdenum is completely etched, both the top electrode and the AlN ring are entirely suspended from each other and supported via the nickel anchor (step #11). Contactless electrodes eliminate the need for bimorph films (*i.e.*, contacting electrode-AlN films) required in conventional piezoelectric resonators and avoid issues commonly associated with bimorph films, such as warping, stress relaxation, and film lamination. XeF_2 etches molybdenum selectively over aluminum, nickel, and AlN.

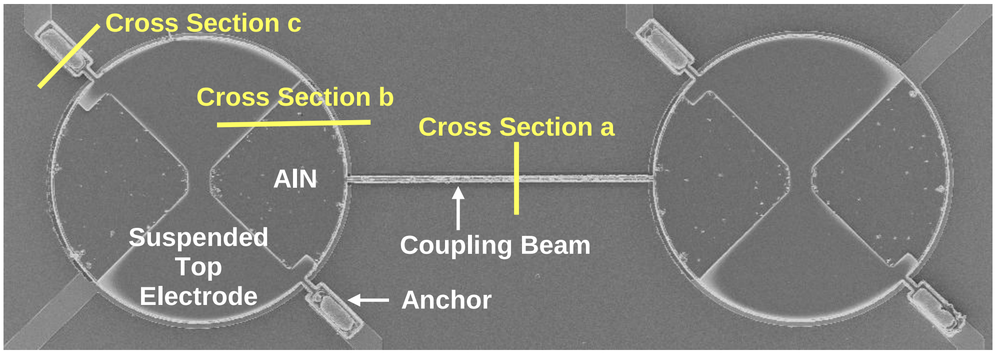

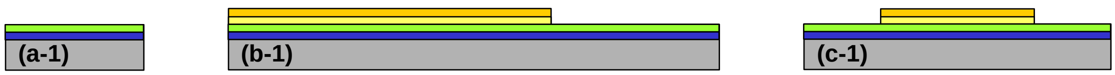

(1) Deposit 250nm-oxide/200nm-nitride isolation layer and lift off 30nm-Al/70nm-Ni as the bottom electrodes and interconnection layers with I-line PR and LOR3A (mask-1).

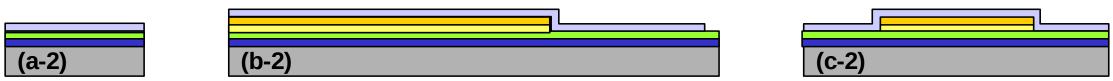

(2) Sputter 250nm molybdenum. Pattern (mask 2) I-line PR and wet etch in pre-mixed aluminum etchant at 50°C. Strip PR.

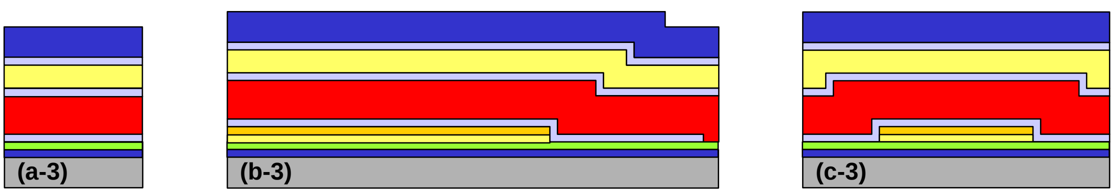

(3) Sputter the following thin films in sequence: 1.5 µm AlN, 250 nm molybdenum, 400 nm aluminum, and 20 nm molybdenum. Finally, deposit 1.2 µm PECVD oxide at 300°C.

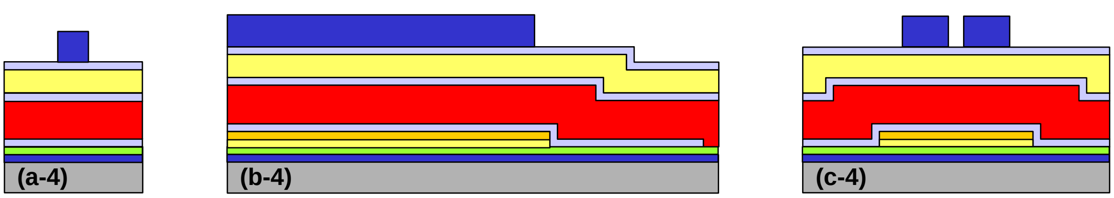

(4) Pattern (mask 3) I-line PR. Dry etch oxide in CF_4/CHF_3 gas. Etch stops on molybdenum. Strip PR.

Fig. 4-9: A WGD resonator array with the fabrication process of each cross-section depicted blow. a: areas without top electrodes, such as coupling beam of resonator arrays and filters; b: edges of the disk and areas with part of the top electrodes removed; c: anchors.

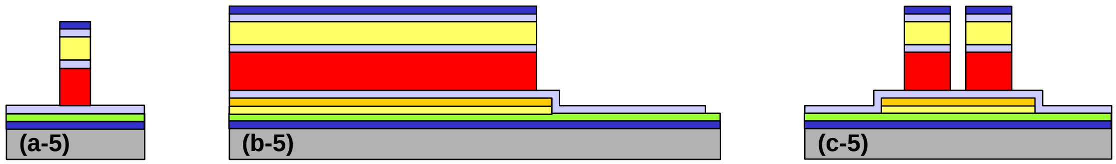

(5) Use the oxide as hard mask to dry etch molybdenum/aluminum/molybdenum/AlN, all with chorine based chemistry but different recipes. Etch stops on molybdenum.

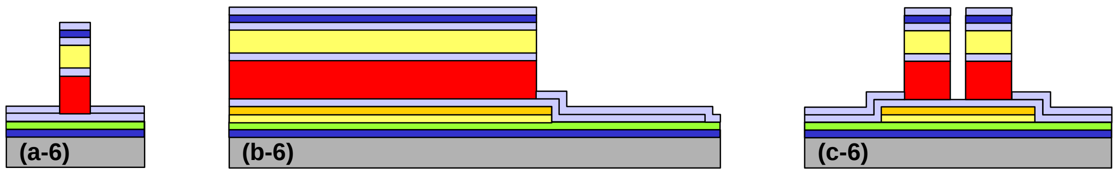

(6) Sputter 20nm molybdenum at low pressure (3 mTorr) to electrically connect the whole wafer for electroplating. This sputter step is done at low pressure to prevent molybdenum deposited on the side-walls and within the trenches.

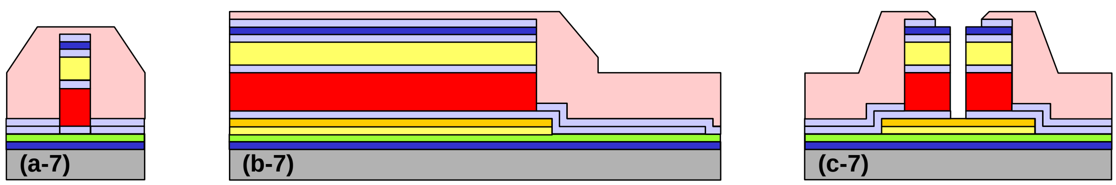

(7) Pattern (mask 4) thick PRS 220 and dry etch molybdenum within the trenches to expose the underlying nickel seed layer for nickel electroplating. Strip remaining PR. Need to repeat twice to etch through the molybdenum layer as the molybdenum dry etch process, which is mixed O_2 and Cl_2, gives little selectivity to PR.

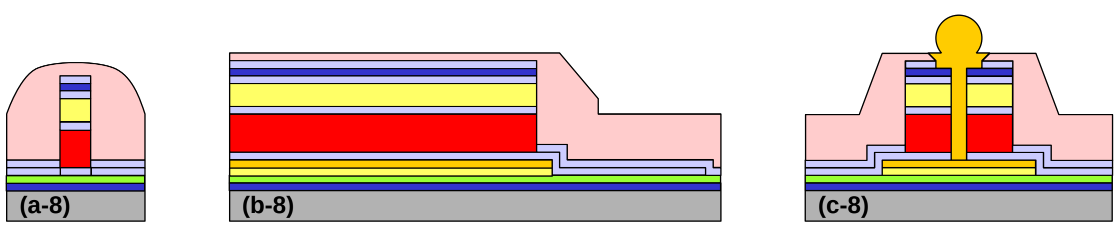

(8) Spin coat 2µm G-line PR, soft bake at 90°C for one minute, Spin coat another 1.5µm G-line PR, soft bake at 90°C for one minute. Pattern (mask 4) to form PR mode. Isotropic oxygen plasma etching at low power (50W) to remove possible PR residuals within the trenches. Electroplate nickel to refill the trenches to form anchors.

Fig. 4-9-3: Step 5 to step 8 of the fabrication process.

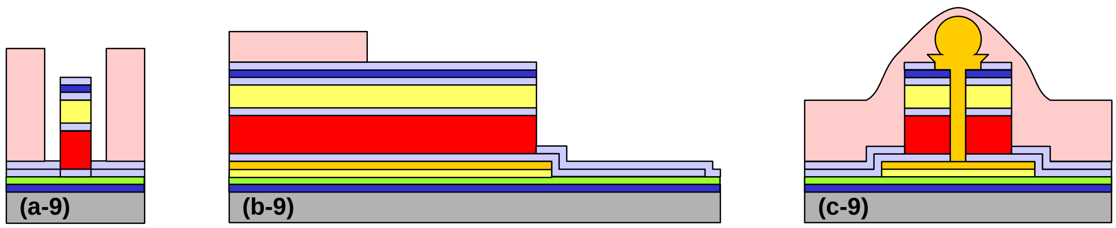

(9) Spin coat 2µm G-line PR, soft bake at 90 °C for one minute, Spin coat another 1.5µm G-line PR, soft bake at 90°C for one minute. Pattern (mask 5) and expose areas where the top electrodes need to be removed.

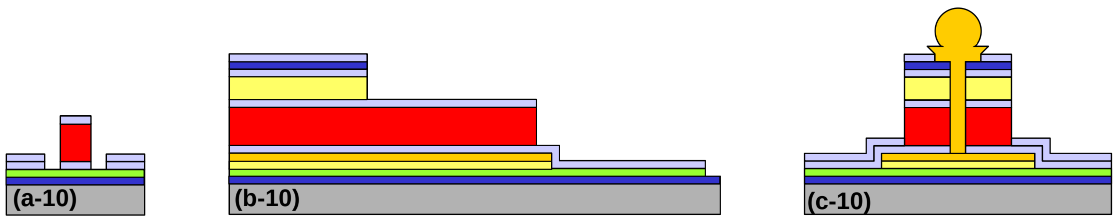

(10) Etch 20nm molybdenum, the remaining (~200nm thick) oxide layer, 20nm-molybdenum, and 400nm-aluminum. Etch stops on the molybdenum between the AlN and aluminum electrode layers. Strip PR.

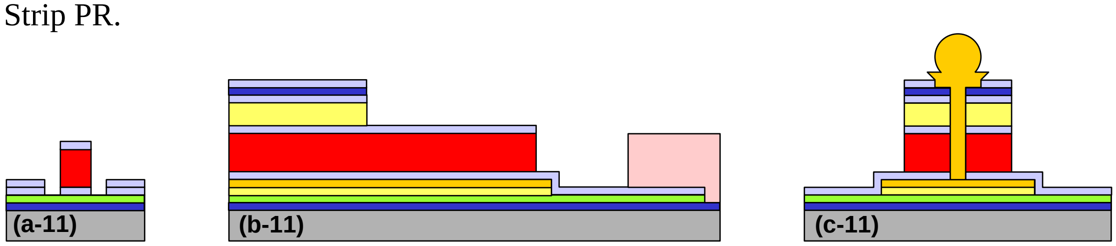

(11) Spin coat 2µm G-line PR, soft bake at 90°C for one minute, Spin coat another 1.5µm G-line PR, soft bake at 90°C for one minute. Pattern (mask 6) and develop in CD-30 to cover the exposed isolation layers.

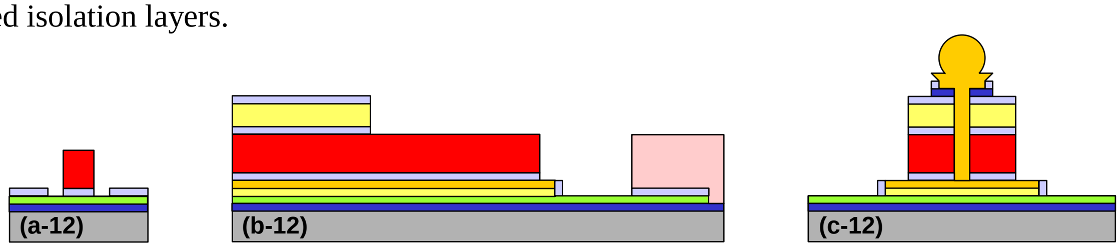

(12) Dry etch 20nm-molybdenum and the remaining (~200nm thick) oxide layer. Etch stops on the molybdenum between the AlN and aluminum electrode layers. No PR is required for this etch step, as the exposed molybdenum layer on areas etched in the last step, where molybdenum/oxide/ molybdenum/aluminum have been removed, and the electroplated nickel anchor protects the underlying layers.

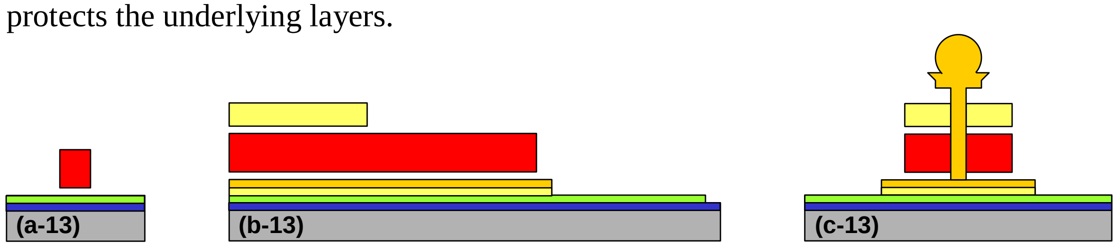

(13) Dry release in XeF_2. Strip PR after release.

Fig. 4-9-3: Step 10 to step 13 of the fabrication process.

4.4.2 Characterization of Lift-off Process

Among many factors that affect the c-axis orientation of sputtered AlN, which can be gauged by the angle of full-width-half-magnitude (FWHM) of the (002) peak in X-ray diffraction measurements, substrate surface roughness is the most critical one. In this

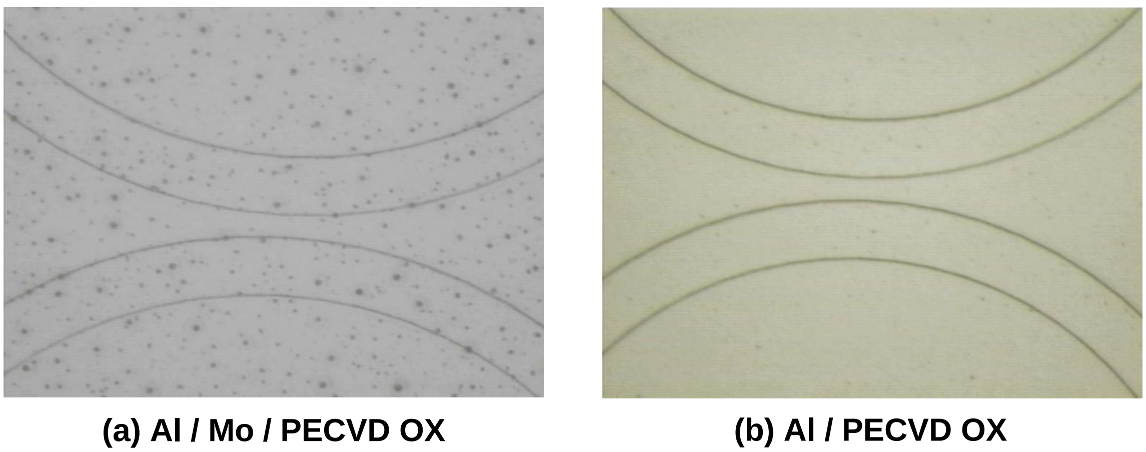

Fig. 4-10: Photos of 300C PECVD oxide deposited on wafers with patterned features and blanket aluminum as the topmost layer. (a) The surface is rough after oxide deposition. (b) Smoother surface is obtained with a 20 nm molybdenum barrier layer that protects the aluminum layer.

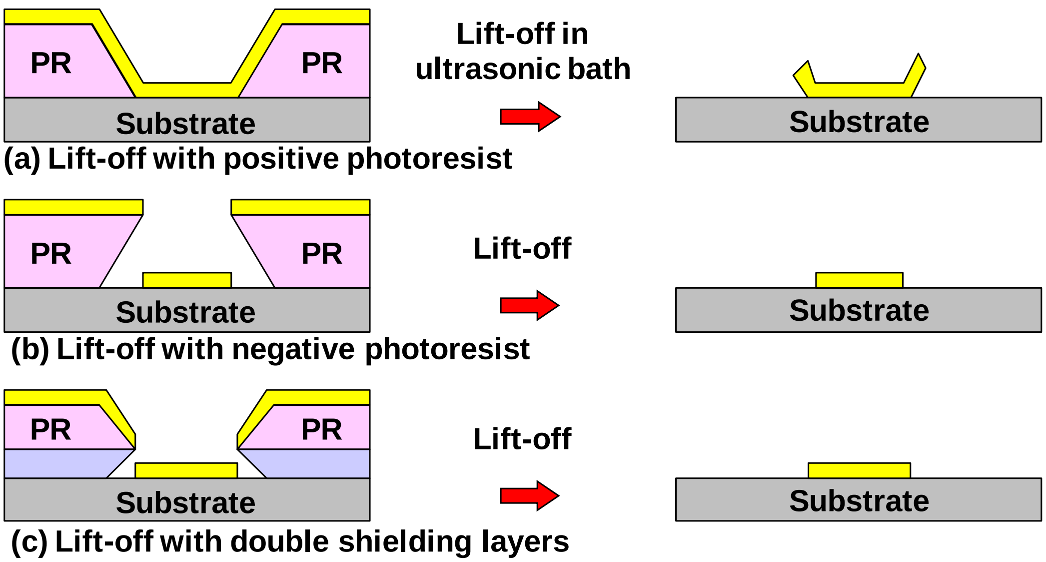

Fig. 4-11: Different PR features affect the results of the metal patterns after lift-off: (a) with sloped positive-PR; (b) with concave negative PR; (c) a combination of (a) and (b) with sloped top layer and concave bottom layer.

capacitive-piezo process, even though molybdenum is used as the sacrificial material to enhance the sputtered AlN quality, which will be discussed in more detail in 4.2.1.2, the roughness on the substrate surface and the bottom electrodes will affect the roughness of the sacrificial molybdenum sputtered on them. To pattern the bottom electrodes without increasing surface roughness on the substrate, wet etching is preferred over plasma dry etching. However, wet etching is not a suitable for patterning high-frequency devices with 1µm interconnecting signal lines, such as 1GHz ring filters. Another solution is lift-off.

In the simplest lift-off process, where positive PR is used, as shown in Fig. 4-11(a), metal is deposited both on top and side-walls of PR patterns and on the areas not covered by metal. Metal patterns on the substrates are then created by etching PR in an ultrasonic bath, where metal deposited on the PR sidewalls will tear apart from the metal adhered to the substrate once the underlying PR is etched away. This physical breaking process leaves rough edges on the metal patterns, shown in Fig. 4-11(a).

Logically, obtaining smooth edges of the metal patterns is not possible as long as the metal deposited on the substrate is connected to the metal on the PR sidewall. Directional metal deposition, such as evaporation, and reverse PR sidewall profile provided by negative PR, shown in Fig. 4-11(b), or double layer PR stack, such as the PR stack shown in Fig. 4-11(c) with I-line as the top layer and G-line as the bottom layer, can solve this issue. The above two common solutions, however, are difficult to achieve pitches smaller than 2 µm.

A specially designed PR for this purpose, LOR3A, is proven to provide both smooth metal edges and pitches as small as 500nm. Fig. 4-12(a) shows the SEM cross-section of the PR stack and metal deposited before lift-off. The cross-section of a strip after metal evaporation and before lift-off shows the concaving features of the bottom layer PR effectively separates metal traces and metals on PR to be removed. In fact, no ultrasonic bath or agitation is required for this lift-off. Figs. 4-12(b)~(c) show zoomed-in SEM on a 1 µm signal line with smooth edges. Note that LOR3A only works for TMAH-based developers (e.g., works for I-line developer OPD4262 but not G-line developer CD-30), which etches aluminum.

The final PR profile is a combination of many process factors, among which LOR3A thickness, soft-bake temperature, exposure time, and the developing time are the most important. To characterize the lift-off process for 30nm Al/70nm Ni, the thickness of LOR3A is fixed at ~300nm and the stepper exposure time and developer time are calibrated to the best results for 1.2µm I-line on 300nm LOR3A and nitride/oxide layers, leaving LOR3A soft bake temperature as the only variable. A series of experiments are run to determine the best soft-bake temperature with the following steps:

1. Spin 300 nm LOR3A. The challenging part here is to hand-spin LOR3A, which is very fluidic, to a film only 300 nm thick. LOR3A must be applied to the center of the wafer and any bubbles in the pipette or particles on the wafers can lead to non-uniform films.
2. Soft-bake LOR3A at various temperatures (150~180°C) for 300 seconds.
3. Spin 1.2 µm I-line and soft-bake at 90°C for 60 seconds. Note that this soft-bake time is much lower than the one in step 2 and will not affect LOR3A underneath I-line PR.
4. Expose the wafer, post-exposure bake at 120°C for 60 seconds and develop in OPD-

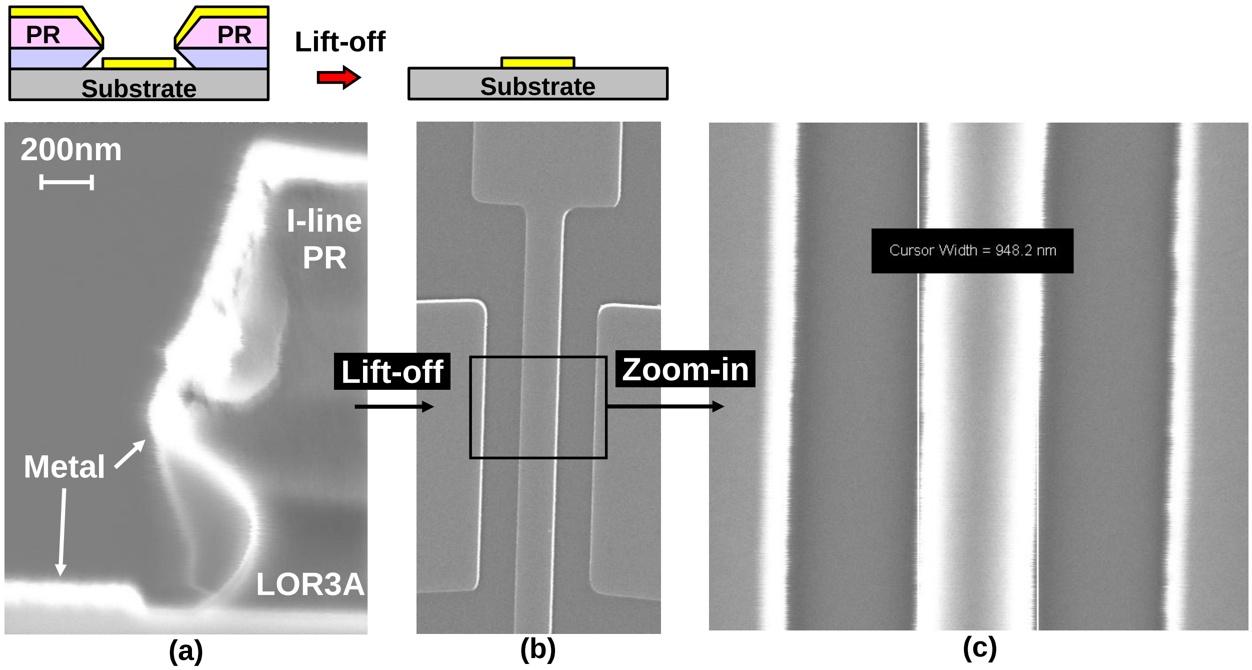

Fig. 4-12: (a) The SEM cross-section of a strip after metal evaporation and before lift-off shows the concaving features of the bottom layer PR effectively separates metal traces and metals on PR to be removed. (b) Smooth metal edges after lift-off. (c) Zoomed-in view of the critical part of the lift-off process with 1 μm pitch.

4262 for 60 seconds. No hard-bake is required.

5. Evaporate 100 nm thick metal on the wafer.
6. Lift-off the metal in PG Remover or PRS 3000 at 80°C.

Fig. 4-13(c) and Fig. 4-14(c) examine the metal interconnects feeding into the anchor at the center of a disk and ring, respectively. In both cases, small pitches are preferred to minimize the discontinuity of the bottom electrodes and the series resistance associated to the signal lines. The metal pattern is wider than desired (*i.e.*, too much LOR3A undercut) at 170°C of soft-bake temperature and narrow than desired (*i.e.*, too little LOR3A undercut) at 180°C. The best soft-bake temperature is 175°C. At this temperature, 1μm metal traces with 1μm pitches are resolved with 100% yield, as shown in Fig. 4-13(a)-(b) for a disk resonator filter and Fig. 4-14(a)-(b) for a ring resonator array.

Another common issue with metal films is poor adhesion. A disk-array filter, as shown in Fig. 4-13(a), has 1μm wide signal lines spanning across the array. Such narrow and long metal traces suffer from poor adhesion to the substrate, shown in Fig. 4-15(a). This issue is resolved with dehydrating baking right before metal deposition, shown in Fig. 4-15(b). The dehydrating baking temperature should be kept below 120°C to prevent distortion of the PR stack profile for lift-off.

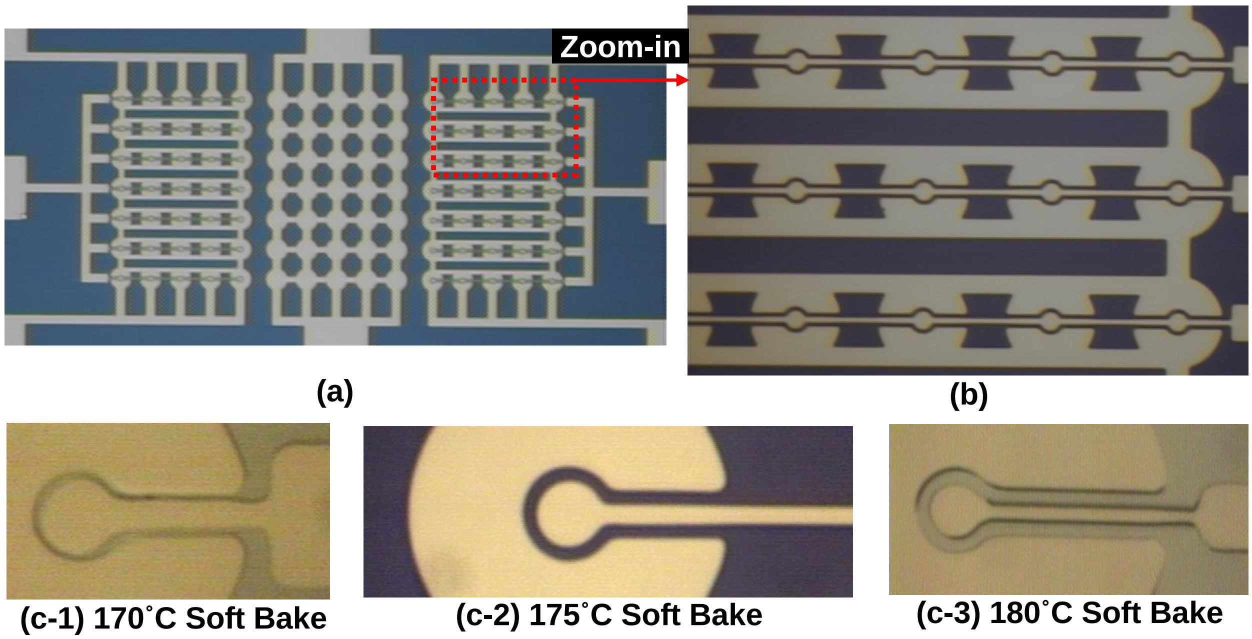

Fig. 4-13: Characterization of lift-off process focusing on the small pitches required for the bottom electrodes and interconnects of a disk array filter.

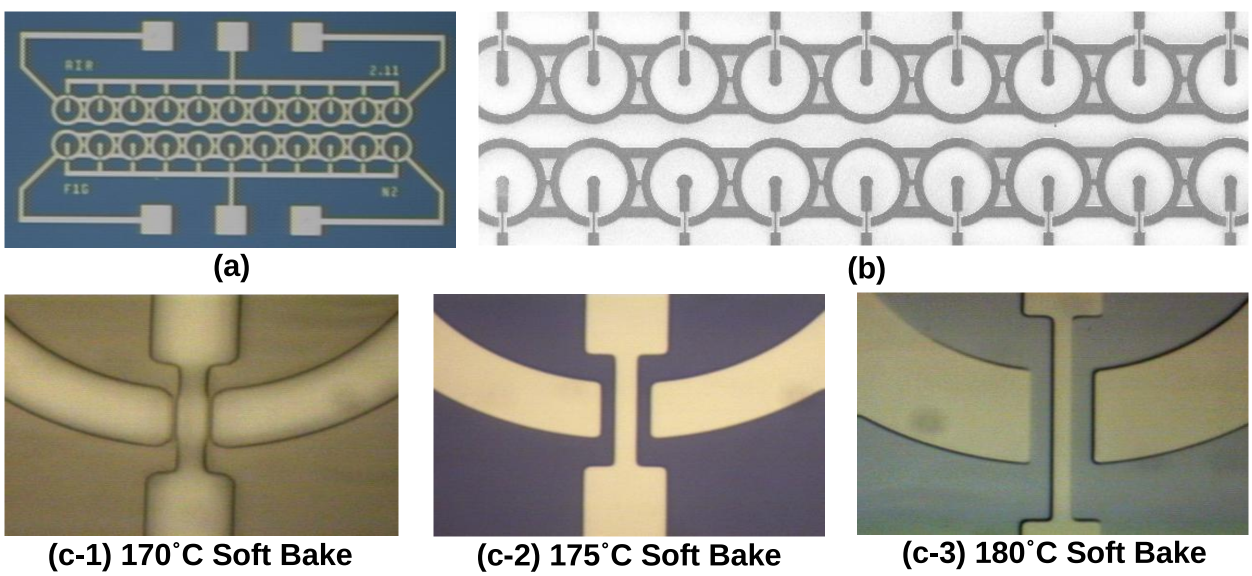

Fig. 4-14: Characterization of lift-off process focusing on the small pitches required for the bottom electrodes and interconnects of a ring resonator array.

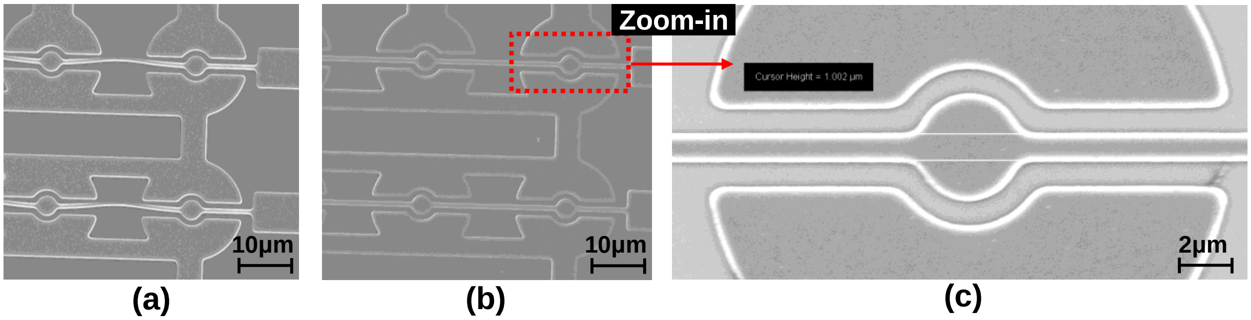

Fig. 4-15: (a) A narrow and long metal traces suffers from poor adhesion to the underlying isolation nitride layer after lift-off; (b) dehydration bake solves the adhesion problem; (c) SEM zoomed-in on the 1 μm metal trace.

4.4.3 AlN and Metal Sputtering

Unlike piezoelectric resonators with contacting electrodes, where AlN is sputtered on patterned metals (*i.e.*, the bottom electrodes), AlN is sputtered on the sacrificial materials for capacitive-piezo resonators. In the first and second attempts for fabricating capacitive-piezo resonators, PECVD polycrystalline germanium deposited at 350°C and sputtered titanium are used as sacrificial materials, respectively. It has been observed that the surface roughness of poly-crystalline germanium is too large (>10 nm) for good AlN c-axis orientation. Sputtered metal, on the other hand, offers a smoother surface, on the order of 5 nm. The fabrication which used titanium as the sacrificial material eventually failed at the last release step due to insufficient etch selectivity of titanium to the isolation layers of nitride and oxide in XeF_2. Molybdenum has therefore been adopted to replace titanium for its high etch rate comparable to silicon in XeF_2. Interestingly, it has been observed that even with equal metal film surface roughness, film stress, and thickness, AlN sputtered on blanket titanium, compared to AlN on blanket molybdenum, has better c-axis orientation and less tensile stress. The obvious difference of the two films is conductivity – molybdenum is 7.9x more conductive than titanium. Realizing that AlN can be sputtered with good c-axis orientation on patterned metals of even more conductive films such as aluminum, AlN should be able to be sputtered on patterned molybdenum. The first molybdenum layer, shown in step #2 of Fig. 4-9, is patterned into a patch for each device, as shown in Fig. 4-16(a) with simple wet etch of aluminum etchant (pre-mixed 80% H_3PO_4, 5% HNO_3, 5% CH_3COOH, 10% DI water) at 50°C. X-ray diffraction (XRD) measurements show that with these square patterns, sputtered AlN shows FWHM of ~1.7° and stress within ±50MPa. Note that the mask pattern is designed such that molybdenum still covers >99% of the entire chip area after etching. Therefore, X-ray diffraction measurement, which covers about 4mm^2 areas around the center of the wafer, faithfully reflects AlN quality on the molybdenum rather than on the isolation layers. Patterning metal into patches probably helps relax the stress within metal films as it heats up during AlN sputtering.

Fig. 4-16(b) shows cross-sectional view of AlN sputtered on 180 nm molybdenum, clearly showing the closely-packed columnar structures. It is found that slight *in-situ* sputter etch with argon immediately before Mo sputtering improves the orientation of the Mo (110)

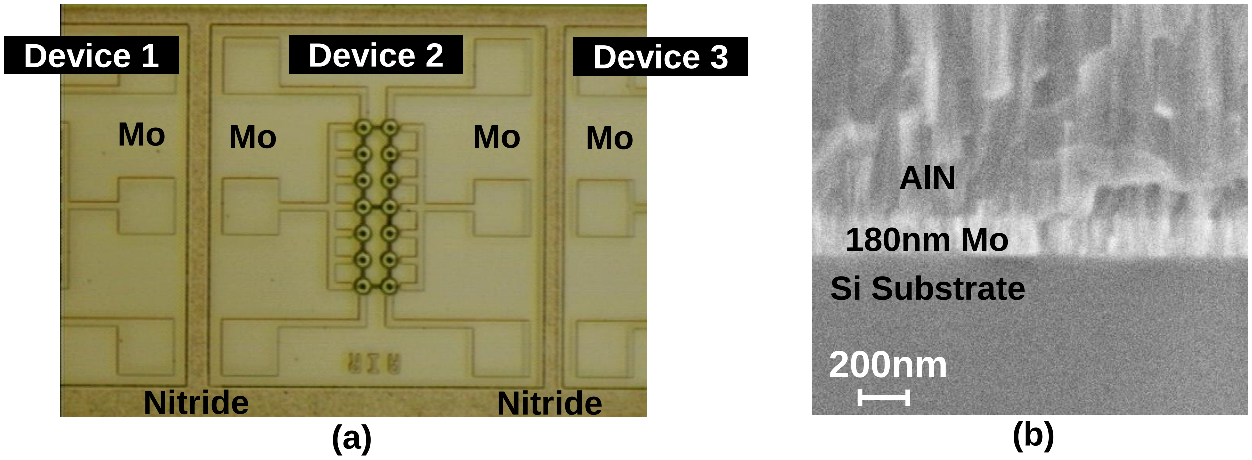

Fig. 4-16: (a) the first sacrificial molybdenum layer is patterned into patches covering individual devices to improve the sputtered AlN quality; (b) SEM cross section of AlN sputtered on 180nm thick, patterned molybdenum.

plane and for the desired (002) AlN growth on them. Too much sputter etching, however, results in a rough surface and degrades AlN quality.

Stress control of all of the thin films sputtered in this process is important for two reasons. First, as opposed to PECVD films with equal film stress acting on both sides of the wafer, material is only sputtered onto one side of the wafer. Large film stress can therefore bow the wafers, making it difficult for fine alignments across the wafer at the following lithography steps. Second, after release, both the AlN resonator and the top suspended electrodes are suspended only by the anchor and are separated by small gaps. If the electrodes and AlN resonators contact with each other due to relaxed film stress, *Q* will be degraded, probably even lower than AlN resonators with contacting electrodes with better resonator-electrode interfaces.

To confine the thin film stress to ±20 MPa, all of the metal films sputtered in this process are performed in a Novellus sputtering system, which provides three variables to tune the metal film stress: sputtering power, pressure, and substrate heating. As a rule of thumb, more tensile film stress can be obtained by increasing the sputtering power and increasing the substrate temperature.

4.4.4 AlN and Molybdenum Dry Etching

The Berkeley Microlab has long and successful history of processing AlN. However, AlN patterning has been limited to a minimum width and via diameter of ~3μm for AlN films thicker than 1.5 μm, due to lithography and etching capabilities. This process used I-line lithography and developed new recipes at the Centura metal etch chamber to enable 1 μm-wide AlN structures for supporting beams of resonators, and 1μm-radius vias for anchors. Fig. 4-17(a)~(c) show SEMs of the patterned 2μm thick AlN structure of a ring

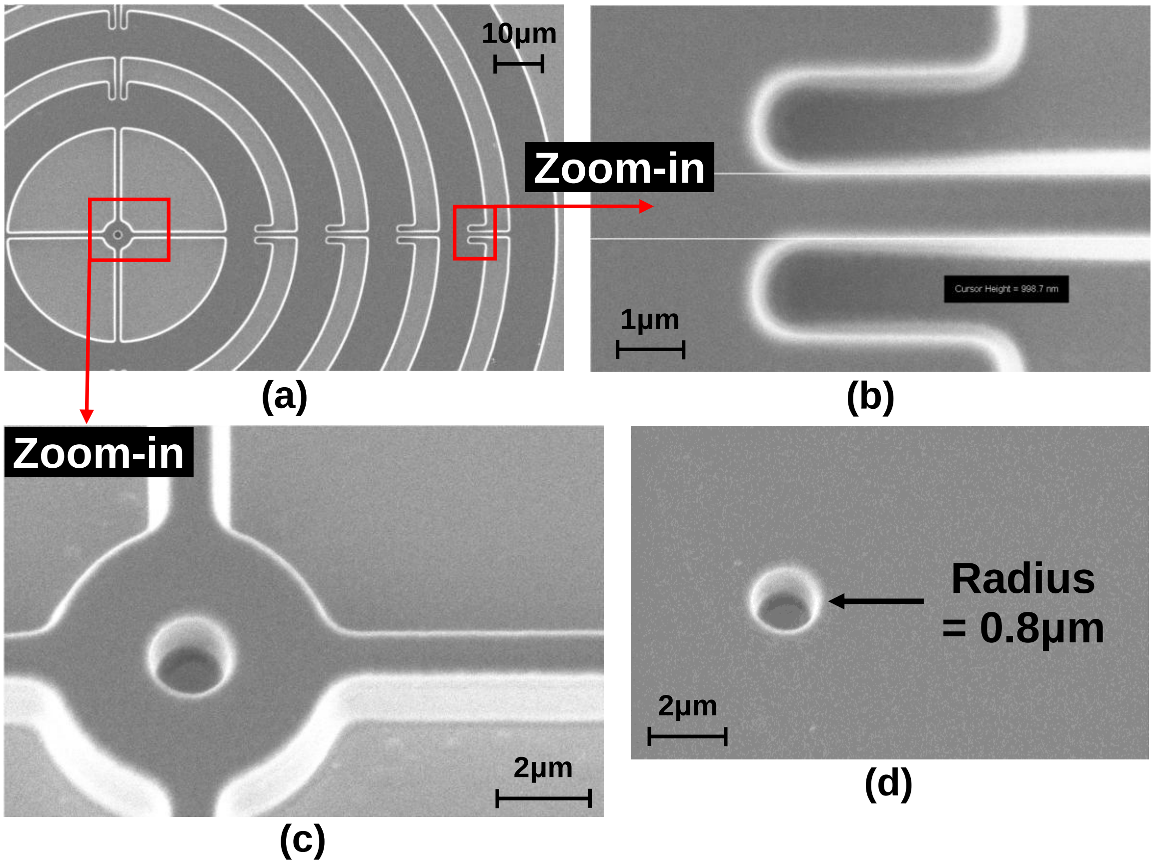

Fig. 4-17: SEMs of patterned AlN structures which are 2 μm high, featuring 1 μm wide beams in (b) and a via with 0.8 μm radius in (d).

resonator array with 1μm-wide coupling beams next to 1μm-wide notches and 1μm-wide supporting beams leading to a 1μm-radius via at the center. Vias with radii as small as 0.8 μm are also successfully resolved at the center of disk resonators, shown in Fig. 4-17(d).

Both AlN and aluminum can be etched by chlorine based chemistry, with the etch rate of aluminum larger than that of AlN, while molybdenum provides a good etch stop for chlorine based chemistry dry etch. However, with a specific ratio of mixed oxygen and chlorine, molybdenum can be etched at up to 200nm/min while the addition of oxygen retarded the etch rate of AlN, aluminum, and oxide. Table 2 lists the dry etch recipes for these materials and their selectivity. For each column, the blue field indicates the target material and the yellow fields indicate the materials where high etch selectivity is required in various steps throughout the fabrication process. In particular, good etch selectivity among these films are important in step #5, where AlN etch stops on molybdenum and nitride, in step #7, where molybdenum etch stops on nickel within the trenches, in step #10, where aluminum etch stops on molybdenum, and in step #12, where oxide etch stops on molybdenum, nickel, and nitride. Note that because oxygen plasma is used in the molybdenum etch, photoresist ashes quickly (573 nm/min) and may leave residuals on the surface due to reaction of oxygen, chlorine, and PR. After step #4 (oxide hard mask etching), the remaining PR is stripped

Table 4-2: Etch rates of different materials in nm/min.

1. Molybdenum etch (in Centura-Metal chamber): Cl_2=90 sccm, O_2=30 sccm, RF power=900 W, bias power=100 W, pressure=10 mTorr.
2. AlN etch (in Centura-Metal chamber): Cl_2=90 sccm, BCl_3=35 sccm, Ar=10 sccm, RF power=900 W, bias power=100 W, pressure=10 mTorr.
3. Aluminum etch (in Centura-Metal chamber): Cl_2=70 sccm, BCl_3=45 sccm, Ar=10 sccm, RF power=900 W, bias power=80 W, pressure=10 mTorr.
4. Oxide Etch (in Centura-MXP): CF_4=15 sccm, CHF_3=45 sccm, Ar=150 sccm, RF power=700 W, pressure=200 mTorr.
5. Oxide Etch (in Lam2): CF_4=45 sccm, CHF_3=15 sccm, Ar=50 sccm, RF power=800 W, pressure=300 mTorr.

	Mo	AlN	Al	Ni	I-Line PR	300˚C PECVD Oxide	250˚C PECVD Oxide	200˚C PECVD Oxide	Nitride
Mo Etch	**330**	**< 3**	**< 3**	**8**	**573**	**3**	**5**	**9**	**< 3**
AlN Etch	**42**	**250**	**630**	**14**	**345**	**70.5**	**102**	**125**	**45**
Al Etch	**20**	**90**	**550**	**11**	**278**	**36**	**70**	**117**	**23**
Oxide Etch (Centura-MXP)	**N/A**	**N/A**	**N/A**	**N/A**	**79.4**	**280**	**380**	**472**	**120**
Oxide Etch (Lam2)	**< 3**	**< 3**	**< 3**	**< 3**	**36.7**	**243**	**315**	**341**	**110**

before the etching continues. As shown in Table 4-2, PECVD oxide deposited at 300°C, compared to 250 °C and 200°C, gives higher selectivity and minimizes the required oxide thickness as a hard mask. For PECVD oxide deposited at temperatures higher than 300°C, the selectivity will be better, but molybdenum fails to be an effective barrier layer between the aluminum and oxide layers.

4.4.5 Nickel Electroplating

To form anchors by electroplating nickel from the bottom of the trench is a critical step – two fabrication runs have failed at this step. A successful anchor refill relies on careful control and characterization of the following factors. Fig. 4-18 summarizes the possible failing mechanisms of this step.

1. (Step #6) 20 nm molybdenum is sputtered on the wafer before electroplating to connect all of the molybdenum patches patterned in step #2. The electroplating may fail to refill the trenches if this thin molybdenum layer is also deposited on the sidewalls of the structures or within the trenches, where during electroplating, nickel will start to grow from the opening of the trench and seal it up before reaching the bottom to form a solid anchor. To avoid this situation, this sputtering is performed at

low pressure (3 mTorr) to achieve a more directional sputtering by increasing the mean-free-path of sputtered metal before it re-deposits on the wafer.

2. (Step #7) Thick G-line PR is patterned to expose only the anchoring areas. The first molybdenum sacrificial layer at the bottom of the trenches, as shown in Fig 4-9(c-7) is then etched away to reveal the underlying nickel seed layer for electroplating. Given that PR is etched much faster than molybdenum and that PR is thinner on the top of the ~4µm high structures, it takes two lithography steps using the same mask to finish etching. The misalignment between the two lithography steps is not harmful. In this step, as the PR pattern has an opening larger than the actual anchoring area to accommodate alignment error, the remaining oxide hard mask around the trench opening protects the underlying structural layers, Al and AlN, from being etched. Unfortunately, the etching suffers from etch loading, where the etch rate is faster in larger opening areas and smaller within trenches of higher aspect ratio. After 50% overetch to ensure that molybdenum within the smallest anchoring trench, with radius of 0.8µm, is cleared, some of the nickel seed layers underneath the wine-glass disk anchoring trenches, with dimensions of 2 µm by 4 µm, are all etched through, which results in only a partially filled anchor or no anchor at all for these WDG devices.

3. (step #8) After etching of the sacrificial molybdenum layer within the trenches, the remaining PR is stripped and G-line PR is applied and patterned again using the same mask. Unlike the previous step, where molybdenum dry etch also removes the PR remaining within the trenches, for this step, only a gentle oxygen plasma can be applied before electroplating to remove PR particles without etching away the PR pattern.

Experiments were performed first to examine whether the electroplated nickel refills the trenches. For this purpose, dummy wafers are first patterned and hard baked to form PR structures of the same height as the real structures on the device wafers. The dummy wafer then went through a second lithography step for the PR pattern for electroplating. Note that this lithography step does not affect the PR structures already on the wafer, which is already hard baked. After electroplating (Fig. 4-19(a)), PR is etched in an oxygen plasma to expose the entire nickel anchors/posts (Fig. 4-19(b)), which can now be easily examined under a microscope or SEM.

To fully expose the 3.5 µm high PR within the 3.5 µm high trenches, the PR on top of the structure, which is only ~1 µm thick, will inevitably be overexposed. The reflective materials, especially the thick aluminum (*i.e.*, the top electrode layer) underneath the remaining thin oxide hard mask and the surrounding molybdenum layer, as shown in step #8 in Fig. 4-9(c), further deteriorates the overexposed issue. Changing the focus of the stepper does not have a significant effect. Eventually, a new dark field mask with patterns smaller than desired was made to accommodate the necessary overexposure. An alternative and more elegant solution is to use negative PR and a clear field mask with patterns only covering the anchoring areas. The exposure dose only needs to be large enough to fully expose ~1µm thick negative PR. The unexposed negative PR within the trenches can then be easily washed away in developer.

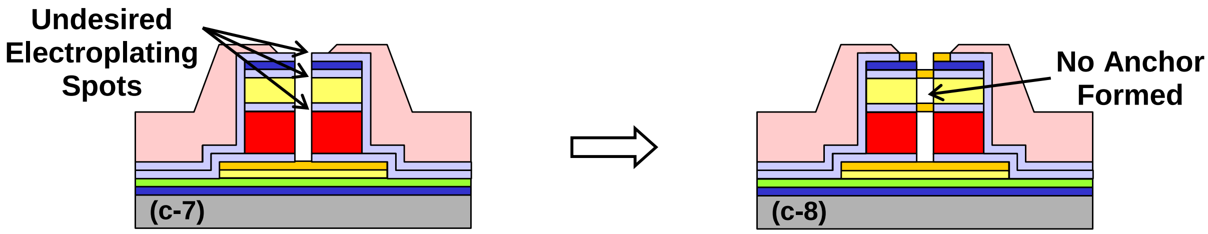

(a) Left: 20 nm molybdenum sputtered on the sidewalls electrically connects the other molybdenum layers, which become undesired electroplating spots. Right: the nickel electroplating solution may not have a chance to reach the bottom of the nickel seed layer and electroplate upward to form an anchor before the trench is sealed up by nickel electroplated from the undesired electroplating spots.

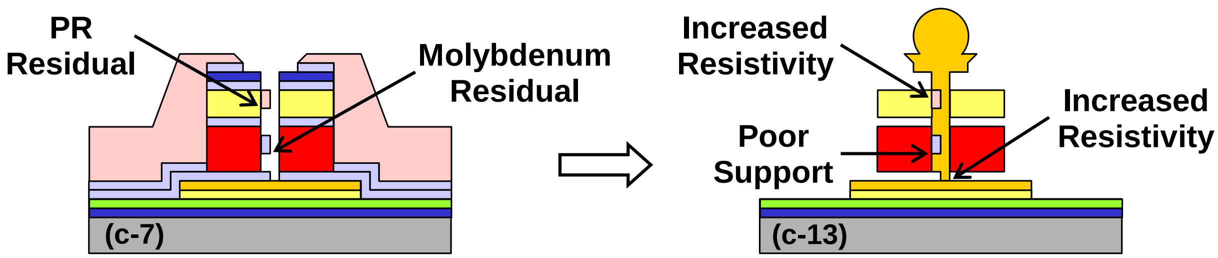

(b) Left: PR and molybdenum residuals remain in the trench before nickel electroplating. Right: PR on the interface of the nickel anchor and top aluminum electrode increases the series resistance. After release etching of molybdenum, reduced anchor contact area with the interconnect increases the resistance.

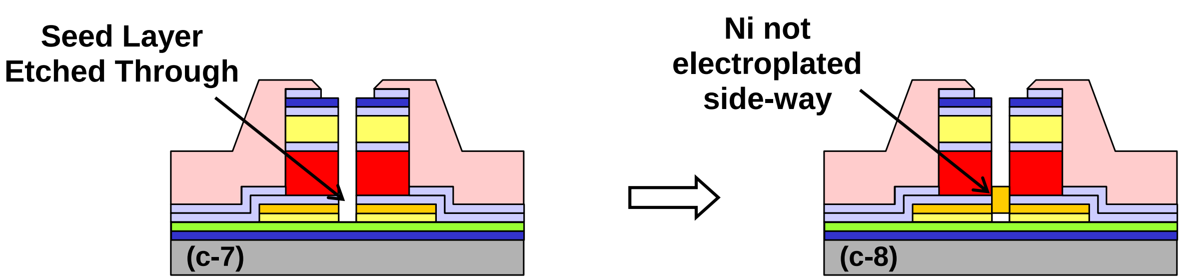

(c) Left: While some overetch is necessary to ensure removal of the molybdenum sacrificial layer above the nickel layer for proper anchors in different sizes of the trenches, too much overetch breaks through the nickel seed layer and even the isolation layers. Right: nickel does not electroplate from the exposed seed layers on the sidewalls. Nickel anchors either form poorly or no anchor is formed.

Fig. 4-18: Three possible situations where nickel electroplating anchors will either be poorly formed or not formed at all: (a) with metal covering the sidewalls of resonator structures; (b) with molybdenum or PR residuals remaining in the trenches; (c) without the seed layer on the bottom of the trench.

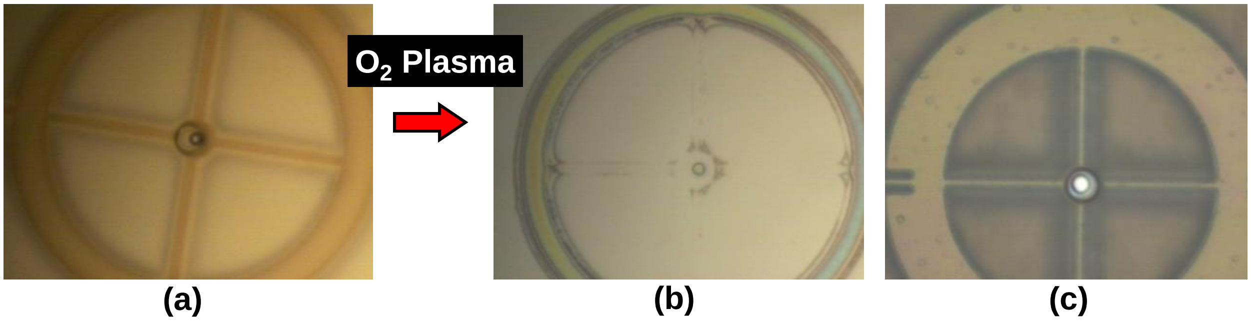

Fig. 4-19: (a)-(b) Use hard baked PR as the structure layer to characterize the nickel electroplating process. After electroplating, oxygen plasma removed both the hard baked PR structure and the PR pattern for electroplating to expose the entire nickel anchor for easy inspection under SEM. (c) Center nickel anchor electroplated for a ring resonator on a device wafer before stripping PR.

4. Nickel electroplating is performed with a homemade electroplating setup for 6” wafers. The wafer is electrically connected to the current supply via a metal clamp attached to the flat of the wafer. The average electroplating rate across the wafer is proportional to the current magnitude, but electroplating is ~1.4x faster at areas close to the metal clamp than the areas on the other end of the wafer due to resistance. This issue is solved by first applying PR to cover the whole wafer except for a ~3mm wide ring around the edges of the wafer, where PR is removed by running EBR (edge beak remover) program on the PR coating track. After electroplating ~1 µm nickel on the exposed area and stripping PR, the wafer now has a nickel ring “clamp” surrounding the edges which helps conduct current to the bottom of the wafer. This extra step reduces the electroplating rate difference to only 1.05x. This method is better than a real metal clamp, as an electroplated nickel ring directly on the wafer provides good contact and good conductivity, without excess mechanical stress which may break the wafer. Note that the flat of the wafer has to remain intact and free from metal for the following process steps in tools which use a laser flat finder.

   Fig. 4-19(c) shows a successful nickel electroplating on a device wafer, where nickel shows lighter color than other areas covered with PR, to form the center anchor of a ring structure with the PR pattern still on the wafer.

4.4.6 XeF_2 Release

In step #13, AlN etch stops on the first sacrificial molybdenum layer but etches the isolation layers on areas not covered by molybdenum. During XeF_2 etch release, XeF_2 can etch away the thinner isolation layers and hollow out the silicon substrate underneath the device. To address this issue, PR is patterned to protect areas not covered by the first molybdenum layer and removed in oxygen plasma after release.

Another area with a thinner isolation layer is the anchors of wine-glass disks. As mentioned in 4.2.1.4, due to etch loading, this process used 50% overetch to assure complete etching of the first molybdenum layer and to assure that the underlying nickel seed layer is exposed for the contour mode ring and disk resonators with anchors of <1 μm radius. This also etched through the nickel seed layer and part of the isolation layers in the anchoring trenches for some wine-glass disks. These spots become an easy path for XeF_2 to etch the silicon substrate. These spots unfortunately happen randomly on wine-glass disk resonators across each die and it is impossible to have a single mask that can work for all die. In order to measure some of the wine-glass disk resonators with good anchors, after step #12 and before XeF_2 release, each die is individually examined and PR is applied manually via probe tips to the anchoring areas without nickel seed layer and nickel anchors. This solution is very time consuming, but it works.

4.4.7 Final Remarks on Fabrication

Even though Al offers high conductance as an electrode material, which is good, the disadvantages outweigh the advantages in three ways: (1) during AlN RIE, the Al top electrode is also etched laterally, which is a more serious problem for thicker Al electrodes due to wider lateral diffusion path for etchant; (2) Al is highly reactive with other materials, causing problems on the interface of Al-Mo and Al-PECVD oxide even at low process temperature. (3) Al sets the upper limit on process temperature when local anneal is desired to release stress, in this case, on the electroplated nickel anchor. An alternative choice of process material combination without using Al will be using Mo as the electrodes, oxide as the sacrificial material, and releasing in HF vapor.

4.4.8 Fabricated Devices

Fig. 4-20 and Fig. 4-21 presents SEM images of different parts of a completed 1.2 GHz contour-mode d_{31}-capacitive-piezo-transduced ring resonator delineating the gaps between the top/bottom electrode and the resonator. For these devices, to reduce electrode resistance, 400 nm thick aluminum is used as the top electrode—something that otherwise would not be permissible in a conventional AlN resonator, since its attached electrode would mass load the resonant structure. This feature is especially important for resonators with thinner AlN structures for higher electrical field across the film.

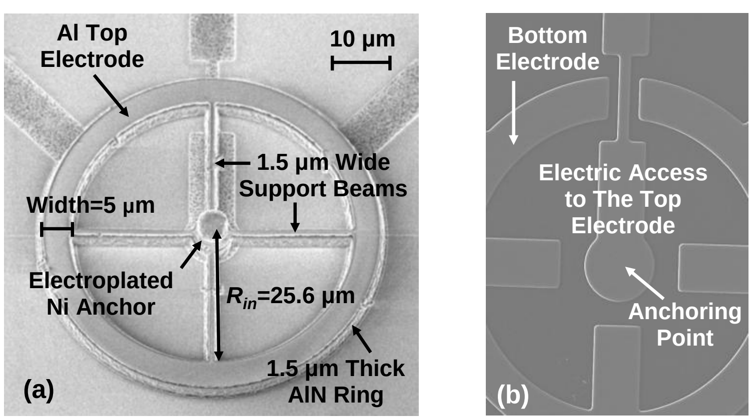

Fig. 4-20: (a) Fabricated 1.2-GHz capacitive-piezo AlN ring resonator; (b) bottom electrode and interconnect configuration, showing anchoring at the very center. The nickel anchor provides electrical connection to the top aluminum electrode.

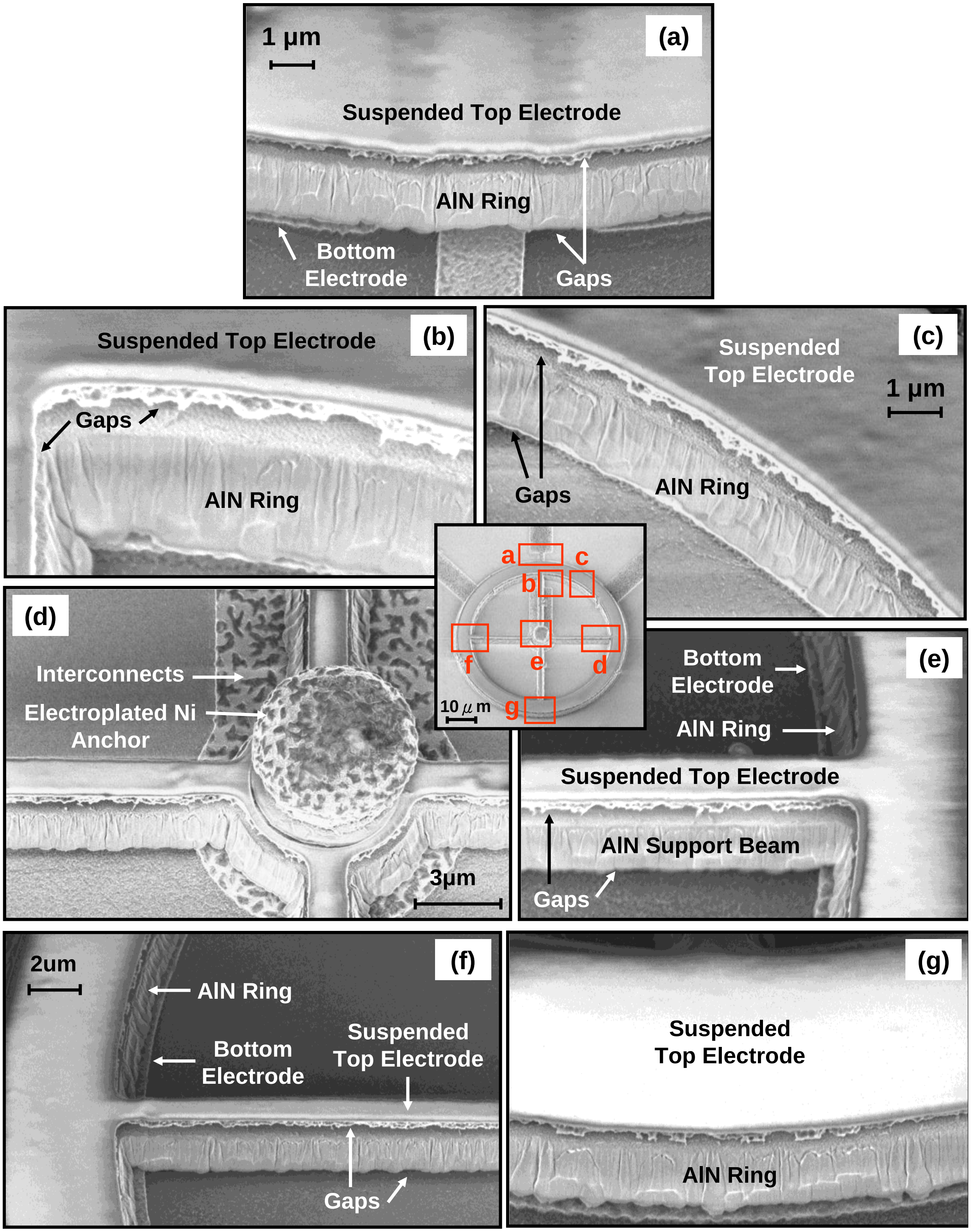

Fig. 4-21: SEM images at different parts of the same resonator confirming that the entire top electrode and the AlN ring resonator are suspended via the electroplated nickel anchor at the center.

4.5 Electrical Measurements

4.5.1 1.2 GHz Contour-Mode Ring Resonators

Fig. 4-22 presents the measured frequency response characteristics for the AlN ring resonator of Fig. 20(a), showing f_s=1.23 GHz, Q=3,073, and R_x=889 Ω at 3 mTorr. Both the input and output are DC grounded via bias-tee's to avoid electrostatic forces that might pull the top and bottom electrodes together and into the AlN resonator. Although the measured Q is still less than predicted by material loss theory, it is still substantially higher than any other measured contour-mode AlN resonator at similar frequencies, as plotted in Fig. 4-23 [30][31][32]. The etch residuals observed in the gaps after release, as shown in Fig. *4-21*, may have affected the measured Q. Moreover, electroplated nickel anchors are mechanically weaker and more poorly attached to the substrate than the PECVD polysilicon anchors used in previous capacitive resonators. This may induce more anchor loss, especially at high frequencies. Finally, due to process difficulties, the supports of the final fabricated resonators deviated from quarter-wavelength dimensions, and this further reduces Q.

It should be noted that the 260 nm gap spacing used in this device is a rather conservative design. In fact, if the gap spacing were reduced from 260 nm to the 100 nm commonly used in capacitive (only) resonators, the impedance could be reduced to 250 Ω.

To evaluate the efficacy of building mechanical circuits using capacitive-piezo transducers, mechanically coupled two-resonator arrays, shown in , were also fabricated and tested. Here, the top electrode on the coupling beam is removed to electrically isolate the output from the input.

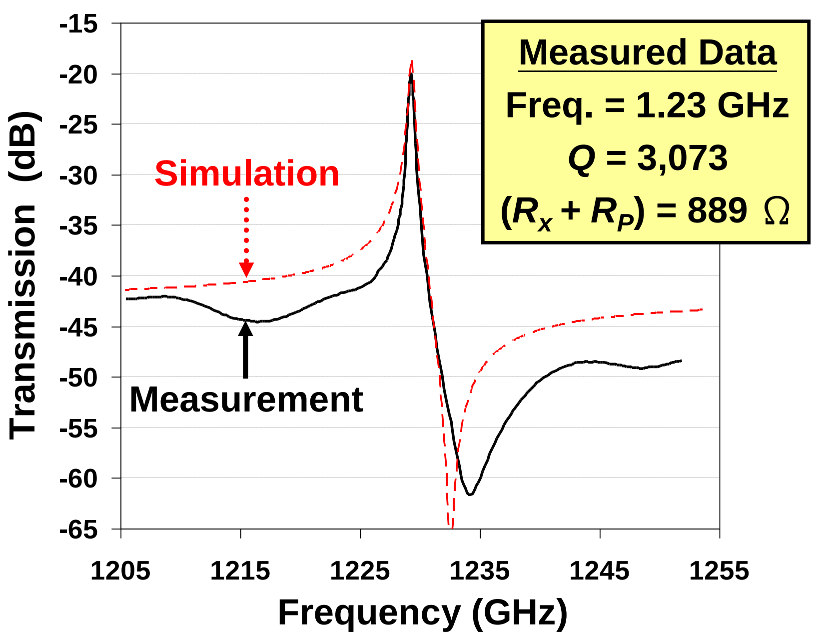

Simulation Parameters

Young's Modulus	350 GPa
Density	3230 kg/m^3
ε_{AlN}	9.0
e_{31}	0.7 C/m^2
Q	3,073
r_m	4.65x10^{-6} Ω
l_m	1.86x10^{-12} H
c_m	9.08x10^{-9} F
η	3.26x10^{-4}
c_P	9.30x10^{-8} F

Fig. 4-22: Measured frequency characteristic for a 1.2-GHz AlN ring resonator with dimensions as shown in 4-20(a) and equivalent circuit of Fig. 4-2(c).

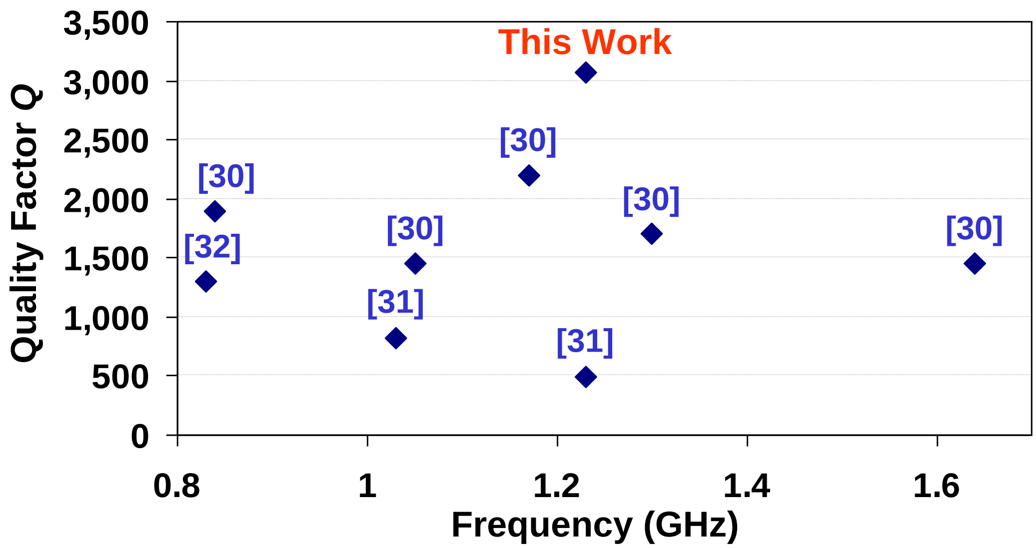

Fig. 4-23: Comparison of *Q*'s achieved via the capacitive-piezo AlN ring resonator of this work versus other ~1 GHz lateral-mode AlN resonators in [30][31][32].

The measured frequency response, shown in Fig. 4-23, exhibits much less feedthrough than seen in single-electrode devices. However, the *Q* is lower for this mechanical circuit than for a single resonator, which might be caused by etch residuals atop the coupling beam formed after dry etching the top electrode.

In particular, it is not unreasonable to expect that future capacitive-piezo equipped resonators with better defined quarter-wavelength supports and stiffer anchors might eventually achieve the *Q*'s in the tens of thousands at GHz range predicted by theory.

4.5.2 50 MHz Wine-Glass Disk Resonator Array

The mode shape of the ring has static points only at the center of the ring, which is difficult to access. The support beams of the 1.2 GHz ring resonators described above are attached to the resonator at the positions with the largest amplitude. Therefore, the resonators suffer from anchor loss and the anchors are made as small as the process allows, in this case, 1.8 μm in diameter, to minimize the anchor loss. As a result, the anchors of the 1.2 GHz ring resonators are not strong enough to withstand cleaning procedures, such as ultrasonic clean, to remove the etch residuals from the resonator surfaces and from within the gaps. To tap the *Q* of sputtered AlN, wine-glass disk (WGD) resonators with larger anchoring areas and support beams attached to the quasi-static points are also measured after each cleaning step to monitor *Q* increases. It is north noting that the composite and equi-volume nature of the wine-glass mode shape, where both longitudinal and shear strain are present and out of phase, makes it difficult to excite and sense the disk with the piezoelectric effect and to obtain high coupling as the ring resonator described in the previous section. After release, the edges of the top electrodes, where the maximum displacement occurs, curl up perhaps due to stress, as shown in Fig. 4-*25*, which makes the effective gap spacing larger and effective coupling even weaker. The above factors together reduce the induced motional current relative to the feed-through current. To obtain a series

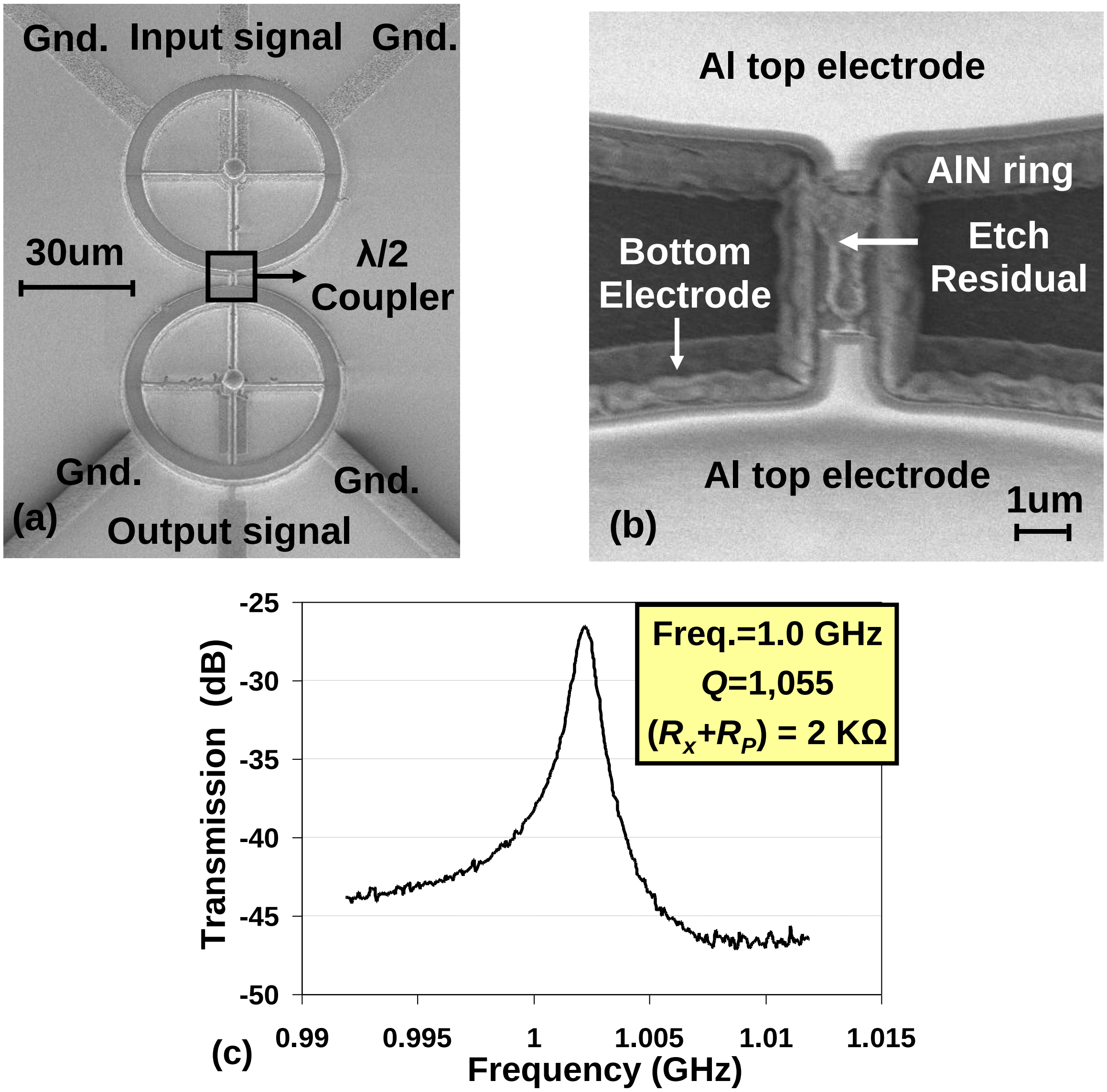

Fig. 4-24: (a) SEM of a capacitive-piezo ring resonator array with λ/2 coupler; and (b) top-view, zoomed-in SEM showing how the electrode is removed from the coupler to electrically isolate the output from the input. (c) Measured frequency characteristic for the resonator in (a) confirming suppression of the parallel resonance peak.

resonant peak free from the anti-resonant peak for more accurate Q measurement, feed-through currents must be reduced accordingly. Considering the rather large size of the disk and the suspended top electrode, to better combat the possible vertical residual stress gradient of the Al electrodes, it is preferred that the top electrodes are supported on both ends (like a clamp-clamp beam), rather than supporting input and output top electrodes individually with each anchor (like a cantilever), as a 2-port single resonator required. Instead, two-resonator arrays were measured. With proper coupling beam design, the Q's of an array have been shown to take the value of individual resonators.

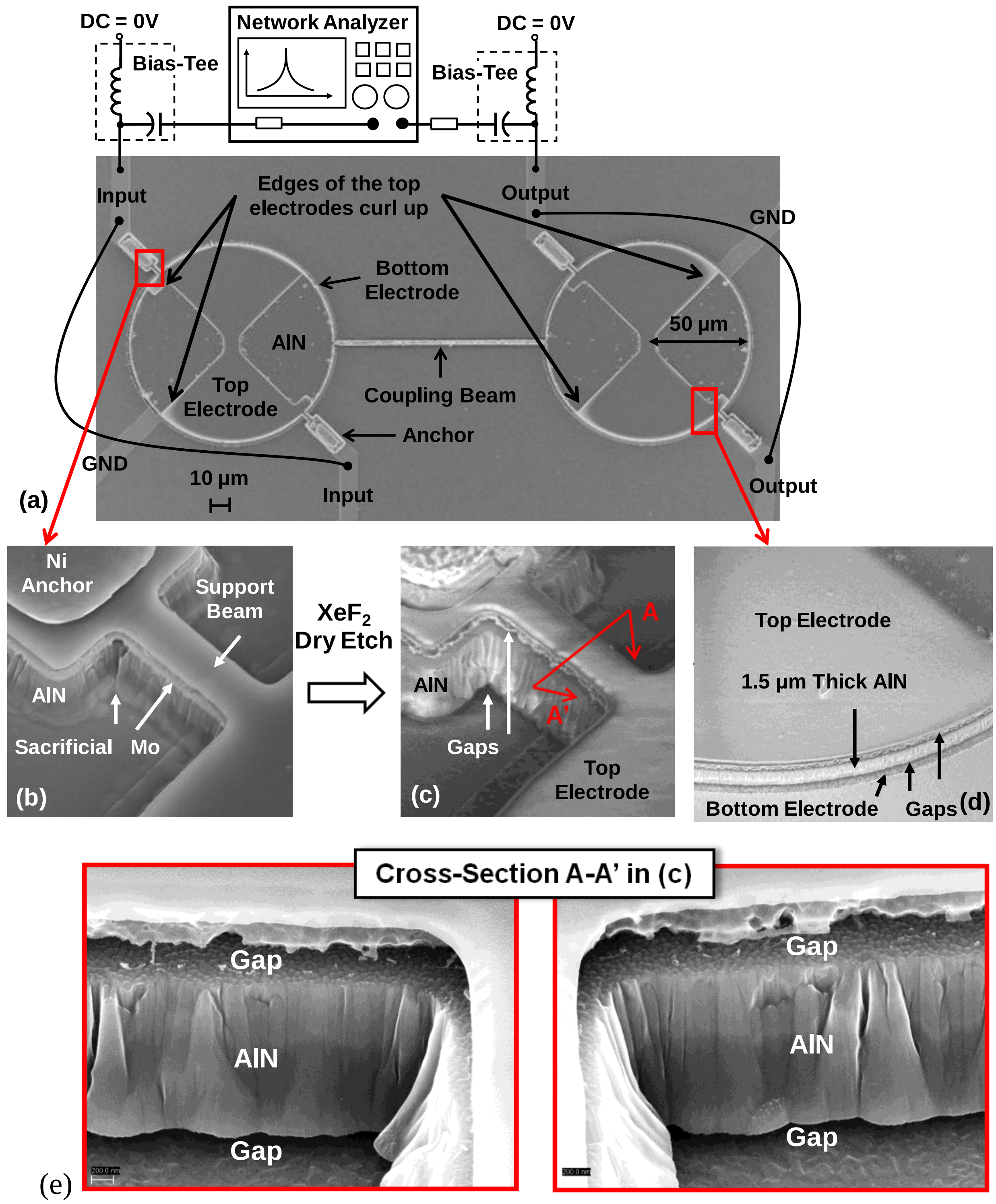

Fig. 4-25: (a) Fabricated AlN disk resonator array and the measurement setup which yields the measured frequency spectrum in Fig. 4-27. (b) and (c) zoomed-in views on the anchor before and after XeF_2 dry release, respectively; (d) side-view of the resonator edge, showing the whole disk lifted between the top and bottom electrodes; (e) zoomed-in SEM figures on the generated gaps after release. After numerous cleaning steps, etch residuals on the AlN disk are noticeably reduced but not completely gone, which can degrade the quality factor.

The resonators with support beam width of 1 µm, 1.5 µm, and 2 µm, as shown in Fig. 4-26, are measured to show *Q* of 8,193, 7,292, and 6,061 after XeF_2 release, respectively, shown in Fig 4-27. Note that at this point, photoresist to protect nitride/oxide isolation layers during release is present on the chip. After oxygen plasma clean, EKC-270 dip, and critical point drying in methanol, *Q* increases for all three cases. After annealing at N_2/H_2 at 500°C for 30 minutes, *Q* further increases to 12,748 for the resonator with 1 µm support beams, posting the highest ever measured for sputtered AlN resonators. *Q* is higher than 10,000 even for resonators with support beams of 1.5 µm. The effects of anneal on enhancing *Q* are not definite. It has been observed that particles inside the gaps close to the edges of the disk, as shown in Fig. 4-25(e), decrease after anneal. Moreover, anneal relaxes the stress of electroplated nickel, an approach used before to enhance *Q* of a comb-drive resonator made of electroplated nickel by 3.5 times [33]. It is also possible that anneal modifies the Ni-AlN interface such that phonon transfer to the substrate, and subsequent dissipation through the nickel anchor, is reduced. Whether anneal at even higher temperatures will further increase *Q* is unknown because aluminum electrodes limit the allowable anneal temperatures.

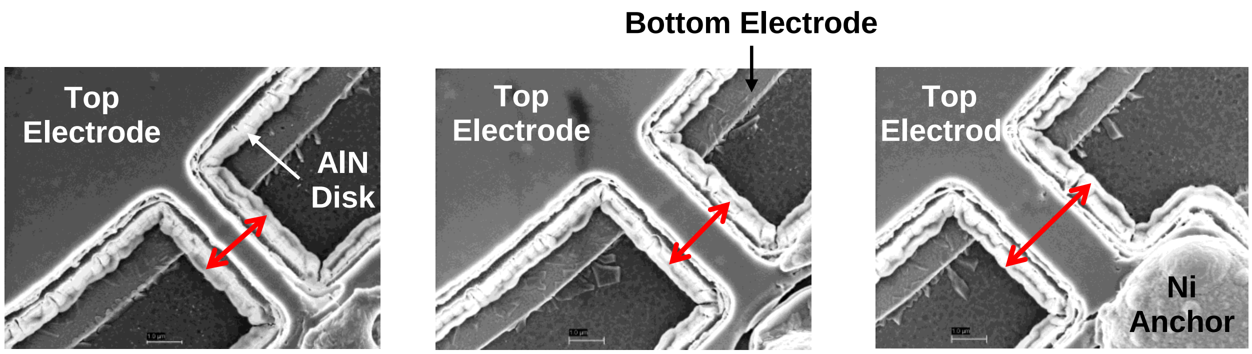

Fig. 4-26: Zoomed-in SEM figures on the anchors of fabricated wine-glass disk resonator with various support beam width as indicated with arrows in the figures: (a) 1 µm; (b) 1.5 µm; (c) 2 µm. All the other geometry are the same for these disk resonators.

Table 4-3: Summary of the measurement data of 50MHz WGD capacitive-piezo resonators with various support beam width after various cleaning and anneal treatments.

Support Beam Width W_s = 1 µm					Support Beam Width W_s = 1.5 µm					Support Beam Width W_s = 2 µm				
#	*Q*	f_o (MHz)	S_{21} Peak (dB)	R_x (KΩ)	#	*Q*	f_o (MHz)	S_{21} Peak (dB)	R_x (KΩ)	#	*Q*	f_o (MHz)	S_{21} Peak (dB)	R_x (KΩ)
1	8,193	50.958	-37.2	7.14	1	7,292	51.042	-38.2	8.03	1	6,061	50.913	-39.8	9.67
2	8,942	50.967	-36.4	6.51	2	7,734	51.049	-37.7	7.57	2	6,366	50.931	-39.4	9.23
3	12,748	50.990	-33.3	4.52	3	10,218	51.883	-35.3	5.72	3	7,076	50.950	-38.4	8.22

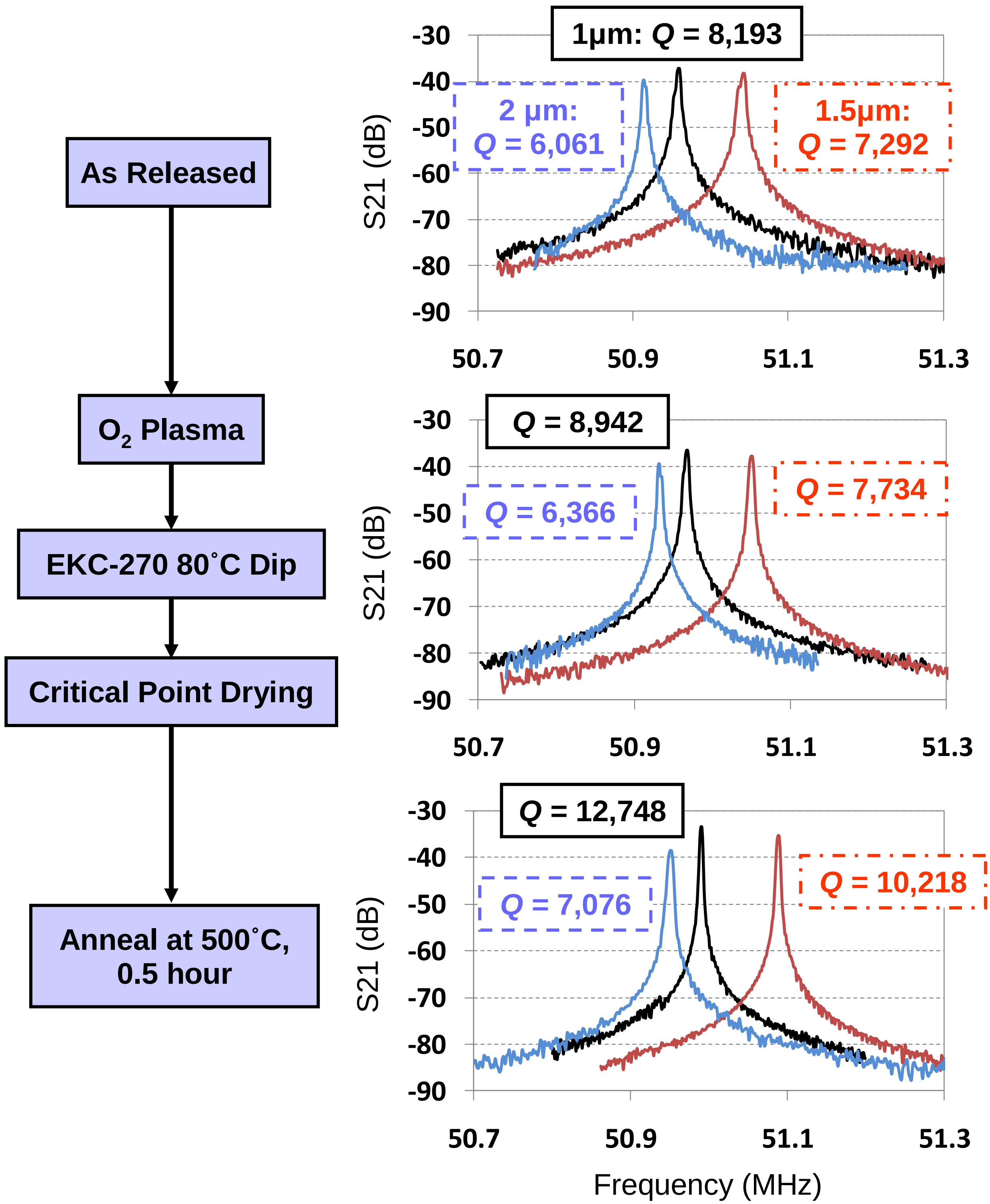

Fig. 4-27: Measured frequency characteristics for the resonator in Fig. 4-25. The resonator *Q* is still limited by the anchor loss, as resonators with thinner support beams render higher *Q*. In particular, the resonators with 1.5 µm and 1 µm support beams achieve *Q* higher than 10,000, the highest two data points ever measured for resonators made of sputtered AlN at any frequency.

4.6 References

[1] S.-S. Li, Y.-W. Lin, Y. Xie, Z. Ren, and C. T.-C. Nguyen, "Micromechanical "hollow-disk" ring resonators," in *Tech. Digest., 17th IEEE Int. MEMS Conf.*, pp. 821-824, 2004

[2] S.-H. Lee, *et. al*., "Influence of electrode configurations on the quality factor …," *J. Appl. Phys*, vol. 92, pp. 4062-4069, 2002.

[3] C.-L. Huang, K.-W. Tay and L. Wu, "Effect of AlN film thickness and top electrode materials on characteristics of thin-film bulk acoustic-wave resonator devices," *J. Appl. Phys*. vol. 44, pp. 1397-1402, 2005.

[4] M. Ueda, T. Nishihara, J. Tsutsumi, S. Taniguchi, T. Yokoyama,

S. Inoue, T. Miyashita and Y. Satoh, "High-*Q* resonators using FBAR/SAW technology and their applications," in *Digest, IEEE Inter. Microwave Symp*., pp. 209-212, 2005.

[5] L. Mai, V.-S. Pham, and G. Yoon, "ZnO-based film bulk acoustic resonator devices on a specially designed Bragg reflector," *J. Applied Physics*, vol. 95, pp. 667-671, 2009.

[6] S. K. Kor, P. K. Mishra, and N. D. Tripathi, "Ultrasonic attenuation in pure and doped n-type silicon," *Physical Review B,* vol. 10, p. 775, 1974.

[7] D. K. Pandey, D. Singh, and R. R. Yadav, "Ultrasonic wave propagation in IIIrd group nitrides," *Applied Acoustics*, vol. 68, pp. 766-777, 2007.

[8] R. Tabrizian, M. Rais-Zadeh, and F. Ayazi, "Effect of phonon interactions on limiting the *fQ* product of micromechanical resonators," in *Tech. Dig., Transducers'07*, 2007, pp. 2131-2134.

[9] Y.-W. Lin, S.-S. Li, Z. Ren, and C. T.-C. Nguyen, "Low phase noise array-composite micromechanical wine-glass disk oscillator," in *Tech. Dig., IEEE Int. Electron Devices Mtg*., 2005, pp. 287-290.

[10] F. Ayazi, S. Pourkamali, G. K. Ho, and R. Abdolvand, "High-aspect-Ratio SOI vibrating micromechanical resonators and filters," in in *Tech. Digest, IEEE MTT-S Int. Microwave Symp.*, 2006, pp. 676-679.

[11] S. V. Krishnaswamy, J. D. Adam, and M. Aumer, "High-*Q* FBARs using epitaxial AlN films," in *Proc. IEEE Int. Ultrasonic Symp.*, 2006, pp. 1467–1470.

[12] A. N. Cleland, M. Pophristic, and I. Ferguson, "Single-crystal aluminum nitride nanomechanical resonators," *Applied Physics Letters*, vol. 79, no. 13, pp. 2070-2072, Sep. 2001.

[13] C. G. Courcimault and M. G. Allen, "High-*Q* mechanical tuning of MEMS resonators using a metal deposition-annealing technique," in *Tech. Dig., Transducers'05,* 2005, pp. 875-878.

[14] J. Wang, J. E. Butler, T. Feygelson, and C. T.-C. Nguyen, "1.51-GHz polydiamond micromechanical disk resonator with impedance-mismatched isolating support," in *Tech. Digest*, 17th *IEEE Int. MEMS Conf.*, 2004, pp. 641-644.

[15] C.-L. Dai, C.-H. Kuo, and M.-C. Chiang, "Microelectromechanical resonator manufactured using CMOS-MEMS technique," *J. Microelectronics*, vol. 38, pp. 672-677, 2007.

[16] C. K Jahnes, J. Coite, J. L. Lund, H Deligiunni, A. Chinthukindi, L. P. Buchwalter, P. Fyer, J. A. Tornello, N. Hoivik, J. H. Mugerlein and D. Seeger, “Simultaneous fabrication of RF MEMS switches and resonators using copper-based CMOS interconnect manufacturing methods,” in *Tech. Digest*, 17th *IEEE Int. MEMS Conf.*, 2004, pp. 789-792.

[17] J. Verd, A. Uranga, G. Abadal, J. L. Teva, F. Torres, J. L. Lopez, E. Perez-Murano, J. Esteve, and N. Barniol, "Monolithic CMOS MEMS oscillator circuit for sensing in the attogram range," *Electron Device Letters, IEEE*, vol. 29, no. 2, pp. 146-148, Feb. 2008.

[18] W.-C. Chen, C.-S. Chen, K.-A. Wen, L.-S. Fan, W. Fang, and S.-S. Li, “A generalized foundry CMOS platform for capacitively-transduced resonators monolithically integrated with amplifiers,” in *Tech. Digest*, 23rd *IEEE Int. MEMS Conf.*, 2010, pp. 204-207.

[19] C-C Lo, F. Chen, and G. K. Fedder, “lntegrated HF CMOS-MEMS square-frame resonators with on-chip electronics and electrothermal narrow gap mechanism,” in *Tech. Dig., Transducers’05*, 2005, pp. 2074–2077.

[20] L.-W. Hung, and C. T.-C. Nguyen “Silicide-based release of high aspect-ratio microstructures,” in *Tech. Digest*, 23rd *IEEE Int. MEMS Conf.*, 2010, pp. 120-123.

[21] N. Abelé1, K. Séguéni, K. Boucart, F. Casset, B. Legrand, L. Buchaillot, P. Ancey, A.M. Ionescu1, “Ultra-low voltage MEMS resonators based on RSG-MOSFET,” in *Tech. Digest*, 19th *IEEE Int. MEMS Conf.*, 2006, pp. 882-885.

[22] S. Basrour, H. Majjad, J. R. Coudevylle and M. de Labachèlerie, “Simulation and characterization of high *Q* microresonators fabricated by UV–LIGA,” *Tech. Proc.*, Int. Modeling and Simulation of Microsystems (MEM) Conf., 2001.

[23] W.-L. Huang, Z. Ren, and C. T.-C. Nguyen, "Nickel vibrating micromechanical disk resonator with solid dielectric capacitive-transducer gap," in *Proc. IEEE Int. Freq. Control Symp*. pp. 839-842, 2006.

[24] W.-L. Huang, S.-S. Li, Z. Ren, and C. T.-C. Nguyen, “UHF nickel micromechanical spoke-supported ring resonators,” in *Tech. Dig., Transducers’07*, 2007, pp. 323–326.

[25] L. Lihua, P. Kumar, L. Calhoun, and D. L. DeVoe, "Piezoelectric $Al_{0.3}Ga_{0.7}As$ longitudinal mode bar resonators," *J. Microelectromechanical Systems*, vol. 15, pp. 465-470, 2006.

[26] R. Besson, “A new ‘electrodeless’ resonator design,” in *Proc. IEEE Int. Freq. Control Symp*. pp. 147-152, 1976.

[27] J. R. Norton and R. Besson, “Tactical BVA quartz resonator performance,” in *Proc. IEEE Int. Freq. Control Symp*. pp. 609-613, 1993.

[28] W. Pang, H. Zhang, H. Yu., C.-Y. Lee, and E. S. Kim, “Electrical frequency tuning of film bulk acoustic resonator,” *IEEE/ASME J. Microelectromech. Syst.*, vol. 16, no. 6, pp. 1303–1313, Dec. 2007.

[29] Y.-W. Lin, S.-S. Li, Z. Ren, and C. T.-C. Nguyen, “Third-order intermodulation distortion in capacitively-driven VHF micromechanical resonators,” in *Proc., IEEE Int. Ultrasonics Symp.*, 2005, pp. 1592-1595.

[30] C. Zuo, J. V. der Spiegel, and G. Piazza, “1.05GHz MEMS oscillator based on lateral-field-excited piezoelectric…,” in *Proc. IEEE Int. Freq. Contr. Symp.*, 2009, pp. 381-384.

[31] P. J. Stephanou and A. P. Pisano, "GHz higher order contour mode AlN annular resonators," in *Tech. Dig., 20th IEEE Int. MEMS Conf.*, 2007, pp. 787–790.

[32] G. Piazza, P. J. Stephanou, and A. P. Pisano, "One and two port piezoelectric higher order contour-mode MEMS resonators for mechanical signal processing," *Solid-State Electronics*, pp. 1596-1608, 2007.

[33] W.-T. Hsu, S. Lee, and C. T.-C. Nguyen, "*In situ* localized annealing for contamination resistance and enhanced stability in nickel micromechanical resonators," in *Tech. Dig.,* 10th Int. *Solid-State Sensors and Actuators Conf.*, 1999, pp. 932-935.

Chapter 5: *Q*-Boosting AlN Array-Composite

5.1 Introduction

Although thin-film AlN micromechanical resonators post lower (hence, better) motional impedances than their capacitively transduced counterparts [1], their lower Q (~1,000 vs. > 10,000 for capacitive) have long disqualified them from emerging applications that demand Q > 10,000. For example, the low-power spectrum analyzer needed at the front-end of a cognitive radio requires small percent bandwidth filters [2] which in turn demand very high Q resonators to avoid excessive insertion loss. As described in Chapter 1, the filter insertion loss depends on resonator Q. To assure less than 3 dB insertion loss, the minimum required resonator Q is only 1,000 for a 1% bandwidth filter, but as high as 10,000 for 0.1% bandwidth, clearly emphasizing the importance of Q when small percent bandwidths are needed. Unfortunately, no previous sputtered AlN resonator has been capable of achieving Q >10,000, and so cannot be used to realize narrow-band filters without excessive insertion loss. Rather, AlN technology has been relegated to wide-band filter applications, where their lower Q is less consequential and their strong electromechanical coupling enables filter termination impedances compliant with conventional values (*e.g.*, 50 Ω).

Interestingly, despite the fact that the highest measured Q of d_{31}-transduced low-temperature sputtered AlN resonators (Q = 5,830 at 43.26 MHz [3]) are 28x less than that of polysilicon counterparts (Q = 161,000 at 61.9 MHz [4]) for the same mode shape at similar frequencies, material loss theory predicts that the material Q of AlN should only be ~2x less than that of silicon [5]. There are many who believe that the low Q results from the use of low-temperature AlN sputter deposition in previous work. An alternative hypothesis, however, rejects material loss as the primary Q-limiting loss mechanism and rather focuses on the difference between capacitive resonators and piezoelectric resonators: in the former, the electrodes do not touch the resonator, whereas in the latter, the electrodes attach directly to the resonator. Although attaching electrodes to a piezoelectric resonator does maximize the electric field strength available to generate the piezoelectric effect, it also exposes the resonator to losses inherent in the electrode material and at the electrode-to-resonator interface. This electrode-based loss can then dominate among dissipation mechanisms, preventing measurement of the actual material Q of AlN. Realizing this, the work presented in Chapter 4 harnessed capacitive-piezo transducers that separated an AlN resonator from its electrodes by small gaps, thereby eliminating electrode losses towards a Q of 3,073 at 1.2 GHz [6] and 12,748 at 50.9 MHz [7]. This Q is higher than previously demonstrated at similar frequencies, but still limited by the losses due to fabrication-derived etch residuals.

This work circumvents the above fabrication difficulties towards finally measuring AlN resonator Q's closer to theoretical prediction by using a mechanical circuit-based approach that mechanically couples electrode-equipped input/output resonators with electrode-less ones, allowing the composite mechanically resonant structure to behave more "electrode-less" when the number of electrode-less resonators is much larger than the number of electrode-equipped resonators. When this is the case, the composite resonator exhibits a higher (*i.e.*, boosted) Q than it would if composed of only electrode-equipped resonators, *i.e.*, the addition of electrode-less resonators "boosts" the original Q. Using this approach, Q = 10,444 [8] is measured for an array-composite resonator structure that combines two electrode-equipped resonators with thirty electrode-less ones. This 3.4x increase in Q over previous work should greatly decrease both insertion loss in filters and phase noise in oscillators.

5.2 *Q*-Boosting Micromechanical Circuits

Fig. 5-1(a) presents a drawing of the Q-boosting mechanical circuit (along with its electrical equivalent) used in this work. Here, two "end" resonators, equipped with electrodes and designed to vibrate in wine-glass mode shapes [9], are mechanically coupled by half-wavelength beams to several "inner" resonators that are electrode-less, but otherwise identical to the end resonators in shape and dimension. The whole structure comprises a single array-composite resonator that can be excited into mechanical resonance by applying a resonance AC voltage across the top and bottom electrodes of one of the electrode-equipped end resonators, thereby generating a vertical electric field that induces lateral strain via the d_{31} coefficient of the AlN piezoelectric material, causing the entire structure to vibrate. The other end resonator then electrically monitors the vibration via output currents provided by the piezoelectric effect.

Proper operation of this structure relies on the same assumption as the work of capacitive-piezo transducers, in that metal electrode-derived loss mechanisms dominate among Q-limiting factors, and so removing metal electrodes from the inner resonators should result in much higher Q than their end resonator counterparts. If this is the case, then energy sharing between resonators in the mechanically-coupled structure should raise (or boost) the Q of the composite structure to a value larger than possessed by each end resonator alone. To understand how a Q-boosting circuit works, it is illustrative to consider the simplest case, where all of the resonators in the array-composite are identical.

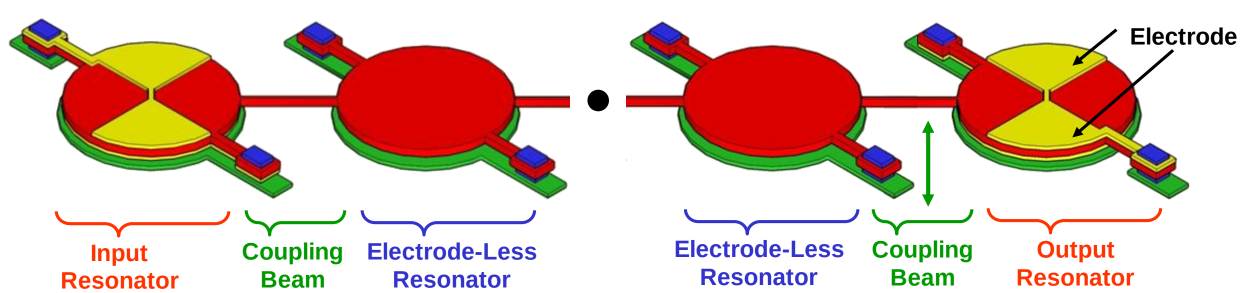

Fig. 5-1: A piezoelectric resonator array-composite where only one resonator on each end of the array-composite has contacting electrodes and serves as the input and output resonators, respectively.

5.2.1 Array-Composite of Identical Resonators

For a mechanically coupled micromechanical resonator array-composite, shown in Fig. 5-2(a), the equivalent Q and impedance of the entire array-composite can be derived either with energy analysis [9] or with the equivalent electrical circuit analysis.

a. Energy Analysis

To quickly illustrate the Q-boosting property, consider that the Q of the composite mechanically-coupled resonator structure is given by the total stored energy E_{Tot} summed among all constituent resonators, divided by the total loss per cycle L_{Tot}, again summed over all resonators. If the quality factor Q_n of a given resonator n in the mechanical circuit of Fig. 5-2(a) can be written as $Q_n = E_n/L_n$, where E_n and L_n are the energy stored and energy lost per cycle, respectively, for resonator n, then one can write for the case where all N array resonators have the same stored energy per cycle E_o

$$Q_{Mckt} = \frac{E_{Tot}}{L_{Tot}} = \frac{\sum_{n=1}^{N} E_n}{\sum_{n=1}^{N} L_n} = \frac{N \cdot E_o}{\sum_{n=1}^{N} L_n} = N \cdot \left(\sum_{n=1}^{N} (L_n / E_o) \right)^{-1} \tag{5-1}$$

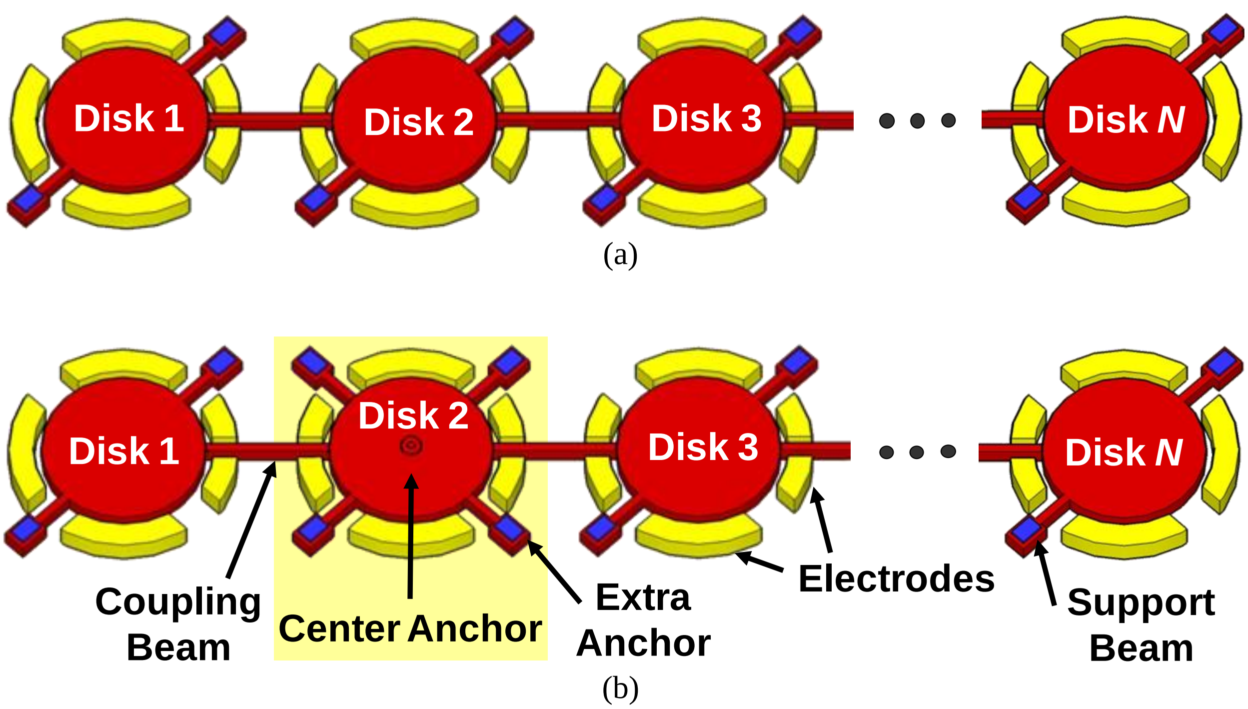

Fig. 5-2: (a) A resonator array-composite composed of N identical resonators mechanically coupled to each other; (b) a resonator array-composite similar to the one in (a) except that one of the resonators (resonator 2) has lower Q than all of the others due to excess anchor losses.

Use of the definition of Q then yields

$$Q_{Mckt} = N \cdot \left(\frac{1}{Q_1} + \frac{1}{Q_2} + \cdots + \frac{1}{Q_n} \right)^{-1} \tag{5-2}$$

For the case where the Q of all of the resonators are the same, say, $Q_1 = Q_2 = \cdots = Q_n = Q_o$, (5-2) predicts that $Q_{Mckt} = Q_o$. As the half-wavelength coupling scheme is ideally lossless and the array-composite resonator is a passive device (*i.e.*, no energy is generated), the mechanical-circuit Q, Q_{Mckt}, should not deviate from the individual resonator.

For the case where the Q of one of the resonators, (*e.g.*, Q_2), is much less than the Q of all other resonators, as shown in Fig. 5-2(b), where resonator-2 suffers from more extra anchor loss due to the center stem and two more side-ways anchors, (5-2) reduces to $Q_{Mckt} = N \times Q_2$.

$$Q_{Mckt} \approx N \cdot Q_2 \tag{5-3}$$

Therefore, when coupled with (N-1) much higher-Q resonators, Q_1 is effectively boosted by N times. In the limit as N goes to infinity, Q_{Mckt} is bounded by the Q of the high-Q devices. In other words, the larger the number of high Q electrode-less resonators coupled to a single low Q electrode-equipped resonator, the more the entire mechanical circuit takes on electrode-less characteristics, and the closer Q_{Mckt} comes to the Q of an electrode-less AlN resonator.

b. Equivalent Circuit Analysis

The motional resistance of a micromechanical resonator (or circuit of such resonators) often governs its utility in a given application [4]. To gauge the impact of adding coupled electrode-less resonators on the motional resistance of a pair of electrode-equipped resonators, Fig. 5-3(b) presents the equivalent electrical circuit model for the resonator array shown in Fig. 5-3(a). Here, the motional circuit elements that model each resonator take on values corresponding to its mass m_{rn}, stiffness k_{rn}, and damping c_{rn}, and the half-wavelength coupling links are modeled by T networks of capacitors with relative values indicated. The coupling coefficients at input and output ports associated with each electrode-equipped resonator are $\eta_{i,n}$ and $\eta_{o,n}$, respectively. This half-wavelength coupled circuit effectively places the motional elements of all resonators in series, so the circuit reduces to that in Fig. 5-3(c), for which

$$m_{r,Mckt} = \sum_{n=1}^{N} m_{rn} \tag{5-4}$$

$$k_{r,Mckt} = \sum_{n=1}^{N} k_{rn} \tag{5-5}$$

$$c_{r,Mckt} = \sum_{n=1}^{N} c_{rn} \tag{5-6}$$

$$\eta_{i,Mckt} = \sum_{n=1}^{n_e} \eta_{i,n} \tag{5-7}$$

$$\eta_{o,Mckt} = \sum_{n=1}^{n_e} \eta_{o,n} \tag{5-8}$$

where $m_{r,Mckt}$, $k_{r,Mckt}$, and $c_{r,Mckt}$ are the mass, stiffness, and damping, respectively, of the composite mechanical circuit; $\eta_{i,Mckt}$ and $\eta_{o,Mckt}$ are the equivalent electromechanical coupling coefficients at the input and output ports, respectively; n_e is the total number of electrode-equipped resonators in the array. Using the circuit in Fig. 5-3(c) and (5-4)-(5-8), the Q and motional resistance of the composite mechanical circuit, Q_{Mckt} and R_{Mckt}, respectively, can be written as

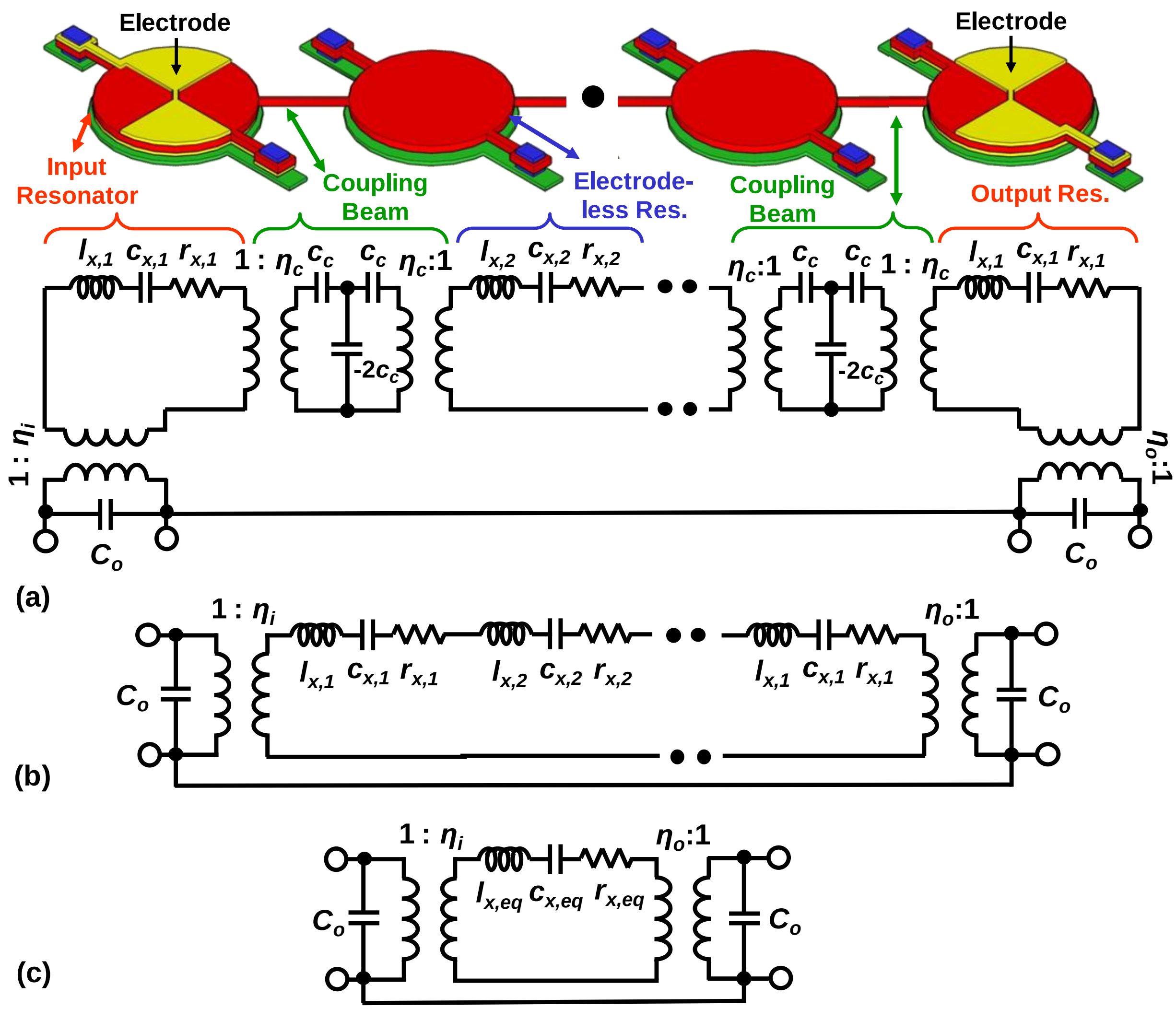

Fig. 5-3: (a) A piezoelectric resonator array-composite and its equivalent electrical circuit where only one resonator on each end of the array-composite has contacting electrodes and serves as the input and output resonators, respectively; (b) a simplified version of the circuit in (b), which can be further simplified to the circuit in (c).

$$Q_{Mckt} = \frac{\sqrt{m_{r,Mckt} \cdot k_{r,Mckt}}}{c_{r,Mckt}} = \frac{\sqrt{(\sum_{n=1}^{N} m_{rn}) \cdot (\sum_{n=1}^{N} k_{rn})}}{\sum_{n=1}^{N} c_{rn}} \tag{5-9}$$

and

$$R_{Mckt} = \frac{c_{r,Mckt}}{\eta_{i,Mckt} \cdot \eta_{o,Mckt}} = \frac{\sum_{n=1}^{N} c_{rn}}{\eta_{i,Mckt} \cdot \eta_{o,Mckt}} \tag{5-10}$$

This analysis can be further generalized to an array of N resonators, all with identical motional mass m_{rn} and stiffness k_{rn}, among which n_e resonators are electrode-equipped and (N-n_e) resonators are electrode-less with Q's α times larger than the former. In this case, (5-9) and (5-10) become

$$Q_{Mckt} = \frac{N}{n_e + (N - n_e)/\alpha} \cdot Q_o \tag{5-11}$$

and

$$R_{Mckt} = \frac{1 + (N/n_e - 1)/\alpha}{n_e} \cdot R_o \tag{5-12}$$

where Q_o and R_o are the Q and motional resistance of a single electrode-equipped resonator, respectively. Fig. 5-4 plots Q_{Mckt} and R_{Mckt} governed by (5-11) and (5-12) with n_e=1 and α's of 10 and 100, respectively, against the total number of resonators in the array, N. As the number of Q-boosting resonators in the array, (N-1), increases, both Q_{Mckt} and R_{Mckt} increase. However, when α is large, as indicated by the α = 100 curve, Q_{Mckt} increases almost linearly with N, while R_{Mckt} barely changes, *i.e.*, Q_{Mckt} can be increased without significant penalty to R_{Mckt}. In fact, when α = 100, a 30× increase in Q_{Mckt} is realized with a less than 50% increase in R_{Mckt}.

It should be noted that the described Q-boosting circuit does not raise the piezoelectric resonator *FOM*, given by $Q \cdot k_t^2$. This is because while the Q boosts by N×, the effective electromechanical coupling k_t^2, defined in (1-38), decreases by N× due to an N× increase in stiffness (or mass), as governed by (5-5) (or (5-4)). In essence, a Q-boosted AlN resonator array trades k_t^2 for higher Q.

5.2.2 Coupling Resonators of Various Sizes

Q-boosting circuits can also be implemented by coupling resonators with the same resonant frequency but with different stiffness and mass. To quickly demonstrate this, consider the circuits in Fig. 5-5(a). The serial combination of capacitor-inductor-resistor, corresponding to the two higher-Q resonators in the middle, can be redrawn to Fig. 5-5(b) with the same electrical response and Q-boosting effect. In the mechanical domain, the circuits in Fig. 5-5(a) and (b) correspond to coupling transduction resonators to more high-Q resonators with less mass and stiffness, or less high-Q resonators with more mass and stiffness.

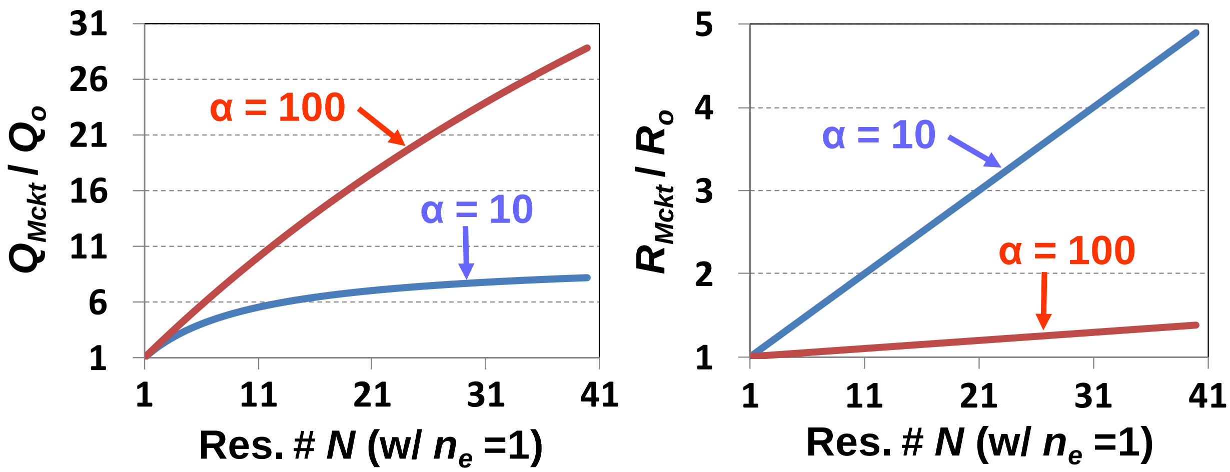

(a) (b)

Fig. 5-4: (a) and (b): theoretical plots of (5-11) and (5-12), respectively, with n_e=1, showing how the overall Q and impedance of the composite mechanical circuit, Q_{Mckt} and R_{Mckt}, change as the number (N-1) of Q-boosting resonators in the array increases. The Q_{Mckt} increases more with less impedance penalty when α is large.

Indeed, from (5-4)-(5-6), the parameters that determine Q_{Mckt} is the summation of the mass, stiffness, and damping factor of individual resonators in the array, regardless the total number of resonators. Q-boosting circuits are most effective when the higher-Q resonators have larger stiffness and mass than the lower-Q resonator.

The following discussion considers an array-composite where the higher-Q resonators have different Q, stiffness, and mass. To simplify the case, all of the N_{low} lower-Q resonators are assumed to be identical. The N_{high} higher-Q resonators have stiffness, mass, and Q as

$$m_{ri} = \beta_i \cdot m_{r,o} \tag{5-13}$$

$$k_{r,i} = \beta_i \cdot k_{r,o} \tag{5-14}$$

$$Q = \alpha_i \cdot Q_o \tag{5-15}$$

where $m_{r,o}$, $k_{r,o}$, and Q_o are the mass, stiffness, and Q of N_{low} identical lower-Q resonators, respectively. β_i and α_i are the ratio of stiffness/mass and Q between the higher-Q and lower-Q resonators, respectively. Note that m_r and k_r need to have the same ratio, β_i, relative to $m_{r,o}$ and $k_{r,o}$, in order to maintain the same resonant frequency. Using the equation of Q, c_{ri} can be expressed as

$$c_{r_i} = \frac{\sqrt{m_r \cdot k_r}}{Q} = \frac{\sqrt{\beta_i m_r \cdot \beta_i k_r}}{\alpha_i \cdot Q} = \frac{\beta_i}{\alpha_i} \cdot \frac{\sqrt{m_r \cdot k_r}}{Q} = \frac{\beta_i}{\alpha_i} \cdot c_{r,o} \tag{5-16}$$

Therefore, the overall Q is, according to (5.4.1)

$$\begin{aligned} Q_{Mckt} &= \frac{\sqrt{(\sum_{n=1}^{N} m_{rn}) \cdot (\sum_{n=1}^{N} k_{rn})}}{\sum_{n=1}^{N} c_{rn}} = \frac{\sqrt{(N_{low} + \sum_{1}^{N_{high}} \beta_i) m_{r,o} \cdot (N_{low} + \sum_{1}^{N_{high}} \beta_i) k_{r,o}}}{(N_{low} + \sum_{1}^{N_{high}} \beta_i / \alpha_i) c_{r,o}} \\ &= \frac{N_{low} + \sum_{1}^{N_{high}} \beta_i}{N_{low} + \sum_{1}^{N_{high}} \beta_i / \alpha_i} \cdot Q_o \end{aligned} \tag{5-17}$$

The modifier of the last term in (5-17) approaches unity and there is minimal Q-boosting effect when

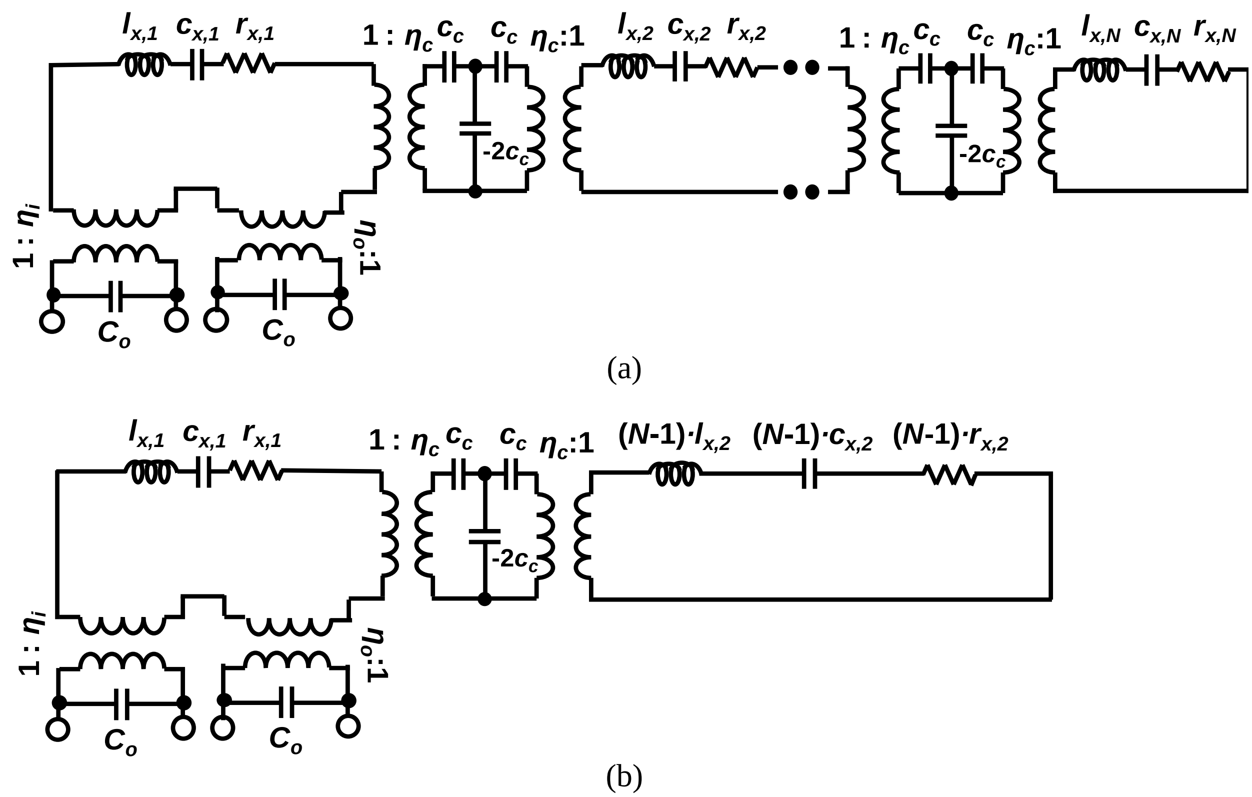

Fig. 5-5: (a) equivalent circuit of a resonator array-composite where one resonator serves as both the input and output resonator and the remaining (N-1) resonators without electrodes have higher Q; (b) a modification of the circuit in (a) by combining (N-1) higher-Q resonators into a single resonator with larger mass and stiffness.

$$\sum_{1}^{N_{high}} \beta_i << N_{low} \tag{5-18}$$

One of the examples of resonators of identical resonant frequency but different stiffness and mass is a contour-mode ring resonator with the same ring width but various average radii. The frequency equations for the contour-mode ring shape can be found in [10] When the average radius of a ring is much larger than its width, the resonant frequency is determined by the width and is independent of the radius, which suggests that both the motional mass and the stiffness are proportional to the radius. This can be implemented as several concentric rings to save layout space, such as shown in Fig. 5-7(a) and (b) with simulation parameters of each ring resonator listed in Table 5-1. The length of each coupling beam and the width of the ring are 4.87 μm and 10 μm, respectively. The average radius of each ring therefore differs by the ring width plus the half-wavelength coupling beam, or 14.87 μm. Fig. 5-7 shows three different coupling and transduction schemes with comparable layout areas. The array-composites in Fig. 5-7 (a) and (b) have electrodes on the inner-most ring and the outer-most ring, respectively, and are otherwise the same. Assuming all of the *Q*-boosting electrode-less resonators exhibit *Q* larger than *Q* of the electrode-loaded resonator by 100 times (*i.e.*, $\alpha_1 = \alpha_2 = \ldots = 100$ in (5-13) to (5-17)), Table 5-1 compares the mechanical circuit *Q* and impedance of each resonator array-composite in Fig. 5-7 compared to those of a transduction resonator of 40 μm average radius. It clearly shows that by coupling resonators with larger mass and stiffness, the *Q* boosting factor is larger with little penalty on impedance increase.

Ideally, it is possible to couple one low-*Q* resonator with a massive, stiff high-*Q* resonator of the same frequency to boost the overall *Q*. There is an immediate advantage of this approach: a system with fewer degrees of freedom has fewer spurious modes to suppress and fewer resonators to trim to obtain a certain target frequency, if necessary.

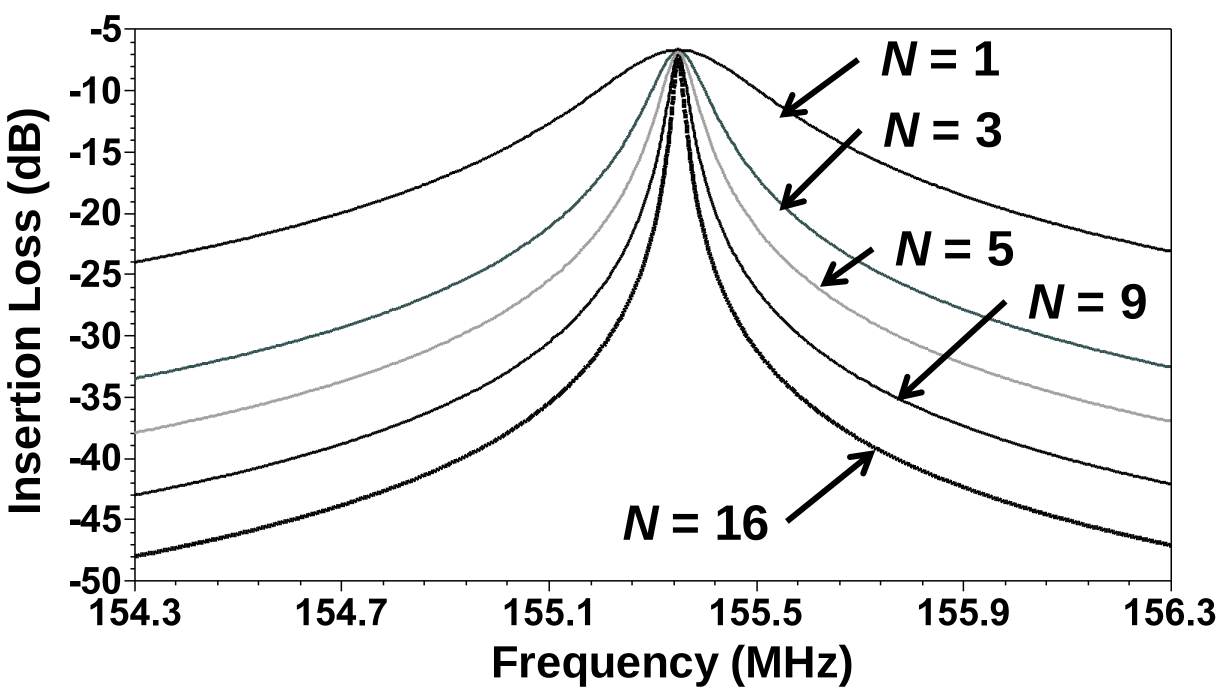

Fig. 5-6: Simulation results of the circuits in Fig. 5-5 with varying *N*.

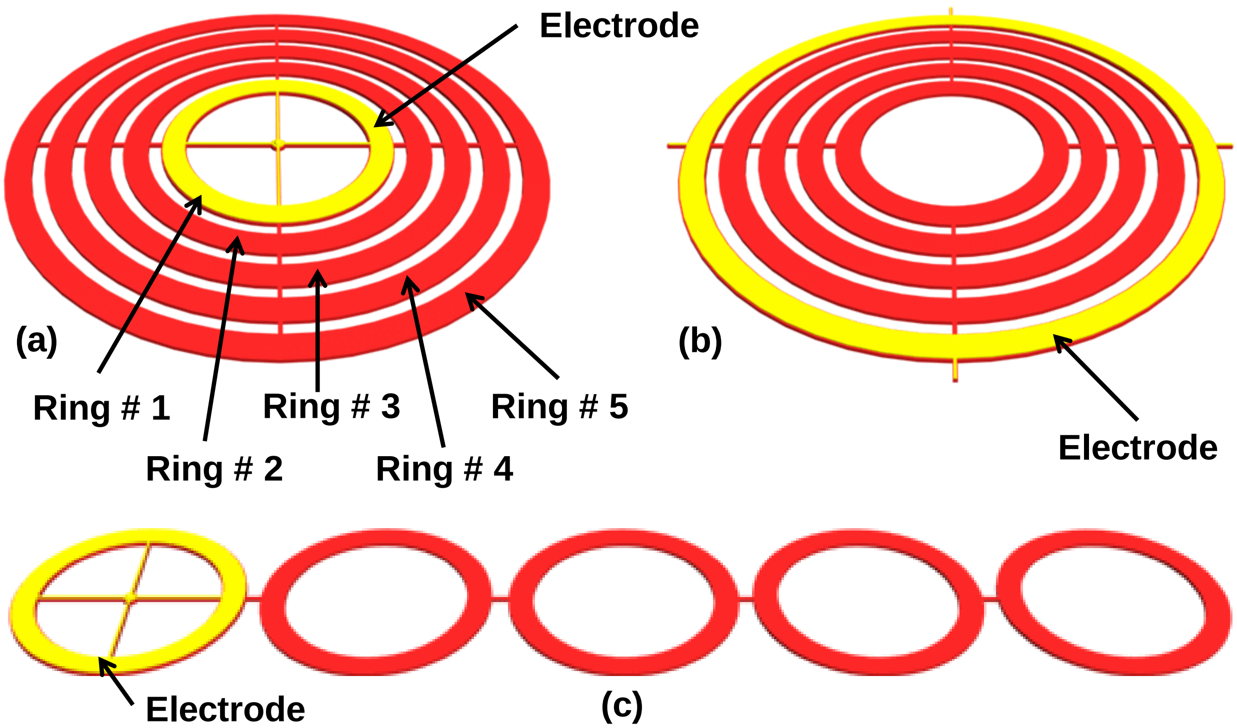

Fig. 5-7: Three resonator-composites that occupy the same areas. The design parameters of each ring is listed in Table 5-1. (a) a concentric rings configuration with electrodes on the smallest ring; (b) a concentric rings configuration with electrodes on the largest ring; (c) a chain of resonators each has the same size as the smallest ring in (a) and (b).

Table 5-1: Design parameters of rings of the same width but various average radii, as shown in Fig. 5-7(a) and (b).

Ring #., n	Ave. Radius, R_{Ave} (μm)	Res. Freq., f_o (MHz)	Res. Freq. Ratio (f_n/f_1)	Stiffness, k_{rn} (N/m)	Stiffness Ratio ($k_{rn}/k_{r1}=\beta_i$)	Mass, m_{rn} (kg/m^3)	Mass Ratio ($m_{rn}/m_{r1}=\beta_i$)
n=1	40	535.81	1	6.86x10^7	β_1 = 1	6.05x10^{-12}	β_1 = 1
n=2	54.87	534.74	0.998	9.40 x10^7	β_2 = 1.37	8.32x10^{-12}	β_2 = 1.37
n=3	69.74	534.28	0.997	1.19 x10^8	β_3 = 1.74	1.06 x10^{-11}	β_3 = 1.75
n=4	84.61	534.05	0.997	1.45x10^8	β_4 = 2.11	1.29 x10^{-11}	β_4 = 2.12
n=5	99.51	533.91	0.997	1.70 x10^8	β_5 = 2.50	1.51 x10^{-11}	β_5 = 2.50

Table 5-2: Performance comparison of the three resonator array-composites in Fig. 5-6.

Array #	Array Mass Ratio (m_{Mckt}/m_{ro})	Array Stiffness Ratio (k_{Mckt}/k_{ro})	Array Damping Ratio (c_{Mckt}/c_{ro})	Array Coupling Ratio (η_{Mckt}/η_{ro})	Array Q Ratio (Q_{Mckt}/Q_o)	Array Impedance Ratio (R_{Mckt}/R_o)
(a)	8.74	8.74	1.0774	1	8.11	1.0774
(b)	8.74	8.74	2.56	2.5	3.50	0.41
(c)	5	5	1.04	1	4.81	1.04

5.2.3 Variation in Coupling Locations

The above analysis assumes all array coupling ratios, η_c, to be identical. This section discusses the possibility of achieving a Q-boosting factor by leveraging η_c values.

This is true when the locations on the resonator where the two coupling beams are attached to share the same stiffness. Close examination on the circuits in Fig. 5-5(b) reveals that the modifier on the values of each circuit element, (N-1), can be absorbed to one of the transformer turn ratios, η_c, without changing the electric response of the circuit. The resulting electric circuit is shown in Fig. 5-8(a) with

$$\frac{\eta_{c2}}{\eta_{c1}} = \sqrt{N-1} \tag{5-19}$$

As discussed in Chapter 1, η_c value greater than unity can be achieved via low-velocity coupling, where the resonators are coupled at locations with lower velocities than the maximum velocity. Such coupling scheme has been implemented with notched supports and been applied to filters for achieving smaller bandwidth without further scaling the coupling beams [11][12]. Fig. 5-9(b) represents one possible implementation of such a Q-booting mechanical circuit corresponding to the electric circuit in Fig. 5-8. Compared to the mechanical circuit in Fig. 5-

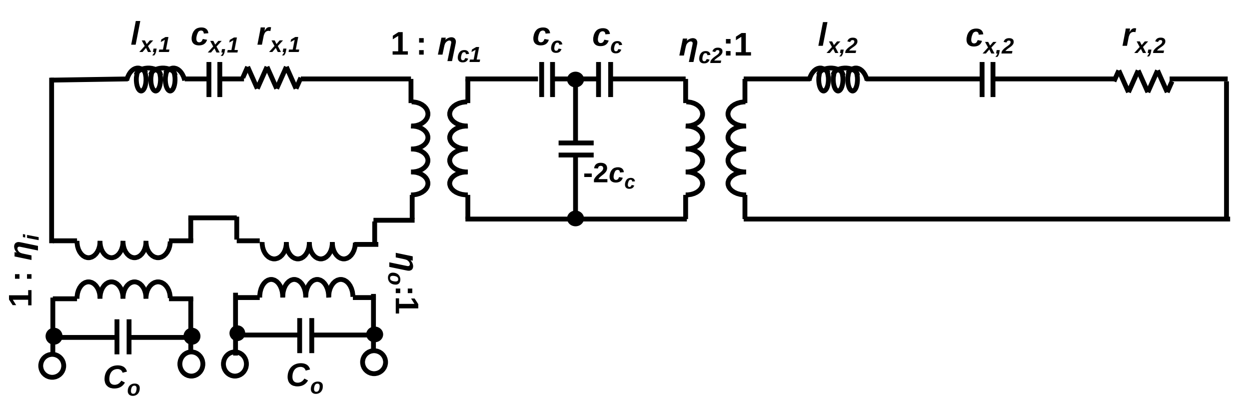

Fig. 5-8: The electrical circuit has the same electrical response when the values of η_{c2} and η_{c1} follow the relationship in (5-19).

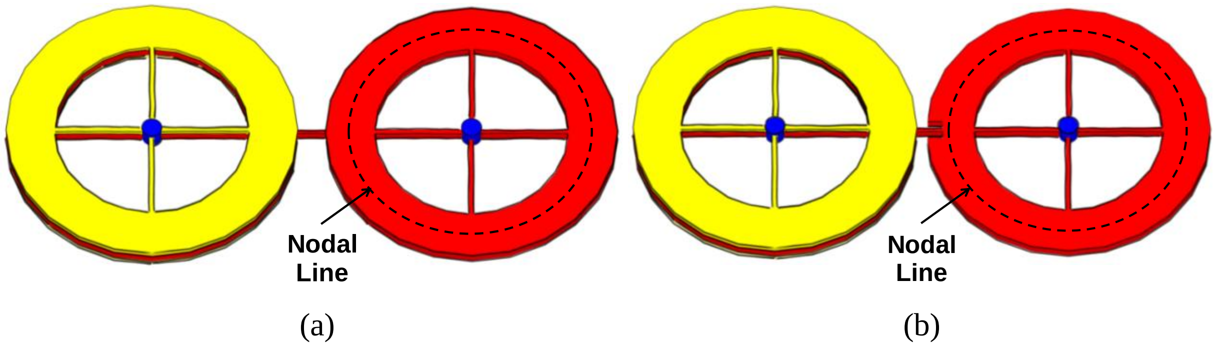

Fig. 5-9: (a) the electrical circuit has the same electrical response when the values of η_{c2} and η_{c1} follow the relationship in (5-19); (a) the corresponding mechanical circuit when $\eta_{c2} = \eta_{c1}$, which is equivalent to the circuit in Fig. 5-5(b) with N = 2; (b) a possible implementation of the circuit in Fig. 5-8(a) using low-velocity coupling on the electrode-less resonators, achieving $\eta_{c2} > \eta_{c1}$.

9(a), the array-composite resonator with low-velocity coupling to the higher-*Q* resonator occupies the same layout area but can achieve higher *Q*-boosting factors. Design on the coupling locations offers is an efficient way to further reduce the layout footprint of *Q*-boosting circuits.

5.3 EXPERIMENTAL RESULTS

5.3.1 Fabrication of AlN *Q*-Boosted Composite-Array

Q-boosting wine-glass disk array-composite resonators were fabricated via the process summarized in Fig. 5-10, which features 1.5μm-thick AlN structural material, 120 nm thick Al top and bottom electrodes, electroplated Ni anchors, and the use of Mo sacrificial layers removed via dry XeF_2 etching. The material set and the fabrication steps used here are similar to those described in Chapter 4. The differences worth-noting are listed below:

1. The lithography performed in step (3) and step (5) both use G-line photoresist and CD-30 developer, as most metal-free developer solutions suitable for CMOS and MEMS processes contain TMAH which attacks Al.
2. The Al bottom electrodes are patterned via wet etch in OPD 4262, a TMAH based-developer. Highly-selective wet etch is preferred over dry etch here to maintain a smooth surface at areas without bottom electrodes, on which the AlN film will form the *Q*-boosting resonators. Surface roughness is essential for proper c-axis orientation of the AlN film sputtered later on in the process. Although the AlN film in *Q*-boosting resonators is not responsible for energy conversion and its d_{31} coefficient is not critical to device performance, experimental results have shown that resonators made of AlN films with smaller FWHM peak of XRD measurement (*i.e.*, better c-axis orientation) tend to achieve not only larger coupling but also higher *Q*.
3. The Al top electrodes are patterned via RIE with chorine based chemistry and the etch

stops on AlN. Wet etch is not convenient here, as most etchants that etch Al also attack AlN. While minimizing the roughness of the top surface of AlN film may be helpful for achieving higher resonator *Q*, it is not as critical as the smoothness requirement of the substrate prior to AlN sputtering.

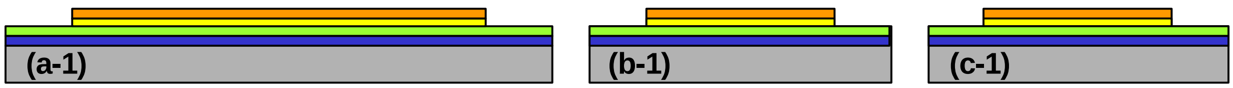

(1) Deposit isolation layers SiO_2/SiN; lift-off Al/Ni as the ground electrodes, interconnect, and bond pads.

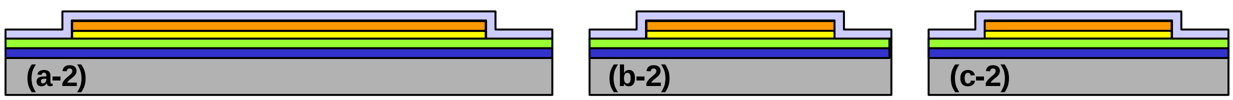

(2) Sputter and pattern sacrificial Mo via wet etch.

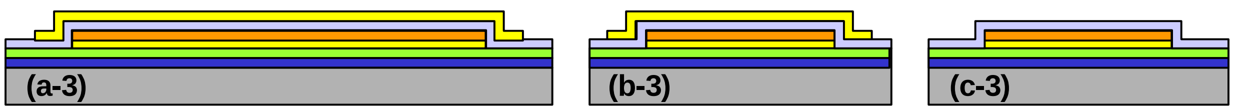

(3) Sputter and pattern bottom Al electrodes via wet etch;

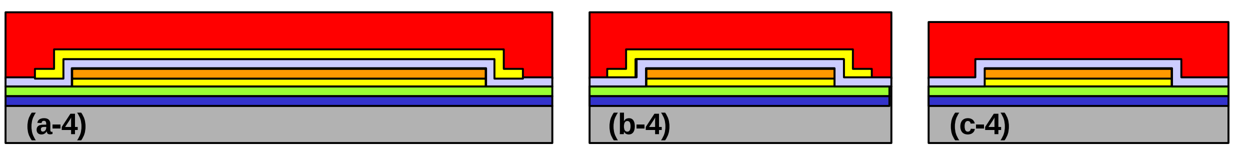

(4) Sputter blanket AlN.

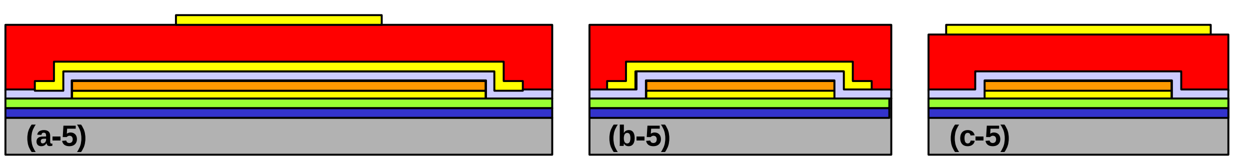

(5) Sputter and pattern top Al electrodes via dry etch.

Fig. 5-10-1: Fabrication process flow using cross-sections from the (a) disk, and (b) and (c) anchor areas, explicitly showing the electrical contact between the electroplated Ni anchor and the bottom and top Al electrodes, respectively.

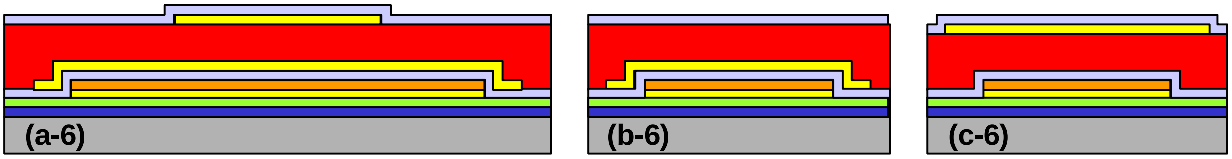

(6) Sputter 20 nm thick Mo as barrier layer before PECVD oxide.

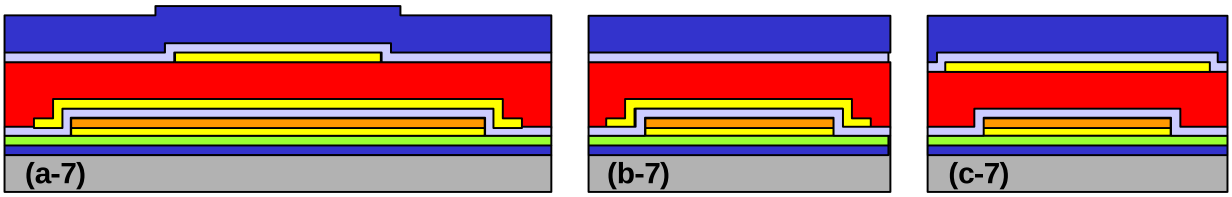

(7) PECVD oxide at 300 °C.

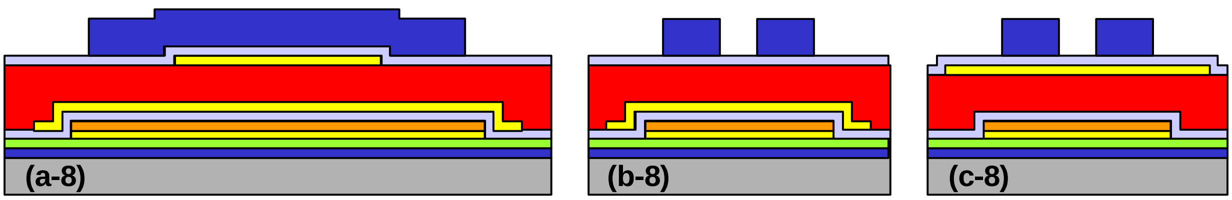

(8) Pattern oxide mask via dry etch; the etch stops on the Mo barrier layer.

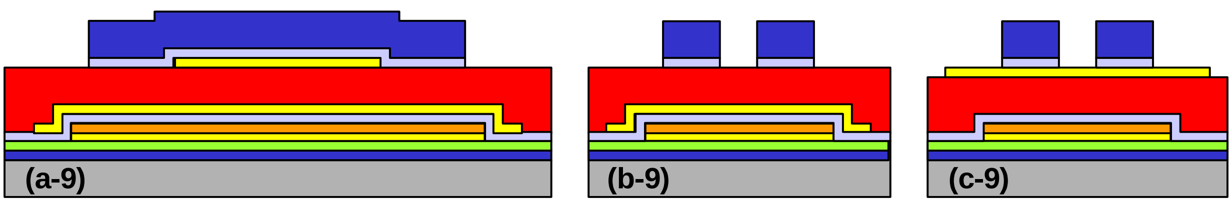

(9) Dry etch Mo barrier layer with $O_2/Cl_2/CHCl_3$ mixed gases; the etch stops on AlN.

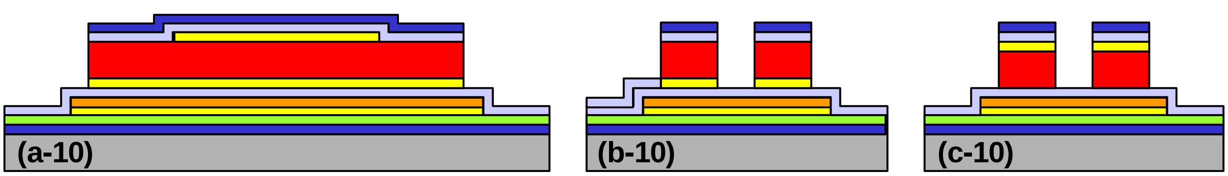

(10) Dry etch AlN with $Cl_2/Ar/CHCl_3$ mixed gases; the etch stops on the first sacrificial Mo layer.

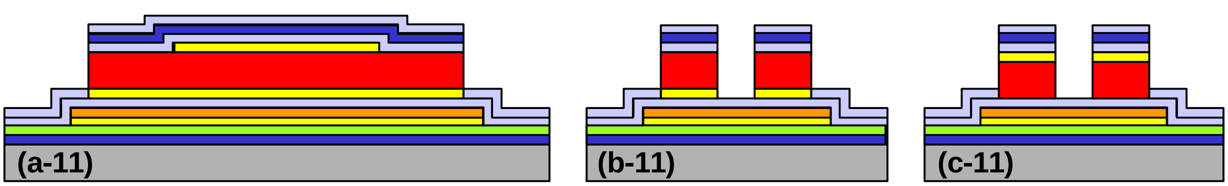

(11) Sputter 20 nm thick Mo layer to electronically connect the entire wafer for electroplating in the next step.

Fig. 5-10-2: Steps 6 to 11 of the fabrication process flow.

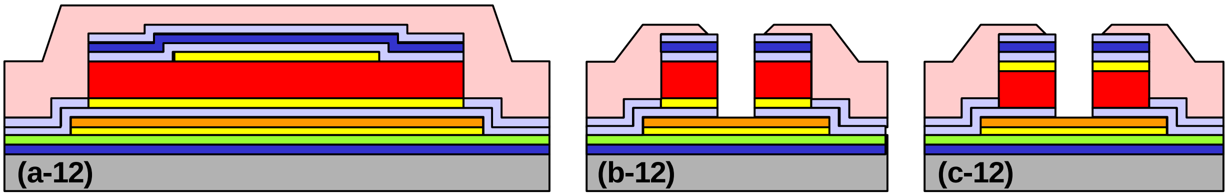

(12) Pattern thick photoresist; dry etch Mo within the trenches to expose the underlying nickel layer as seed layer for electroplating.

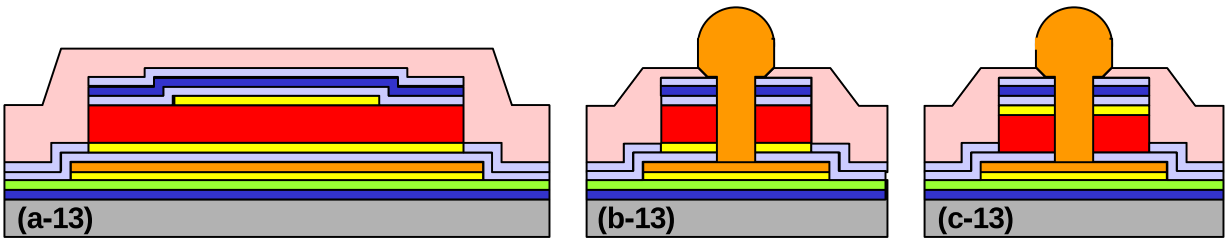

(13) Electroplate nickel upward from the bottom Ni seed layer to fill the trenches as conductive anchors.

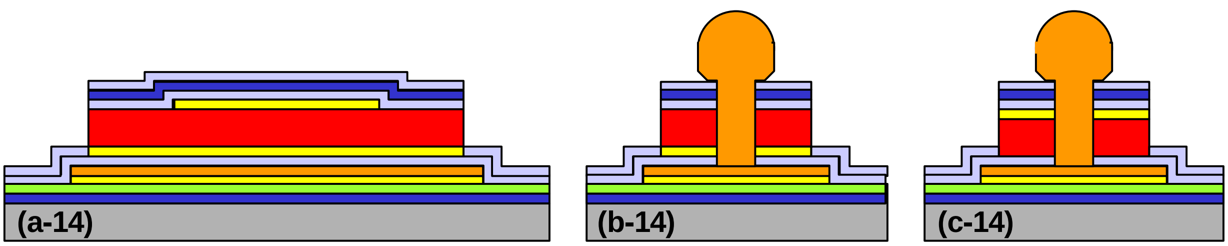

(14) Strip thick PR in oxygen plasma.

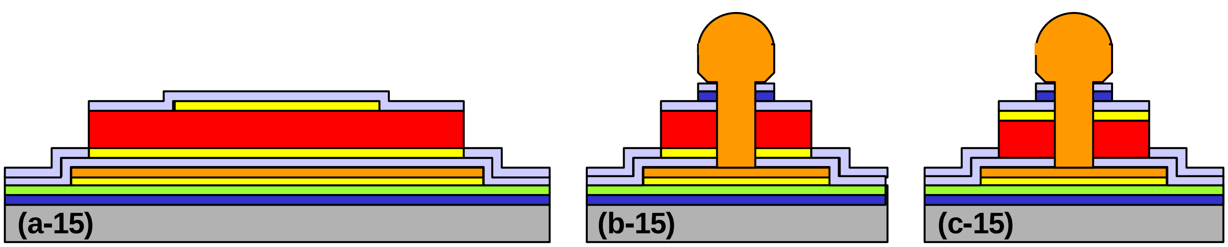

(15) Dry etch the thin Mo layer and the remaining oxide hard mask.

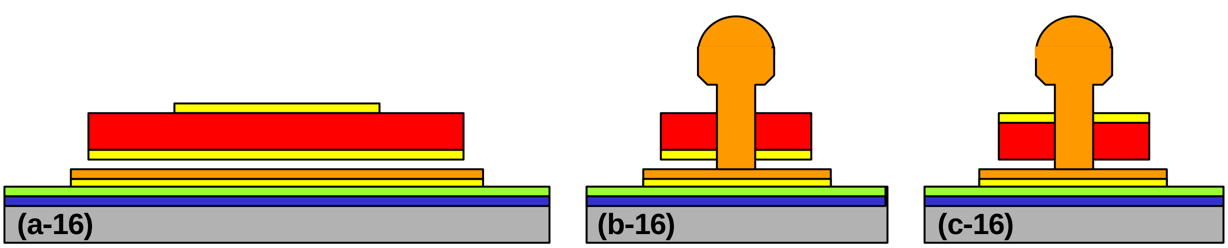

(16) Release in XeF_2/N_2 mixed gases.

Fig. 5-10-3: Steps 12 to 16 of the fabrication process flow.

Fig. 5-11(a) and (c) present the microscopic images of the resulting structures in step (5) with photoresist patterns and before Al dry etching. The electrodes are patterned such that each anchor provides electrical access to either the top or the bottom electrode. For ring resonators each supported by a single anchor at the center, 2-resonator arrays are used such that each anchor electrically connected to the top and bottom electrodes, respectively, as shown in Fig. 5-11(c). For wine-glass disk resonators with two anchors at two of the four quasi-nodal points of the wine-glass mode shape, shown in Fig. 5-11(b), each anchor is connected to either the top or the bottom electrodes. All of the bottom electrodes are electrically connected to the grounding electrode of each resonator to prevent undesired electrodes between the bottom and grounding electrodes. Grounding electrodes also apply to resonators without top and bottom electrodes to prevent undesired electrostatic forces caused by dielectric charging on either AlN or the isolation dielectric layers. Fig. 5-11(c) presents the microscopic image of a ring resonator array after step (5), with clear distinguishment of the resonators with and without electrodes.

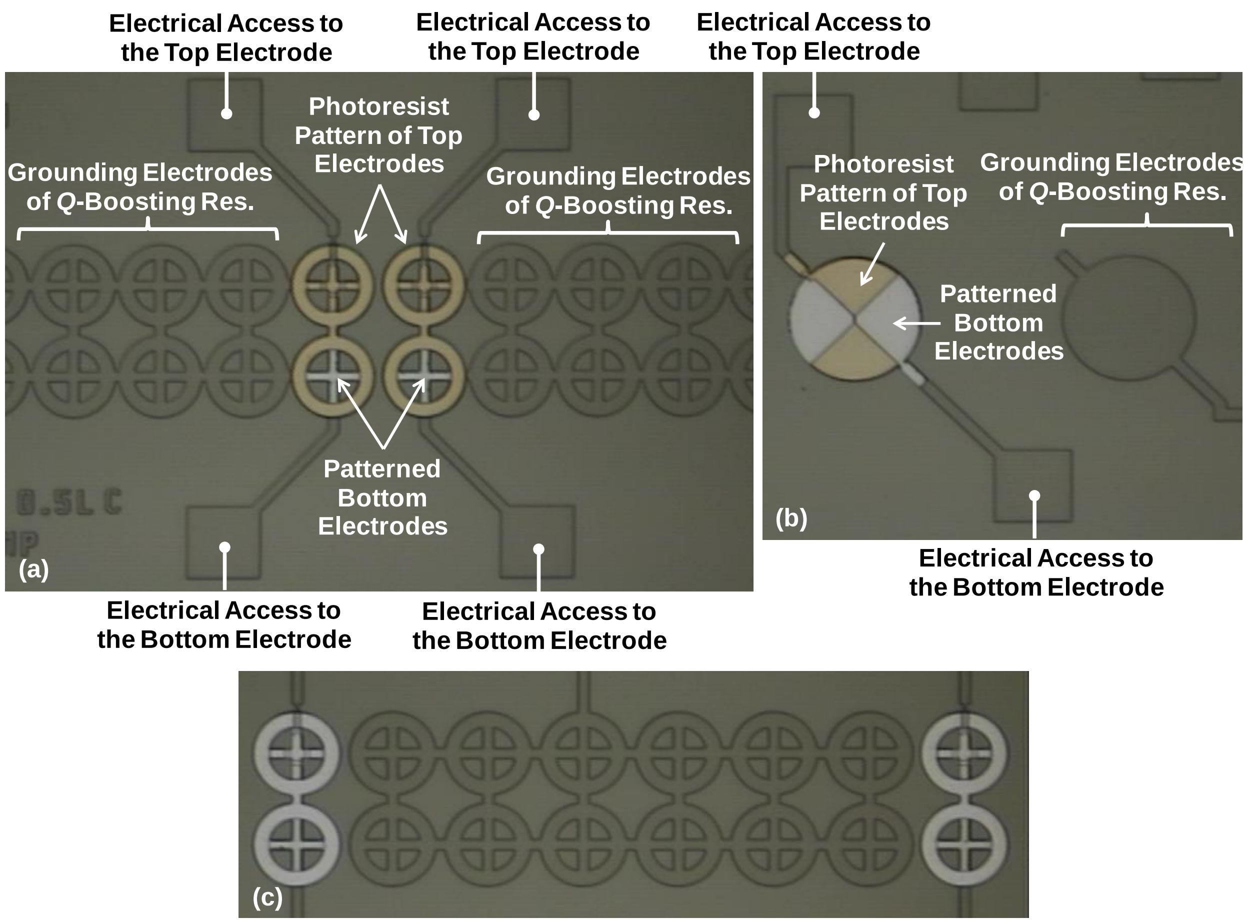

Fig. 5-11: (a) and (b) show microscopic images of *Q*-boosting ring and wine-glass disk resonator array-composites, respectively, after step (5) in and before removing the photoresist; (c) an array-composite similar to the one in (a) after the photoresist is removed, clearly showing the electrodes only on certain resonators while the others are electrode-less.

Fig. 5-12 presents SEM's of a 125-MHz version using four disk resonators, each supported by two support beams attached at quasi-nodal points of the wine-glass mode, and all mechanically coupled to one another via half-wavelength coupling beams. Fig. 5-12(a) and (c) present zoomed-in views on an electrode-equipped and an electrode-less resonator, respectively. For each electrode-equipped resonator, Ni anchors provide electrical access to the electrodes, one connecting to the top electrode and the other to both the bottom and ground plane electrodes. Ground plane electrodes are also used in the electrode-less resonators to prevent charging of their AlN films during electrical measurement. Fig. 5-12(d) zooms-in on the edge of an electrode-less resonator, showing the disk suspended above the substrate after release.

Fig. 5-13 presents SEM images of fabricated AlN *Q*-boosting array-composites. For each array-composite, there is one electrode-loaded resonator on each end, which is coupled to various numbers of *Q*-boosting resonators between them. The largest array contains thirty *Q*-boosting resonators. Overhanging bridges made of Al/AlN/Al film stacks and supported by electroplated nickel posts, shown in Fig. 5-13(f), helps simplify the interconnection of such large mechanical circuits.

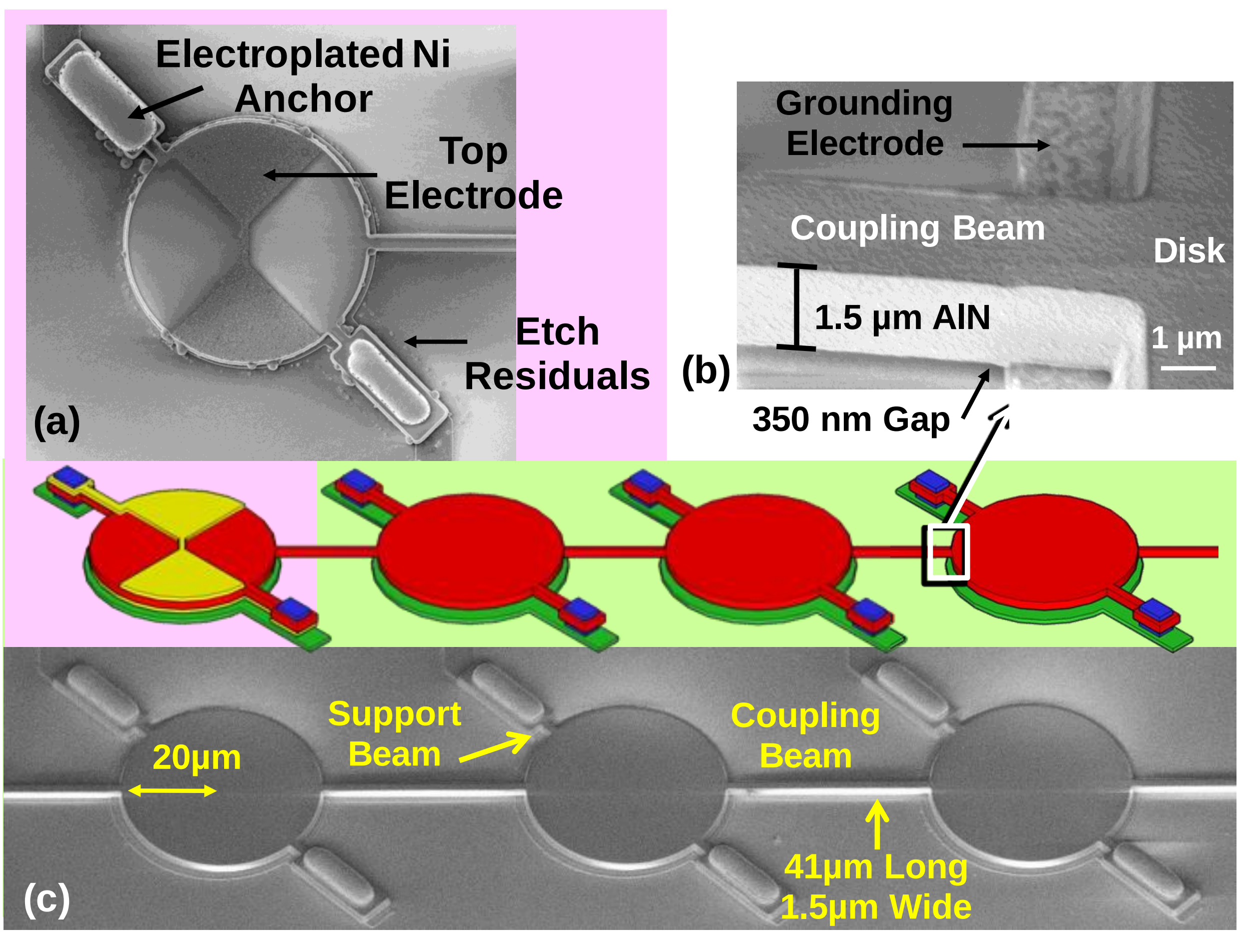

Fig. 5-12: SEM images of fabricated AlN *Q*-boosting resonator array-composite: (a) electrode-loaded resonator; (b) zoomed-in view on the edge of a disk resonator and (c) electrode-less resonators.

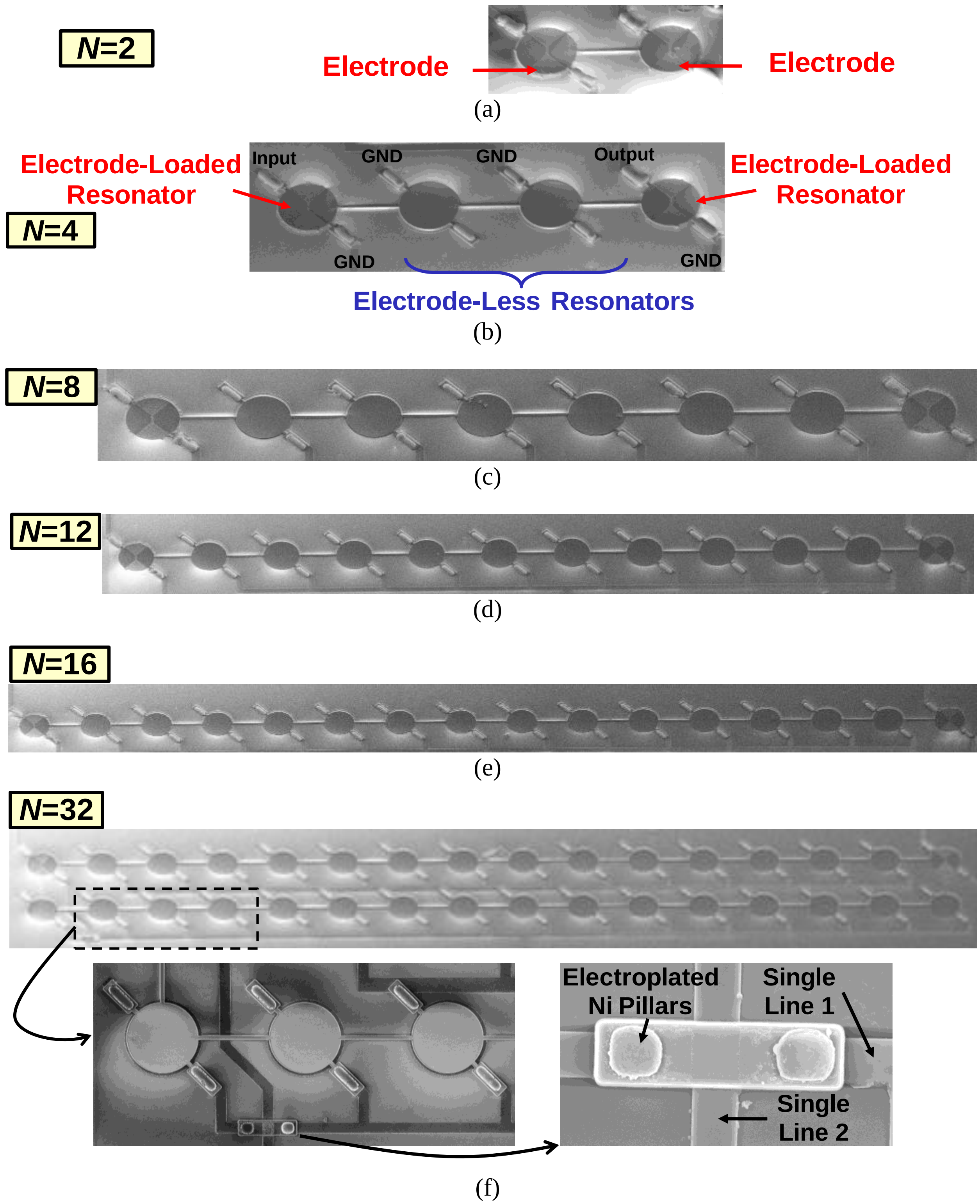

Fig. 5-13: (a)-(f) Fabricated AlN *Q*-boosting array-composites each with two electrode-loaded resonators and number of electrode-less (*Q*-boosting) resonators ranging from 0 to 30. (f) also shows the zoomed-in views on the interconnect bridges used to implement more complicated mechanical circuits.

5.3.2 Electrical Measurements

The *Q*-boosting resonator array-composites were measured using the setup in Fig. 5-14(a), where the chamber pressure is 3 mTorr. The input signal is applied to the top electrode on one of the electrode-loaded resonator and the output currents are collected from the top electrode on the other electrode-loaded resonator. As AlN has low electrical conductivity, the output port is electrically isolated from the input port, resulting in minimum feed-through currents. The two electrode-loaded resonators are placed at the two ends of the array-composite to further minimize the feed-through currents capacitively coupled from the isolation layers and the substrate. Unlike electrostatic resonators, no DC bias is required to actuate the piezoelectric resonators. However, DC bias can be useful to tune the frequencies of individual resonators to possibly reduce the spurious modes and maximize the output power if large frequency differences occurred from fabrication process variations. Furthermore, all of the bottom and ground electrodes are grounded to prevent vertical electrostatic forces that can pull the resonators down to the substrate.

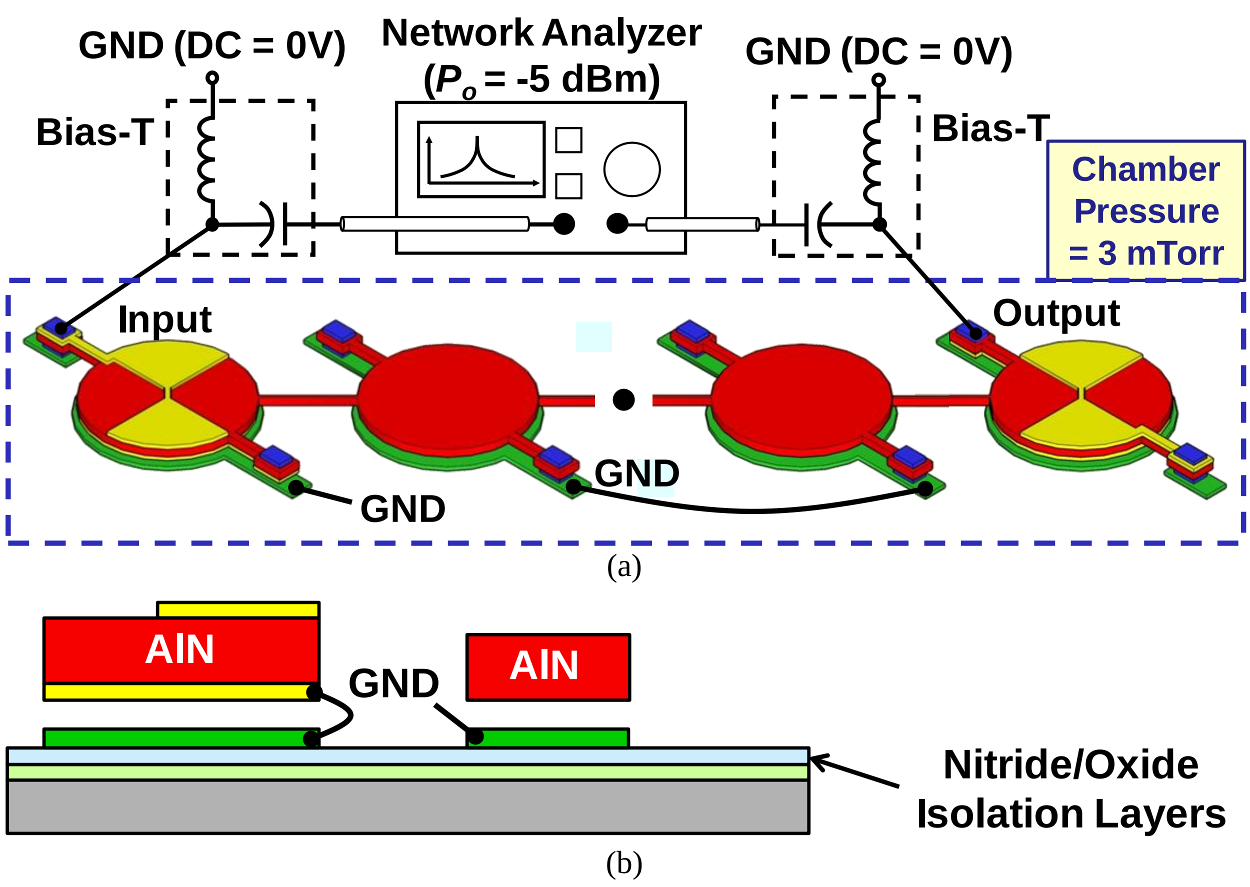

Fig. 5-14: (a) Measurement setup for *Q*-boosting resonator array-composites, where the input and output ports are electrically isolated for minimum feedthrough currents; (b) all of the grounding electrodes and bottom electrodes are properly grounded to prevent vertical electrostatic forces that may pull resonators down to the substrate.

Fig. 5-15 presents measurement results using the scheme of Fig. 5-14(a), where the top electrodes of the left and right end resonators serve as input and output ports, respectively, and all bottom and ground plane electrodes are grounded. Before Q-boosting, an array comprising two electrode-equipped resonators exhibits a measured Q = 1,755 (Fig. 5-13(a)) that is lower than previous work [3], probably due to etch residuals at the AlN/Al interfaces that are visible in Fig. 5-13(b). Nevertheless, as shown in Fig. 5-15(b)-(f), as the number of Q-boosting electrode-less resonators in the array-composite increases, its Q increases, reaching as high as 10,444 for the 32-resonator circuit, shown in Fig. 5-15(f), which is the highest measured so far for any resonator constructed in sputtered thin-film AlN. The peak height changes very slowly as the number of resonators is increased, confirming that impedance is not impacted until Q_{Mckt} is on the order of that of the high-Q resonators. Table 5-3 summarizes these measurement results.

Although the piezoelectric work in Chapter 4 demonstrates higher Q by lifting off the electrodes from the resonator body to eliminate the electrode losses, the etch residuals in the gap spacing possibly reduce Q and prevent the resonator from revealing the material Q of the AlN material. The electrode-loaded resonators in this work suffer from similar metal contamination issues, where etch residuals appear on the edges of electrode-loaded disks where electrodes remain. This issue arises from direct etching of metal and AlN film stacks. Electrode-less resonators, on the other hand, remain clean and free from etch residuals after release and can be a better way to tap the material Q of AlN without the influence of electrodes and etch residuals.

Fig. 5-16(a) plots measured data of Q_{Mckt} alongside the governing equation for Q_{Mckt} given by (5-11) with the number of electrode-equipped resonators n_e=2 and with the Q of electrode-equipped resonators Q_o = 1,755. All measured data points are clearly bounded by curves generated when assuming electrode-less resonator Q of Q_{AlN}=14,040 (*i.e.*, α = 8) and Q_{AlN} = 15,795 (*i.e.*, α = 9) in (5-5), suggesting that the Q of an electrode-less AlN resonator is somewhere between these values, and confirming that AlN is capable of achieving high-Q (Q > 10,000) when metal electrodes are not present. The Q of the electrode-less resonators affect not only the measured Q_{Mckt} but also the impedance, R_{Mckt}. Similar procedures can be applied to extrapolated Q_{AlN} by plotting measured data of R_{Mckt} alongside the governing equation for R_{Mckt} given by (5-12), as shown in Fig. 5-16(b). This approach gives the same range of Q_{AlN} as using the Q_{Mckt} data.

Table 5-3: Summary of measurement results of various Q-boosting resonator array-composites.

Total # of Total Res., n	# of Q-Boosting Res., n_e	Measured Array Q, Q_{Mckt}	Q-Boosting Factor (Q_{Mckt}/Q_o)	Measured Array R, R_{Mckt}	Impedance Ratio (R_{Mckt}/R_o)
2	0	1,755 = Q_o	1	3137	1
4	2	3,162	1.8	3545	1.13
8	6	5,167	2.9	4360	1.39
12	10	6,264	3.6	5175	1.65
16	14	7,711	4.4	5990	1.91
32	30	10,444	6.0	9249	2.95

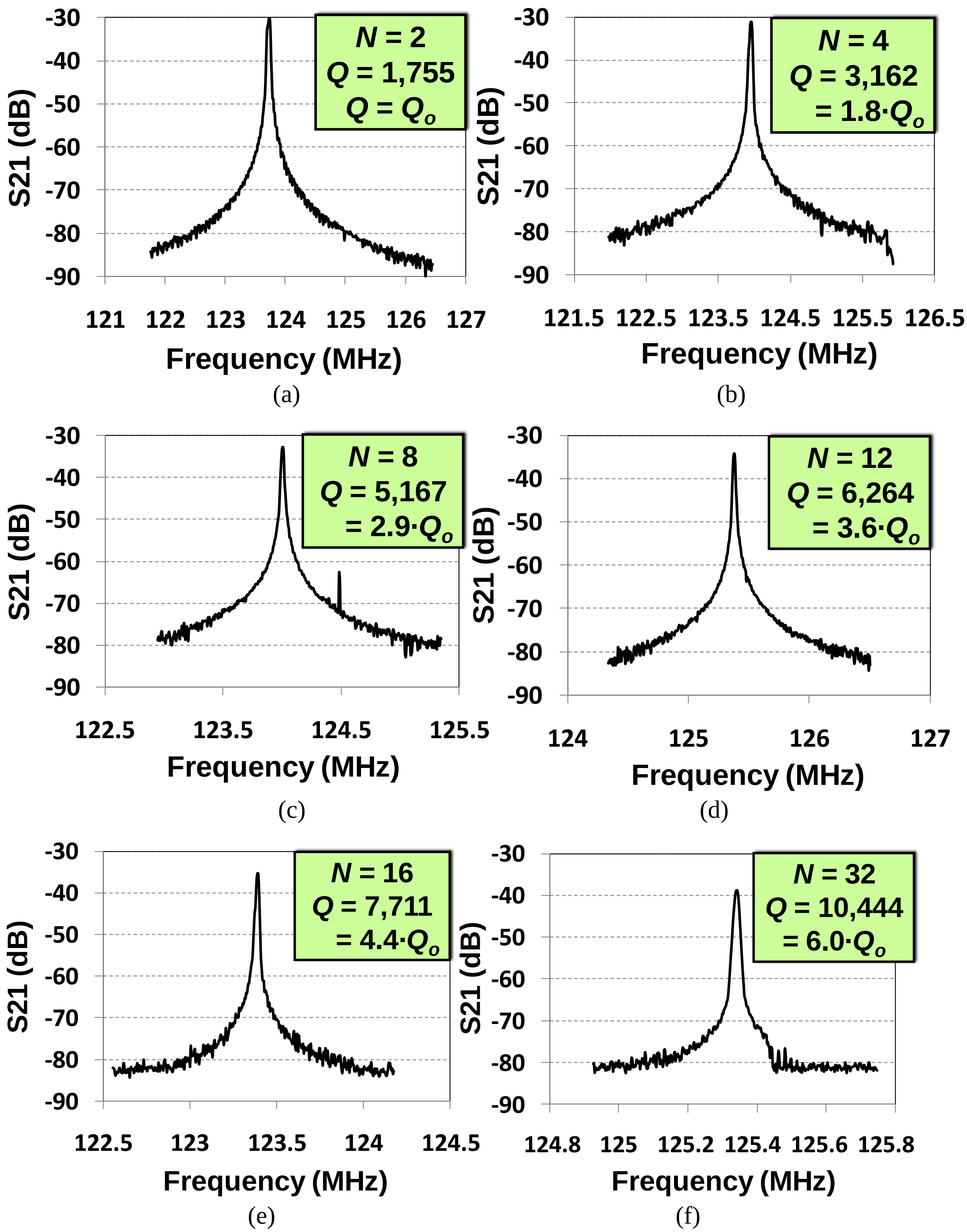

Fig. 5-15: Electrical measurement results of *Q*-boosting resonator array-composite of various numbers of *Q*-boosting resonators in the array.

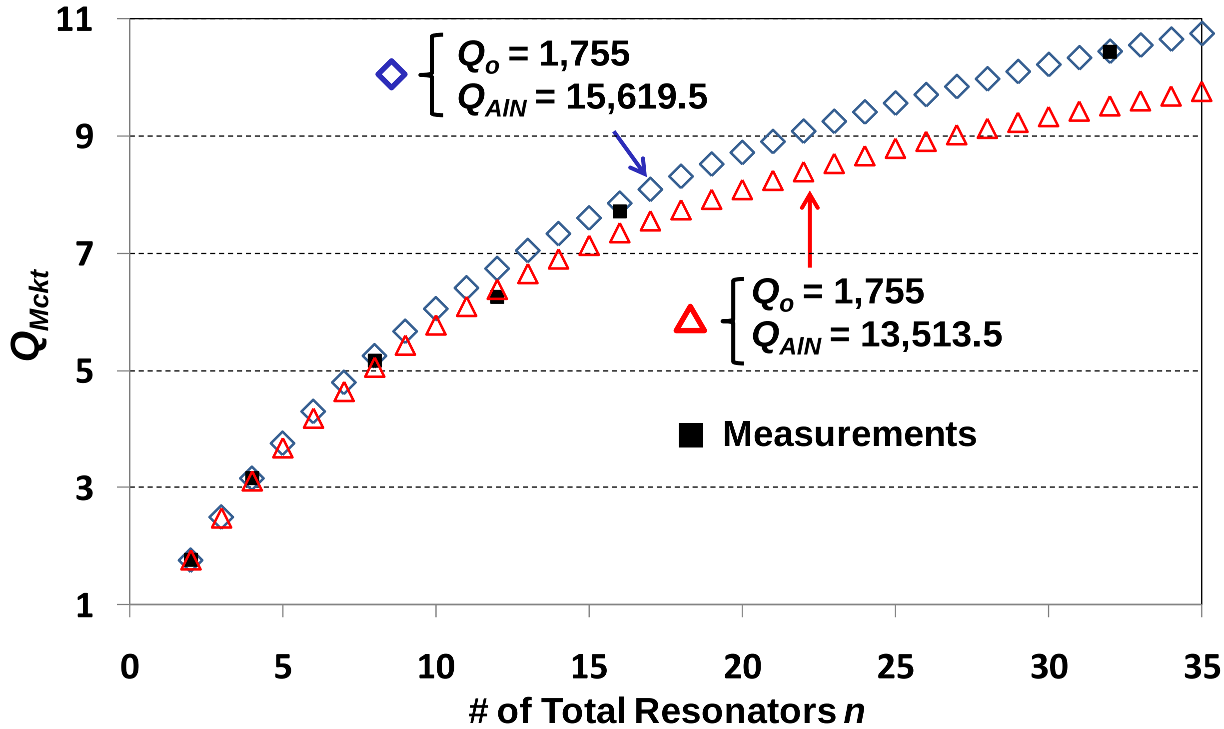

(a)

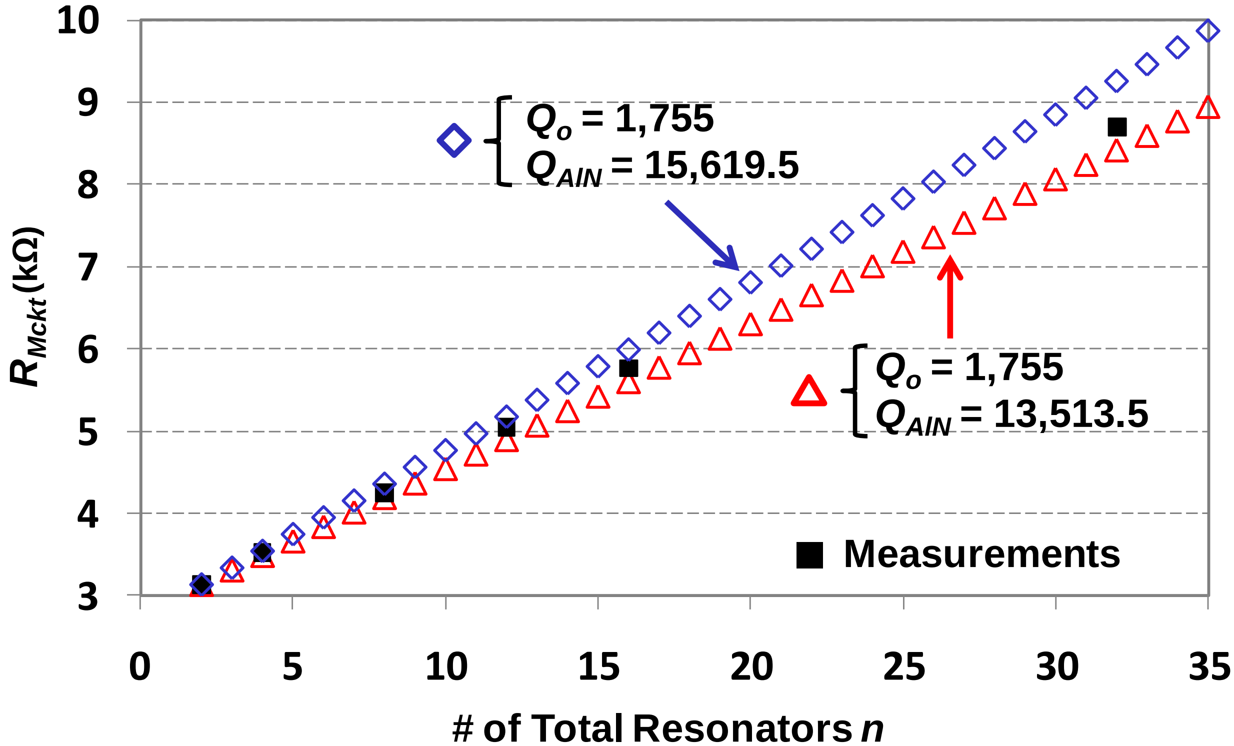

(b)

Fig. 5-16: Plots of theoretical prediction and the measured data of resonator array-composite with different numbers of Q-boosting resonators to extrapolate Q_{AlN} (a) using and the measured data of Q_{Mckt}; (b) using and the measured data of R_{Mckt}.

5.4 Conclusions

Via use of a *Q*-boosting mechanical circuit, array-composite resonator *Q* as high as 10,444 has been achieved, and curve-fitting reveals *Q* = 14,040~15,795 for electrode-less AlN resonators — more than 8× larger than the *Q*=1,755 of electrode-equipped versions. These numbers confirm that AlN itself is indeed a high *Q* material and losses associated with electrodes, not the material, are most responsible for the lower *Q* historically measured for AlN resonators. The *Q*-boosting method demonstrated here further constitutes an attractive approach to achieving the simultaneous high *Q* and strong electromechanical coupling sought by many emerging applications, such as RF channel-selecting communication transceivers. The method's ability to boost *Q* is certainly extendable to other piezoelectric materials, such as ZnO and PZT, and even higher *Q* should be possible if piezoelectric resonators can be coupled to resonators constructed of higher *Q* materials, such as poly-crystalline diamond [13].

5.5 References

[1] J. Wang, J. E. Butler, T. Feygelson, and C. T.-C. Nguyen, "1.51-GHz polydiamond micromechanical disk resonator with impedance-mismatched isolating support," in *Tech. Digest*, Int. IEEE Conf. on Micro Electro Mechanical Systems (MEMS'04), 2004, pp. 641-644.

[2] C. T.-C. Nguyen, "Integrated micromechanical RF circuits for software-defined cognitive radio," *26th Sym. on Sensors, Micromachines, and App. Sys*., 2009, pp. 1-5.

[3] G. Piazza, P. J. Stephanou, and A. P. Pisano, "Piezoelectric aluminum nitride vibrating contour-mode MEMS resonators," *J. Microelectromechanical Systems*, vol. 15, pp. 1406-1418, 2006.

[4] Y.-W. Lin, S.-S. Li, Z. Ren, and C. T.-C. Nguyen, "Low phase noise array-composite micromechanical wine-glass disk oscillator," *Technical Digest*, IEEE Int. Electron Devices Mtg. (IEDM'05), 2005, pp. 287-290.

[5] R. Tabrizian, M. Rais-Zadeh, and F. Ayazi, "Effect of phonon interactions on limiting the *f·Q* product of micromechanical resonators," *Dig. of Tech. Papers*, Int. Conf. on Solid-State Sensors & Actuators (Transducers'07), 2007, pp. 2131-2134.

[6] L.-W. Hung, and C. T.-C. Nguyen, "Capacitive-piezo transducers for higher *Q* contour-mode AlN resonators at 1.2 GHz," *Solid-State Sensor Actuator Workshop*, Hilton Head, 2010, pp. 463-466.

[7] L.-W. Hung, and C. T.-C. Nguyen "Capacitive-piezoelectric AlN resonators with *Q* > 12,000," in *Tech. Digest*, 24th Int. IEEE Conf. on Micro Electro Mechanical Systems (MEMS'11), 2011, pp. 173-176.

[8] L.-W. Hung, and C. T.-C. Nguyen , "*Q*-boosted AlN array-composite resonator with *Q*>10,000," *Technical Digest*, IEEE Int. Electron Devices Mtg. (IEDM'10), 2010, pp. 162-165.

[9] Y.-W. Lin, L.-W. Hung, S.-S. Li, Z. Ren., and C. T.-C. Nguyen, “Quality factor boosting via mechanically-coupled arraying,” *Dig. of Tech. Papers*, Int. Conf. on Solid-State Sensors & Actuators (Transducers’07), 2007, pp. 2453-2456.

[10] S.-S. Li, Y.-W. Lin, Y. Xie, Z. Ren, and C. T.-C. Nguyen, "Micromechanical "hollow-disk" ring resonators," in Tech. Digest., 17th IEEE Int. MEMS Conf., pp. 821-824, 2004.

[11] F. D. Bannon, J. R. Clark, and C. T.-C. Nguyen, “High-*Q* HF microelectromechanical filters,” *J. Solid-State Circuits*, vol. 35, no. 4, pp. 512–526, 2000.

[12] S.-S. Li, Y.-W. Lin, Y. Xie, Z. Ren, and C. T.-C. Nguyen, “Small percent bandwidth design of a 431-MHz notch-coupled micromechanical hollow-disk ring mixer-filter,” *Proceedings*, IEEE Int. Ultrasonics Symposium, Sept. 18-21, 2005, 1295-1298.

[13] J. Wang, J. E. Butler, T. Feygelson, and C. T.-C. Nguyen, “1.51-GHz nanocrystalline diamond micromechanical disk resonator with material-mismatched isolating support,” *Proceedings*, 17th Int. IEEE Micro Electro Mechanical Systems Conf., Maastricht, The Netherlands, Jan. 25-29, 2004, pp. 641-644.

Chapter 6: Conclusions

6.1 Achievements

The work presented in this dissertation successfully demonstrates four new approaches to improve the performance of both capacitive and piezoelectric resonators. Specifically, two new approaches are demonstrated to facilitate fabrication of gap spacing on the order of 20 nm. Such small gap spacing is the most efficient way to improve the coupling efficiency of capacitive transducers and to reduce the impedance of capacitive resonators. Another two approaches aim to improve the Q of piezoelectric resonators by eliminating the losses associated with contacting electrodes common used for piezoelectric resonators. Although this work targets at applications for wireless communication, other applications which require unconventional microfabrication techniques, capacitive transducers, or piezoelectric transducers are likely to benefit from the results of this work as well.

Conventionally there are three ways for forming suspended microstructures: wafer bonding, anisotropic etching, and release etch. While wafer bonding can achieve ideally unlimited aspect ratio, it is usually not a cost and layout area efficient process. Whenever there is an etching step involved in the release process, the mass transportation rate and the etch selectivity together limit the maximum achievable aspect ratio of the microstructure. Instead of directly etching a small gap, ALD partial-gap filling was used to reduce the gap spacing from 97 nm to an effective gap spacing of 32 nm, resulting in 7x increase in the coupling coefficient. Even with Q reductions caused by partial-ALD-gap filling that in turn result in R_x's only 2.7X better than those of larger air gap devices, the impact of this work is still enormous. This impact is perhaps best gauged by considering the effect of partial-ALD-gap filling on the demonstrated differential disk array filter of [1]. Here, a reduction in gap spacing from 80 nm to 32 nm of the resonators used in this micromechanical circuit would reduce the needed filter termination resistors R_Q from 2.8kΩ to only 72Ω, which is now compatible with present-day board-level impedances. Since the Q's of the radial-mode disk resonators used in the work of [1] were only 10,500, the Q of 10,510 of this work can maintain the same low insertion loss of 2.43 dB for 0.06 % bandwidth performance of that filter, but with much smaller matching impedances. Work to actually demonstrate such a filter using partial-ALD-filled gaps is in progress.

Another approach, silicide-induced gaps, removes the etching entirely from the release process. By utilizing a volume shrinkage-based method for forming gaps between structural layers and thereby avoiding the need for etching, the silicide-based release process demonstrated in this work is cheaper, cleaner, and faster than conventional etch-based methods, as it requires no etching, consumes no chemicals, and has little dependence on mass transport processes. This is the first time that silicide is used to form internal gaps and to release microstructures. As the required annealing time is independent of the lateral dimension of the devices, this method can form internal gaps by annealing the device for only seconds or a few minutes, compared to tens of minutes or even hours required by etch release. For example, using this method, structures with aspect-ratios exceeding 260:1 have been released in less than two minutes—substantially less than the 40 minutes otherwise required by an etch-based release process. A titanium beam resonator released by silicidation is demonstrated to confirm the efficacy of this approach applied to a real application. The type of metal and semiconductor material used, the annealing conditions, the phase of the silicide formed, and the thickness of the metal together determine the final gap spacing. By sputtering thinner metal films, gap spacing as small as 32 nm is achieved. Furthermore, nickel silicide formed at less than 350 °C can be used for applications that have thermal budget constraints.

Piezoelectric resonators have conventionally been measured to show lower Q than capacitive ones. Therefore, there is a common belief that AlN sputtered at low temperatures is not a high Q material. The measurement results of both the capacitive-piezoelectric resonators and the Q-boosting AlN resonator array-composite confirm that losses associated with the electrodes are more responsible for the lower Q measured before.

The first approach eliminates the losses associated with the electrodes by separating the electrodes from the resonators. As the electrodes no longer mass loading the resonators, even thicker electrodes can be used to reduce the resistive loss, therefore higher Q. This scaling advantage is especially when smaller lateral dimensions of the resonators and the support beams are required for higher resonant frequencies. The coupling coefficient is a function of the gap spacing; the smaller the gap spacing, the larger the coupling coefficient. Unlike the ~ 20 nm requirements on the capacitive transducers for narrow-band filters at GHz frequencies, capacitive-piezoelectric transducers require no smaller than ~ 100 nm gap spacing, which can be achieved with conventional sacrificial material etching. A 1.2-GHz capacitive-piezoelectric contour-mode AlN ring resonator achieve a motional resistance of 889 Ω and Q = 3,073, confirming that resonators equipped with "capacitive-piezo" transducers can achieve higher Q than so far measured for any other d_{31}-transduced piezoelectric resonator at this frequency and at the same time maintain high electromechanical coupling. Further, by applying capacitive-piezo transduction to separate a 50-MHz AlN two-disk array-composite resonator from its electrodes by nano-scale gaps, a Q as high as 12,748 has been measured, which is the highest measured so far for any AlN resonator. The results of this work experimentally confirm theoretical predictions that AlN is a high Q material, capable of achieving the Q >10,000 needed for some RF channel-select wireless communication front-ends. They also confirm that it is most likely electrode loss, not material loss that dictates the lower Q's previously measured for AlN resonators with contacting electrodes. Given evidence that anchor losses probably still dominate the Q's of the devices used in this work, it would not be surprising if future use of capacitive-piezo transduction in more effective anchor-isolating designs yields devices with even higher Q's.

The last part of this work also sets out to prove that sputtered AlN is a high Q material. Q-boosting mechanical circuit consists of electrode-equipped and electrode-less resonators coupled to each other via half-wavelength coupling beams. Electrode-equipped resonators provide high coupling coefficients but lower Q while the electrode-less resonators can achieve high Q but are not involved in the energy conversion process. Via use of a Q-boosting mechanical circuit, where the energy stored in the higher Q resonator is shared with the lower-Q resonators, the overall array Q is 'boosted' to be higher than the Q of the electrode-equipped resonators. A Q-boosting AlN array-composite resonator Q as high as 10,444 has been achieved, and curve-fitting reveals Q = 14,040~15,795 for electrode-less AlN resonators — more than 8× larger than the Q=1,755 of electrode-equipped versions. These numbers confirm that AlN itself is indeed a high Q material and losses associated with electrodes, not the material, are most responsible for the lower Q historically measured for AlN resonators. The Q-boosting method demonstrated here further constitutes an attractive approach to achieving the simultaneous high Q and strong electromechanical coupling sought by many emerging applications, such as RF channel-selecting communication transceivers.

6.2 Future Research Directions

The work presented in this dissertation successfully implemented four new techniques to achieve high-Q and low-impedance micromechanical resonators by either fortifying the electromechanical coupling of capacitive resonators or enhancing the Q of piezoelectric resonators. These techniques are useful for capacitive and piezoelectric transducers and forming high-aspect-ratio microstructures using microfabrication in general and, as a result, seed future research.

As either capacitive resonators equipped with sub-50 nm transduction gap spacing or capacitive-piezoelectric resonators with ~100 nm air gaps can achieve $Q > 10{,}000$ and sufficient coupling, it is now possible to implement narrow-band and low-loss MEMS filters at GHz frequencies. In particular, capacitive-piezoelectric resonators provide unique research opportunities in the following directions:

1. Filters implemented with the capacitive-piezoelectric resonators do not suffer from feedthrough currents and obsolete the need for differential operation to cancel the feedthrough currents as capacitive resonators [1].
2. Oscillators implemented with the capacitive-piezoelectric resonators can possibly achieve better far-from-carrier phase noise than capacitive ones due to larger power handling capability and maintain high Q, low impedance and high linearity necessary for minimizing far-from-carrier phase noise low at the same time.
3. The capacitive-piezoelectric resonators are suitable for CMOS-MEMS integration. The majority of the fabrication process for the capacitive-piezoelectric resonators demonstrated in this work has process temperature less than 300 °C. The only exception is the deposition of the isolation layers of low-stress nitride and thermal oxide, which are chosen to minimize the surface roughness before the actual fabrication starts. When integrated onto a CMOS chip, the intermediate isolation dielectric (ILD) layer followed by standard chemical mechanical polishing (CMP) can replace the need for the current high temperature deposition of isolation layers.

The silicide-induced gap is a method for releasing microstructures or forming internal gaps that is fundamentally different than all of the conventional ones. This method can be applied to a wide range of MEMS devices. On the other hand, more studies on material properties will help the researcher harness the silicidation process. For example, while silicidation dynamics have been studied for 30+ years, effects of silicide-induced gaps, where the capping layer imposes non-trivial boundary conditions on the reactive diffusion, is new to the field. To experimentally verify a proposed model, samples of various silicides can be *in-situ* annealed during X-ray diffraction measurements, which will reveal the progressive change in sub-surface film composition.

6.3 References

[1] S.-S. Li, Y.-W. Lin, Z. Ren, and C. T.-C. Nguyen, “An MSI micromechanical differential disk-array filter,” Dig. of Tech., the 14th Int. Conf. on Solid-State Sensors & Actuators (Transducers’07), Lyon, France, June 11-14, 2007, pp. 307-311.